

N 66-12265	
(ACCESSION NUMBER)	(T. (RU))
308	1
(PAGES)	(CODE)
	03
(NASA CR OR TMX OR AD NUMBER)	(CATEGORY)

NASA CR-54752
ER-6497

GPO PRICE \$ _____

CFSTI PRICE(S) \$ _____

Hard copy (HC) 7.00

Microfiche (MF) 1.75

653 July 65

NASA

BRAYTON CYCLE CAVITY RECEIVER

DESIGN STUDY

By

TRW POWER SYSTEMS DEPARTMENT

Prepared for

NATIONAL AERONAUTICS AND SPACE ADMINISTRATION
SPACE POWER SYSTEMS DIVISION
LEWIS RESEARCH CENTER

Contract NAS 3-2779

BRAYTON CYCLE CAVITY RECEIVER

DESIGN STUDY

by

TRW POWER SYSTEMS DEPARTMENT

prepared for

NATIONAL AERONAUTICS AND SPACE ADMINISTRATION

November 22, 1965

CONTRACT NAS 3-2779

Technical Management
NASA Lewis Research Center
Cleveland, Ohio
Space Power Systems Division
J. A. Milke

TRW EQUIPMENT LABORATORIES
A DIVISION OF TRW INC. • CLEVELAND, OHIO 44117

FOREWORD

This report presents the results of a design study of a Brayton Cycle Cavity Receiver performed under Contract NAS 3-2779 during the period from June 25, 1963 to June 15, 1965. The study was conducted for the Space Power Systems Division, Lewis Research Center, National Aeronautics and Space Administration, under the supervision of John A. Milko, Project Manager.

ACKNOWLEDGMENTS

The writers wish to acknowledge the assistance of Dr. G. L. Schrenk, of the University of Pennsylvania, and Mr. A. Lowi, of the Aerospace Corporation, for their individual contributions to the computer programming applied to this study.

ABSTRACT

The Lewis Research Center of the National Aeronautics and Space Administration is currently sponsoring studies leading to the design and development of solar dynamic power conversion systems which operate on the Brayton cycle. One of the components required in these systems is a solar absorber. The Equipment Laboratories Division of TRW Inc. was asked to conduct a design study of cavity-type receivers which employ lithium fluoride as the heat storage medium. The work effort included design and analysis of full scale flightweight receivers, conduction of a series of small scale experiments and an experimental corrosion properties investigation on selected materials. This topical report presents the results of the full scale design studies and of the small scale experiments. The results of the corrosion investigation are presented in TRW topical report No. ER-6561, "The Corrosion of Superalloys by Lithium Fluoride in a Cyclic High Temperature Environment." (Ref. NASA CR-54781)

BLANK PAGE

TABLE OF CONTENTS

	<u>Page</u>
1.0 SUMMARY OF RESULTS	1
2.0 INTRODUCTION	3
2.1 Initial Specifications	4
2.2 Revised Specifications	4
3.0 PRELIMINARY DESIGN ANALYSIS	5
3.1 Initial Design Investigations	5
3.2 Argon and Lithium Fluoride Property Values	21
3.3 Cavity Configuration Studies	24
4.0 SMALL SCALE EXPERIMENTS	37
4.1 Thermal Conductivity Experiments	37
4.2 Heat Input Experiments	49
4.3 Heat Release Experiments	67
5.0 FULL SCALE FLIGHTWEIGHT RECEIVER DESIGN STUDIES	91
5.1 Four Percent Gas Pressure Drop Design	91
5.2 Two Percent Gas Pressure Drop Design - Initial	103
5.3 Two Percent Gas Pressure Drop Design - Revised	118
5.4 Summary of Receiver Designs	120
6.0 CAVITY TEMPERATURE DISTRIBUTION	124
6.1 Incident Flux Distributions	124
6.2 Cavity Radiation Solutions	129
6.3 Lithium Fluoride Resistance Determinations	129

TABLE OF CONTENTS (Continued)

	<u>Page</u>
6.4 Computer Program Integration	133
6.5 Shade Time Calculations	139
6.6 Sun Time Results	139
6.7 Comparison of Analog, Experimental and Computed Cavity Wall Temperature Variations	147
7.0 RECOMMENDATIONS FOR FUTURE WORK	164
8.0 APPENDICES	165
8.1 References	166
8.2 Nomenclature	169
8.3 Lithium Fluoride Properties	174
8.4 Heat Input Analysis	182
8.5 Radiation Analog Investigation	199
8.6 Test Module Stress Analysis	207
8.7 High Temperature Properties of Haynes 25 and Waspaloy	229
8.8 Structural Analysis	236
8.9 Aperture Control Design Analysis	257
8.10 Cavity Temperature Distribution Analysis	278
8.11 Reliability Estimates	296

LIST OF FIGURES

<u>Figure No.</u>	<u>Title</u>	<u>Page</u>
1	Variation of Gas-to-Log Mean Temperature Difference Ratio with Gas Side Temperature Difference for Several Ratios of Wall-to-Gas Temperature Difference at a Constant Wall-to-Gas Temperature Difference at the Tube Outlet of 65° F.	9
2	Variation of the Factor K for Laminar Flow in Circular Tubes with Gas Side Temperature Difference and Pressure Drop Ratio.	10
3	Variation of the Factor K for Turbulent Flow in Circular Tubes with Gas Side Temperature Difference and Pressure Drop Ratio.	11
4	Variation of the Minimum Tube Projected Area With The Factor K for Laminar Flow in Circular Tubes.	13
5	Variation of the Minimum Tube Projected Area With The Factor K for Turbulent Flow in Circular Tubes.	14
6	Variation of the Tube Projected Area With Reynolds Number at a Constant K Factor Level.	15
7	Typical Results for Heater Tube Parameters with Turbulent Flow in Circular Tubes.	16
8	Comparison of Tube Geometry in Laminar and Turbulent Flow for a Fixed Pressure Drop and Gas Temperature Difference.	17
9	Variation of Thermal Resistances with Frozen Fluoride Thickness for Two Typical Preliminary Design Configurations.	19
10	Viscosity of Argon	22
11	Thermal Conductivity of Argon	23
12	Heat Content Above Room Temperature, Btu/lb	25
13	Density of Lithium Fluoride	26
14	Preliminary Design Configuration of a Single Orbit Cavity Receiver with a Hemispherical Fluoride Container.	29

LIST OF FIGURES (Continued)

<u>Figure No.</u>	<u>Title</u>	<u>Page</u>
15	Preliminary Design Configuration of a Single Orbit Cavity Receiver with a Conical Fluoride Container.	31
16	Preliminary Design Configuration of a Single Orbit Cavity Receiver with a Cylindrical Fluoride Container.	33
17	Brayton Cycle Test Module	39
18	Thermal Conductivity Test Module - Brayton Cycle.	41
19	Schematic - Electrical and Plumbing - Brayton Cycle.	45
20	Thermal Conductivity - Lithium Fluoride	50
21	Heat Input Rate, $\text{Btu/ft}^2, \text{hr}$	53
22	Computer Results: Cavity Wall Surface Temperature ($^{\circ}\text{F}$) vs Heat Input Flux, Btu/hr-ft^2 .	54
23	Sketch of Heat Input Test Modules.	55
24	Exploded View of Module No. 5 Prior to Final Assembly Weld.	56
25	End View of Module No. 6 Prior to Final Assembly Weld.	57
26	End View of Module No. 7 Prior to Final Assembly Weld.	58
27	View of Module A	59
28	View of Top Plates of Modules B and C After Initial Fin Brazing.	60
29	View of Test Assembly	62
30	View of Test Assembly with High Temperature Insulation Installed.	63
31	View of Test Assembly in Position for Melting Lithium Fluoride.	64
32	Typical Variation of Top Plate Temperature with Heating Time at Several Power Levels - Module No. 5.	66

LIST OF FIGURES (Continued)

<u>Figure No.</u>	<u>Title</u>	<u>Page</u>
33	Top Plate Temperature vs. Heat input Module Test Results.	68
34	Variation of Maximum for Plate Temperature with Heat Input Flux Level for Modules A, B and C at a Constant Coolant Flow of 0.5 lb/min.	69
35	View of Module No. 2 Sectioned After Completion of Testing.	70
36	View of Module 4 Sectioned After Testing.	71
37	View of Module 7 Sectioned After Testing.	72
38	View of Module B Sectioned After Testing.	73
39	View of Module C Sectioned After Testing.	74
40	Electric Analog Method to Determine Melt Line Motion During Freezing.	76
41	Typical Melt Line Pattern.	78
42	Electric Analog Schematic.	79
43	Geometrical Resistance ($X L/A$) of Freezing LiF.	80
44	View of Module No.3 Sectioned After Completion of Testing.	83
45	Section View of Dummy Module No. 2 After Testing.	85
46	Geometrical Resistance ($X L/A$) of Freezing LiF.	86
47	Variation of Top Plate Temperature at End of Melting with Heat Input Flux - Module D.	88
48	Variation of Top Plate at End of Melting with Heat Input Flux, Module E.	89
49	Variation of Tube Inside Diameter with Number of Tubes.	93
50	Variation of Heater Tube Surface Area Required with Number of Tubes.	94

LIST OF FIGURES (Continued)

<u>Figure No.</u>	<u>Title</u>	<u>Page</u>
51	Variation of Tube Projected Area Required with Number of of Tubes.	95
52	Cavity Receiver 300 NM - 30 foot Mirror Brayton Cycle.	99
53	Combined Cavity Temperature Control and Aperture Closure Device - Brayton Cycle.	101
54	Variation of Gas Temperature with Instantaneous Change of 10% Gas Flow Rate.	104
55	Variation of Gas Pressure Drop with Instantaneous Change of 10% in Gas Flow Rate.	105
56	Effect of $\Delta P/P_{in}$ on Receiver Weight - 300 NM Orbit, 30 Foot Mirror.	106
57	Variation of the Transitional Reynolds Number in Curved Tubes with the Ratio of Tube Radius to Radius of Curvature.	107
58	Thirty-tube Receiver Design.	109
59	Concept Heat Release Doors - Brayton Cycle.	113
60	Cavity Receiver - Brayton Cycle.	119
61	Radial Variation in Cavity Incident Flux with Collector perfectly Oriented.	125
62	Radial and Circumferential Variation in Cavity Incident Flux with Collector Misoriented 1/4 Degree in Direction of Major Axis.	126
63	Radial and Circumferential Variation in Cavity Incident Flux with Collector Misoriented 1/2 Degree in Direction of Major Axis.	127
64	Variation of Cavity Incident Flux in Radial and Circumferential Directions with Collector Misoriented 1/2 Degree Along Cavity Major Axis.	130
65	Additional Melt Line Pattern.	132

LIST OF FIGURES (Continued)

<u>Figure No.</u>	<u>Title</u>	<u>Page</u>
66	Electric Analog Simulation Heat Addition.	134
67	Variation of Wall-to-Melt Line Geometrical Resistance Factor with Amount of Fluoride Melted.	135
68	Variation of Melt Line-to-Tube Geometrical Resistance Factor with Amount of Fluoride Melted.	136
69	Typical Gas Temperature Variation Along Heater Tube During Shade Time Operation.	137
70	Typical Variation of Gas Pressure Along Heater Tube During Shade Time Operation.	140
71	Variation of Heater Tube Flux Along Tube During Shade Time.	141
72	Variation of Solar Flux on Cavity Wall for Perfectly Oriented Collector ($\beta = 0^\circ$) - (β is the Angle Measured from the Optic Axis).	142
73	Typical Variation of Total Cavity Wall Flux for the Perfectly Oriented Collector ($\beta = 0^\circ$).	143
74	Typical Variation of Total Cavity Wall Flux for the Perfectly Oriented Collector with High Wall Emissivity.	144
75	Typical Variation of Total Cavity Wall Flux for the Perfectly Oriented Collector ($\beta = 0^\circ$) with low Emissivity.	145
76	Typical Cavity Wall Temperature Distribution for Perfectly Oriented Collector ($\beta = 0^\circ$).	146
77	Typical Variation of Heater Tube Flux Along Tube Length During Sun Time.	148
78	Typical Variation of Gas and Tube Wall Temperatures Along Tube Length During Sun Time.	149
79	Typical Variation of Gas Pressure Along Tube Length During Sun Time.	150
80	Typical Variation of Heater Tube Flux Along Tube Length During Sun Time with Gas Flow Rate 10% Above Design Flow Rate.	151

LIST OF FIGURES (Continued)

<u>Figure No.</u>	<u>Title</u>	<u>Page</u>
81	Typical Variation of Gas Temperature Above Tube Length During Sun Time with Flow Rate 10% Above Design Flow Rate.	152
82	Typical Variation of Gas Pressure Along Tube Length During Sun Time with Flow Rate 10% Above Design Flow Rate.	153
83	Typical Variation of Heater Tube Flux Along Tube Length During Sun Time with Flow Rate 10% Below Design Flow Rate.	154
84	Typical Variation of Gas Temperature Along Tube Length During Sun Time with Flow Rate 10% Below Design Flow Rate.	155
85	Typical Variation of Gas Pressure Along Tube Length During Sun Time with Flow Rate 10% Below Design Flow Rate.	156
86	Typical Wall Temperature Distribution During Sun Time for Collector Misoriented 1/4 Degree from the Sun.	157
87	Typical Wall Temperature Distribution During Sun Time for Collector Misoriented 1/2 Degree from the Sun.	158
88	Variation of Maximum Cavity Wall Flux with Melting Time.	159
89	Variation of Cavity Wall Temperature with Melting Time at Cavity Location Where Maximum Cavity Wall Flux Occurs.	160
90	Variation of Top Plate Temperature of Module D in Run No. 7 with Melting Time.	162
91	Comparison of Analog, Experimental and Computed Cavity Wall Temperature Variations with Melting Time.	163
92	Section of Module Employed in Analog Computations.	201
93	Total Heat Input vs Heat Input Rate of Module Section.	206
94	Top Plate Final Surface Temperatures vs Fin Thickness of Module Section.	208
95	Melting Time vs Fin Thickness of Module Section.	209
96	Progress of Melting Front in Module Section.	210

LIST OF FIGURES (Continued)

<u>Figure No.</u>	<u>Title</u>	<u>Page</u>
97	Progress of Melting Front in Module Section.	210
98	Progress of Melting Front in Module Section.	211
99	Progress of Melting Front in Module Section.	211
100	Computer Recorder Sheets	213
101	Computer Recorder Sheets	215
102	Computer Recorder Sheets	217
103	Test Model Basic Dimensions	220
104	Analytical Model of Top and Bottom Plate.	221
105	Required Top and Bottom Plate Thickness vs Temperature.	223
106	Analytical Model of Side Plates	224
107	Stress in Side Plates vs. Thickness	227
108	Required Side Plate Thickness vs Temperature.	228
109	High Temperature Properties Haynes Alloy No. 25.	231
110	Larson-Miller Parameter Haynes 25.	232
111	High Temperature Properties Waspaloy	233
112	Larson-Miller Parameter Waspaloy	234
113	Larson-Miller Parameter Hastelloy X	235
114	Brayton Cycle Cavity Receiver	237
115	Light Bottom Design	238
116	Reinforced Header	239
117	Structural and Thermal Load	240
118	Structural and Thermal Load	241

LIST OF FIGURES (Continued)

<u>Figure No.</u>	<u>Title</u>	<u>Page</u>
119	Waspaloy	243
120	Haynes 25	243
121	Gas Manifold	248
122	Bellows Cycle Life	275
123	Vapor Pressure of NaK (78)	276
124	Density of Liquid NaK (78)	277
125	Definition of Terms Used in the Heat Receiver Analysis.	291
126	Infinitesimal Area Geometry Used for Calculation of $K(x, x')$	293
127	Co-ordinate System and Geometry Used for Calculations of $K(x, x')$ for Case Where dS and dS' are both in a Hemisphere.	294
128	Definition of Quantities Used in Calculation of $K(x_1, x')$.	295

LIST OF TABLES

<u>Table No.</u>		<u>Page</u>
I	Summary of Liquid Lithium Fluoride Thermal Conductivity Results	48
II	Summary of Solid Lithium Fluoride Thermal Conductivity Results	48
III	Heat Input Modules - Series I	48
IV	Heat Input Modules - Series II	51
V	Heat Release Modules	75
VI	Specifications (Cavity Receivers)	96
VII	Comparison of Friction-Factor Values at Various Reynolds Numbers	116
VIII	Gas Properties	117
IX	Summary of Receiver Designs Attempted with Pertinent Notes	123
X	Summary of Analog Results	205
XI	Top and Bottom Plate Thicknesses	224
XII	Tube Station Locations	292

BLANK PAGE

1.0 SUMMARY OF RESULTS

The design study of a Brayton cycle cavity receiver for a dynamic solar power conversion system resulted in the following:

1. Concept designs were developed for receivers operating on four per cent and two per cent allowable gas pressure drop, in combination with a 30-foot diameter rigid solar collector in a nominal 300 nautical mile earth orbit. Variations were established for use with a 20-foot diameter collector in a synchronous orbit.
2. Parametric studies were conducted to determine the effect of gas temperature rise and gas pressure drop. The effect of collector misorientation up to 1/2-degree maximum was also studied.
3. Concept designs were developed for cavity maximum temperature control and aperture closure devices.
4. Experiments were conducted to obtain data from which:
 - a) Thermal conductivity of lithium fluoride near the melting temperature was established.
 - b) Heat input rates possible with lithium fluoride, using fins and other extended surfaces, were confirmed.
 - c) Heat release rates from molten lithium fluoride to a gas coolant were both calculated and experimentally verified.
 - d) Melting and freezing characteristics of lithium fluoride and resultant void volume were determined and used to demonstrate controlled freezing techniques.
5. Electric analog techniques were developed and applied to measure the result of simultaneous heat addition and extraction for two tube sections. These results were incorporated in a digital computer program which was used to calculate values or quantity of the variables at definite time intervals on a quasi-steady-state basis. The variables calculated were:
 - a) Cavity receiver temperature distribution.
 - b) Net flux into the cavity wall.
 - c) Heat exchange from cavity wall to fluoride.
 - d) Heat exchange from fluoride melt line to the gas.

- e) Tube wall temperature.
 - f) Mean gas temperature.
 - g) Gas pressure drop.
 - h) Volume of fluoride melted.
 - i) Fluoride resistances.
6. The computer program results also indicate that cavity reradiation losses are less than black-body radiation. The ratio of the calculated loss to black-body loss was in the range from 0.55 to 0.65.

2.0 INTRODUCTION

The process of energy addition to the working fluid in a solar dynamic power conversion system includes solar energy interception and concentration by the collector, reception and absorption of the concentrated energy by the absorber and heat exchange from the absorber to the working fluid. Those systems which are designed to operate in the earth's shadow must incorporate some form of energy storage or an alternate source of energy. Previous studies have shown that a cavity type of receiver is most suitable for a solar absorber, and thermal energy storage is readily adapted to cavity receivers.

In this case, excess energy must be supplied during the sun time to melt the storage material. Thus, the concentrated energy must be absorbed by the storage material and heat transferred continuously from the storage material to the working fluid. During the shade time, the storage material freezes as energy is removed continuously by the cooler working fluid. These alternate processes of melting and freezing the storage salt occur during each typical orbital cycle. Because of the alternate melting and freezing, the storage material seldom, if ever, reaches steady-state operating conditions. Since the storage material is operating under transient conditions most of the time, design information must be obtained to properly reflect the transient nature of the storage bath.

In the previous work on the Sunflower program as reported in Reference 1, the transient heat input and heat release design parameters were determined experimentally. Analog predictions of the heat release performance were made and compared with the experimental results. The experiments confirmed the basic validity of the heat release analog. In the present program, NASA requested analytical predictions of the heat input performance and experimental verification thereof. In addition, analog predictions of the heat release performance and similar experiments were to be made to reconfirm the validity of the analog method. Also, a literature search by NASA and TRW personnel failed to uncover thermal conductivity data near the melting point for lithium fluoride. In view of the lack of data, determinations of the thermal conductivity of lithium fluoride for both the solid and the liquid near the melting point were specified. This information is vital in the prediction of the fluoride thermal resistances.

The major purpose of this program is the design of a full scale lightweight cavity receiver to NASA specifications. The resulting design is to employ the transient information obtained on the heat transfer characteristics of lithium fluoride to the fullest extent possible. When the work effort on this program began in July, 1963, a gas pressure drop allowance equal to four percent of the inlet pressure was permitted. Subsequent studies indicated that this pressure drop allowance could be reduced to two percent of the inlet pressure without seriously affecting the design of the cavity receiver. The specifications were then revised to include this improvement. The initial and revised specifications are presented in Sections 2.1 and 2.2 of this report, respectively.

This report presents the results of the cavity receiver design study conducted under Contract NAS 3-2779 and includes the work specified in the original contract (Task I) and Amendments 4 and 6.

2.1 Initial Specifications

Nominal values of the argon Brayton cycle state points and flow rates are as follows:

- Temperature at receiver inlet - 1446°R
- Temperature at receiver outlet - 1950°R
- Pressure at receiver inlet - 13.72 psia
- Pressure at receiver exit - 13.17 psia
- Flow rate for 30 ft diameter collector - 36.7 lb/min
- Flow rate for 20 ft diameter collector - 14.7 lb/min

The above values are subject to variation as the cycle analyses and design studies progress.

2.2 Revised Specifications

The analyses and design efforts required herein shall be performed for a receiver/heat storage unit suitable for use with a 30-foot diameter collector orbiting at 300 nautical miles.

The nominal applicable values of the argon Brayton cycle state points and system specifications to be employed are as follows:

- Receiver inlet temperature - 1446°R
- Receiver exit temperature - 1950°R
- Receiver inlet pressure - 13.72 psia
- Total ΔP (inlet to exit flange) - 0.275 psia (2%)
- Argon flow rate - 36.7 lb/min
- Total shade time capacity - 38 minutes
- Sun time (ecliptic) - 60 minutes (300 n. mi.) per orbit
- Sun time (all-sun) - 96 minutes per orbit
- Design life - 10,000 hours

The solar collector characteristics to be employed in the cavity temperature distribution analysis are specified by the contract as those predicted for the 30-foot aluminum honeycomb mirror studied under Contract NAS 3-2789. A six per cent shadow factor for collector obscuration shall be assumed as originating at the center of the collector.

The work effort on Task I, the receiver design study, began with a preliminary analysis of the design and the design requirements. These efforts are discussed in the next section.

3.0 PRELIMINARY DESIGN ANALYSIS

A preliminary design analysis of the cavity receiver was conducted to examine the broad field of design possibilities, to identify the empirical design information needed from the small-scale experiments, to provide the argon and lithium fluoride properties data for use throughout the program and to evaluate the technical feasibility of several design configurations.

In the broad area of design possibilities, items of interest included design variations with gas temperature rise and allowable gas pressure drop, laminar flow operation versus turbulent flow operation, bare tubes versus finned tubes - both external and internal - large numbers of tubes versus small numbers of tubes and fins attached to the cavity surface versus a plain cavity surface. These design areas are discussed under Section 3.1 below.

The information needed from the small-scale experiments include lithium fluoride thermal conductivity data on the solid and the liquid near the melting point, cavity surface temperature variation with heat input both with and without several forms of extended surface, confirmation of heat release predictions and operation of selected storage bath geometrical configurations. The small-scale experiments and their corresponding analytical predictions are presented in Section 4.0 of this report.

The argon gas and lithium fluoride material properties were obtained and specified in a literature search. The properties pertinent to this design study are listed in Section 3.2 below. Additional information on the properties of lithium fluoride is given in the appendix, Section 8.3.

Several potential design configurations were examined in considerable detail to evaluate their technical feasibility. Criteria employed included thermal and mechanical performance, fabricability, reliability, cavity performance and other factors. A summary of these evaluations is presented in Section 3.3 below.

3.1 Initial Design Investigations

As stated previously, the intent of the initial studies was to provide information on the design changes encountered as the gas temperature rise and allowable gas pressure drop are permitted to vary. Other items of interest included information leading to decisions on heater operation in laminar or turbulent flow designed with and without fins. Further features investigated included heater tube number and the use of fins attached to the cavity surface.

For the purpose of a generalized comparison, standard textbook equations were employed. Typical equations selected for circular tubes are as follows:

Heat Transfer

Laminar Flow

$$Nu = \frac{h D}{k} = 4.12$$

Turbulent Flow

$$Nu = 0.023 Re^{0.8} Pr^{0.4}$$

Pressure Drop

$$\Delta P = f \frac{L}{D} \frac{G^2}{\rho \cdot 2 g_c}$$

Friction Factor

Laminar Flow

$$f = \frac{64}{Re}$$

Turbulent Flow

$$f = \frac{0.316}{Re^{0.25}}$$

(The symbols are defined in the Appendix on Nomenclature, Section 8.2)

All gas properties were based on the bulk temperature, unless specifically noted.

The heater duty is:

$$Q_H = w C_p (t_{g0} - t_{gi}) = w C_p \Delta t_g$$

The heat exchange is also defined by:

$$Q_H = h A \Delta t_m$$

Since the two must be equal in a successful design, it follows that:

$$\frac{\Delta t_g}{\Delta t_m} = \frac{h A}{w c_p}$$

The right hand term above is equivalent to

$$S_T \frac{A}{A_c}$$

and for circular tubes

$$\frac{A}{A_c} = \frac{\pi D L}{\frac{\pi}{4} D^2} = 4 \frac{L}{D}$$

thus
$$\frac{\Delta t_g}{\Delta t_m} = 4 S_T \frac{L}{D}$$

By definition

$$S_T = \frac{Nu}{Re Pr}$$

For gases Pr was assumed equal to 0.7 during the preliminary investigation of gas temperature change and pressure drop variations. For all design activity, the Prandtl number was calculated based on the actual gas properties.

In laminar flow

$$S_T = \frac{4.12}{0.7 Re} = \frac{5.886}{Re}$$

and

$$\frac{\Delta t_g}{\Delta t_m} = \frac{5.886}{Re} \frac{4 L}{D} = \frac{23.544}{Re} \frac{L}{D}$$

In turbulent flow

$$S_T = \frac{0.023 Re^{0.8} (0.7)^{0.4}}{Re^{0.7}} = 0.0285 Re^{-0.2}$$

and

$$\frac{\Delta t_g}{\Delta t_m} = \frac{0.0285}{Re^{0.2}} \frac{4 L}{D} = \frac{0.1140}{Re^{0.2}} \frac{L}{D}$$

The pressure drop parameter of interest is defined as:

$$K_L = \frac{\Delta P \bar{\rho}^2 g_c}{64 \bar{\mu}^2} \quad (\text{Laminar Flow})$$

$$K_T = \frac{\Delta P \bar{\rho}^2 g_c}{0.316 \bar{\mu}^2} \quad (\text{Turbulent Flow})$$

and

$$K_L = R_e \frac{L}{D} \frac{1}{D^2}$$

$$K_T = R_e^{1.75} \frac{L}{D} \frac{1}{D^2}$$

A third equation relating the heater design variables is:

$$R_e = \frac{4 w}{\pi \bar{\mu} N D}$$

But there are four variables, R_e , N , D and L and only three equations. Thus, a single, unique solution is not possible. As a result, it should be possible to design heaters for operation at a variety of Reynolds numbers. The geometry of each heater would depend on the Reynolds number selected.

The basic variation of the temperature difference ratio, $\Delta t_g / \Delta t_m$, with the gas side temperature difference is shown in Figure 1. The wall-to-gas temperature difference ratio, $\Delta t_w / \Delta t_g$ for a given design will vary with orbital time from 0 at the time when the fluoride is all liquid to some finite ratio at the time when the fluoride is all solid. Figure 1 indicates that $\Delta t_g / \Delta t_m$ increases with increasing gas side temperature difference and increasing wall-to-gas temperature difference ratio. The exact $\Delta t_g / \Delta t_m$ required for a given design cannot be predicted directly.

The variation of the factor K_L with gas side temperature difference is presented in Figure 2 for several pressure drop ratios. It can be observed that the factor K_L increases with increasing gas side temperature difference and permissible pressure drop ratio. Similar results for turbulent flow are given in Figure 3.

The heater geometry is defined by D , L and N . The product of these three, NDL , is the tube projected area required. The heater surface area required is πNDL . Thus, the product, NDL , defines the tube projected area and is proportional to the tube surface area. It is desirable to minimize the tube projected area to provide minimum cavity surface area requirements. The variation of the minimum tube projected area, NDL , with the factor K_L

VARIATION OF GAS-TO-LOG MEAN TEMPERATURE DIFFERENCE RATIO
WITH GAS SIDE TEMPERATURE DIFFERENCE FOR SEVERAL RATIOS OF WALL-
TO-GAS TEMPERATURE DIFFERENCE AT A CONSTANT WALL-TO-GAS
TEMPERATURE DIFFERENCE AT THE TUBE OUTLET OF 65°F

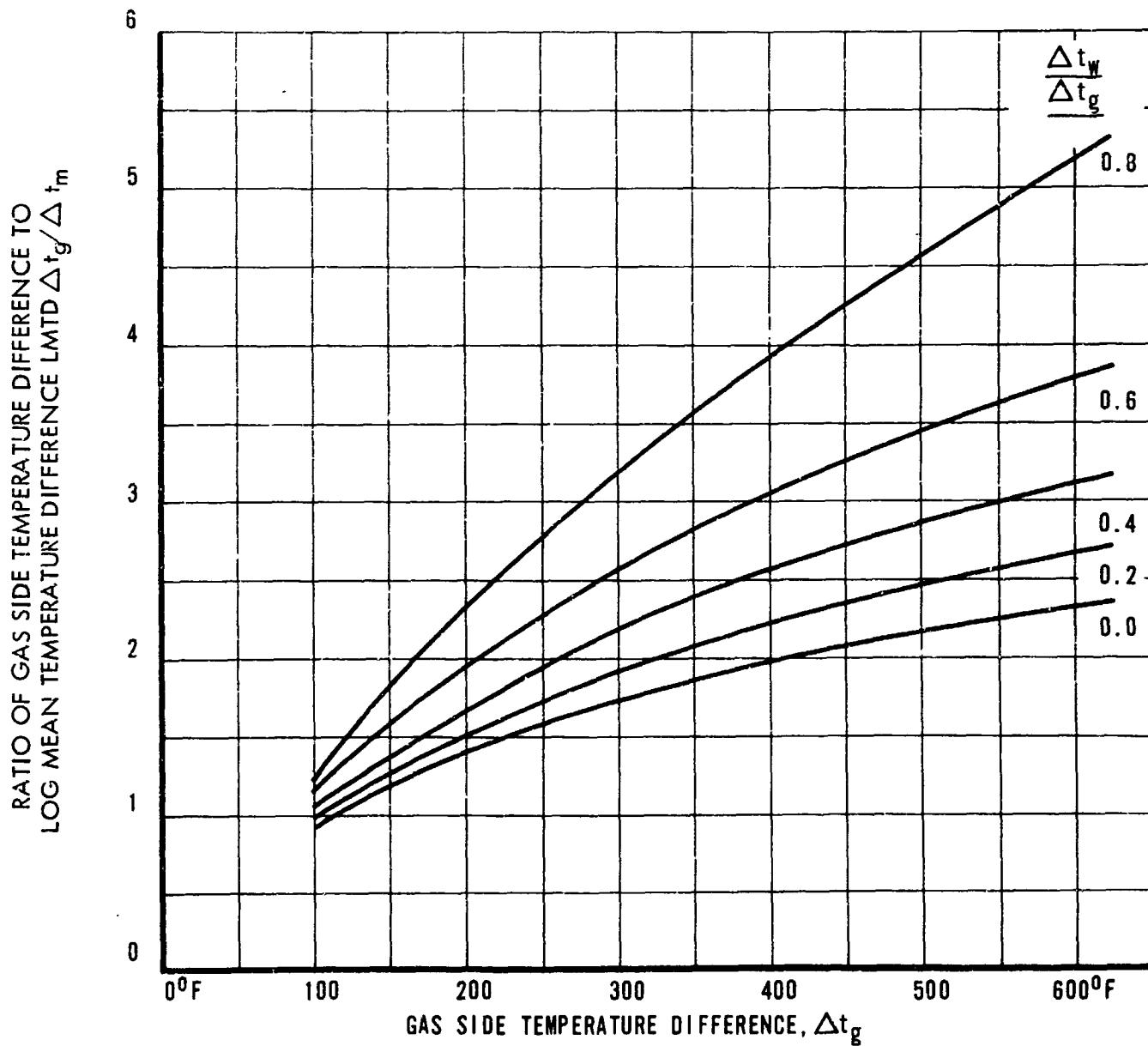
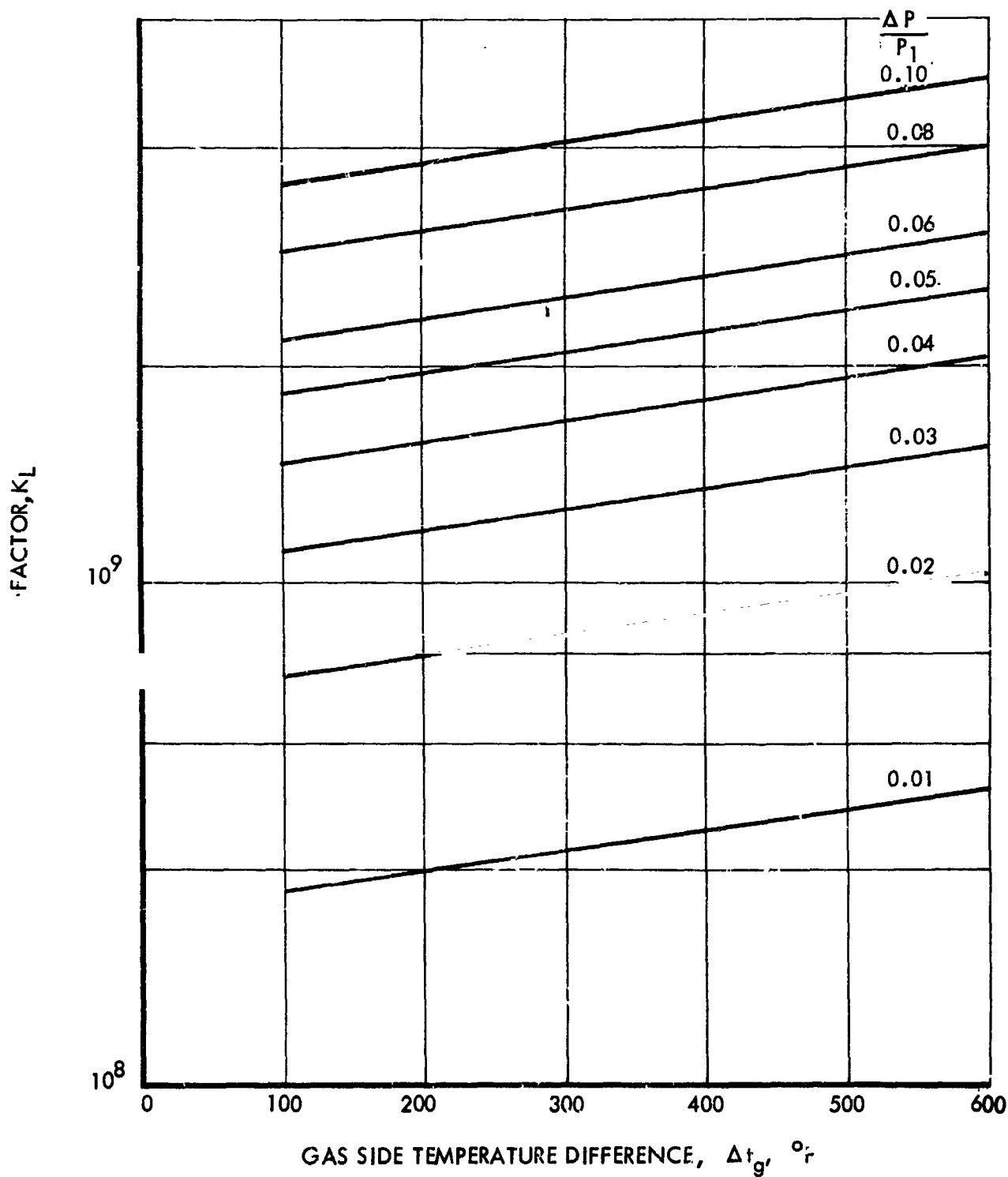


FIGURE 1

VARIATION OF THE FACTOR K FOR LAMINAR FLOW IN CIRCULAR TUBES
WITH GAS SIDE TEMPERATURE DIFFERENCE AND PRESSURE DROP RATIO



VARIATION OF THE FACTOR K FOR TURBULENT FLOW IN CIRCULAR TUBES
WITH GAS SIDE TEMPERATURE DIFFERENCE AND PRESSURE DROP RATIO

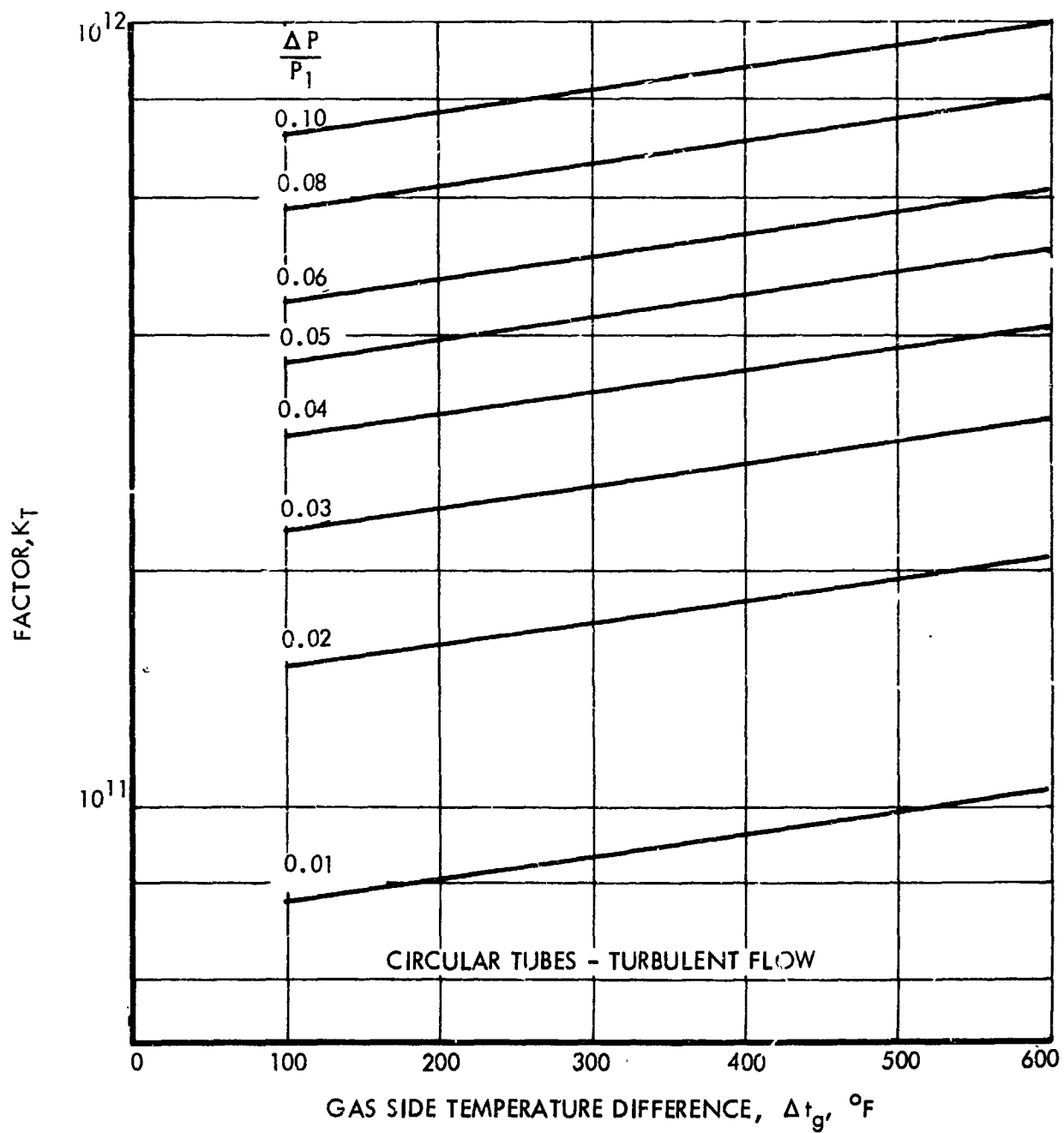


FIGURE 3

(laminar flow) is shown in Figure 4 for a given level of $\Delta t_g/\Delta t_m$ required. The similar variation of the minimum tube projected area with the factor K_T (turbulent flow) is presented in Figure 5 for several levels of $\Delta t_g/\Delta t_m$. Each level of $\Delta t_g/\Delta t_m$ represents a different heat exchange requirement, of course. The desirability of operating at the higher values of K_L or K_T is clearly evident in these two figures. However, the power conversion system requirements and considerations dictate the maximum level of the factor K allowed. Furthermore, the entire pressure drop allowed may not be available for the tube design. This situation is particularly true in multi-tube designs wherein pressure losses occur in the inlet and exit manifolds. These losses decrease the value of ΔP to be assigned to the tubing and applied in the calculation of the factor K .

In the preliminary analysis, it was demonstrated that the tube projected area varies with the gas Reynolds number as illustrated in Figure 6. This variation is for given values of the factor K and $\Delta t_g/\Delta t_m$ in turbulent flow. The tube projected area required increases with increasing gas Reynolds number. Although not presented herein, the increase of tube projected area with gas Reynolds number is even more pronounced in laminar flow. Thus, a conclusion may be drawn that it is desirable to operate at as low a gas Reynolds number as possible. This conclusion must be limited to designs based on the gas correlations previously discussed.

The variation of the tube dimensions, D and L , and the tube number, N , with gas Reynolds number for a particular case in turbulent flow is given in Figure 7. The decrease in tube number and increase in tube diameter and length with increasing gas Reynolds number is typical for both laminar and turbulent flow. Figure 6 has already indicated that operation should be at a low gas Reynolds number with an attendant high tube number.

The next question of interest in the preliminary analysis was which region the heater should be designed for - laminar or turbulent? To answer this one graphically, the variations with gas Reynolds number were calculated for each region and placed on a common graph. The results are shown in Figure 8 for $\Delta t_g/\Delta t_m = 2.75$ and $\Delta P/P_1 = 0.022$. It can be observed from Figure 8 that heaters designed for bare tubes in laminar flow require larger numbers of tubes which are shorter and smaller in diameter than heaters designed for bare tubes in turbulent flow. The tube projected area required is approximately equivalent, but a slight advantage is available at low Reynolds numbers in laminar flow. The packaging problem becomes severe, if not prohibitive, with the large number of tubes (4000 \rightarrow 8000) required at the low laminar Reynolds numbers. After reviewing the magnitude of the packaging problem, it was decided to design for operation in turbulent flow.

The next item of potential controversy was the use or non-use of fins attached to the tubes. The fins can be potentially attached to either the inner or the outer surface. In either case, the use of fins must be based upon a definite requirement to lower the thermal resistance involved. The possible use of fins attached to the outer tube surface was considered first.

It was shown in Reference 3 that the total thermal resistance to heat flow is:

$$R_t = R_g + R_w + R_f$$

VARIATION OF THE MINIMUM TUBE PROJECTED AREA WITH
THE FACTOR K FOR TURBULENT FLOW IN CIRCULAR TUBES

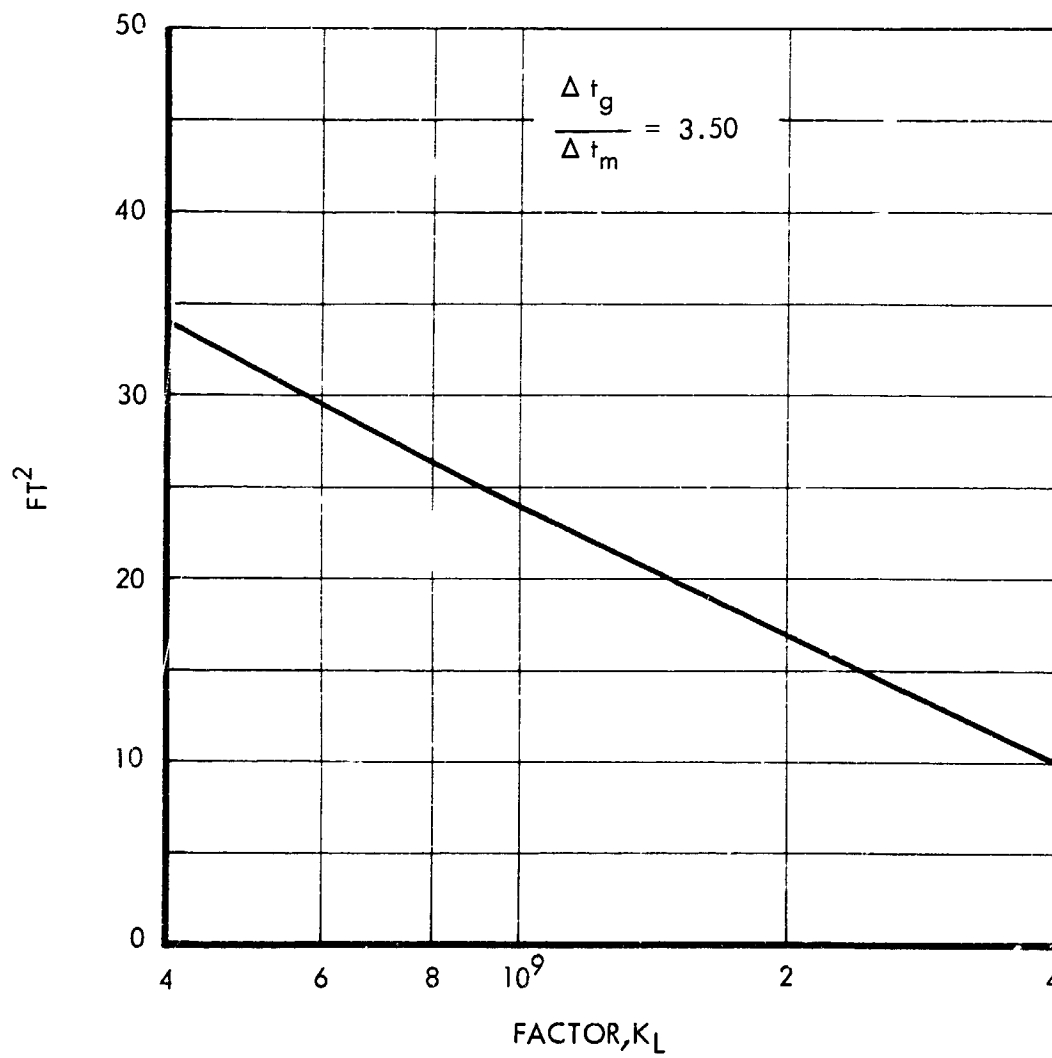


FIGURE 4

VARIATION OF THE MINIMUM TUBE PROJECTED AREA WITH
THE FACTOR K FOR TURBULENT FLOW IN CIRCULAR TUBES

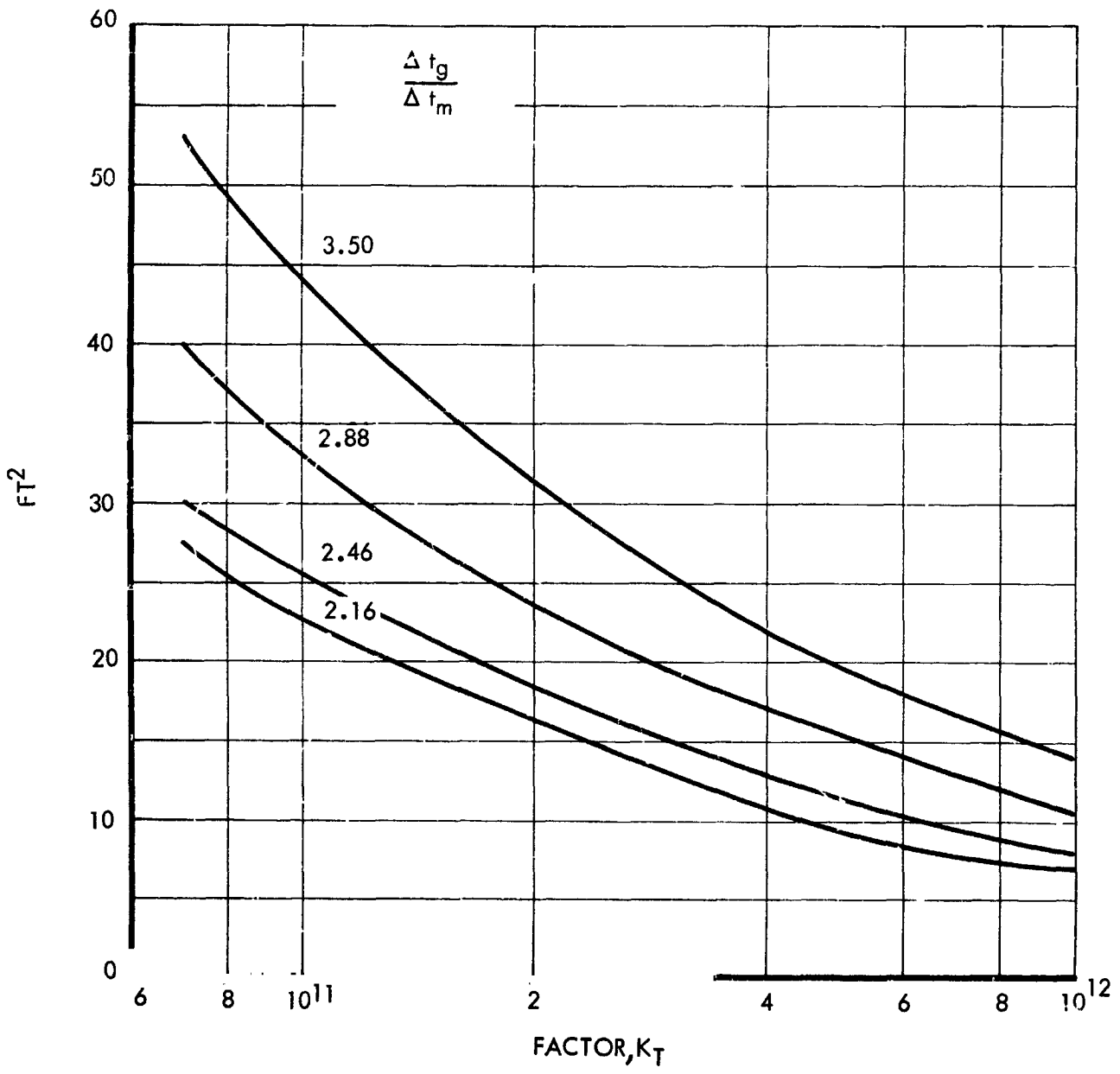


FIGURE 5

VARIATION OF THE TUBE PROJECTED AREA WITH
NUMBER AT A CONSTANT K FACTOR LEVEL

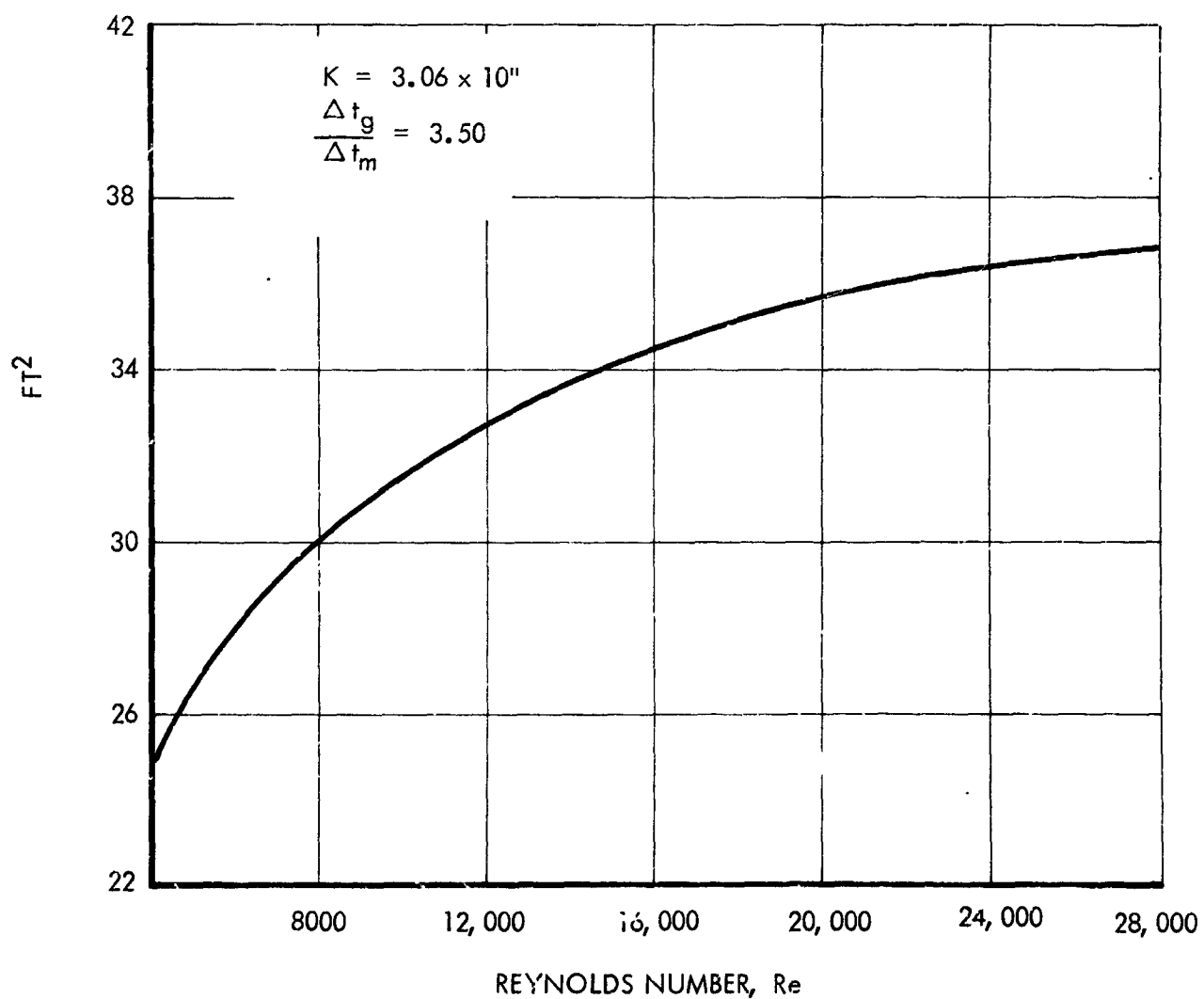
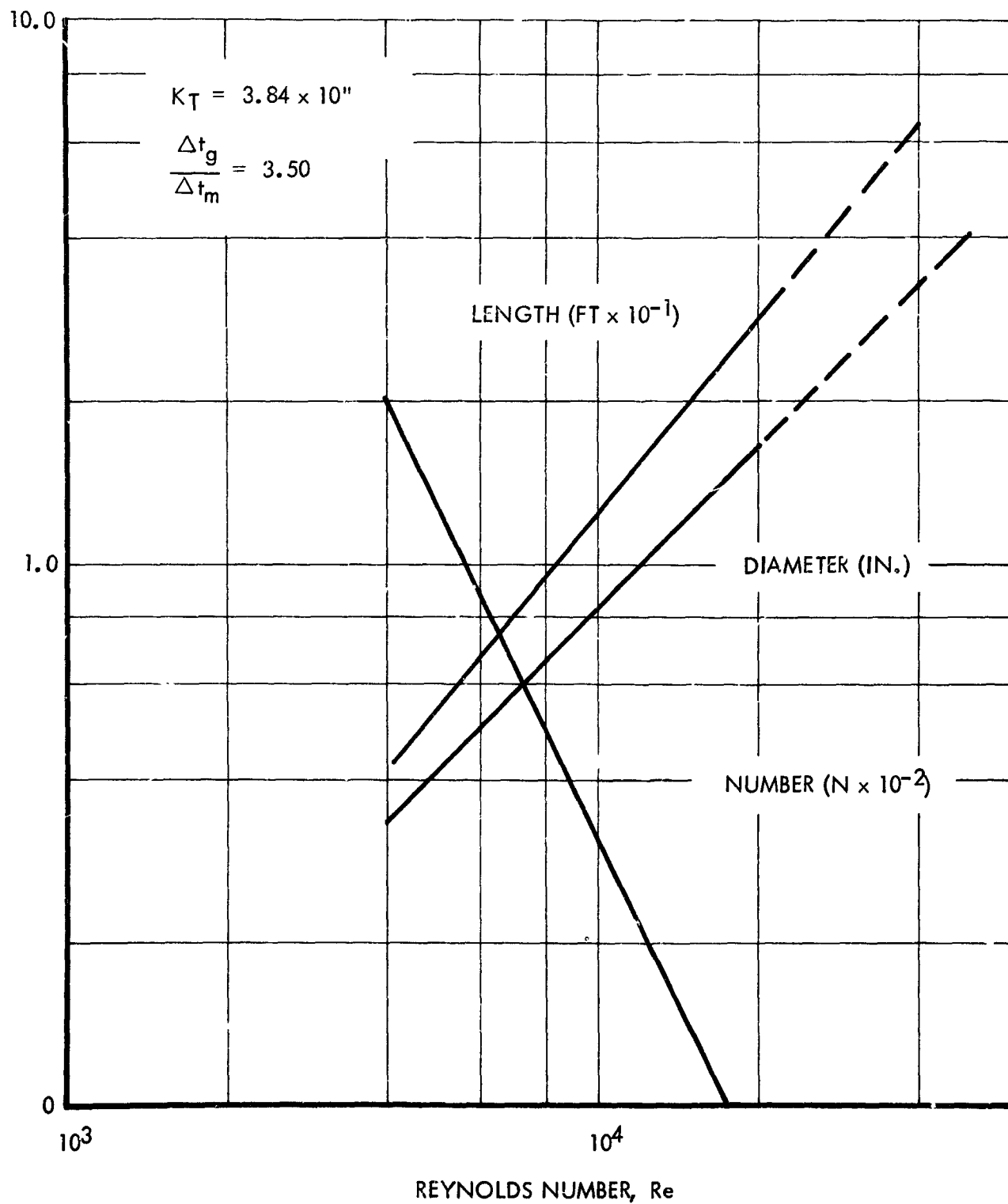
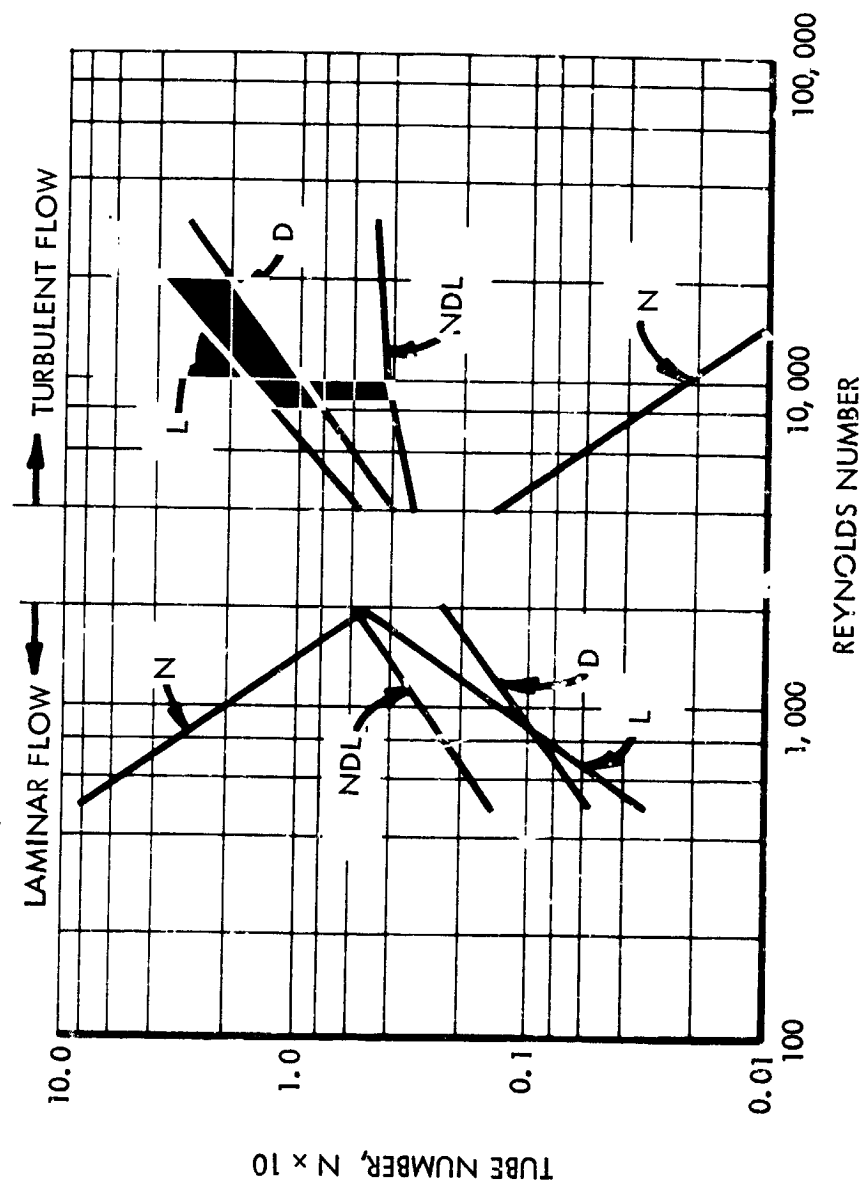


FIGURE 6

TYPICAL RESULTS FOR HEATER TUBE PARAMETERS
WITH TURBULENT FLOW IN CIRCULAR TUBES



COMPARISON OF TUBE GEOMETRY IN LAMINAR AND TURBULENT FLOW
FOR A FIXED PRESSURE DROP AND GAS TEMPERATURE DIFFERENCE



for the classical case of a multi-walled cylinder immersed in an infinite bath. Under these conditions, the heat flow per unit length of tube is:

$$Q/L = \frac{t_f - t_g}{R_f}$$

Each of the resistance elements are listed below:

$$R_g = \frac{1}{2 \pi r_i h}$$

$$R_w = \frac{1}{2 \pi k_w} \ln \frac{r_o}{r_i}$$

$$R_f = \frac{1}{2 \pi k_f} \ln \frac{r_m}{r_o}$$

In Reference 3, an estimate of the value for the solid thermal conductivity of lithium fluoride was obtained from Reference 4. The value employed was 1.5 Btu/hr-ft/°F. At the time, no known experimental data were available. Since that time, experimental values were obtained as a part of this program and were published in Reference 5. These experiments are discussed in Section 4.1. The average experimental value of 5.1 Btu/Hr-Ft-°F is about three times the original estimate but would not alter the conclusions reached on external fins.

The level of the fluoride resistance depends on the amount of fluoride frozen around the tube. When the fluoride is completely molten, the resistance of the solid is zero. As the amount of frozen fluoride increases, the radius to the melt line increases and the fluoride thermal resistance increases too. The fluoride resistance reaches a maximum when all of the fluoride is frozen. Two potential designs were calculated for Reference 3 and the results are presented in Figure 9. It can be observed from Figure 9 that in both cases the fluoride resistance was less than the gas-side resistance at all times. Since the experimental value of the solid fluoride thermal conductivity is higher than the original estimate, the revised fluoride resistance would be even lower than that shown in Figure 9. Since the gas thermal resistance is larger than the fluoride thermal resistance at all times, the gas thermal resistance is rate-controlling at all times. On the basis of the results in Figure 9, there is no need to lower the fluoride thermal resistance by adding fins on the external surface of the tubes. Nothing that has occurred in the program since this conclusion was originally drawn has served to alter it in any way. It is as valid now as it was then and even more valid because of the higher measured fluoride conductivity and resultant lower thermal resistance.

VARIATION OF THERMAL RESISTANCES WITH FROZEN FLUORIDE THICKNESS FOR TWO TYPICAL PRELIMINARY DESIGN CONFIGURATIONS

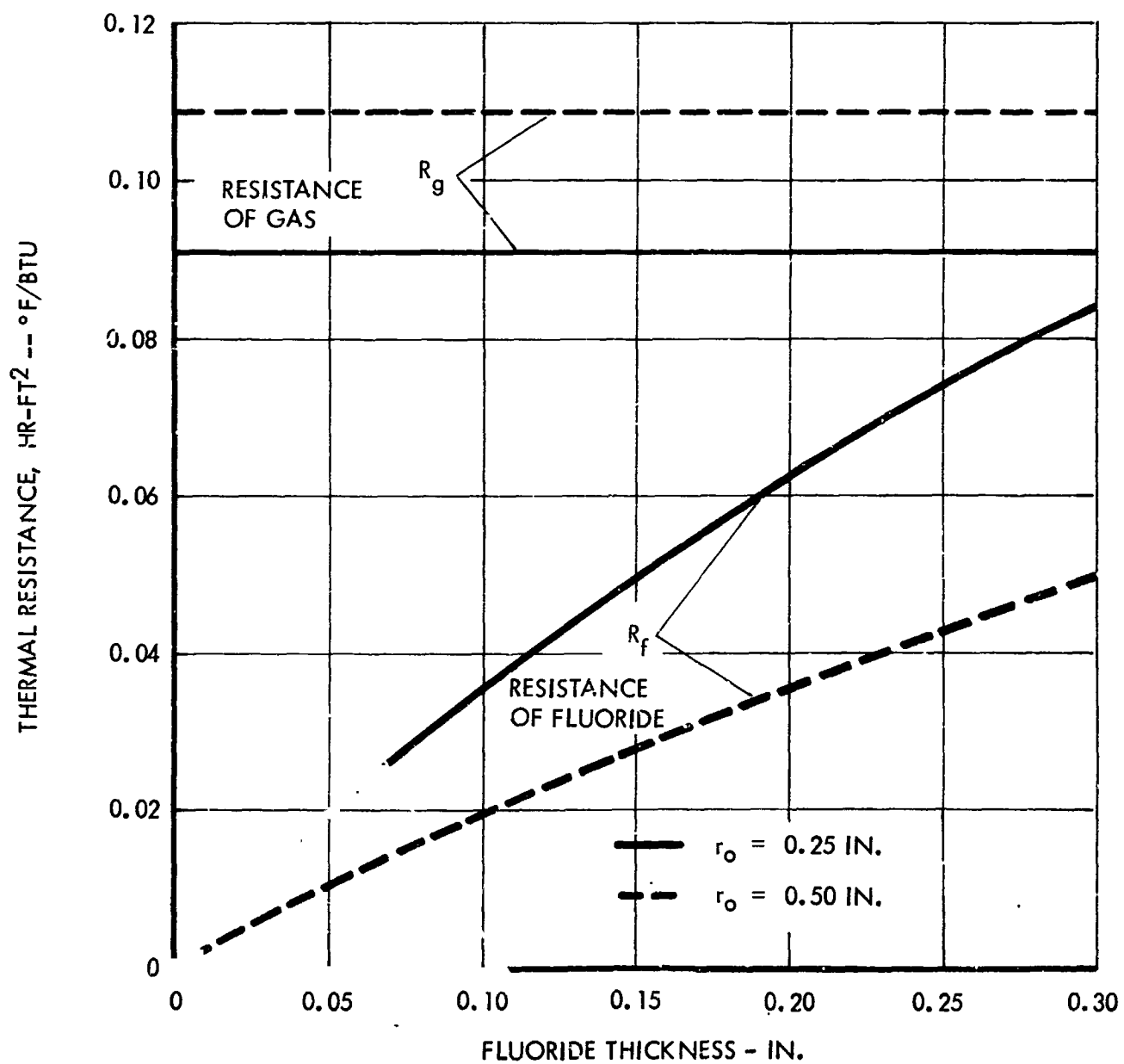


Figure 9 also indicates that if any fins are to be added they should be on the internal surface of the tubes, thereby lowering the gas thermal resistance. The advisability of using internal fins was investigated. Internal fins contribute to additional gas pressure drop and complicate the fabrication process. The most difficult part in the manufacturing process is the procurement, or production, of the correct type of internally finned tubing. It is not readily available commercially and could necessitate a fabrication development program.

Flow analysis of the desirability for internally finned tubes was based on the amount of heat transferred per unit of pressure drop. It was demonstrated that the amount of heat transferred per unit of pressure drop was a maximum with bare tubes and lower with internally finned tubes. In view of this result, the pressure drop limitation which is very important to the overall system and the fabrication problems inherent in internally finned tubes indicated that every effort should be made to use base tubes if possible. The analytical results that the heat transfer per unit of pressure drop is a maximum with a bare tube was confirmed in the experiments of Reference 6.

The potential use of a large number of tubes as required by a design operating at a low Reynolds number in the laminar region has been mentioned previously. The worst problem with this approach is the packaging difficulty. In addition, the overall fabrication problem is significant when one considers welding over 1000 tubes into inlet and outlet tube sheets. These general physical and practical mechanical limitations preclude the use of large numbers of tubes in a cavity receiver. Therefore, a small number of tubes was considered desirable and operation in turbulent flow indicated.

Finally, fins can be attached to the cavity surface to promote heat transfer between the cavity surface and the lithium fluoride to reduce the thermal resistance between the cavity surface and the lithium fluoride, and thus to reduce the temperature difference between the cavity surface and the lithium fluoride melt line for a given heat transfer flux level. It is well known and understood that all forms of extended surface can reduce the thermal resistance. In general, any of the various forms of extended surface can be employed for this purpose, but each of them complicates the fabrication of the inner shell and the subsequent assembly of the basic container. Therefore, for the sake of simplicity and reliability in design and assembly, it is desirable to avoid the complication of fins attached to the inner shell. If the resulting surface temperature is higher than the material of construction can safely withstand, it becomes obvious that some form of extended surface must be employed to reduce the surface temperatures required for melting the fluoride. At the time of the preliminary analysis, no definite information was available on which to base a final decision. Hence, the approach was to proceed on the optimistic hope that fins would not be required. Subsequent events discussed in Section 4.2 indicated that the initial units will require fins until zero-g test results indicate otherwise.

The above discussion completes the generalized preliminary design analysis. The next section presents the important gas and lithium fluoride property data employed in both the preliminary and flightweight design stages.

3.2 Argon and Lithium Fluoride Property Values

3.2.1 Argon Properties

Source: Reference 7

Temperature Range: 1400° R to 2000° R

3.2.1.1 Specific Heat

$$C_p = 0.1242 \text{ BTU/Lb-}^\circ\text{R}$$

3.2.1.2 Specific Heat Ratio

$$\frac{C_p}{C_v} = 1.667$$

3.2.1.3 Gas Constant

$$R = 38.7 \text{ ft-lb/lb-}^\circ\text{R}$$

3.2.1.4 Viscosity

Variable, per Figure 10

3.2.1.5 Thermal Conductivity

Variable, per Figure 11

3.2.1.6 Prandtl Number

$$Pr = 3600 \frac{C_p \mu}{k}$$

3.2.2 Lithium Fluoride Properties

3.2.2.1 Melting Temperature

Source: References 8 and 9

$$t_m = 848^\circ\text{C} \pm 1^\circ (1560^\circ\text{F} \pm 1.8^\circ)$$

VISCOSITY OF ARGON

SOURCE: NBS CIRCULAR 564

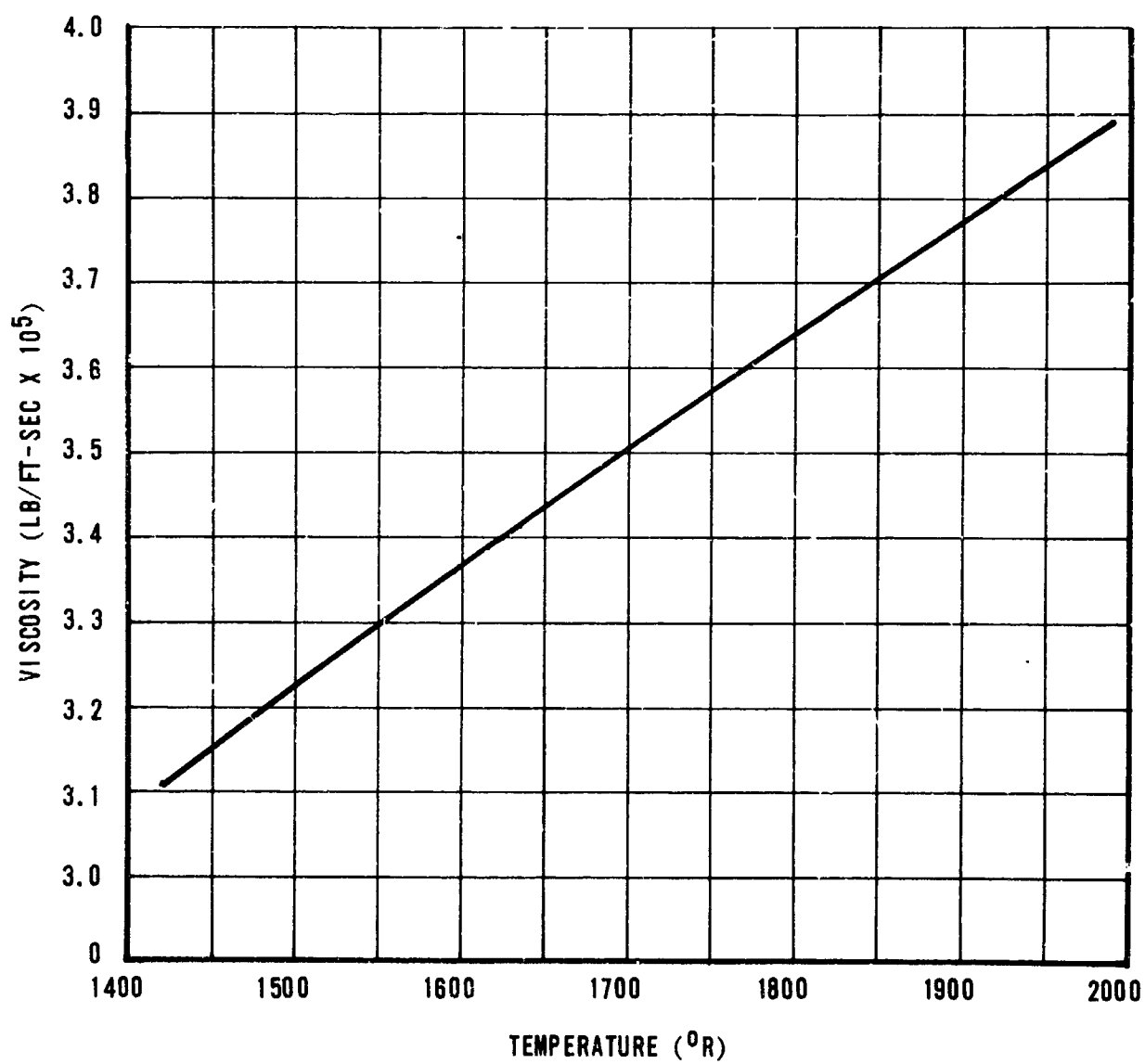


FIGURE 10

THERMAL CONDUCTIVITY OF ARGON

SOURCE: NBS - CIRCULAR 564

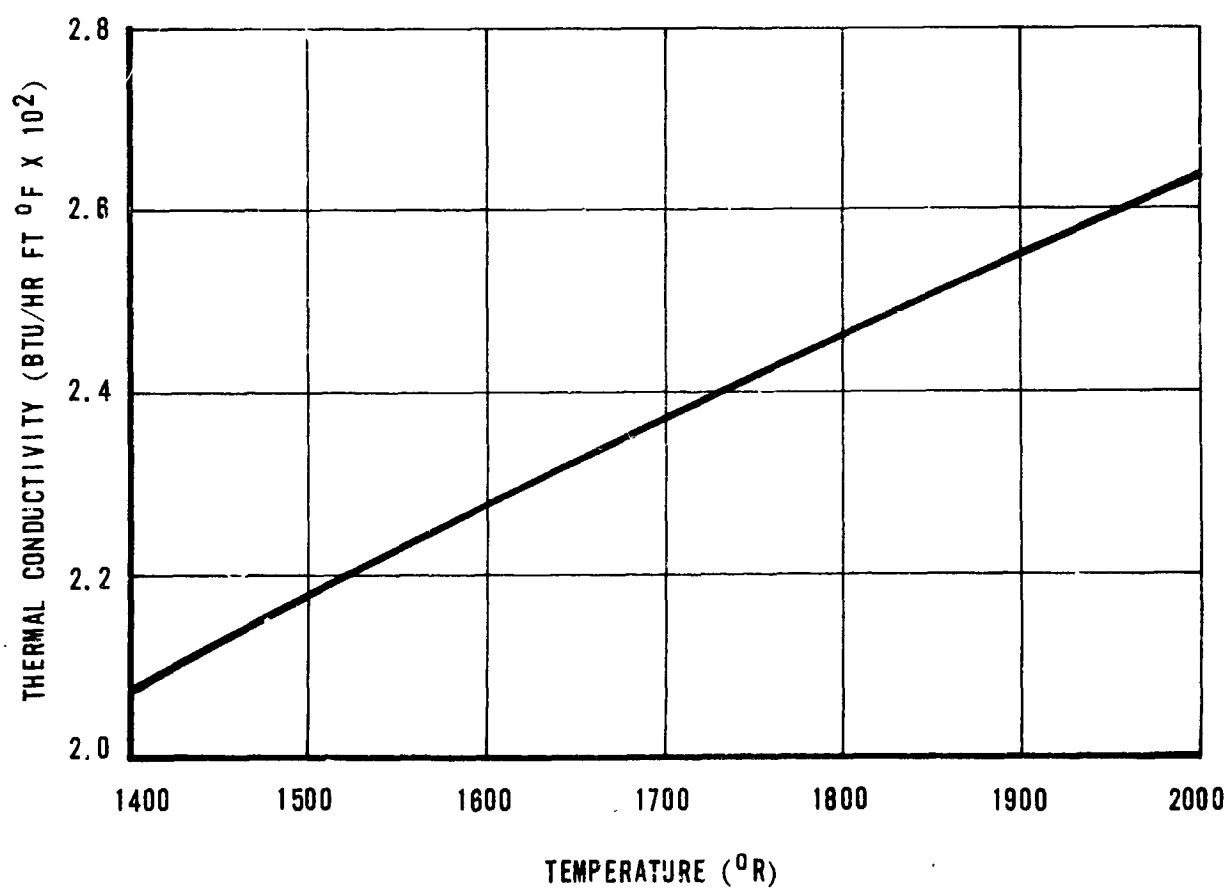


FIGURE 11

3.2.2.2 Heat of Fusion

Source: References 8 and 9

$$h_f = 6.470 \text{ kcal/MOLE (449 Btu/Lb)}$$

Note: Both References 8 and 9 lean heavily on Reference 10 for this type of data.

3.2.2.3 Heat Content

Source: Reference 9

Variable, per Figure 12

3.2.2.4 Density

Solid - Source: Reference 8

$$\rho_s = 2.63905 \pm 0.0001 \text{ gm/cm}^3 (25^\circ \text{C})$$

Liquid - Source: Reference 8

$$\rho_e = 1.789 \text{ gm/cm}^3 (870^\circ \text{C})$$

$$\rho_e = 2.201 - 0.000474 t \text{ gm/cm}^3 (887^\circ \rightarrow 1058^\circ \text{C})$$

Liquid - Source: Reference 11

$$\rho_e = 1.729 + 5 \times 10^{-4} (1000 - t)$$

where t is in degrees centigrade.

Values selected by TRW are shown in Figure 13.

3.2.2.5 Additional Data

Reference 8 is reproduced in its entirety including its bibliography.

3.3 Cavity Configuration Studies

In addition to the various possibilities on tube design and heater operation, several shapes were considered as potential candidates for the cavity surface and storage bath container. The major shapes investigated were the hemisphere, cone and cylinder. A fourth shape, the inverted cone with an internal conical section for multiple reflections, was not seriously considered for this application because of the complexity involved and the ultimate requirement for an all sun orbit. The inverted cone was included, however, in the cavity evaluation conducted under contract NAS 3-2789 and reported in Reference 12. Each of the three shapes will be discussed in order.

HEAT CONTENT OF LITHIUM FLUORIDE

SOURCE: KELLEY, K.K. BUREAU OF MINES BULLETIN 584

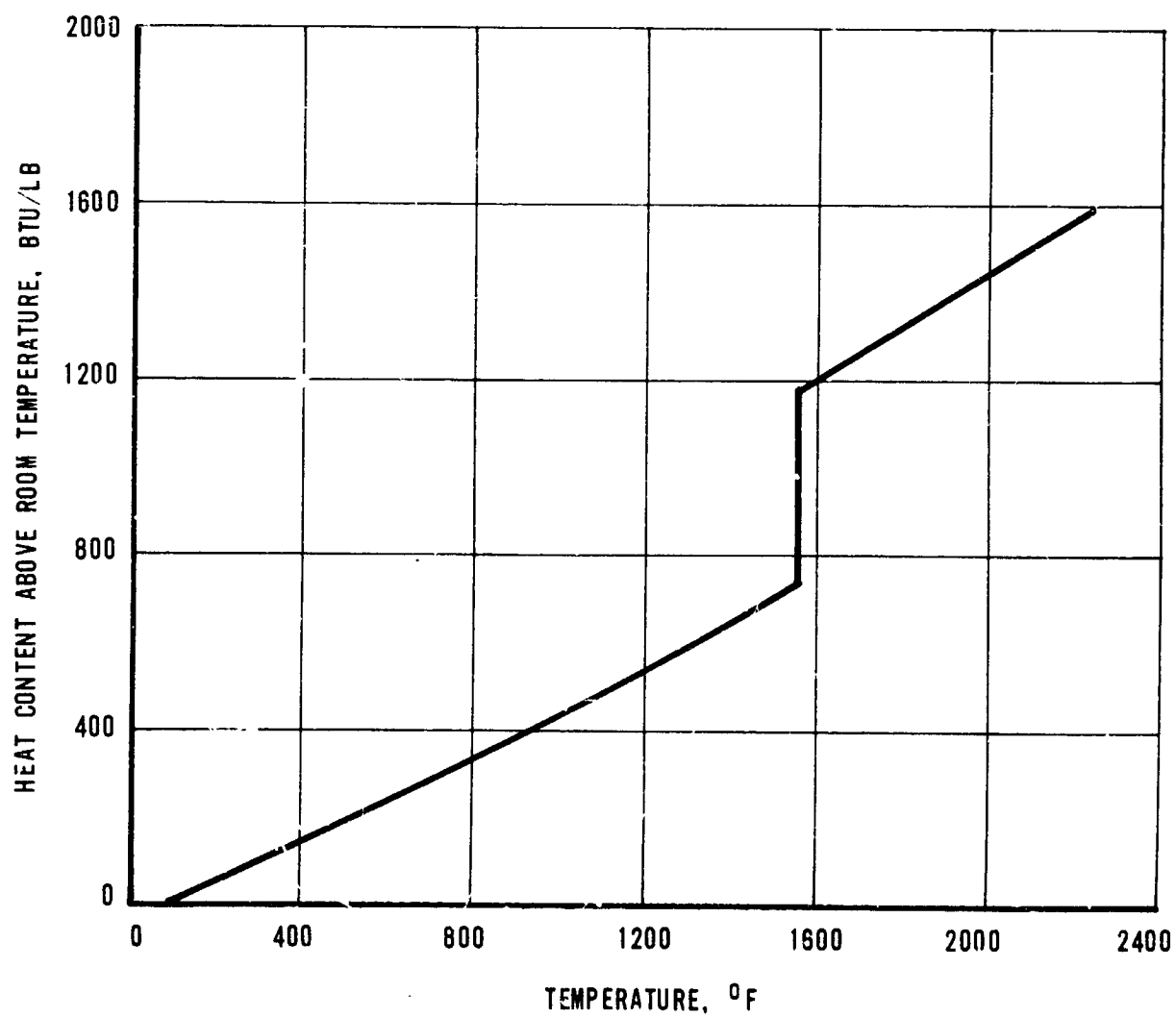


FIGURE 12

DENSITY OF LITHIUM FLUORIDE
SOURCE: LITHIUM CORP. OF AMERICA - BULLETIN 23.762

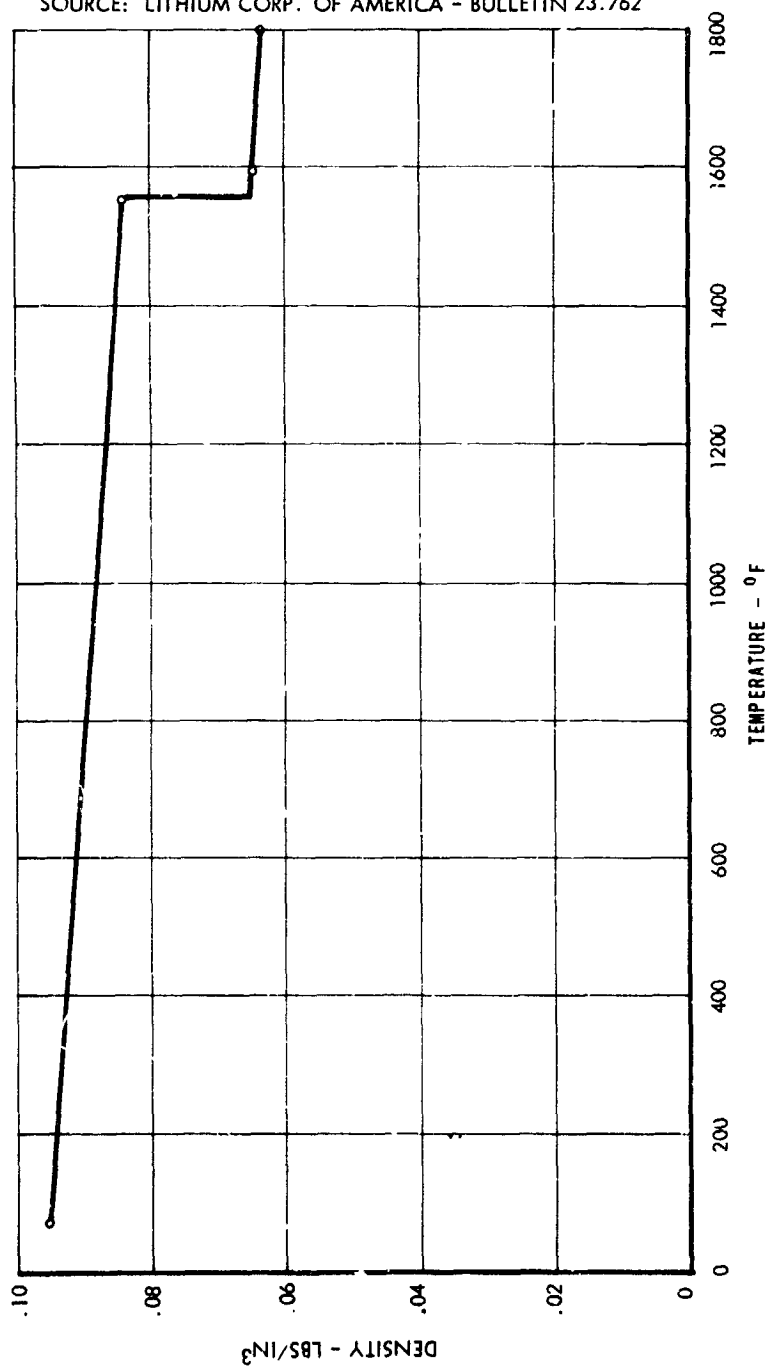


FIGURE 13

3.3.1 Hemispherical Container

The hemispherical container is composed of an inner shell, an outer shell, an inlet tube sheet and manifold, an outlet tube sheet and manifold assembly, the heater tubes and an aperture cone assembly. An early version of this type of design for single orbit operation is shown in Figure 14. The lithium fluoride is to be loaded into the resulting void volume in the basic container. The important geometrical dimensions for this hemisphere are listed below:

Tube Length	2.87 ft	(34.44 in.)
Tube Diameter	.0352 ft	(0.422 in.)
Tube Number	130	
Cavity Diameter	4.78 ft	(57.36 in.)
Receiver Diameter	5.0 ft	(60.0 in.)
Reynolds Number	5400	

The above dimensions were published previously in Reference 13. They were obtained on the basis of optimum packaging of the entire unit.

3.3.2 Conical Container

The conical container is essentially a compromise between the hemisphere and the cylinder. The conical container retains the hemisphere's features of a single inlet and gas flow in one direction only. In addition, it permits a longer tube length and a reduced number of tubes. One version of a conical container is illustrated in Figure 15. The conical container is composed of the same essential elements as the hemisphere, inner and outer shells, inlet and outlet tube sheets and manifold assemblies, heater tubes and an aperture cone assembly. The pertinent dimensions are listed below:

Tube Length	4.27 ft	(51.24 in.)
Tube Diameter	.0542 ft	(0.65 in.)
Tube Number	60	
Cavity Diameter	4.51 ft	(54.12 in.)
Receiver Diameter	4.83 ft	(57.96 in.)
Reynolds Number	7600	

3.3.3 Cylindrical Container

An early version of a cylindrical type of container is presented in Figure 16. Though the version in Figure 16 included rectangular tubes, circular tubes were also considered. The cylinder requires gas flow in opposite directions for any two adjacent tubes. Because of this, at least three manifolds are needed. Either the inlet or the outlet manifold can be common, but the other one must be duplicated. The version in Figure 16 employed a common outlet manifold with two inlet manifolds. The inlet manifolds were tapered in a decreasing area from front to rear and the outlet manifold was tapered in an increasing area from front to rear. Other items in the assembly included the inner and outer shells, the heater tubes and the aperture cone assembly. The pertinent dimensions are as follows:

Tube Length	11.72 ft	(140.64 in.)
Tube Diameter	.0762 ft	(0.914 in.)
Tube Number	30	
Cavity Diameter	3.6 ft	(43.2 in.)
Receiver Diameter	3.95 ft	(47.4 in.)
Reynolds Number	10,800	

3.3.4 Feasibility Evaluation

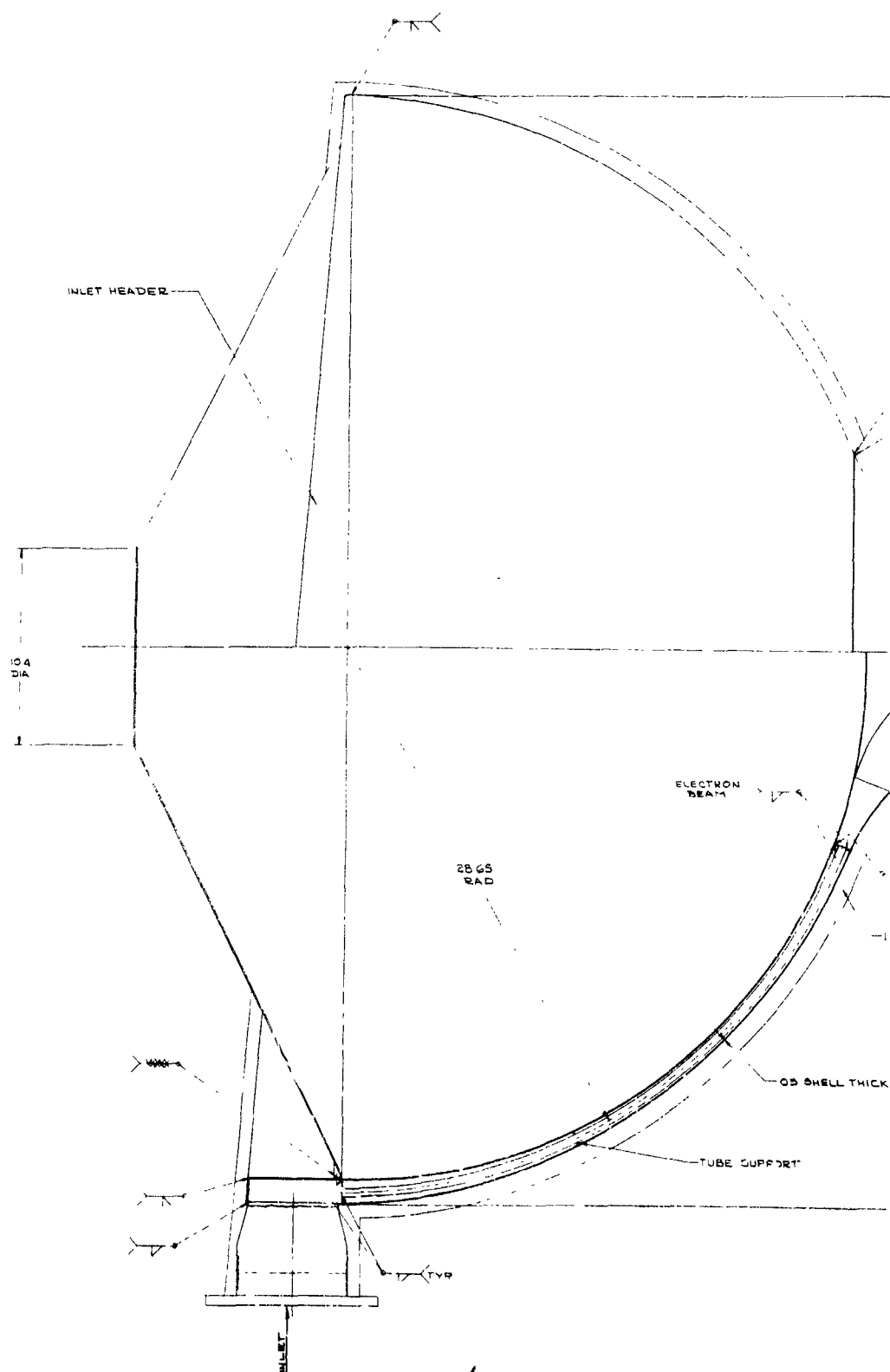
The choice of a basic cavity and container shape was made on the results of a design review and feasibility evaluation. This procedure extended over several calendar months. Engineering, design, manufacturing, reliability, quality assurance and materials personnel contributed to various portions of the design review and subsequent evaluation. The entire process resulted in the selection of an optimum shape for use in the flight type design. To aid in the evaluation, numerical ratings were assigned to each of the three shapes in several important areas. A summary of these ratings is included below.

<u>Item</u>	<u>Container Evaluation</u>		
	<u>Hemisphere</u>	<u>Shape</u> <u>Cone</u>	<u>Cylinder</u>
Simplicity	3	2	1
Fabrication	3	2	1
Performance			
Thermal	1	2	3
Stress	1	2	3
Cavity	1	2	3
Overall Reliability	1	2	3
	10	12	14

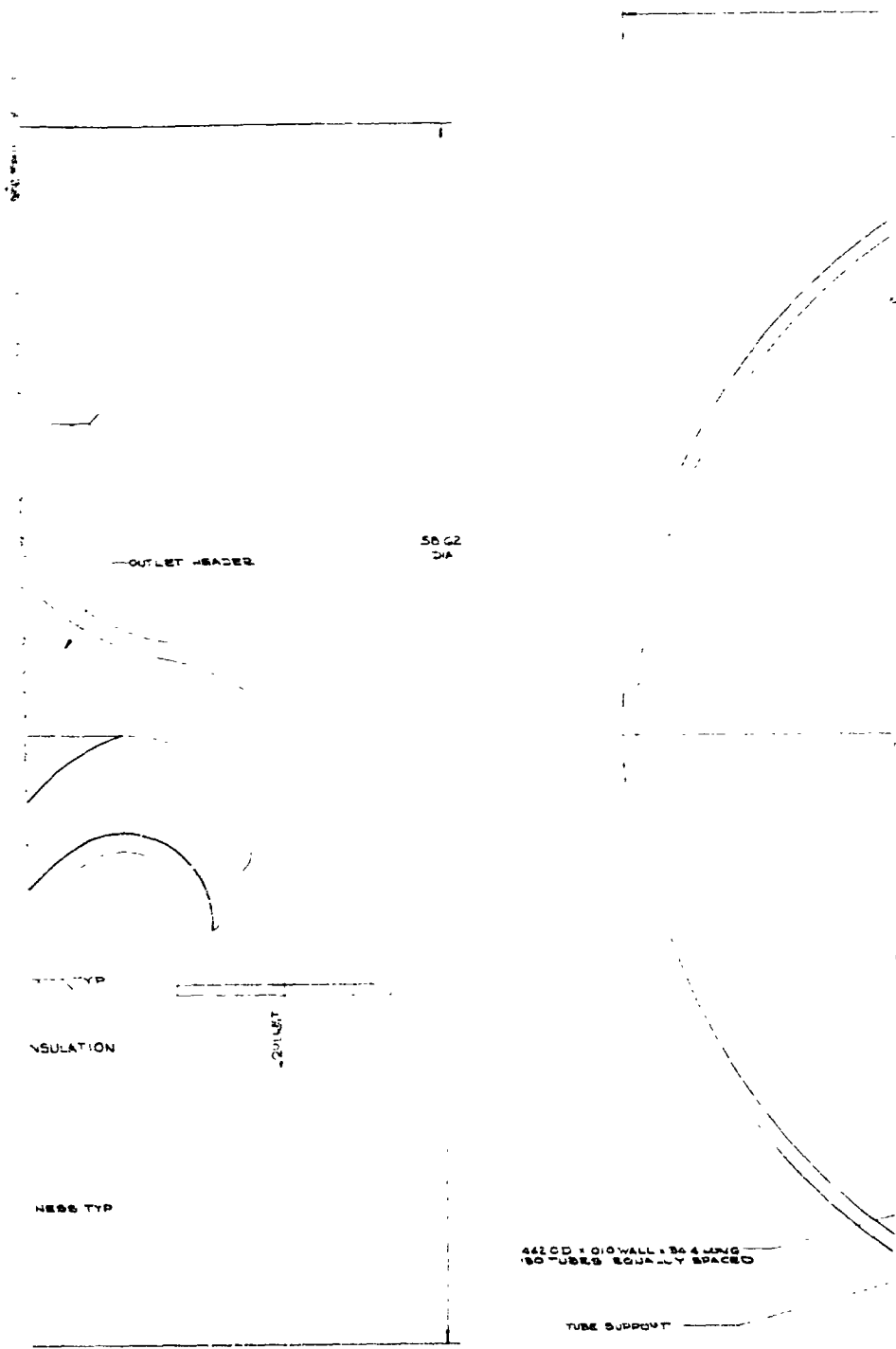
The numerical ratings are not truly indicative of the relative position of each shape in that the difference between a number 1 and a number 2 could be very slight, and the difference between the number 2 and the number 3 could be quite large. Thus, a completely true picture cannot be obtained from the simple listing above.

One of the factors which influenced the evaluation significantly was the desire to minimize welding on the high temperature inner cavity surface. This consideration reduces significantly the ease of fabrication and manufacture which the cylinder would otherwise possess. In view of the diameter of these designs, all shells which require minimum welds must be formed by the power spinning process. It is well known that the cylinder is a difficult shape to form by this process. With these considerations, the cylindrical shape resulted in difficult fabrication problems.

The cylinder did provide the smallest receiver outer diameter and thus afforded the minimum collector shadowing. However, the stresses inherent in the cylinder were much higher than



PRELIMINARY DESIGN CONFIGURATION OF A SINGLE ORBIT
CAVITY RECEIVER WITH A HEMISPHERICAL FLUORIDE CONTAINER



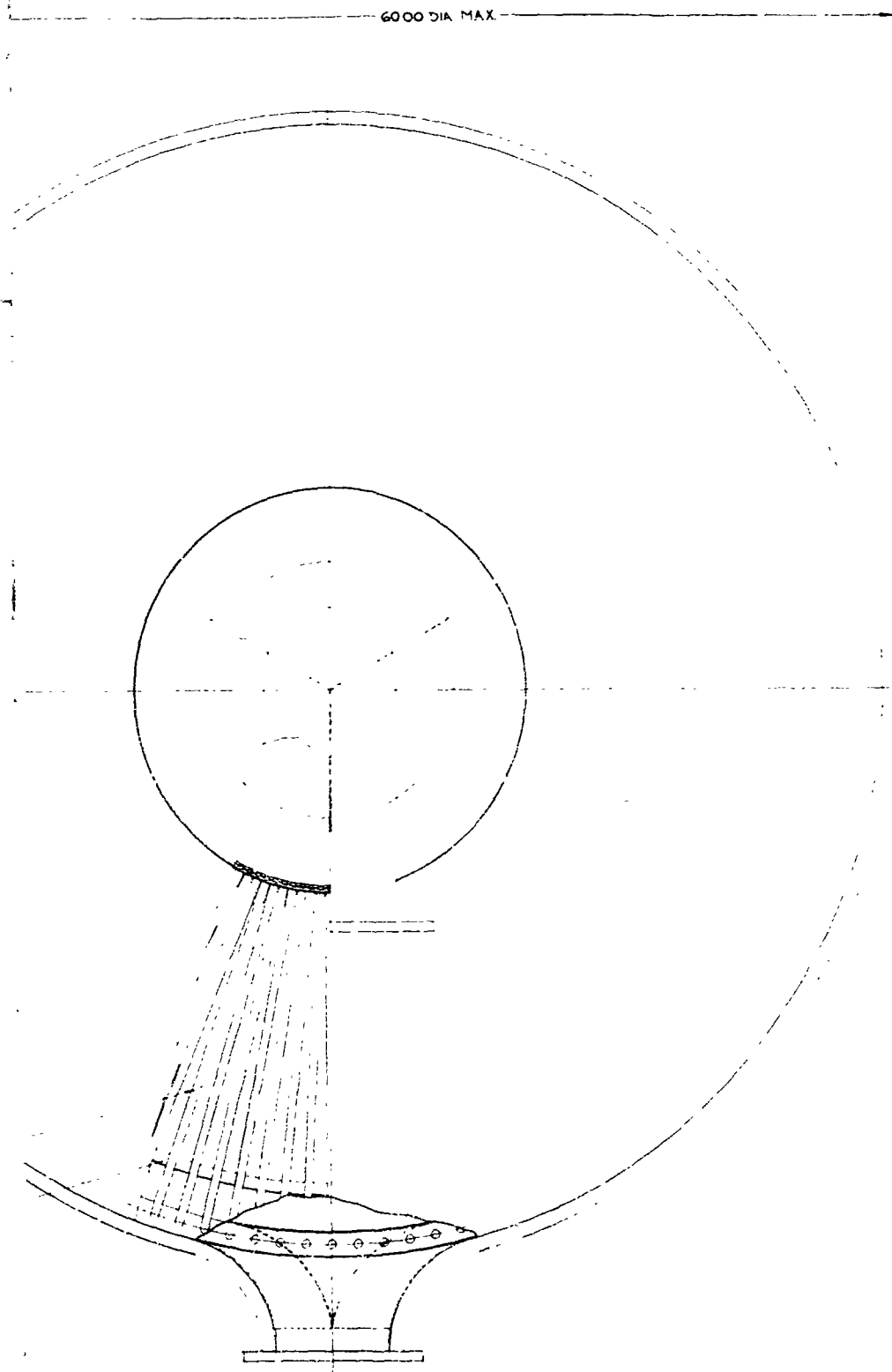
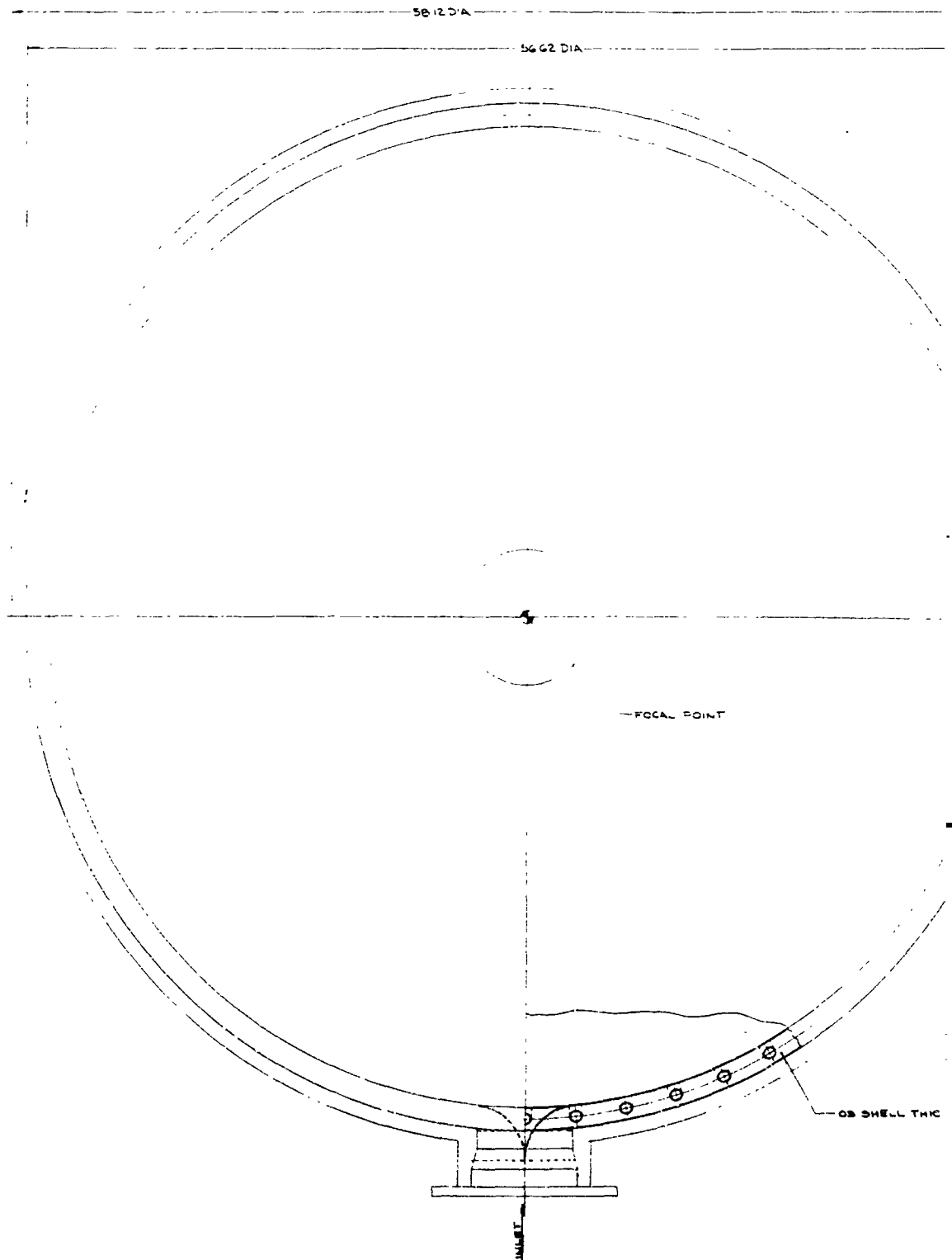
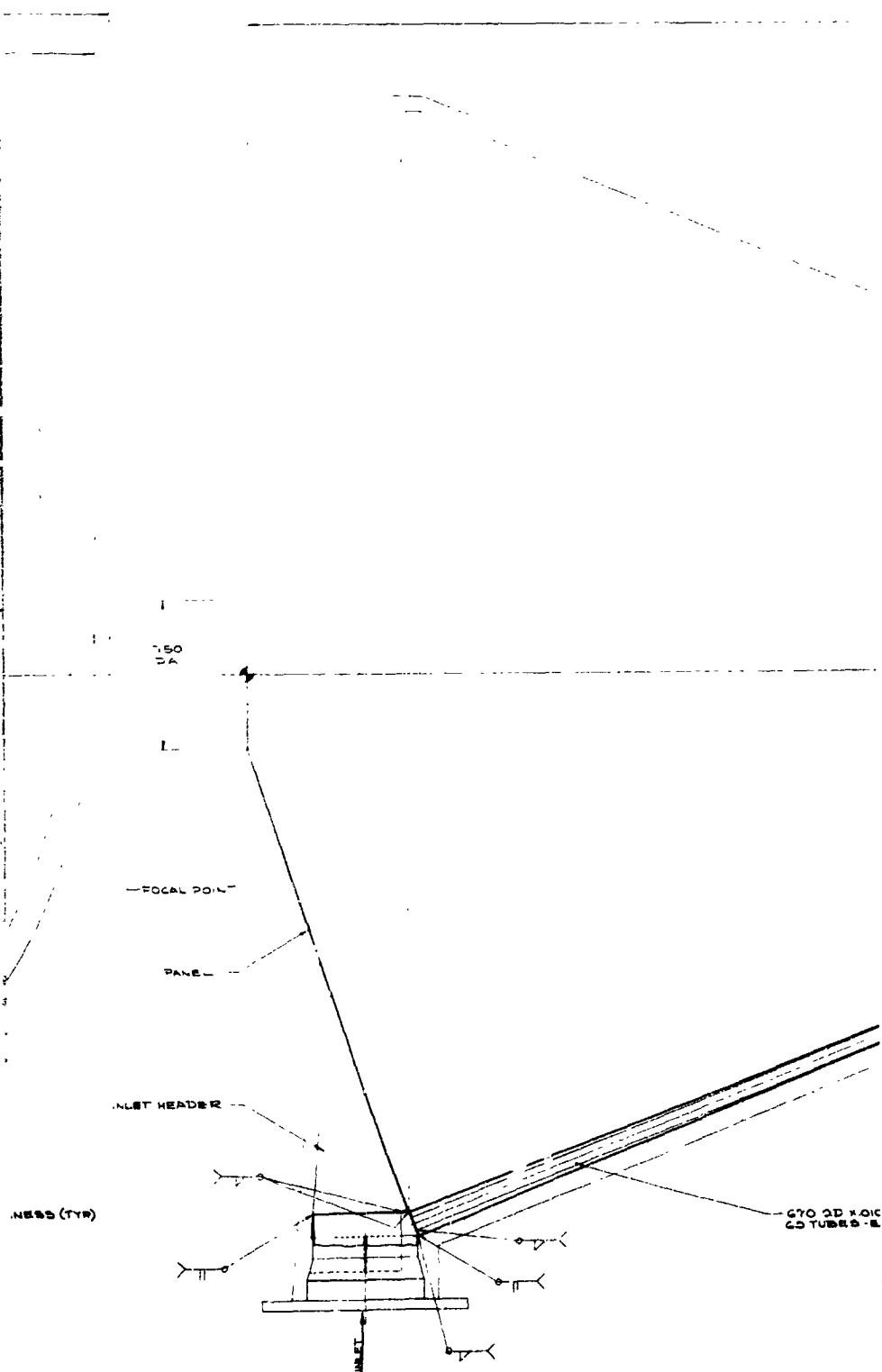


FIGURE 14



PRELIMINARY DESIGN CONFIGURATION OF A SINGLE ORBIT CAVITY RECEIVER WITH A CONICAL FLUORIDE CONTAINER



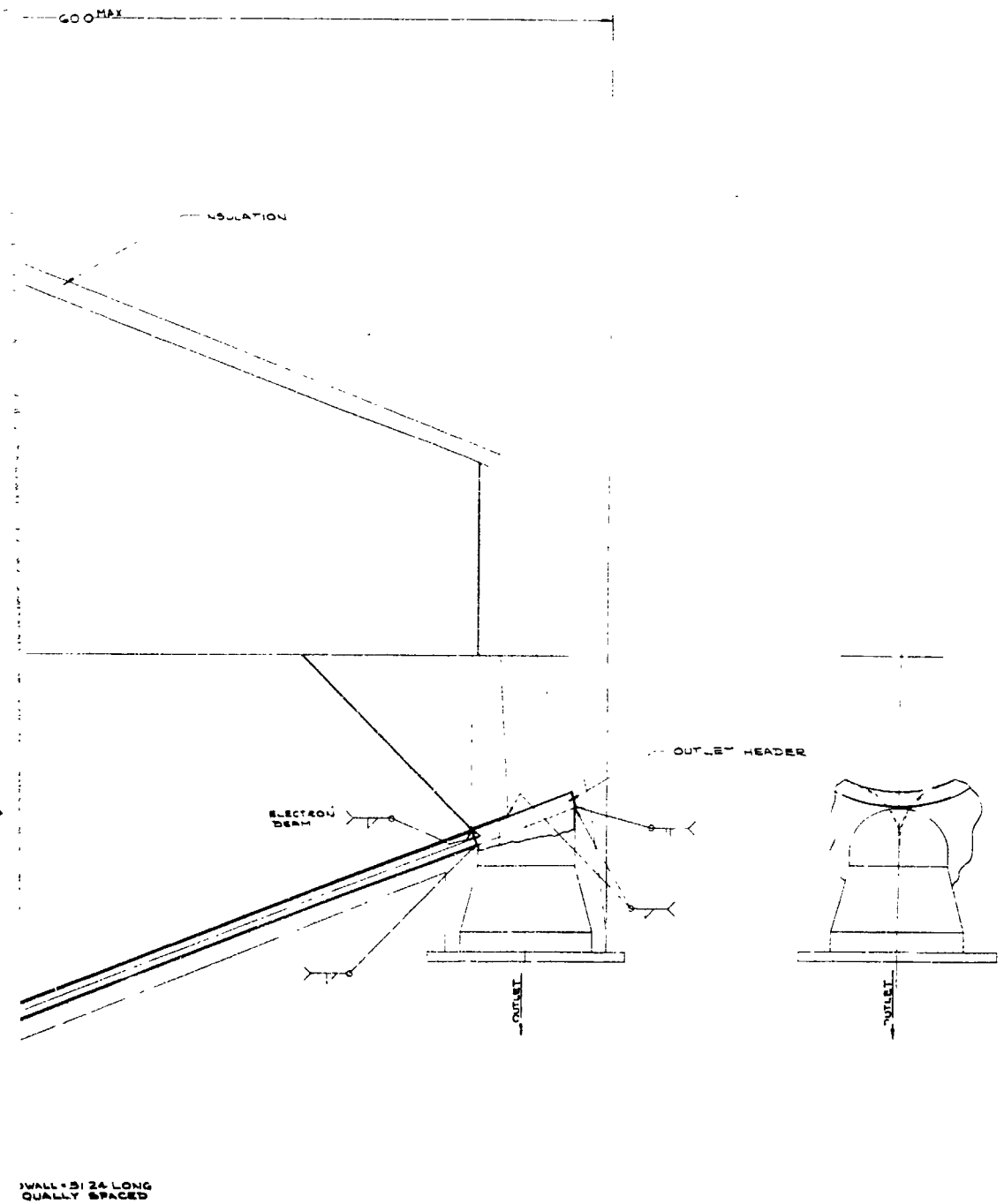
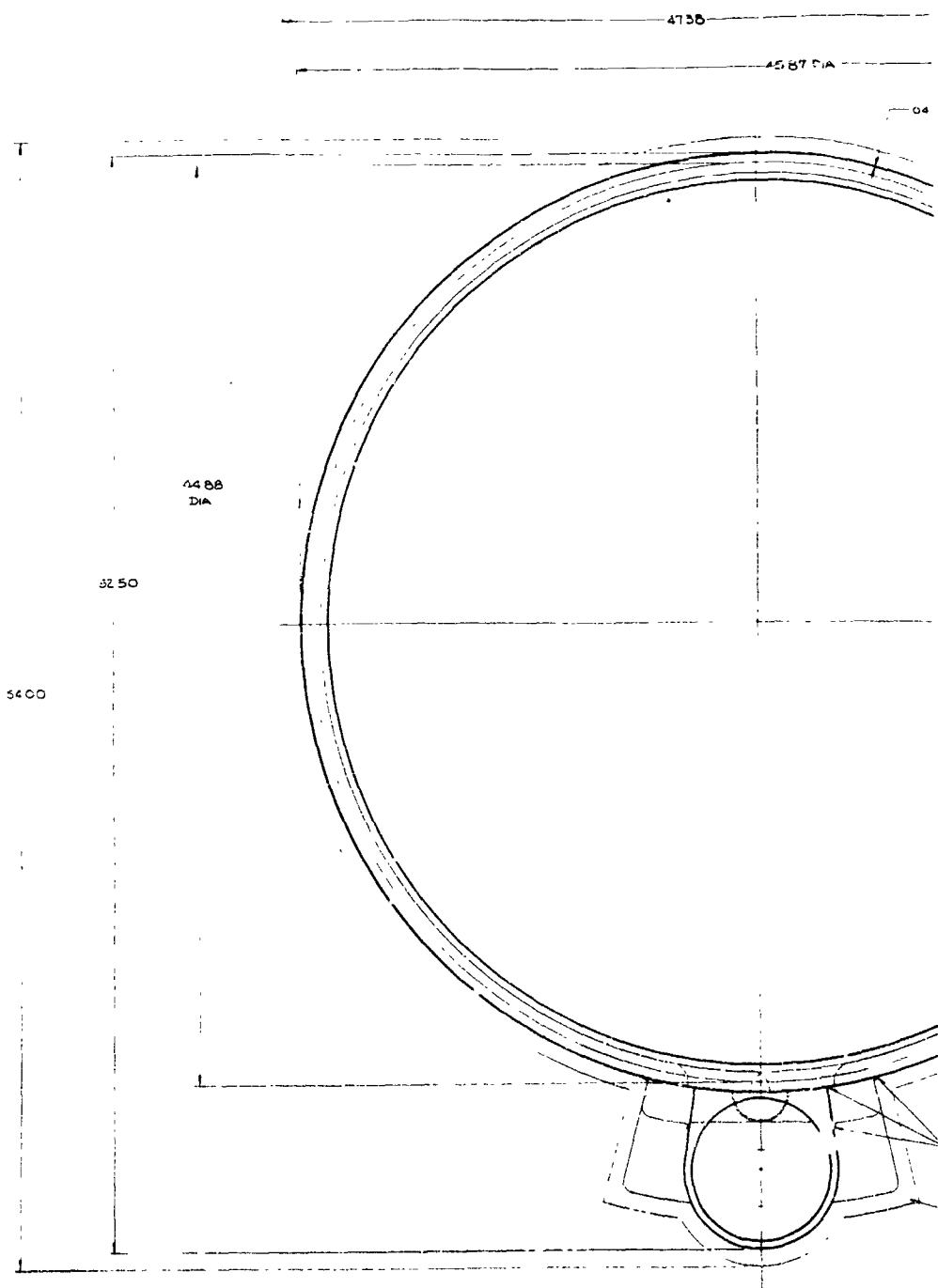
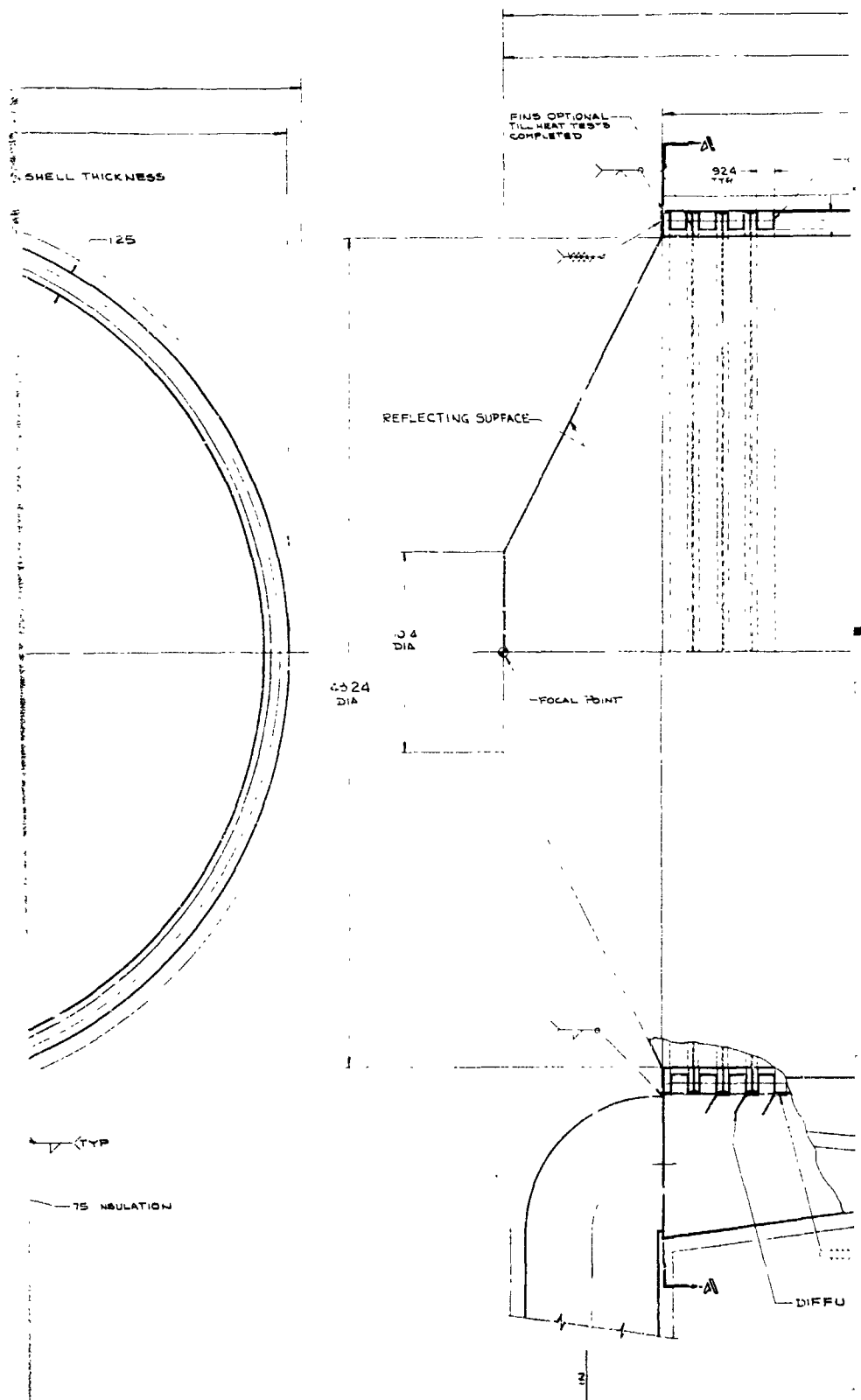


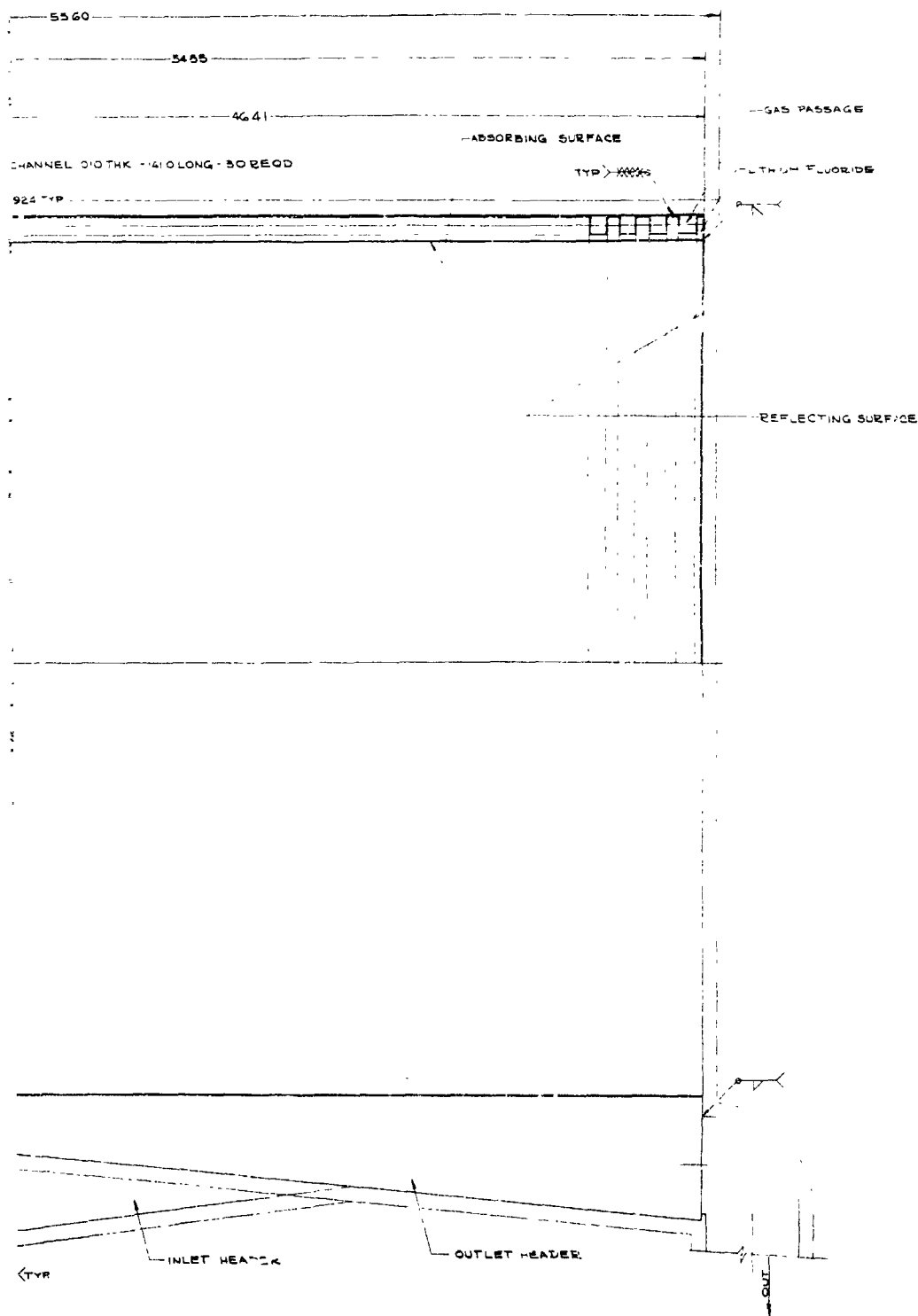
FIGURE 15



SECTION A-A

PRELIMINARY DESIGN CONFIGURATION OF A SINGLE ORBIT CAVITY RECEIVER WITH A CYLINDRICAL FLUORIDE CONTAINER





NOTE: ALL WELDS MAY BE BRAZED

the corresponding stresses in the hemisphere. The stress levels became a very important factor because of the low stress-to-rupture fatigue strength properties of the candidate materials at the predicted operating temperatures.

Cavity performance calculations were made employing the method of Reference 14. The results of these calculations indicated that the cylinder could not retain sufficient energy to meet the heater duty required. At that time, it was learned from other sources such as Reference 15 that results from the method of Reference 14 tended to be optimistic.

The cone was marginal in its capability to retain sufficient energy to meet the heater duty, according to the results from the method of Reference 14. In view of the possible optimum of these results, both the cylinder and the cone were eliminated from further consideration. The cavity performance results for the hemisphere indicated that it was safely in the valid operating zone.

One of the most serious objections to the hemispherical design resulting from the preliminary design studies was the large number of tubes (130) specified. Reliability and manufacturing considerations indicated that fewer tubes were desirable. After the hemisphere had been selected as the optimum shape, a further design effort was made to reduce the number of tubes required to as low a value as practical. The limit is set by the heater tube characteristics as determined from NASA specifications and the free lithium fluoride volume required. Thus, the effort in the full scale flightweight design studies was directed toward a hemispherical container with the lowest practical number of tubes.

Prior to presentation of the full scale flightweight design studies, the small scale experiments conducted on this program will be discussed in the next section. The results of the small scale experiments were necessarily applied to the full scale flightweight design studies.

PRECEDING PAGES BLANK NOT FILMED

4.0 SMALL SCALE EXPERIMENTS

The small scale experiments which were conducted on this program were intended to determine the following:

1. The thermal conductivity of lithium fluoride in the liquid and solid states near the melting point.
2. The heat input possible to lithium fluoride containers with several forms of extended surface.
3. The heat release characteristics of lithium fluoride to a gas coolant.
4. Insight into the melting and freezing characteristics of lithium fluoride and the resultant void formation.

An analytical effort was expended to supplement the above experiments in the heat input area. This effort was directed toward the development of analytical procedures which could be employed to predict the temperature variation with melting time. A complete discussion of the analysis is presented in the Appendix, Section 8.4. Examination of the final equations indicated that their solution by strictly analytical means would be rather formidable and costly in terms of manpower hours. Therefore, recourse was taken to a heat flow analyzer and the solutions obtained on it. The heat flow analyzer effort is discussed in the Appendix, Section 8.5. The important results from the heat flow analyzer solutions will be given for comparison with the experimental results in Section 4.2. Each of the above experimental areas will now be discussed in order.

4.1 Thermal Conductivity Experiments

As noted, previously, the thermal conductivity experiments were conducted to determine measured values of the thermal conductivity of lithium fluoride in the solid and liquid states near the melting point. Since this program is fundamentally a development program and not a research program, the experiments were confined to the temperature region of interest for this development. This temperature region is just below and just above the melting temperature. No attempts were made to obtain measurements at room temperature or at temperatures between room and the melting temperature region or at temperatures above the melting temperature region. The original literature search failed to uncover any experimental data on lithium fluoride thermal conductivity, but later some data were located in sources such as Reference 16.

4.1.1 Experimental Apparatus

The apparatus employed in these experiments was basically the same for the heat addition, heat removal and conductivity testing. The test assembly was designed to handle the heat input and heat release tests primarily. It was essentially similar to the lithium hydride tests on the Sunflower program, as reported in Reference 1 and was not specifically designed for

thermal conductivity measurements. A cutaway view is shown in Figure 17. As can be observed from Figure 17, the test bed consisted essentially of the test module mounted below a quartz-tube radiant heater. A coolant chamber was installed beneath the test module. A sheet of 1/4-inch thick Min-K insulation was placed beneath the test module and the coolant chamber to provide more uniform heat removal. The heater-module-coolant chamber assembly was covered with one inch of Min-K insulation.* This assembly was placed on a Marinite* support structure. The outside container was constructed of 1-inch thick Marinite, which itself is a type of insulation. The void between the heater-module-coolant chamber assembly was filled with Perlite which is a bulk insulation. Thus, the test bed consisted essentially of insulation surrounding the heater-module-coolant chamber assembly.

The layout for the thermal conductivity module is illustrated in Figure 18. The dimensions were selected based on an anticipated value of thermal conductivity on the order of 1.5 Btu/Hr-Ft-°F. The thermocouple instrumentation throughout the test module can be observed in Figure 18. Additional thermocouples were installed at various places throughout the test bed to determine the temperatures at these locations. These additional readings were needed to estimate the heat losses to various parts of the test bed.

The test rig schematic is presented in Figure 19. The coolant air was supplied by a plant-wide system. The incoming air was filtered, regulated and measured. The flow rate was determined by two methods - through an orifice and a rotameter. The flow control valve was located between the orifice and the rotameter. From the rotameter, the air went directly to the coolant chamber and then vented to atmosphere. The air pressure was measured at the regulator and the rotameter, and the orifice pressure difference was obtained from a water manometer reading. The air temperature was measured at the inlet and outlet of the coolant chamber.

The electrical schematic is also included in Figure 19. Heater power was controlled by variacs. Voltmeter, ammeter and wattmeter readings were obtained. All low temperature readings were obtained with iron-constantan thermocouples and recorded by a 24-point 0-800°F Honeywell temperature recorder. The high temperature readings were obtained with chromel-alumel thermocouples and recorded by a 24-point 0 → 2000°F Honeywell temperature recorder.

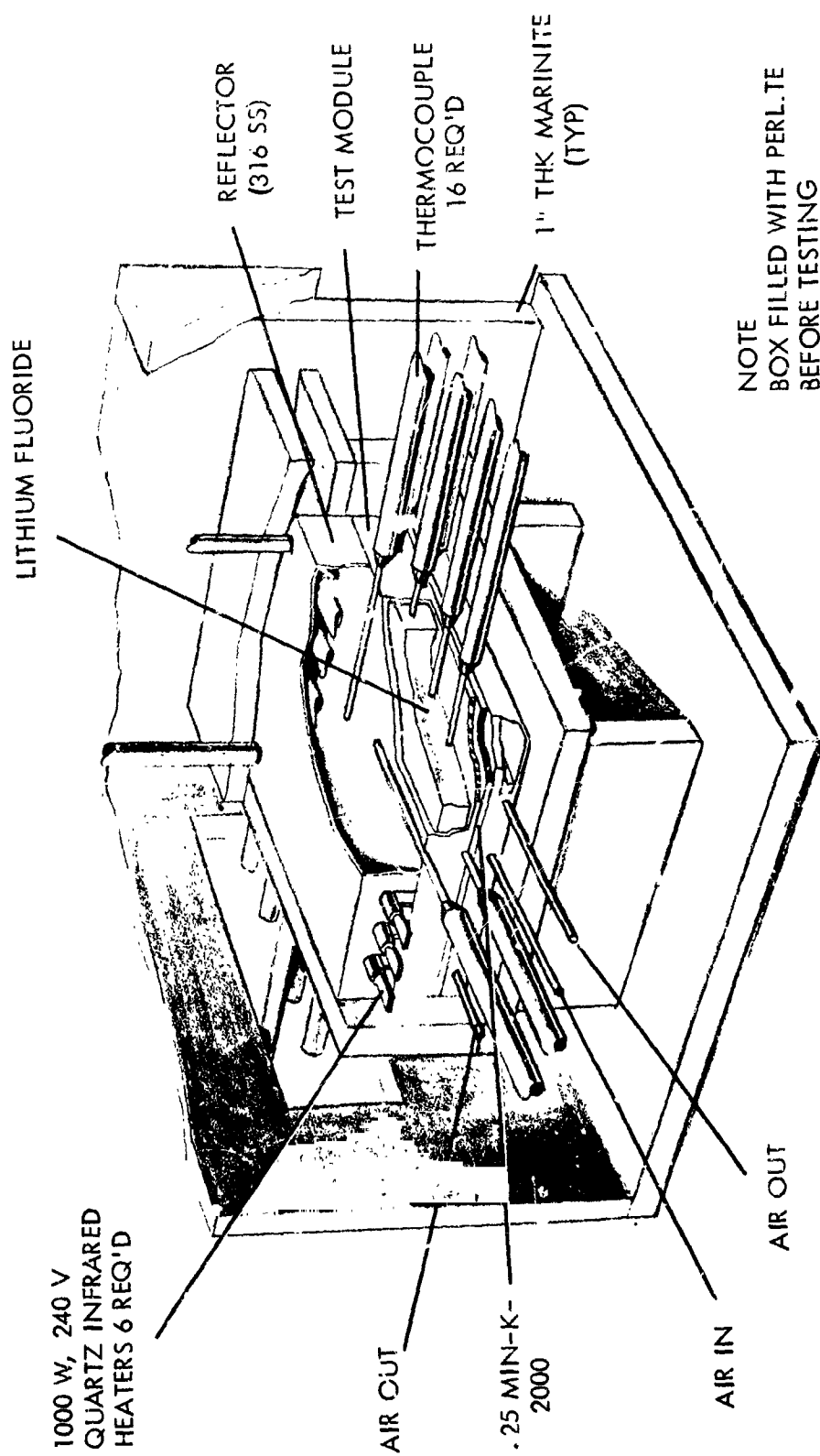
The test module was fabricated, assembled and loaded at TRW with 12.0 lb of lithium fluoride. During the initial melting process, a vacuum was pulled on the lithium fluoride to remove the corrosive hydrogen fluoride vapor.

4.1.2 Experimental Procedure

After the test bed installation was complete and all heater and thermocouple leads and coolant supply lines were connected, a vacuum was drawn on the module to make certain

*See Appendix Section 8.1.1

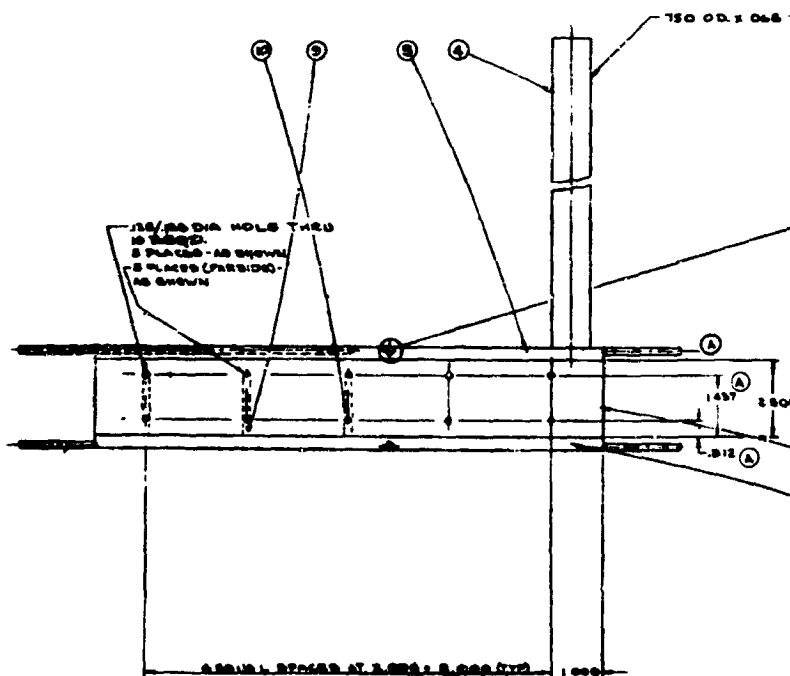
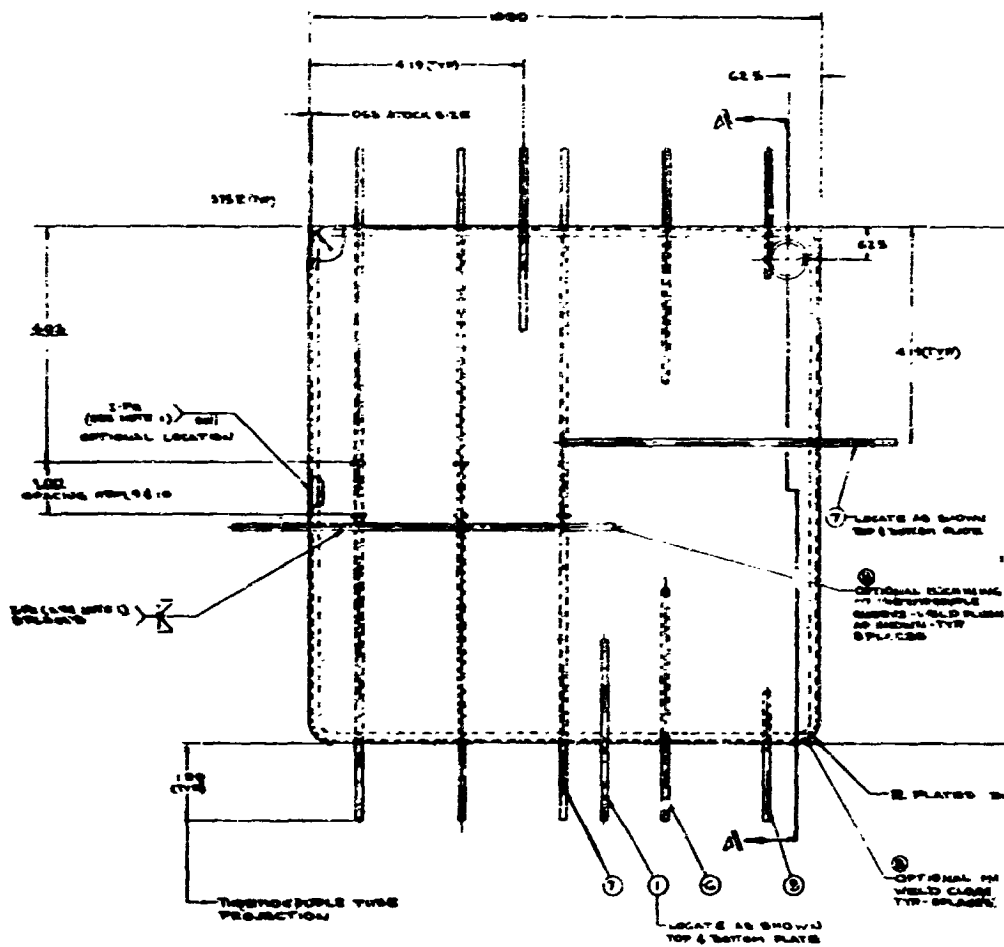
BRAYTON CYCLE TEST MODULE



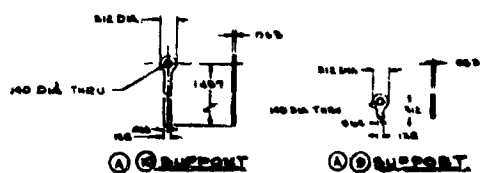
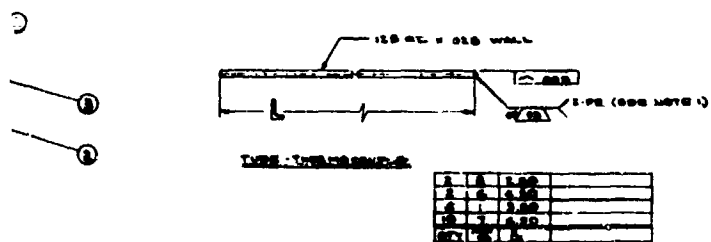
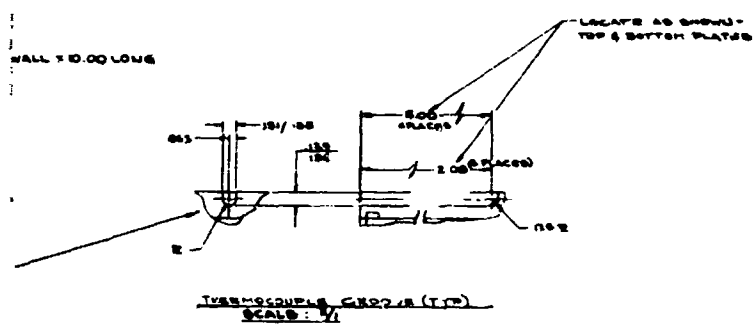
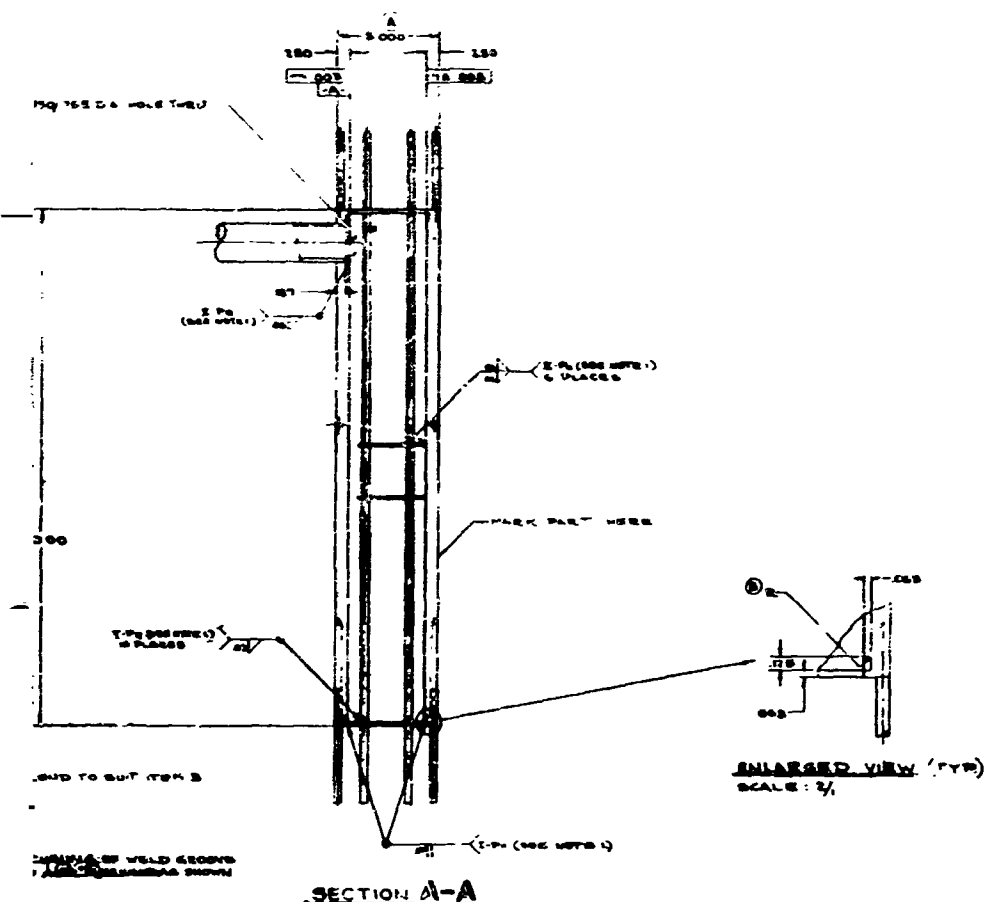
NOTE
 BOX FILLED WITH PERLITE
 BEFORE TESTING
 BOX SIZE 20" x 20" x 19" HIGH

FIGURE 17

THERMAL CONDUCTIVITY



TEST MODULE BRAYTON CYCLE



BLANK PAGE

220V

VARIAC

0.15 A

0.3000 W

0.300 V

100W, 240V INCANDESCENT LAMP

10A

10A

10A

SWITCH

TEST AREA

CELL

1A TEMP PTS PICKED UP ON MODULE

ELECTRICAL SCHEMATIC

43

the connections were tight. The vacuum attained was in the 20 micron range at room temperature. The vacuum pump continued to operate during heating, but the vacuum level increased to the high micron range, 300 to 500. These actions were generally true of all modules tested.

When it was ascertained that the system was acceptably tight, heating was initiated. During the first heat, the fluoride was completely melted and maintained molten for several hours in an effort to remove any additional corrosive vapors not previously removed. The temperatures of the molten fluoride bath and the test bed were stabilized without any coolant flow. The heater power required under these conditions was that needed to overcome losses from the module to the test bed and out the heater reflector. At the conclusion of the initial test run, the heater power was shut off and coolant flow initiated to assist in freezing the fluoride. It was desired to leave the fluoride in a frozen condition at the end of the day. The initial set of runs were made with no coolant flow and included several runs with the fluoride molten and several with the fluoride solid at temperatures just below the melting temperature. In each instance, the temperatures of all parts were stabilized and the total heat losses obtained from the heater power required. It was planned to apply these values on the later runs to estimate the heat transferred to the fluoride.

The second set of runs concentrated on obtaining data for the liquid fluoride at temperatures just above the melting temperature. Care was taken during these runs to make certain that all of the fluoride was molten. This fact was indicated when the thermocouples located in the bottom plate of the module were recording 1560° F or above. Initially, the molten condition is easier to verify than the frozen condition, and thus, the liquid thermal conductivity was investigated first. Many runs were made in an effort to obtain reproducible results. In each case, all bath temperatures were held stable within 1° F for one hour for a test to be considered valid and data taken.

The third set of runs were intended to determine the data for the solid fluoride at temperatures just below the melting temperature. Again, care was taken to make certain that all of the fluoride was solid. This could be assured with the thermocouples located in the top plate of the module recording 1560° F or below and heat flowing. Several runs were made to obtain repeatable data. The same temperature stability criterion of 1° F per hour was employed in these runs to consider the data valid and suitable for recording.

4.1.3 Data Evaluation and Analysis

The major objective in the data reduction process was to provide flux data for the measured thermal gradients. The thermal conductivity was evaluated on the basis of its definition:

$$k = \frac{Q/A}{\Delta T/X}$$

The temperatures of the two rows of thermocouples immersed in the lithium fluoride bath were recorded during all valid runs. Since the distance between the two rows was fixed during fabrication, the temperature gradient was readily calculated as the temperature difference divided by the distance between the rows. The temperature pattern was investigated at each of the two rows for uniformity and to determine if any gradients existed. It was found that the temperatures were remarkably uniform, but slight gradients did exist from the central portion to the outer walls. Continued examination of the data revealed a central region in which no lateral temperature gradients existed. The central region so defined was then employed as the area in the above equation, and the temperature gradient was calculated on the basis of the values in the central regions. The remaining outer portions of the bath in which lateral temperature gradients were indicative of lateral heat losses were considered as a type of guard heaters. Normally, in thermal conductivity measurements, guard heaters would be employed to prevent undesirable heat losses normal to the direction of heat transfer.

During the thermal conductivity runs, it was observed that the measured temperature differences were very low at low heater powers. To reduce the potential error in the temperature gradient, the heater powers were increased to the high end of the available range for all of the valid runs. Attempts were made to calculate the heat flow through the fluoride by subtracting the measured steady-state heat losses obtained in the first set of runs from the heater power settings in the valid runs. As a check on the results, the heat flow through the fluoride was calculated by the addition of known, or measured, heat losses. These included the heat removed by the coolant and the heat lost to the sides and conducted down to bottom of the module. Sufficient assembly instrumentation was available to make direct calculations of these quantities. The results demonstrated that the former method did not provide heat flow values that were compatible and consistent with the rest of the data. The latter method, however, did provide consistent and compatible results; hence, the latter method was employed to evaluate the heat flow to the fluoride. The total heat flow to the fluoride was calculated as the sum of the heat removed by the coolant plus one-half of the side losses minus the heat conducted down the sides. Since the central region received only a part of the total heat flow to the fluoride, its heat flow was calculated on a straight percentage of the total heat flow. This method of calculating the heat flow in the central region contributed to the overall potential error.

In the following error analysis conducted for one of the solid runs, the above possible error was not included.

4.1.3.1 Error Analysis

$$Q_{\text{bath}} = \left[\frac{k A \Delta T}{x} \right] \text{LiF}$$

$$Q_{\text{bath}} = Q_{\text{air}} + 1/2 Q_{\text{loss}} - Q_{\text{cond.}}$$

Since $Q_{\text{bath}} \approx Q_{\text{air}}$, the major errors in evaluating the heat flow rate occur in the heat transfer to the air flow. In the sample calculation below, it is shown that $1/2 Q_{\text{loss}} - Q_{\text{cond}}$ equals 3.6 percent of Q_{air} for the liquid case examined therein. For solid lithium fluoride which is necessarily at a lower temperature level than the liquid case, the above difference is an even lower percentage of Q_{air} .

During the test, a temperature change of 1°F/hr was permitted as a maximum. This corresponds to an undetected change of 4 Btu/hr in the lithium fluoride bath. Such a change in heat content is also negligible.

$$k_{\text{LiF}} = Q_{\text{bath}} \left[\frac{x}{A \Delta T} \right]_{\text{LiF}} \approx Q_{\text{air}} \left[\frac{x}{A \Delta T} \right]_{\text{LiF}}$$

$$k_{\text{LiF}} \approx (\dot{m} c_p \Delta T)_{\text{air}} \left[\frac{x}{A \Delta T} \right]_{\text{LiF}}$$

Assuming no error in c_p for air, the differential elements become

$$\frac{dk}{k} = \frac{\delta \dot{m}}{\dot{m}} + \frac{\delta(\Delta T_{\text{air}})}{\Delta T_{\text{air}}} + \frac{\delta x}{x} - \frac{\delta A}{A} - \frac{\delta(\Delta T_{\text{LiF}})}{\Delta T_{\text{LiF}}}$$

In the worst case, the errors can become additive:

$$\frac{dk}{k} = \frac{0.3 \text{ lb/hr}}{30.0 \text{ lb/hr}} + \frac{2.0^\circ\text{F}}{229^\circ\text{F}} + \frac{.020 \text{ in.}}{1.125 \text{ in.}} + \frac{0.20 \text{ in.}^2}{100 \text{ in.}^2} + \frac{2.0^\circ\text{F}}{24.3^\circ\text{F}}$$

$$dk/k = 0.010 + 0.0087 + 0.0178 + 0.0020 + 0.0823$$

$$dk/k = \underline{\underline{0.1208}}$$

Thus, an error of 12 percent is possible in this solid case. It should be noted that the maximum contributing component is the possible error in the lithium fluoride temperature difference.

A typical calculation is presented next.

4.1.3.2 Sample Calculation

Run Number: 11-8

Test Data: Average temperature at top level = 1680°F
Average temperature at lower level = 1656°F

Air flow rate, $\dot{m}_r = 30.0 \text{ lb/hr}$

Air inlet temperature = 65°F

Air Outlet temperature = 294°F

Calculations:

$$Q_{\text{loss}} = 255 \text{ Btu/hr @ } 1668^\circ \text{F (average side wall temperature)}$$

$$Q_{\text{sides, conduction}} = Q_{\text{cond}} = k \frac{A \Delta T}{x}$$

$$k = 15.15 \text{ Btu/hr-ft-}^\circ\text{F (HS 25 @ } 1668^\circ \text{F)}$$

$$A = \frac{.063 (40)}{144} = 0.0175 \text{ ft}^2$$

$$\Delta T = 1680 - 1656 = 24^\circ \text{F}$$

$$x = \frac{1.125}{12} = 0.0937 \text{ ft}$$

$$Q_{\text{cond}} = \frac{15.15 (.0175) 24}{0.0937} = 67.9 \text{ Btu/hr}$$

$$Q_{\text{air}} = \dot{m} c_p \Delta T = 30 (.241) (294 - 65) = 1656 \text{ Btu/hr}$$

$$Q_{\text{bath}} = Q_{\text{air}} - Q_{\text{cond}} + 1/2 Q_{\text{loss}}$$

$$= 1656 - 67.9 + 0.5 (255) = 1716 \text{ Btu/lb}$$

$$K_{\text{LiF}} = \frac{Q_{\text{bath}} x}{A_{\text{bath}} \Delta T} = \frac{1716 (.0937)}{0.676 (24)} = \underline{\underline{9.92 \text{ Btu/hr-ft-}^\circ\text{F}}}$$

4.1.4 Results and Discussion

A summary of the thermal conductivities obtained for liquid lithium fluoride is given in Table I as follows:

TABLE I
SUMMARY OF LIQUID LITHIUM FLUORIDE
THERMAL CONDUCTIVITY RESULTS

<u>Test No.</u>	<u>Thermal Conductivity</u>	<u>Percent Deviation from Average</u>
II-3	12.35 Btu/hr. ft °F	9.3
II-4	12.90 Btu/hr. ft °F	14.1
II-7	10.25 Btu/hr. ft °F	9.3
II-8	9.92 Btu/hr. ft °F	12.2
II-9	11.10 Btu/hr. ft °F	1.8
II-11	9.84 Btu/hr. ft °F	12.8

Average $k = 11.3$ Btu/hr. ft °F

Maximum potential error = ± 27.5 percent

Typical values obtained for solid lithium fluoride are listed in Table II below. It must be emphasized that the values in both tables pertain only to temperatures near the melting temperature.

TABLE II
SUMMARY OF SOLID LITHIUM FLUORIDE
THERMAL CONDUCTIVITY RESULTS

<u>Test No.</u>	<u>Thermal Conductivity</u>	<u>Percent Deviation from Average</u>
II-5	4.81 Btu/hr. ft °F	5.7
II-10	5.37 Btu/hr. Ft °F	5.3
III-2	5.56 Btu/hr. ft °F	9.0
III-3	4.84 Btu/hr. ft °F	5.0

Average $k = 5.1$ Btu/hr. ft °F

Maximum potential error = ± 19.5 percent

After Reference 5 was published, a copy of Reference 16 was obtained. Figure 2-1 of Reference 16 presents data for the thermal conductivity of solid single crystals and extrapolates the experimental data from the measured temperatures to the melting temperature and to room temperature. The extrapolated estimate for the solid thermal conductivity at the melting temperature is approximately 5.3 Btu/hr-ft-°F. Reference 16 states that "It is expected that the thermal conductivity of solid lithium fluoride composed of many crystals will be considered lower." The earlier estimate in Reference 4 agreed with the above statement in Reference 16, but the extrapolated value of 5.3 Btu/hr-ft-°F in Reference 16 agrees remarkably well with the experimental value of 5.1 Btu/hr-ft-°F obtained on this program. Figure 2-1 of Reference 16 is reproduced as Figure 20 herein.

The experimental value of the solid conductivity was higher than expected. As a consequence the test module design was based on a much lower anticipated conductivity and higher temperature differences. The lower temperature differences encountered magnified the potential errors in temperature measurement and increased the over-all potential error. However, it is believed that the averaged experimental values presented herein are sufficiently accurate for engineering design purposes. This statement is particularly true for Brayton cycle cavity receiver designs in which the heat exchange rate-controlling resistance is on the gas side anyway. In Rankine cycle applications, the salt-side resistance would be rate-controlling much of the time, and the thermal conductivity values attain much more importance.

The above discussion completes the material on the thermal conductivity tests. The lithium fluoride heat input tests are discussed next.

4.2 Heat Input Experiments

Two series of heat input modules were constructed and tested on this program. The breakdown for the first series is given in Table III below, and the second series modules are listed in Table IV below.

TABLE III
HEAT INPUT MODULES - SERIES I

Module No.	Type of Extended Surface	Material	
		Module	Extended Surface
2	None	HS 25	
4	6 - 1/16 x 1-1/4 in. x 9 in. Fins	316 SS	316 SS
5	6 - 1/8 x 1-1/4 in. x 9 in. Fins	316 SS	316 SS
6	3/4 in. x .020 in. wall sq. honeycomb	316 SS	316 SS
7	3/8 in. x .020 in. wall sq. honeycomb	316 SS	316 SS

THERMAL CONDUCTIVITY - LITHIUM FLUORIDE

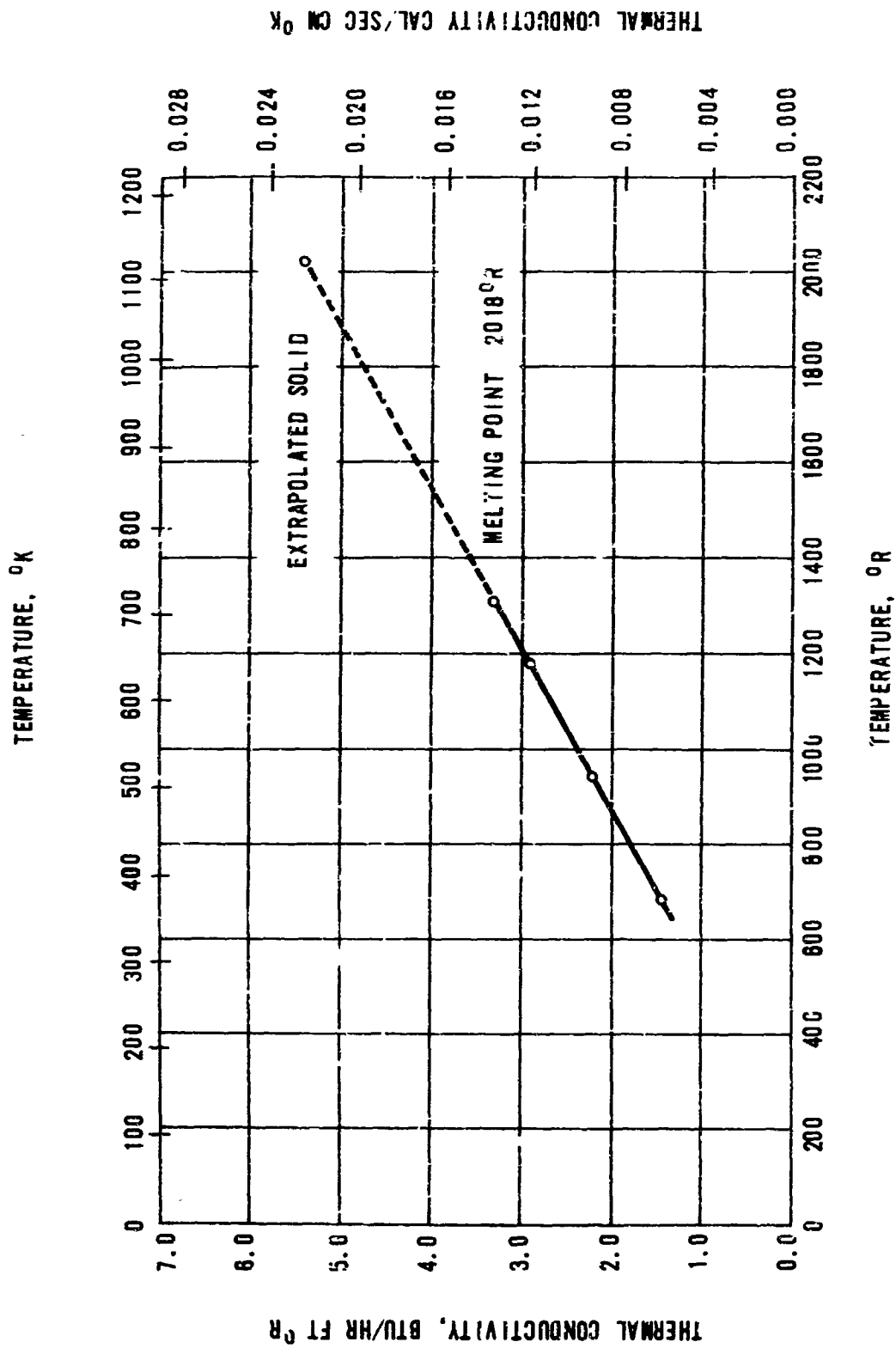


FIGURE 20

TABLE IV
HEAT INPUT MODULES - SERIES II

Module No.	Type of Extended Surface	Material	
		Module	Extended Surface
A	None	HS 25	
B	13 - 1/32 in. x 1-1/4 in. x 9 in. Fins	HS 25	Grade "A" Nickel
C	13 - 1/16 in. x 1-1/4 in. x 9 in. Fins	HS 25	Grade "A" Nickel

The purpose of each of the tests with the modules containing extended surface was to obtain experimental data on the amount of top plate temperature reduction that could be provided by the extended surface in comparison to the performance of the bare modules. In addition, it was desired to develop an analysis which could be employed to predict the various temperatures involved. The analytical investigation will be discussed first.

4.2.1 Analytical Prediction of Heat Input Performance

The analysis showed that the heat conduction problem is nonlinear because the change in phase of the lithium fluoride involves a moving boundary whose location is unknown. No analytical techniques were readily available to obtain exact solutions. Therefore, approximate methods were considered and the heat balance integral was selected.

The equations which resulted from the analytical investigation are presented in Section 8.4. Examination of these equations indicated that hand calculation of the solutions would require a prohibitive amount of manpower hours. In view of these manpower estimates, alternate methods were explored. Finally, it was decided to obtain the solutions by analog techniques.

A complete discussion of the analog investigation and its results is given in Section 8.5. Three basic cases were examined; one without fins, one with 1/32-in. grade "A" nickel fins, and one with 1/16-in. nickel fins. These cases were selected to be comparable to modules A, B and C for direct comparison. The solution for each case was obtained at three different heat input rates.

A summary of the important results from the analog solutions is presented in Table V. In addition, graphs were provided for the following:

1. Top plate upper and lower surface temperatures versus time.
2. Bottom plate upper and lower surface temperature versus time.
3. Lithium fluoride surface temperatures versus time.

4. Lithium fluoride temperatures versus time at two distances from bottom plate in solid state.
5. Location of the melting front versus time.

The variation of the melting time with the heat input rate is illustrated in Figure 21. The similar variation for the top plate surface temperatures is given in Figure 22. Additional curves for a typical case are contained in Section 8.5.

4.2.2 Test Module Construction

The basic design for the Series I test modules is shown in Figure 23. The various forms of extended surface were attached to the top plate of each new module. Figure 24 is a view of module number 5 prior to the final assembly weld. Figures 25 and 26 are similar views of modules 6 and 7. The extended surfaces were brazed to the top plate in each case with AMS 4778 brazing alloy which has a chemical composition of:

90.0 - 92.0%	Nickel & Cobalt
2.2 - 3.5%	Boron
1.5% max	Iron
4.0 - 5.0%	Silicon
.06% max	Carbon

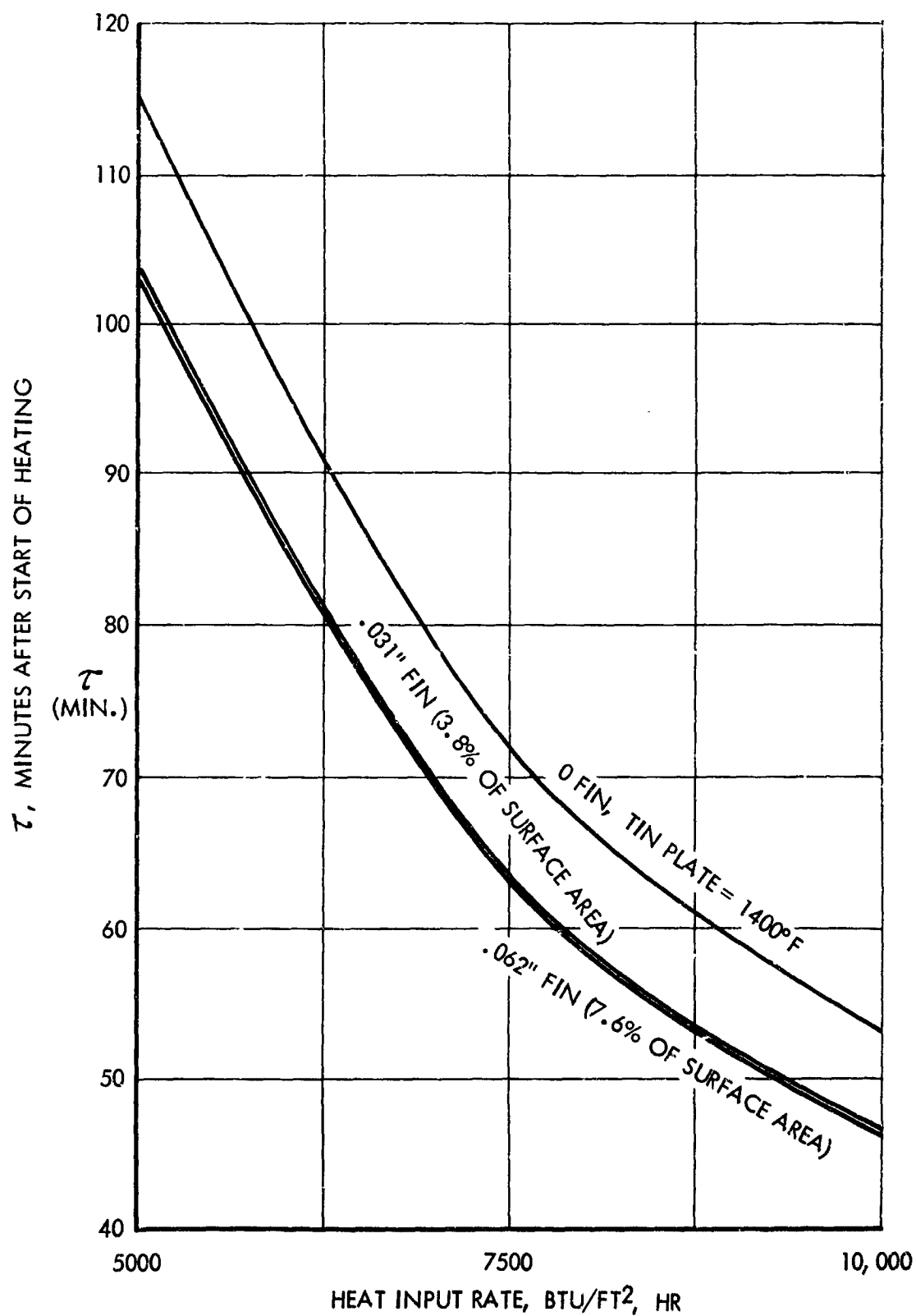
The brazing operation was performed in a furnace with a dry hydrogen atmosphere. The other parts of the modules were joined by hand welding using conventional TIG techniques.

The basic design for the Series II test modules was similar to that of the Series I modules except that the top and bottom plate thicknesses were increased to 1/2-inch based on the results of stress analysis and the maximum height available for the fluoride bath was fixed at 1.5 inches. The stress analysis performed is presented in Section 8.6. In Series I, the plate thicknesses were 3/8-inch and the maximum bath height was 1.4 inches. The same methods of joining and assembling the modules were employed. Figure 27 shows Module A as assembled and Figure 28 illustrates the top plates of Modules B and C after initial fin brazing. A second brazing operation was required to obtain acceptable joints.

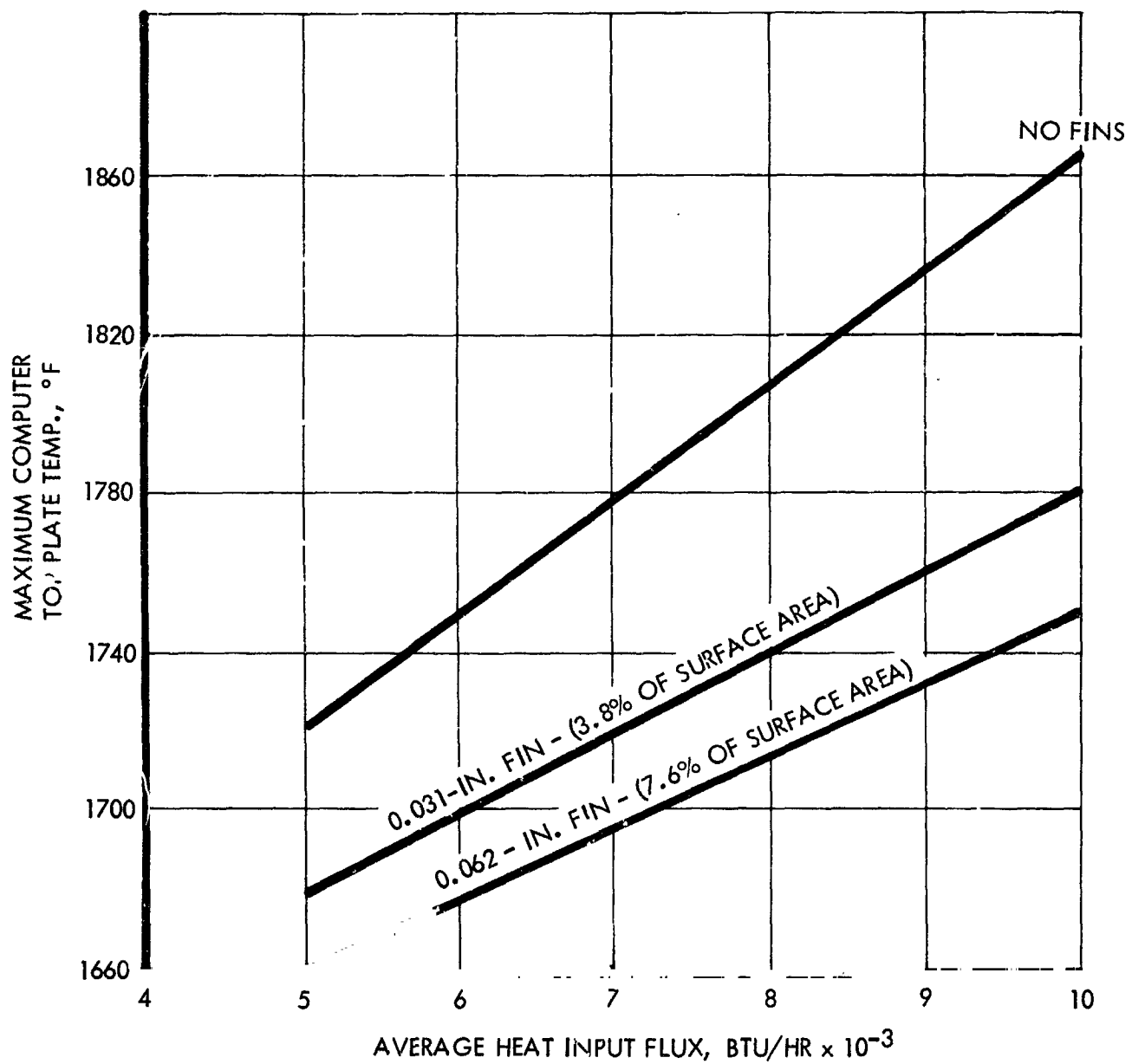
4.2.3 Experimental Apparatus

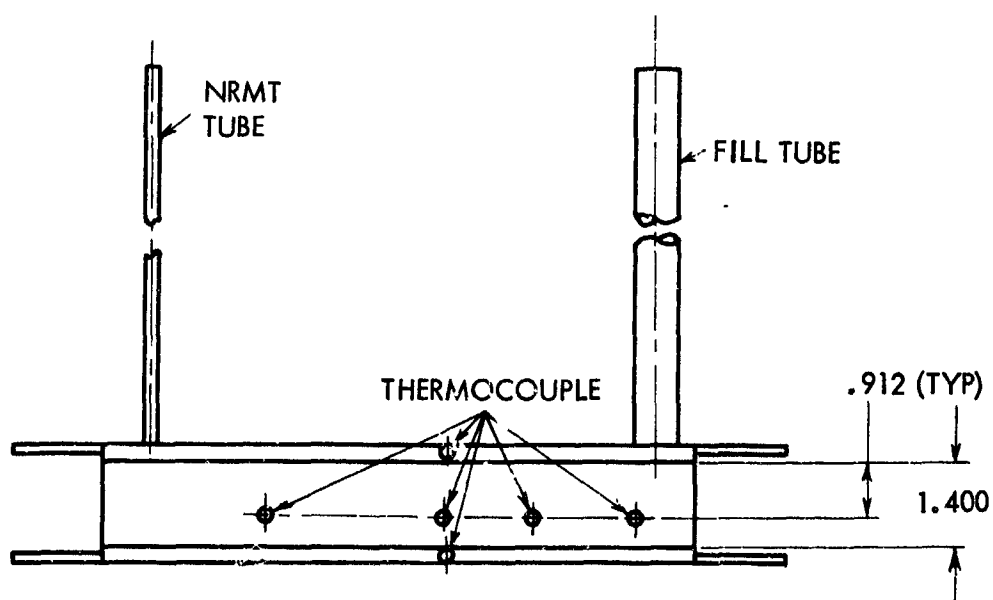
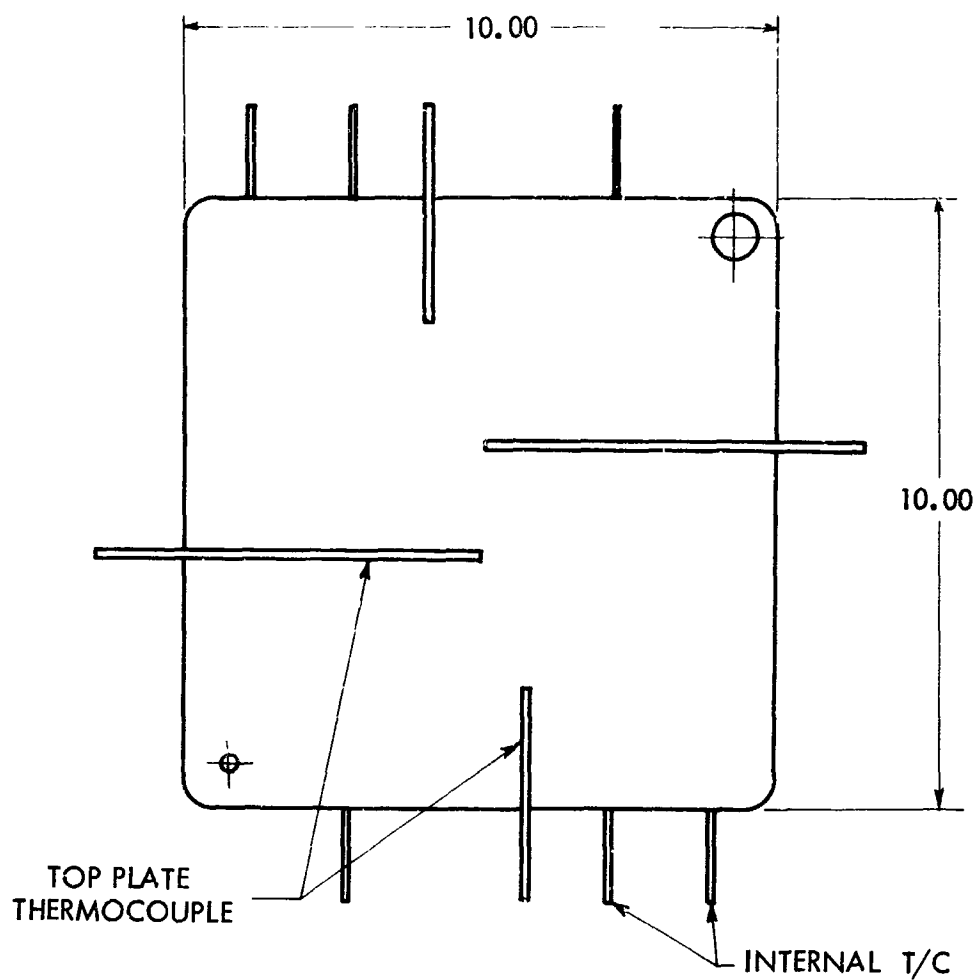
The basic apparatus for these experiments was described in Section 4.1.1. Only the changes will be discussed here. The Series I test modules were designed to be loaded with lithium fluoride by the Lithium Corporation of America at their Bessemer City, North Carolina facility. The bulk lithium fluoride powder was melted in a furnace with an air atmosphere. After the fluoride was molten, a vacuum was drawn to remove the water vapor and hydrogen fluoride vapors. A small tube was attached to the top plate to ease the evacuation problem.

MELTING TIME VS. HEAT INPUT RATE



COMPUTER RESULTS: CAVITY WALL SURFACE
TEMPERATURE (°F) VS HEAT INPUT FLUX, BTU/HR-FT⁻²





SKETCH OF HEAT INPUT TEST MODULES

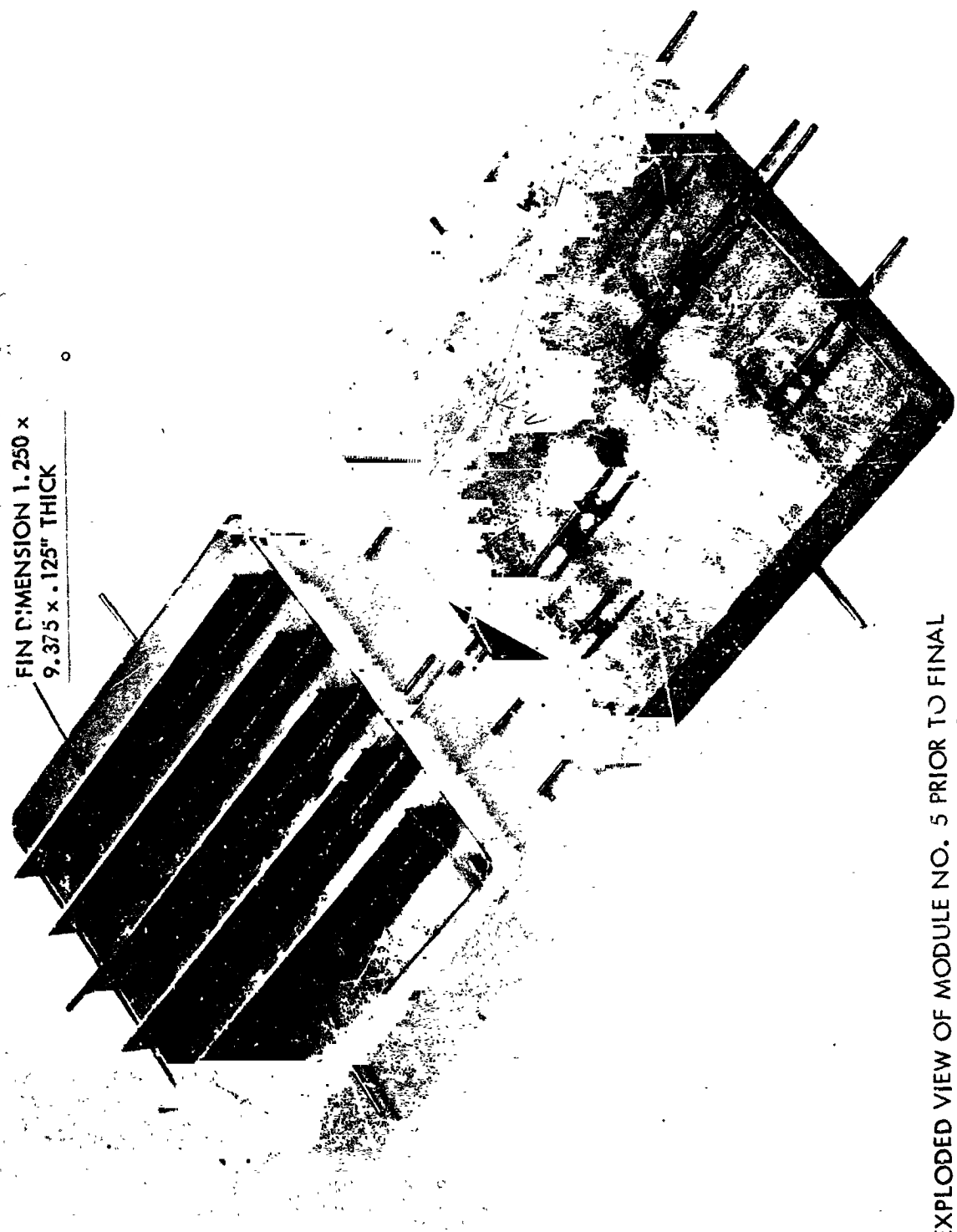
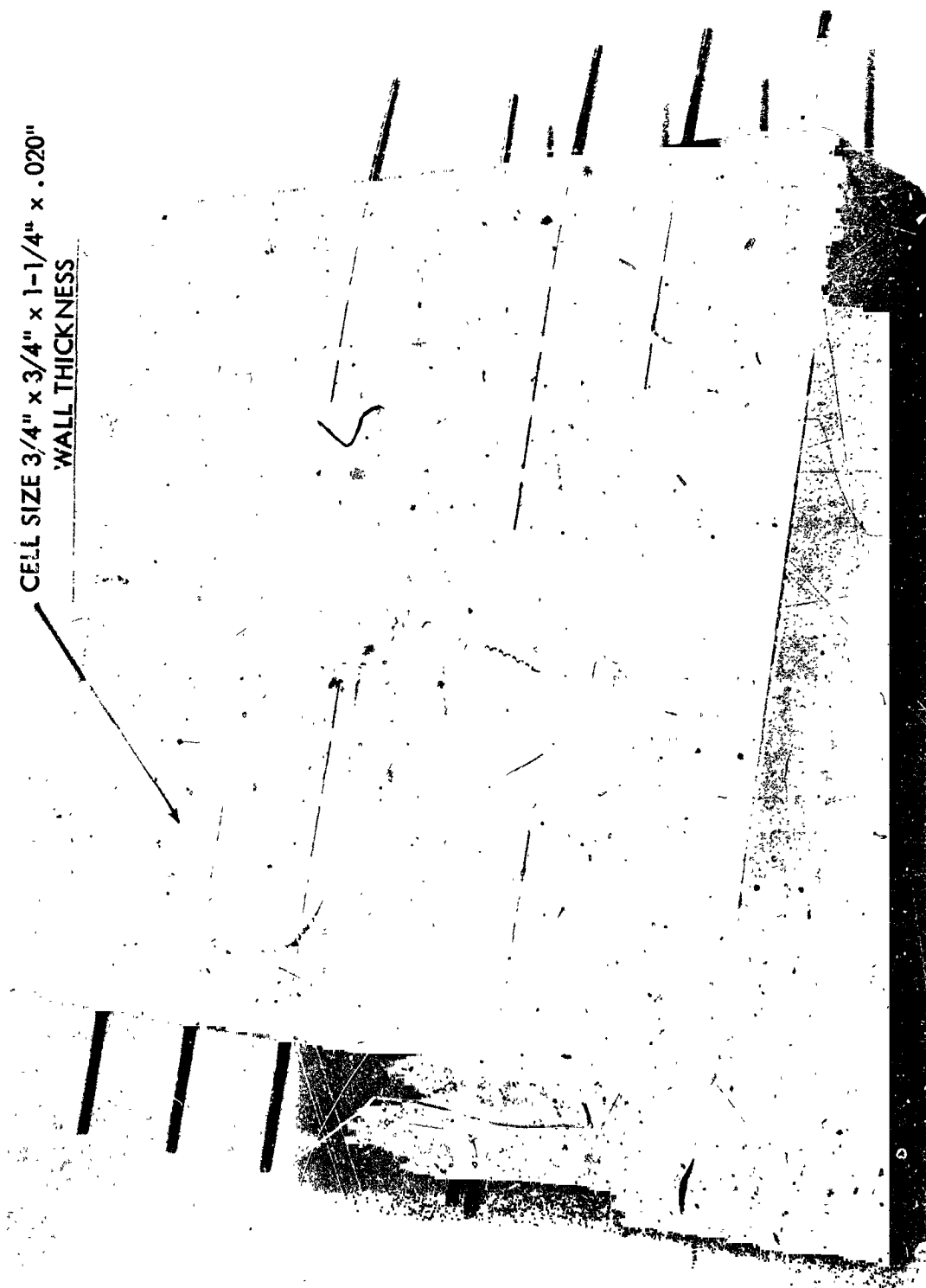


FIGURE 24

CELL SIZE $3/4"$ x $3/4"$ x $1-1/4"$ x $.020"$
WALL THICKNESS

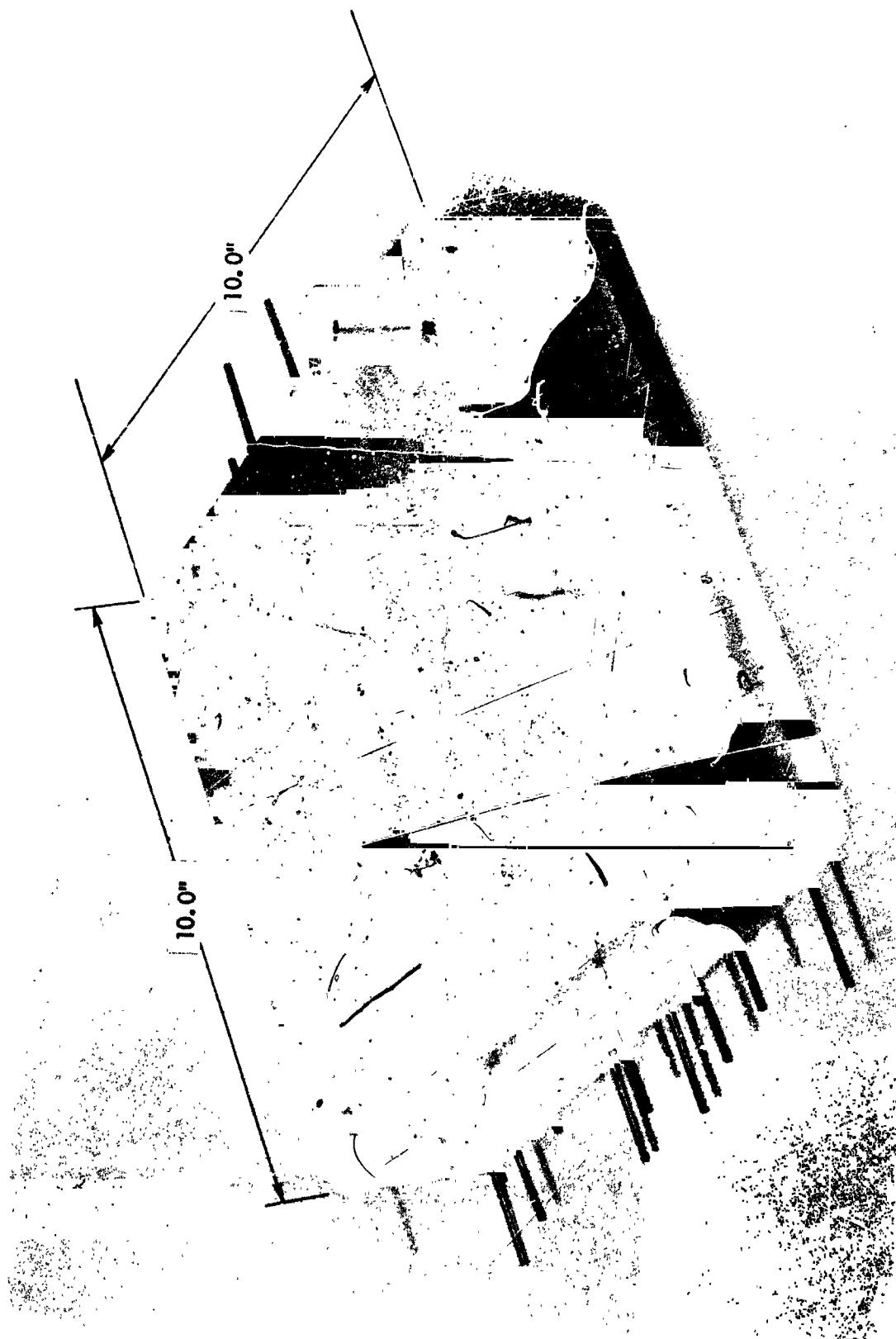


END VIEW OF MODULE NO. 6 PRIOR TO FINAL ASSEMBLY WELD

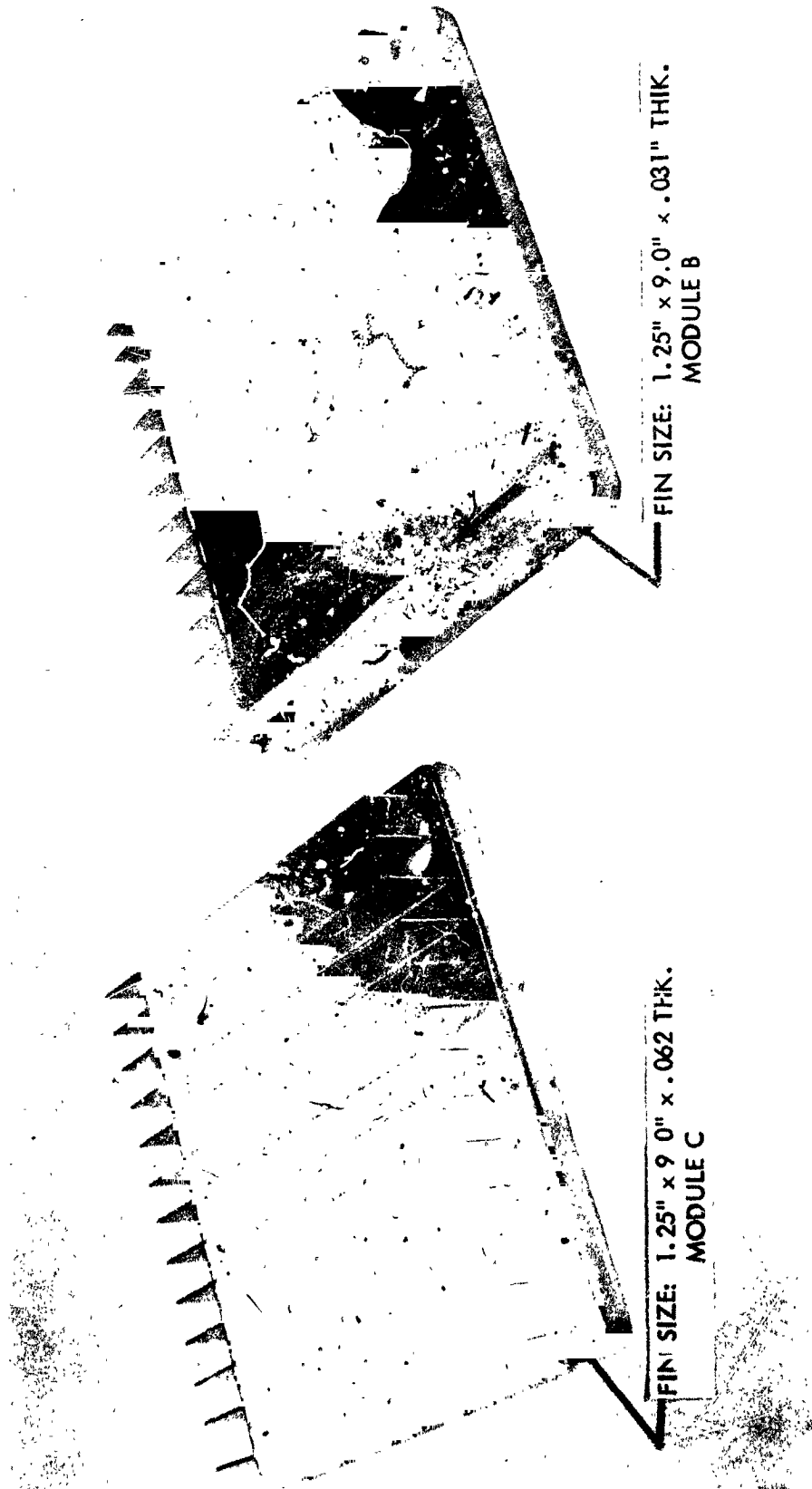
CELL SIZE
EQUALS
 $3/8" \times 3/8" \times 1-1/4"$ HIGH
.020" WALL
THICKNESS



END VIEW OF MODULE NO. 7 PRIOR TO FINAL ASSEMBLY WELD



VIEW OF MODULE A



VIEW OF TOP PLATES OF MODULES B AND C
AFTER INITIAL FIN BRAZING

The second series of test modules were loaded by TRW. The lithium fluoride powder was loaded into the hopper and the system sealed. A vacuum was drawn on the entire system at room temperature prior to initial melting. The vacuum was maintained on the system during the initial melt and throughout the test. After the lithium fluoride was molten, it was transferred from the hopper to the module by rotating the test fixture. Figure 29 is a view of the test assembly. The hopper and its heater reflector are shown above a module and its heater reflector. The long tube at the top permitted viewing the fluoride through a plexiglas flange. The modified outer box is also shown. The high temperature insulation was installed for Figure 30. Figure 31 is a view of the test assembly in position for the initial melting of lithium fluoride.

4.2.4 Experimental Procedure

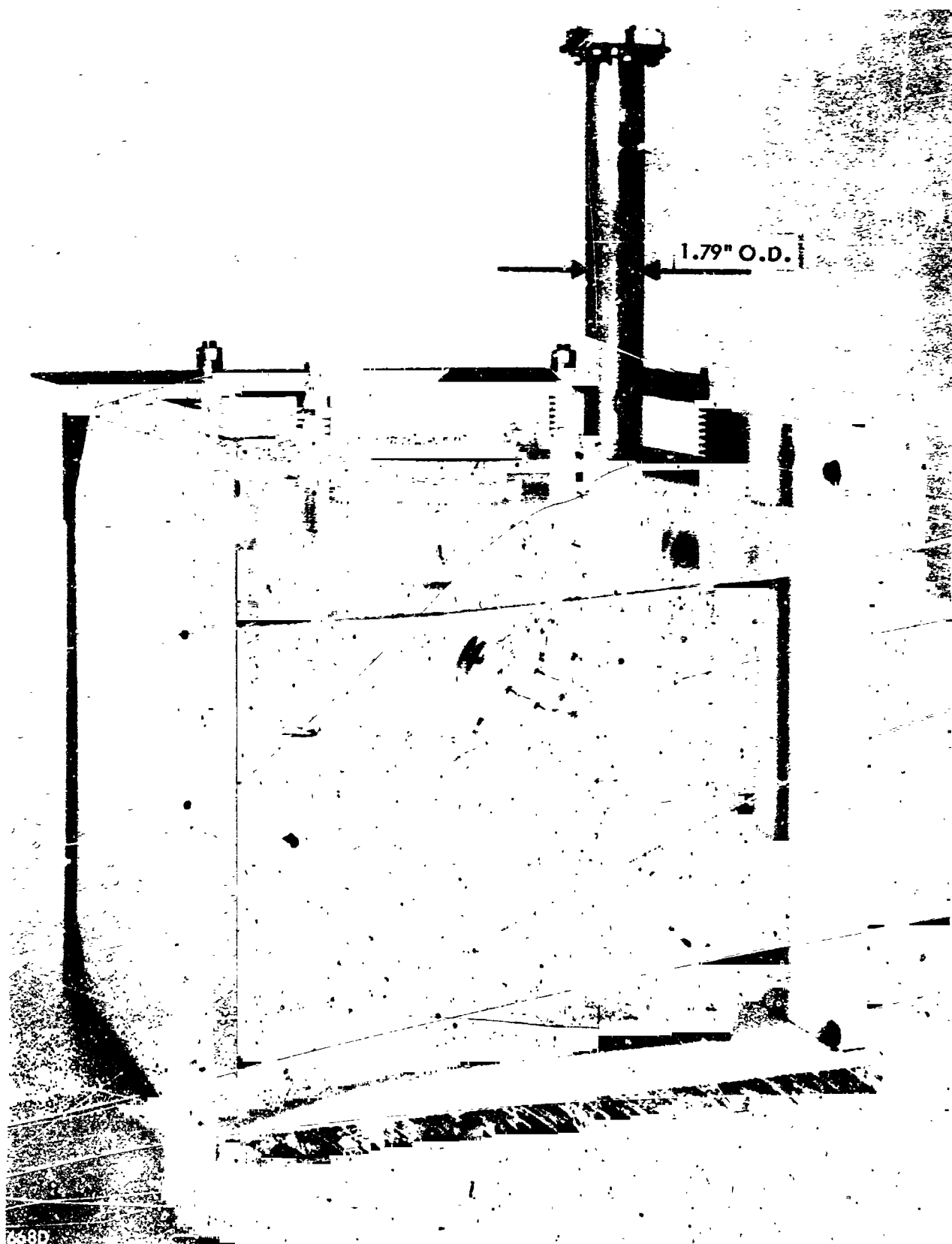
The heat input tests were necessarily cyclical in nature. The tests were started by melting the fluoride and stabilizing the liquid temperature at $1600 \pm 25^\circ\text{F}$. This procedure provided a common starting point and known conditions. The next step was to freeze all the fluoride. Initially, this was accomplished by shutting off all heater power and starting coolant flow simultaneous at the bottom plate of the module. Later, it was decided to set the heaters at low power levels, 500 watts or less, to prevent fluoride freezing on the top plate surface and/or crawling up the tubes attached to the top plate. The coolant flow at the bottom plate of the module was held constant throughout the test.

It was desired to be certain that all of the fluoride was frozen before the heaters were turned on. Therefore, the bath temperatures were allowed to go below 1550°F and the top plate temperatures followed. On some occasions, the top plate temperatures went as low as 1400°F before the heaters were turned on. In any event, it was necessary that all of the fluoride be frozen for the sequence to be valid. When the heaters were turned on, the rate was set at a constant value and maintained until all of the fluoride was melted. Again, temperatures were permitted to overshoot to be certain that the fluoride was completely molten.

Several cycles of alternate freezing and melting were completed at each of three heater power settings, 2000, 2500, and 3000 watts. The tests on each module were terminated when repeatable data had been obtained at each power setting.

4.2.5 Data Evaluation and Analysis

The major items to be determined from the test data included time to freeze, time to melt, top plate temperature at the end of melting and the heat input flux. The time required to freeze all the fluoride was taken as the time from heater shutoff to the point when all bath and module temperatures were below 1560°F . The time to melt was taken as the time from heater power start to the point when selected thermocouples, No. 15 and 16, which were located on the bottom plate, read 1560°F or above. The top plate temperatures at the time defined as the end of melting were recorded and an average temperature determined for the four centrally located thermocouples. This average temperature was then defined as the top plate temperature at the end of melting. The heat input flux was calculated



VIEW OF TEST ASSEMBLY



VIEW OF TEST ASSEMBLY WITH HIGH TEMPERATURE
INSULATION INSTALLED



VIEW OF TEST ASSEMBLY IN POSITION FOR MELTING LITHIUM FLUORIDE

in a manner similar to that given in Section 4.1.3 except that the heat input in BTU/hr was computed as the sum of the fluoride latent heat plus the heat removed by the coolant plus the fluoride sensible heat plus the module sensible heat plus one half the side losses minus the heat conducted down the sides.

It should be noted that the top plate thermocouples were actually located 1/8-inch from the top surface. The thermocouples were thus 3/8-inch above the surface exposed to the fluoride. The thermocouple position above the surface exposed to the fluoride left open the possibility that the thick top plate might have a transient temperature through it at the end of melting. Under these conditions, it could be possible for the surface exposed to the fluoride to be at a significantly lower temperature than the thermocouple reading. Consequently, a transient temperature analysis for the top plate was made using a conventional Schmidt* plot. The results of the transient analysis indicated that by the time the fluoride is approaching the all-molten condition, the top plate temperature gradient is essentially that corresponding to the steady-state condition. The same result was obtained in the analog investigation as shown in Figure 22. Therefore, no correction was applied to the thermocouple data to make the temperatures equivalent to the bottom surface temperatures of the top plate. The temperature difference between the two surfaces ranged from 16 to 28° F.

4.2.6 Experimental Results and Discussion

A typical variation of top plate temperature with heating time is shown in Figure 32. This type of variation was characteristic for all modules tested and had been predicted by the analog investigation.

During the testing of module number 2, it was observed that severe heater burnout was occurring and numerous heater tubes were replaced. This situation was abnormal and this test was interrupted for disassembly of the test. Visual inspection of the module indicated an apparent lithium fluoride leak which subsequent examination indicated had occurred after a failure in the small tube attached to the top plate. During the previous freeze, the heater power had been turned off completely. The fluoride had risen in the tube to a height greater than the heater reflector. During the next heating period, a local area in the tube was melted and the resulting increase in volume apparently caused a local failure in the tube wall. The fluoride spilled out of the tube onto the top surface of the module and into the joint between the tube and the top plate. Later, this joint failed and more fluoride spilled out of the module. A significant loss in fluoride occurred, and the top plate thermocouples were no longer reading correctly nor could they be removed from their respective wells. Therefore, new grooves were cut in the top plate and thermocouple wells provided. A new charge of lithium fluoride was added to that remaining in the module to bring the total up to the desired weight. The test was repeated and completed without further incident.

*See Appendix Section 8.1.1.

TYPICAL VARIATION OF TOP PLATE TEMPERATURE WITH HEATING TIME
AT SEVERAL POWER LEVELS - MODULE NO. 5

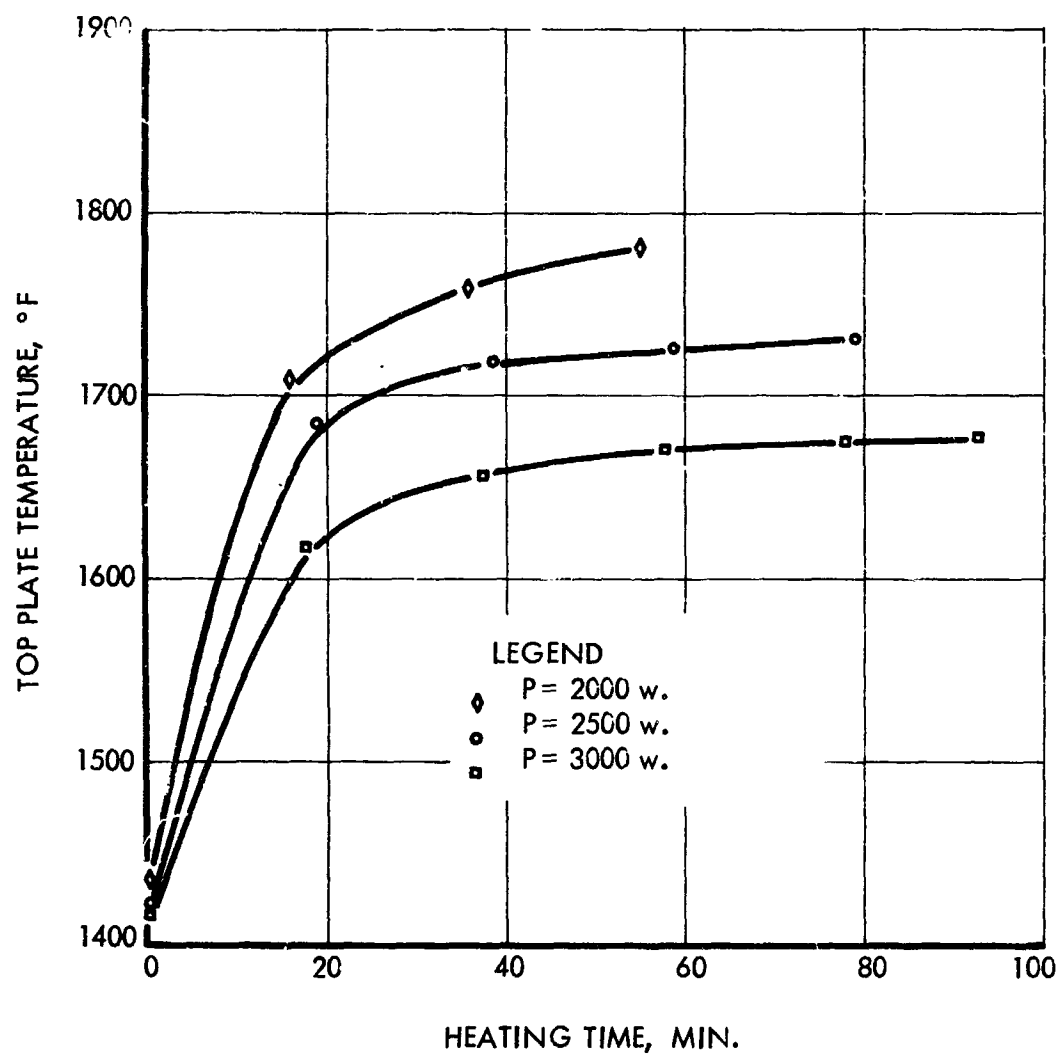


FIGURE 32

Post-test inspection indicated that a significant dip, approximately 0.3 in., was present in the top plate surface. A check of the fabrication and assembly records showed that the dip in the top surface had been introduced by the machining operations for the second set of thermocouple well grooves. Calculation of the height of the lithium fluoride bath in the molten state demonstrated conclusively that the liquid fluoride would contact the bottom surface of the top plate prior to the all-molten condition. Thus, a direct heat conduction path was inadvertently provided from the top plate to the bath. As a consequence, the test results obtained for this module were not comparable to the test results for the other modules since they all featured heat exchange by radiation and/or extended surface. Since module number 2 was a bare module, it had been intended to employ its test results as a basis for comparison. Since no valid basis for comparison was available at the conclusion of the Series I tests, it was necessary to obtain a valid basis by testing module A in Series II. Module A was essentially the same as module number 2, and the test results for Module A provide the desired basis for comparison.

The test results for Modules 4, 5, 6 and 7 are presented in Figure 33 with the top plate temperature at the end of melting as the ordinate and the heat input flux as the abscissa. Similar results are shown in Figure 34 for modules A, B and C. The applicable curves from the analog investigation, as indicated in Figure 22, are included in Figure 34 for comparison of analytical and experimental results.

After the test of Module 2 was completed, it was cut open to inspect the fluoride freezing pattern. Figure 35 is a view of the sectioned module. A sizable portion of the fluoride can be seen attached to the bottom surface of the top plate. The top plate curvature can be observed also. Sectional views of Modules 4, 7, B and C are included in Figures 36, 37, 38 and 39, respectively. It can be observed from Figures 38 and 39 that no fluoride was frozen to the bottom surface of the top plate. These views demonstrate that the technique of maintaining the heater power at a low level effectively prevents freezing on the top surface and controls the fluoride movement.

The heat release tests will be discussed in the next section.

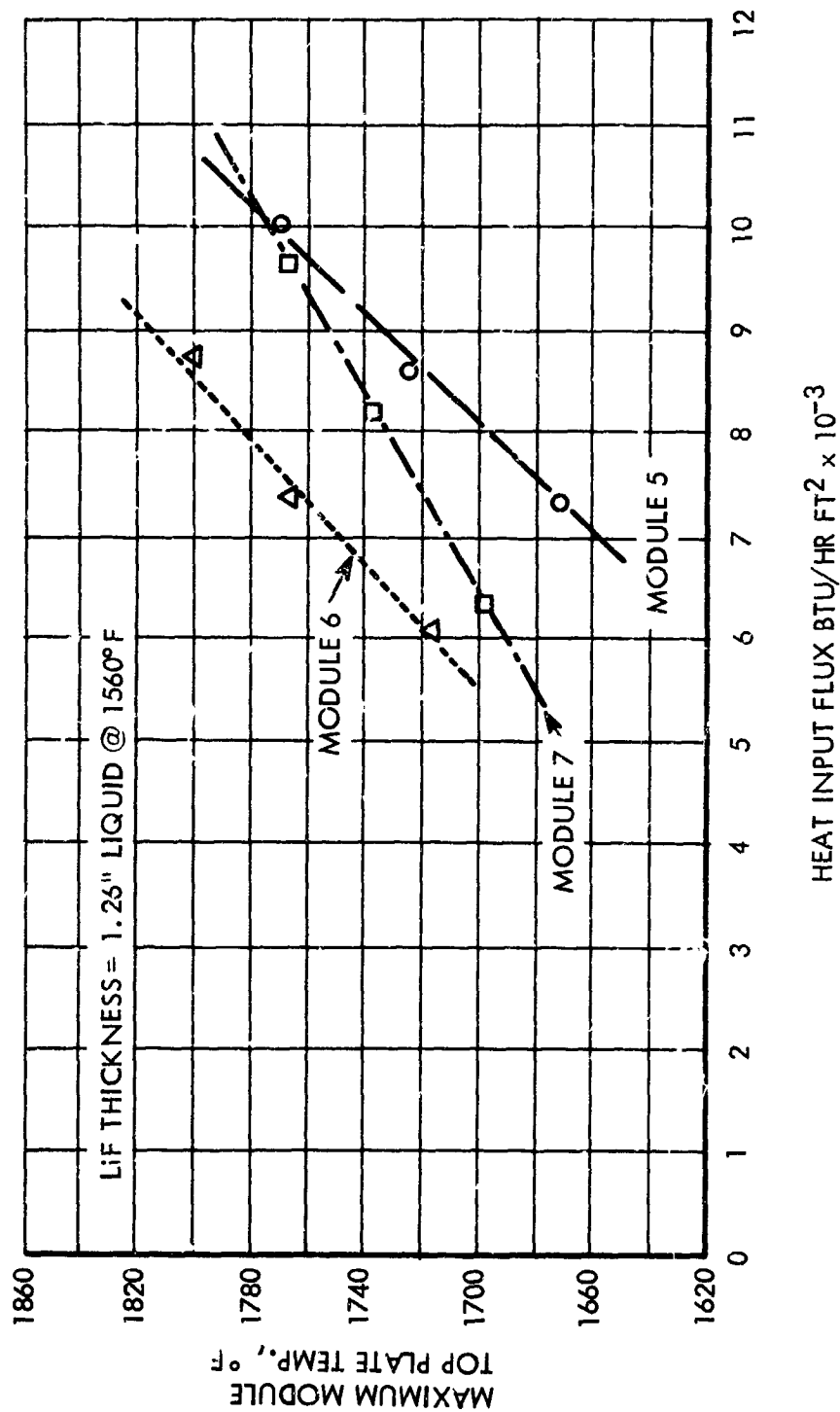
4.3 Heat Release Experiments

The heat release experiments were conducted in both series also. The heat release modules in each series are identified in Table V.

In addition to the modules listed in Table V, two dummy modules with the configuration of Module D were constructed and tested in the Series II tests. The fundamental purpose in testing the dummy modules was to demonstrate a desired, controlled freezing pattern.

The purpose of the Module 3 and 8 tests was to determine the experimental performance of the lithium fluoride in releasing heat to a gas coolant in module geometries simulating the heater inlet and outlet conditions of the four per cent pressure drop flightweight unit. Additional insight into the fluoride void formation was also sought.

TOP PLATE TEMPERATURE VS HEAT INPUT MODULE TEST RESULTS



VARIATION OF MAXIMUM FOR PLATE TEMPERATURE WITH HEAT INPUT FLUX LEVEL
FOR MODULES A, B AND C AT A CONSTANT COOLANT FLOW OF 0.5 LB/MIN

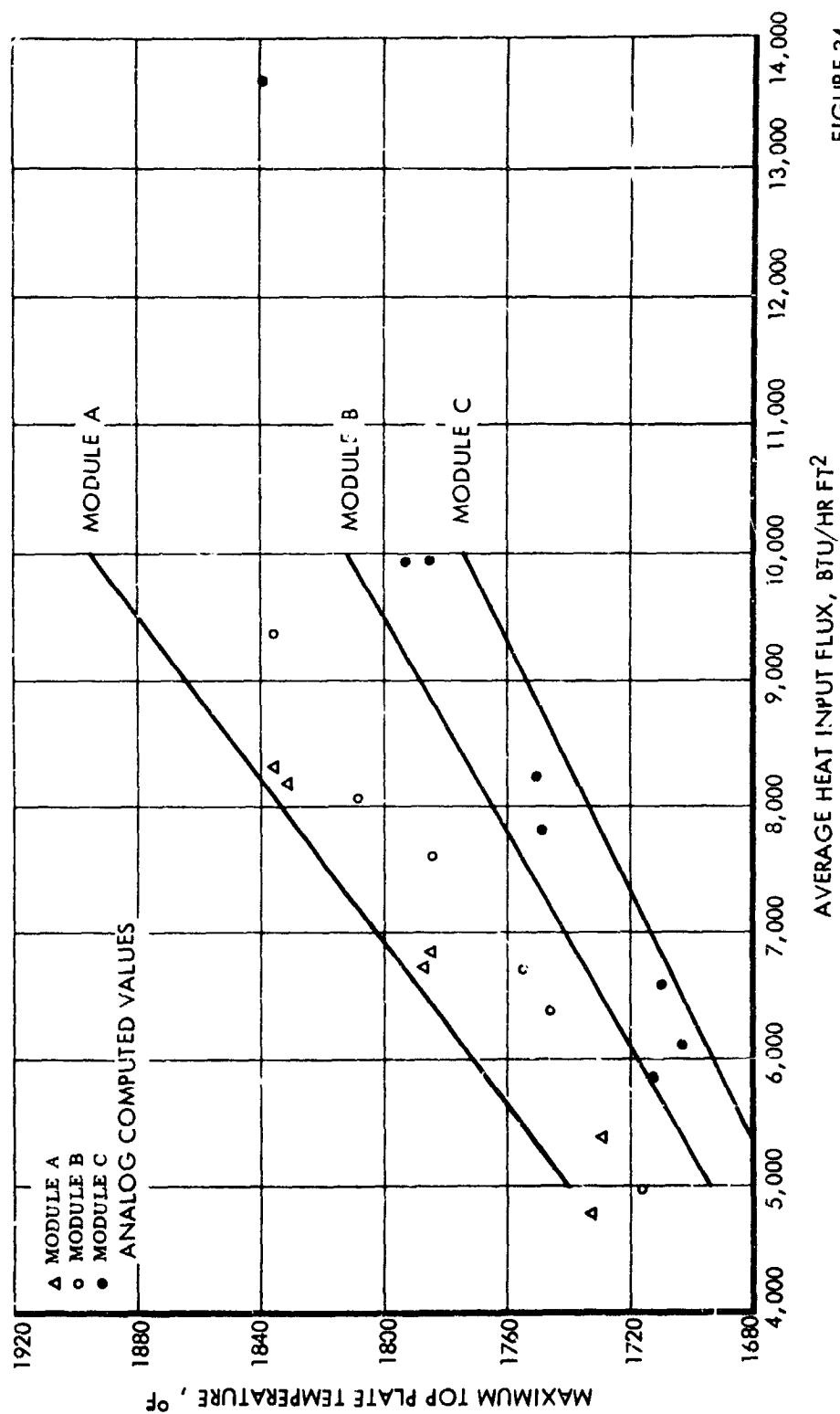


FIGURE 34



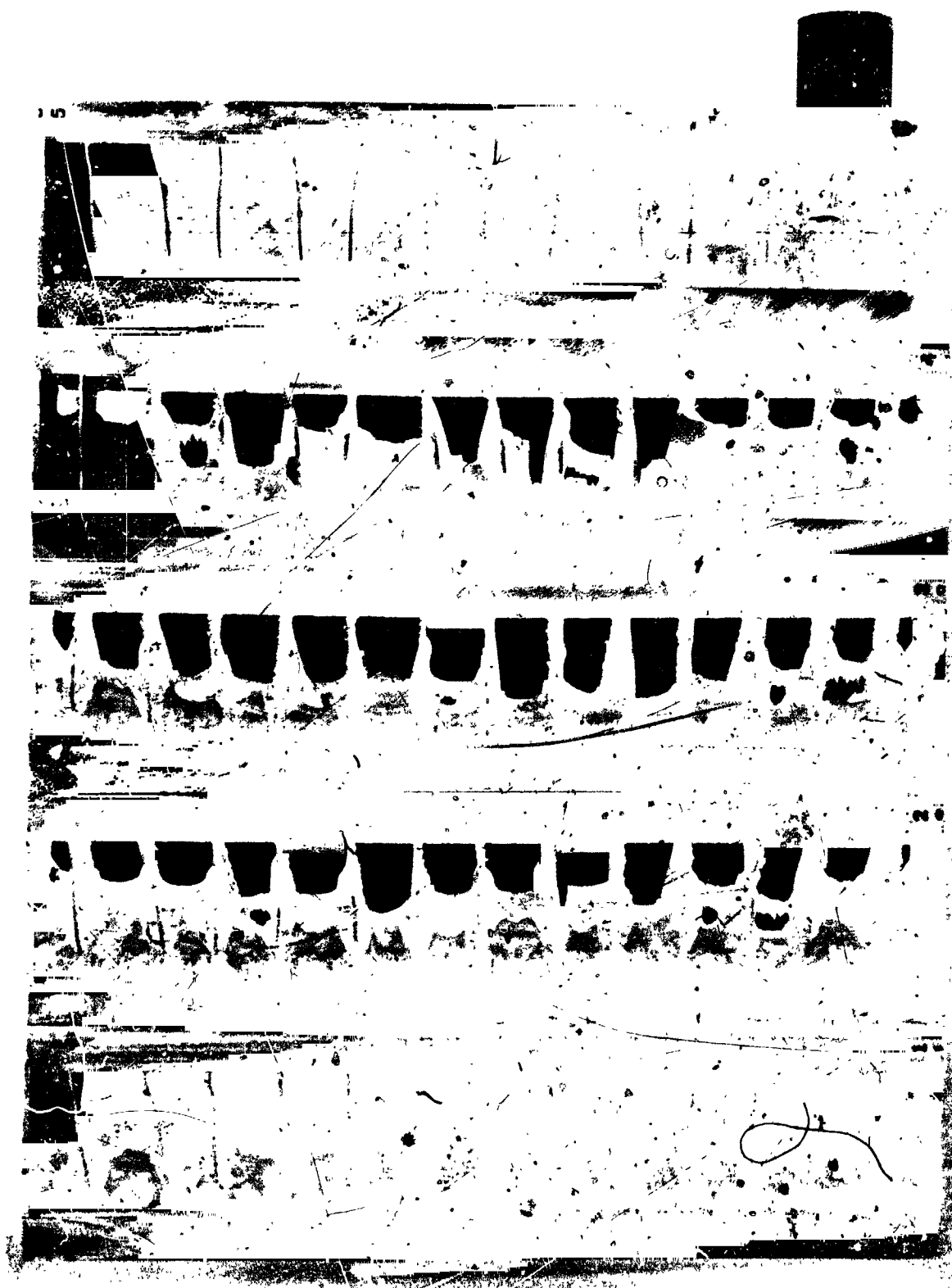
VIEW OF MODULE NO. 2 SECTIONED AFTER COMPLETION OF TESTING



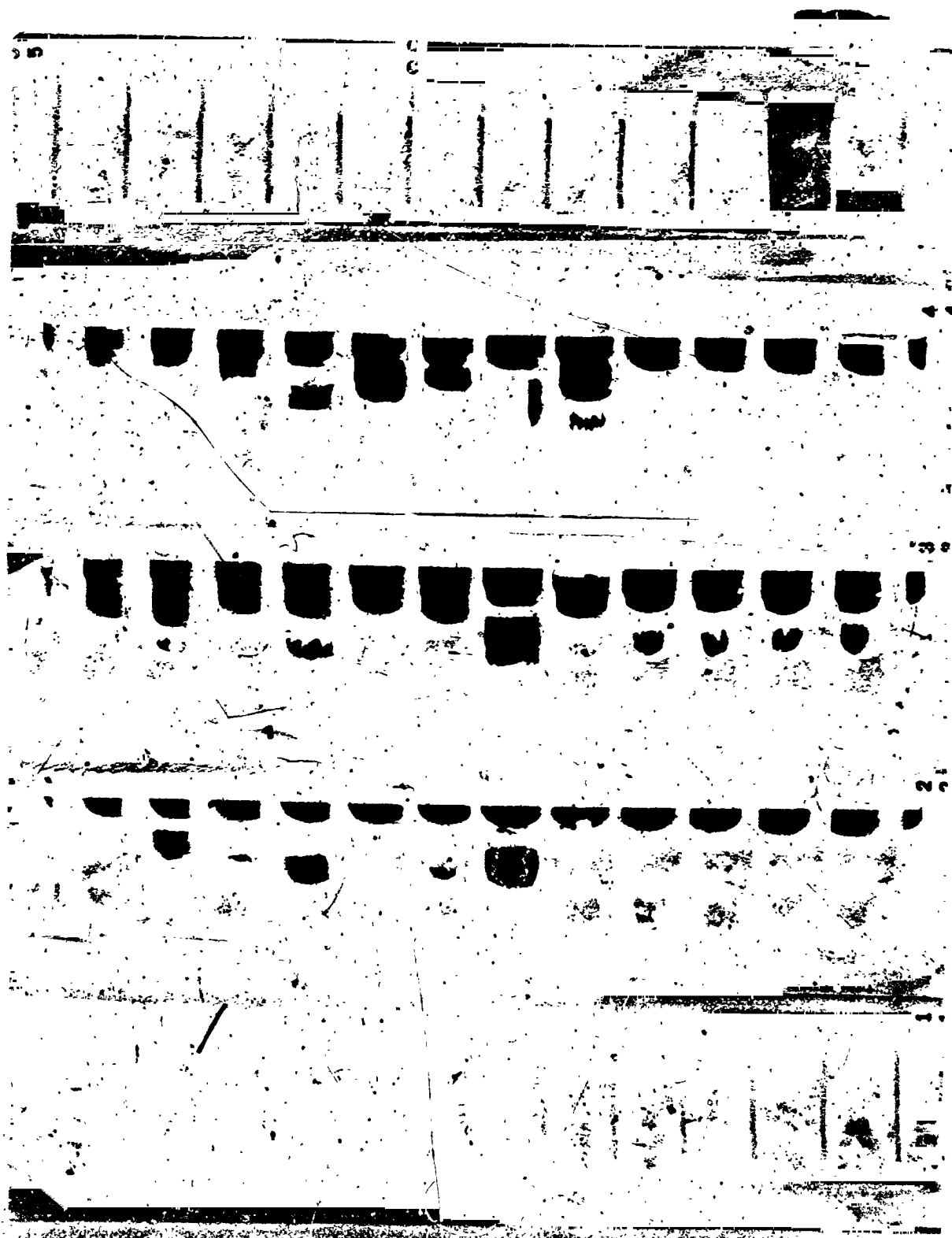
VIEW OF MODULE 4-SECTIONED AFTER TESTING



VIEW OF MODULE 7 SECTIONED AFTER TESTING.
HONEYCOMB WALL THICKNESS WAS 0.020-IN.



VIEW OF MODULE B SECTIONED AFTER TESTING FIN DIMENSIONS
WERE 1/32 IN. WIDE x 1-1/4 IN. HIGH x 9 IN. LONG



VIEW OF MODULE C SECTIONED AFTER TESTING FIN DIMENSIONS
WERE 1/16 IN. WIDE x 1-1/4 IN. HIGH x 9 IN. LONG

TABLE V
HEAT RELEASE MODULES

Module No.	Series	Material		Maximum Bath Height	Tube O. D.
		Module	Fins		
3	I	HS 25	- -	1.40 in.	.500 in.
8	I	316 SS	- -	0.866 in.	.500 in.
D	II	HS 25	- -	1.30 in.	1.050 in.
E	II	HS 25	Grade "A" N ₂	1.30 in.	1.050 in.
.050 in. x .350 in. x 9 in.					

The purpose of testing Modules D and E was to determine the fluoride heat release characteristics near the heater tube inlet with the geometry simulating the two per cent pressure drop flightweight design. The controlled freezing techniques demonstrated in the dummy modules test were employed for both modules.

The fluoride resistance characteristics during freezing were predicted analytically by the electric analog technique developed and verified experimentally in the work reported in Reference 1. The analytical predictions will be discussed first.

4.3.1 Analytical Prediction of Fluoride Geometrical Resistance During Freezing

As described in Section 3.2.2 of Reference 1, the analog is based on the fact that the melt line between the liquid and the freezing solid is at a constant temperature. If an isotherm is located in the solid freezing around a tube from which heat is being removed, a set of curvilinear areas can be identified through which the heat flows are equal as illustrated in Figure 40. The heat removed through each of these areas in a given length is obviously equal to that removed through every other area. This heat is used to freeze the fluoride during the shade time and to melt it during the sun time. The former case pertains to the freezing process and the heat removed must equal the heat of fusion times the weight of fluoride frozen

$$\tau Q_n = \rho_s \oint_n \Delta n h_f$$

The above expression defines the total heat removed through each curvilinear area in terms of the dimensions of the area and unit length of tube. Since the density of the solid and the heat of fusion are constants, the product of the two area dimensions is also constant.

ELECTRIC ANALOG METHOD TO DETERMINE MELT LINE MOTION DURING FREEZING

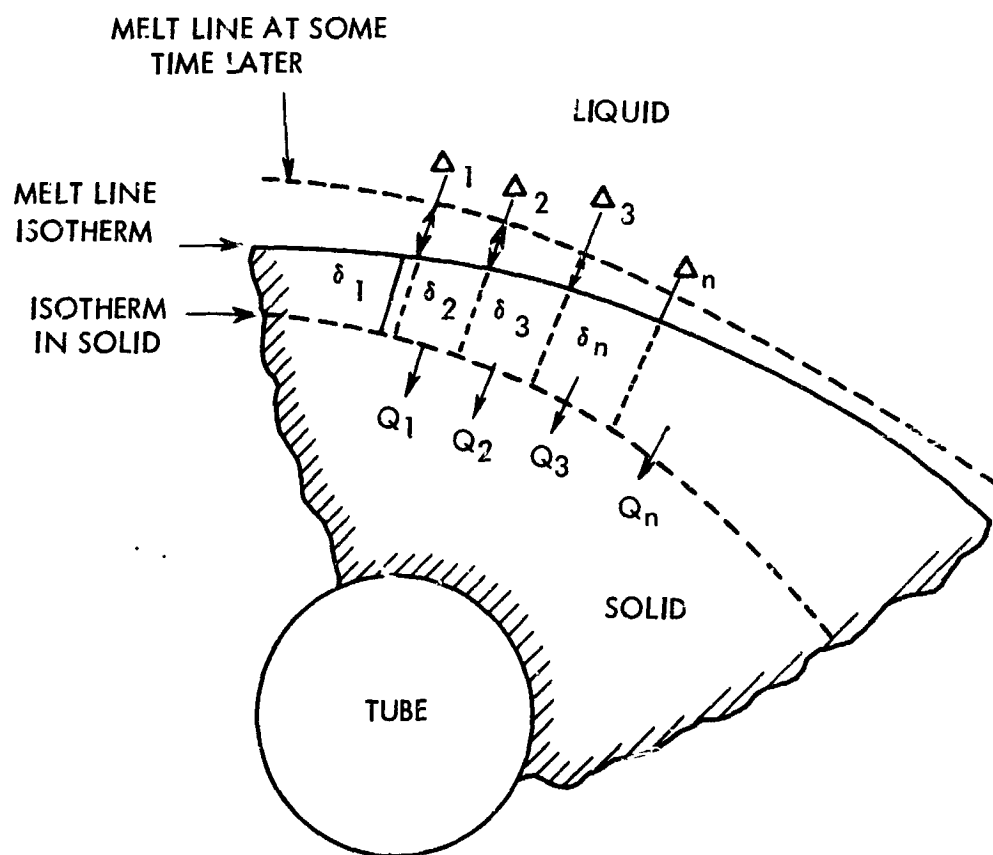


FIGURE 40

Stated in another manner, this means that the local movement of the melt line is inversely proportional to the distance from an isotherm in the solid to the melt line. Therefore, the procedure to be used with the analog is to locate an isotherm, measure local distances from the isotherm to the melt line and construct a new melt line employing the constant area relationship above. This procedure is repeated until all the fluoride is frozen. In construction of the basic analog, a transition from the actual geometry to the analog geometry is required. The analog geometry is selected to represent an area element within lines of symmetry. The analog area element is usually bounded by the inner and outer shells, the tube centerline and a line representing the midpoint between tubes. If the tube is spaced midway between the shells, it is possible to consider one shell only as shown in Figure 41. The electric analog is constructed with "Teledeltos"* electric conducting paper to four or more times actual size. The isotherms - in the solid, the tube wall and the melt line - are drawn on the paper using a silver electric conducting paint which has a low resistance. A direct current voltage is applied between the tube and the melt line. With the aid of a voltage divider, a constant potential line which represents an isotherm is drawn between the melt line and the tube at a small, but measurable distance from the melt line. The local distances are measured and a new melt line drawn as indicated in Figure 41. The new melt line is reproduced on another piece of "Teledeltos" paper and the procedure repeated until all the fluoride is frozen. A schematic of the electric circuit is shown in Figure 42.

From each of the analogs, the volume of frozen fluoride can be readily determined and the electrical resistance from the melt line to the tube measured. These measurements can be easily converted to the actual volume frozen per unit length of tube and the geometrical resistance factor, which is dimensionless but is essentially based on dimensions of square inches divided by square inches. The volume conversion is based strictly on the geometry scaling factor of four divided by 16, or $1/4$. The geometrical resistance factor is the measured electrical resistance divided by the electrical resistance of one square of the "Teledeltos" paper.

The results of the freezing analogs are presented in Figure 43 as the geometrical resistance variation with volume of fluoride frozen. It was necessary to determine the resistance variation at several sections along the tube. The theoretical resistance for fluoride freezing around a tube immersed in an infinite bath is also shown for comparison.

4.3.2 Test Module Construction

The two modules in the Series I tests were sized to simulate the geometry intended for the four percent pressure drop design. In the four percent full scale design, both the annular space between the shells and the tube spacing were varied along the length of the tube. Because of this variation, it was decided to build one module with the bath geometry near the tube inlet and a second module with the bath geometry near the tube outlet with

*See Appendix: Section 8.1.1

TYPICAL MELT LINE PATTERN

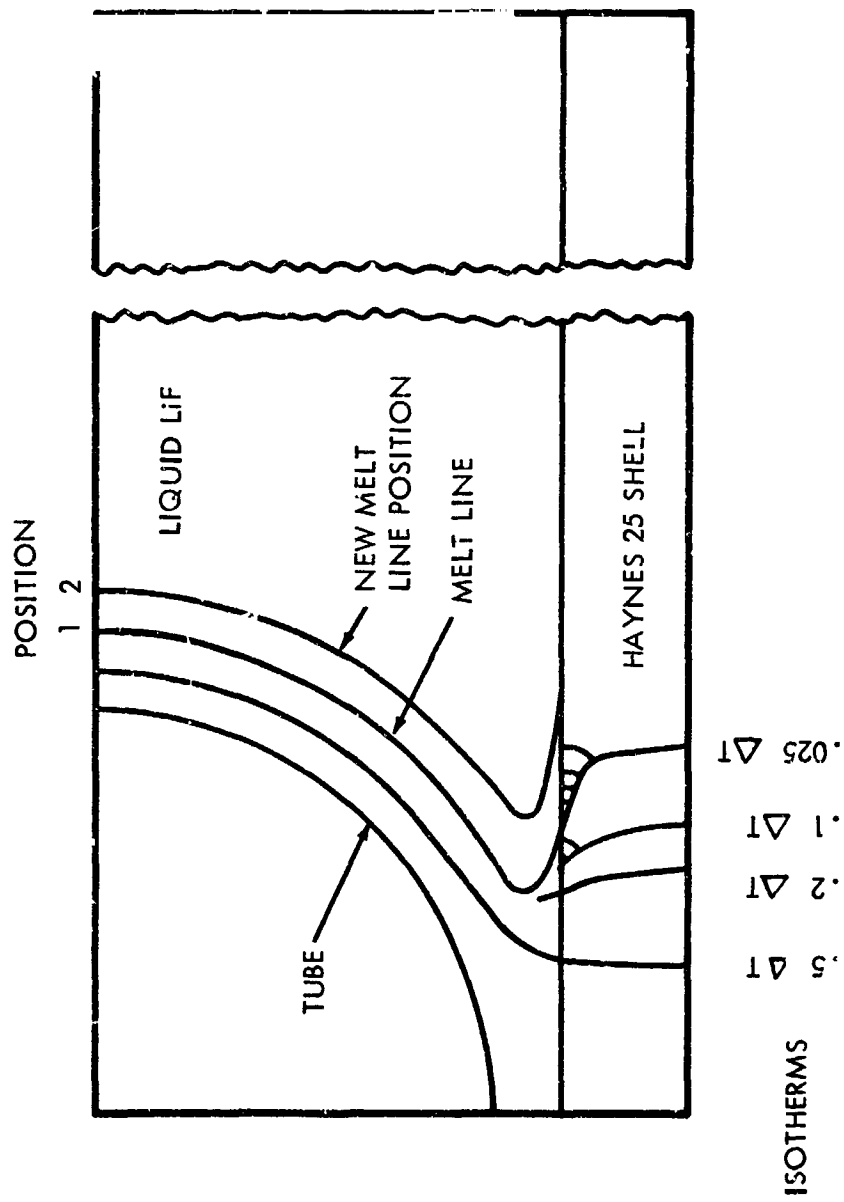
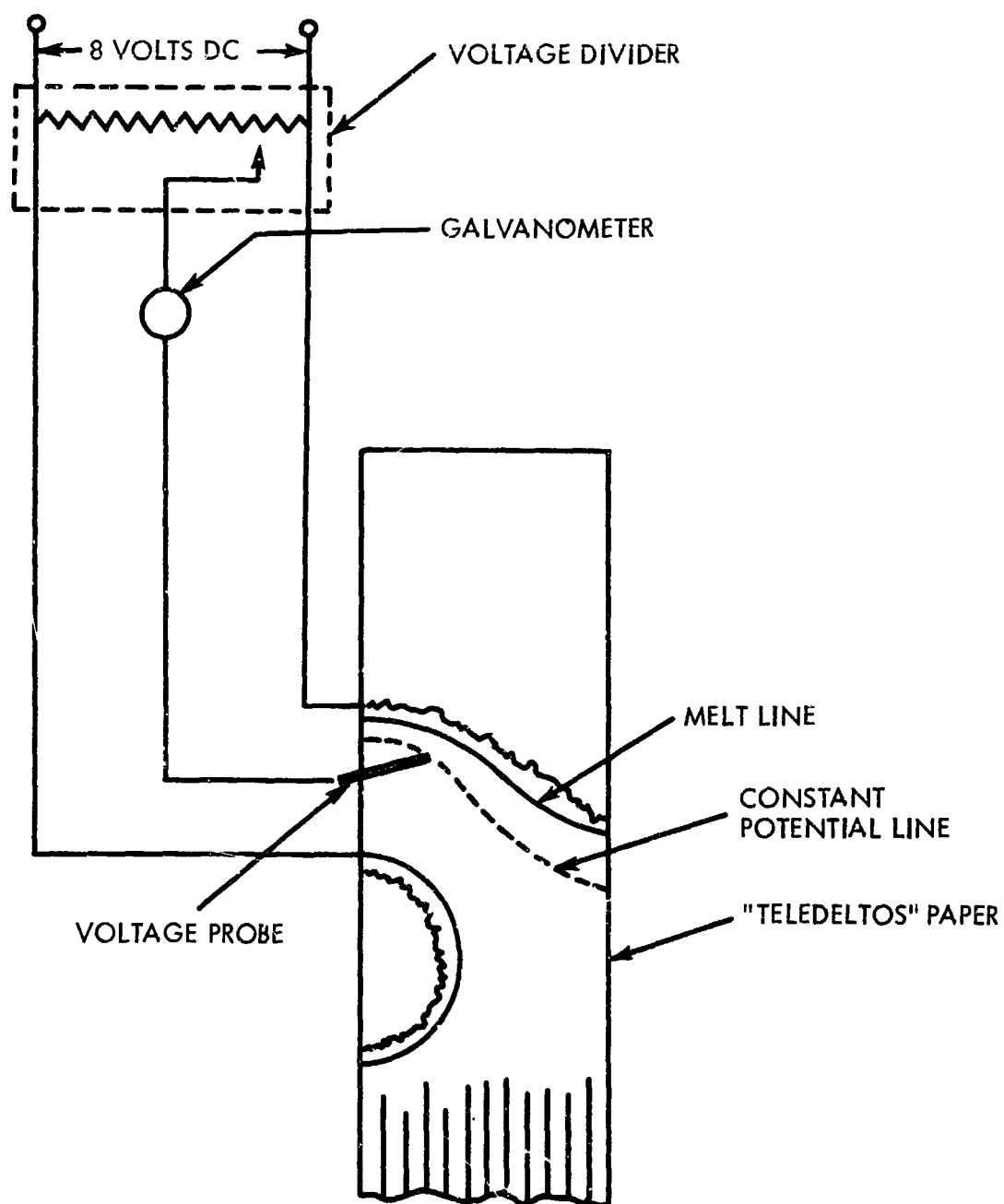


FIGURE 41

ELECTRIC ANALOG SCHEMATIC

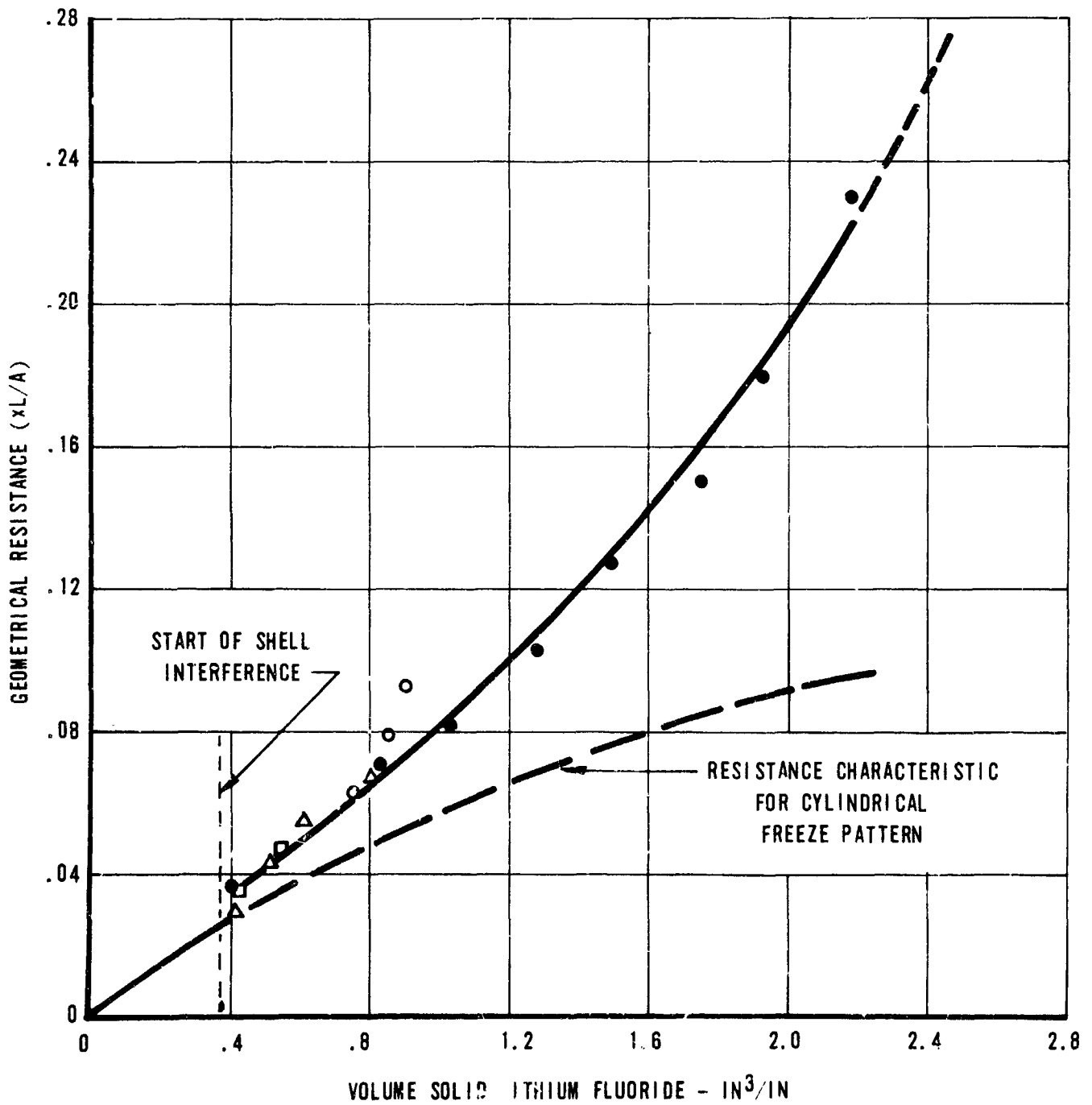


GEOMETRICAL RESISTANCE (xL/A) OF FREEZING LITHIUM FLUORIDE

TUBE DIAMETER - 1.10 IN

SHELL SPACING - 1.30 IN

- TUBE SPACING - 5.63 IN
- △ TUBE SPACING - 1.55 IN
- TUBE SPACING - 1.3 IN



dimensions noted in Table V. Module 3 represented the geometry near the inlet and Module 8 simulated the geometry near the outlet. The bath height for Module 3 was 1.4 inches. To gain additional insight into the melting and freezing of the fluoride and the resultant void formation, two sets of four tubes each were specified. One set of four tubes had a tube spacing of 1.450 inches which was equivalent to that near the tube inlet. The second set of tubes had a tube spacing of 0.670 inches which was similar to the tube outlet. The bath height for Module 8 was 0.866 inches and the tube spacing was constant at 0.570 inches. Module 8 had a total of 16 tubes.

The modules fabricated in Series II were intended to simulate the bath geometry of the two per cent pressure drop design at a tube position near the inlet. Additional thermocouple wells were provided to measure the tube wall temperature and obtain data on the experimental thermal resistance. An attempt was made to design into these modules a capability to remove the correct full scale heat rate. The coolant air was capable of removing heat at a far greater rate than the full scale unit could. Therefore, resistance to heat flow was built into the modules by two concentric tubes within the full scale tube. The coolant air passed through the central tube, and the radiation resistance from the full scale tube to the intermediate tube plus the radiation resistance from the intermediate tube to the central tube were believed to provide sufficient resistance to limit the heat removal rate to the full scale value. The bath height for Modules D and E was set at 1.30 inches and the tube spacing at 1.625 inches. With this tube spacing only five tubes could be built into each module because the basic 10-in. x 10-in. dimensions were retained.

The central tube of the five tubes was provided with three thermocouple wells attached to the full scale tube. Each adjacent tube was provided with one thermocouple well attached to the full scale tube in the direction toward the central tube. The three wells on the central tube were located at positions 3 inches, 5 inches and 7 inches from the inlet end and at radial positions of 90°, 180° and 270° from the bottom, respectively. The two wells in the adjacent tubes were positioned 5 inches from the inlet end.

Fins were attached to the top plate of Module E to obtain experimental evidence of the performance with extended surface. Otherwise, the configuration for Module E was the same as that for Module D. The fins were parallel to the coolant tubes and fabricated of commercial Grade "A" nickel. The fin dimensions were .050-in. x 0.35-in. x 9 in. and two fins were installed per tube.

4.3.3 Experimental Apparatus

The basic apparatus was the same as that described in Sections 4.1.1 and 4.2.3. Only the changes made will be discussed here. The coolant tubes in Module 3 were fed by four supply lines from a common manifold. Thus, the manifold was able to supply coolant flow to either set of four tubes each but not both sets simultaneously. For Module 8, the manifold was modified to supply coolant to all tubes simultaneously.

The coolant air was fed to the five coolant tubes in Modules D and E through supply lines from a common manifold. Hand operated shutoff valves located in each supply line permitted the test engineer to select the flow pattern desired. A similar setup was employed with the two dummy modules.

4.3.4 Experimental Procedure

The prime interest in the test of Modules 3 and 8 was to gain insight into the melting and freezing characteristics of lithium fluoride with configurations simulating the full scale design. Thus, the procedure employed in these tests was very similar to that described in Section 4.2.4 for the heat input tests. The fluoride was frozen in both modules with the modules in the horizontal position. Since the manifold was able to supply only four tubes in the Module 3 tests, the final freeze was performed with coolant flowing through the set of tubes with the larger spacing to permit a better view of the freezing pattern obtained around a tube.

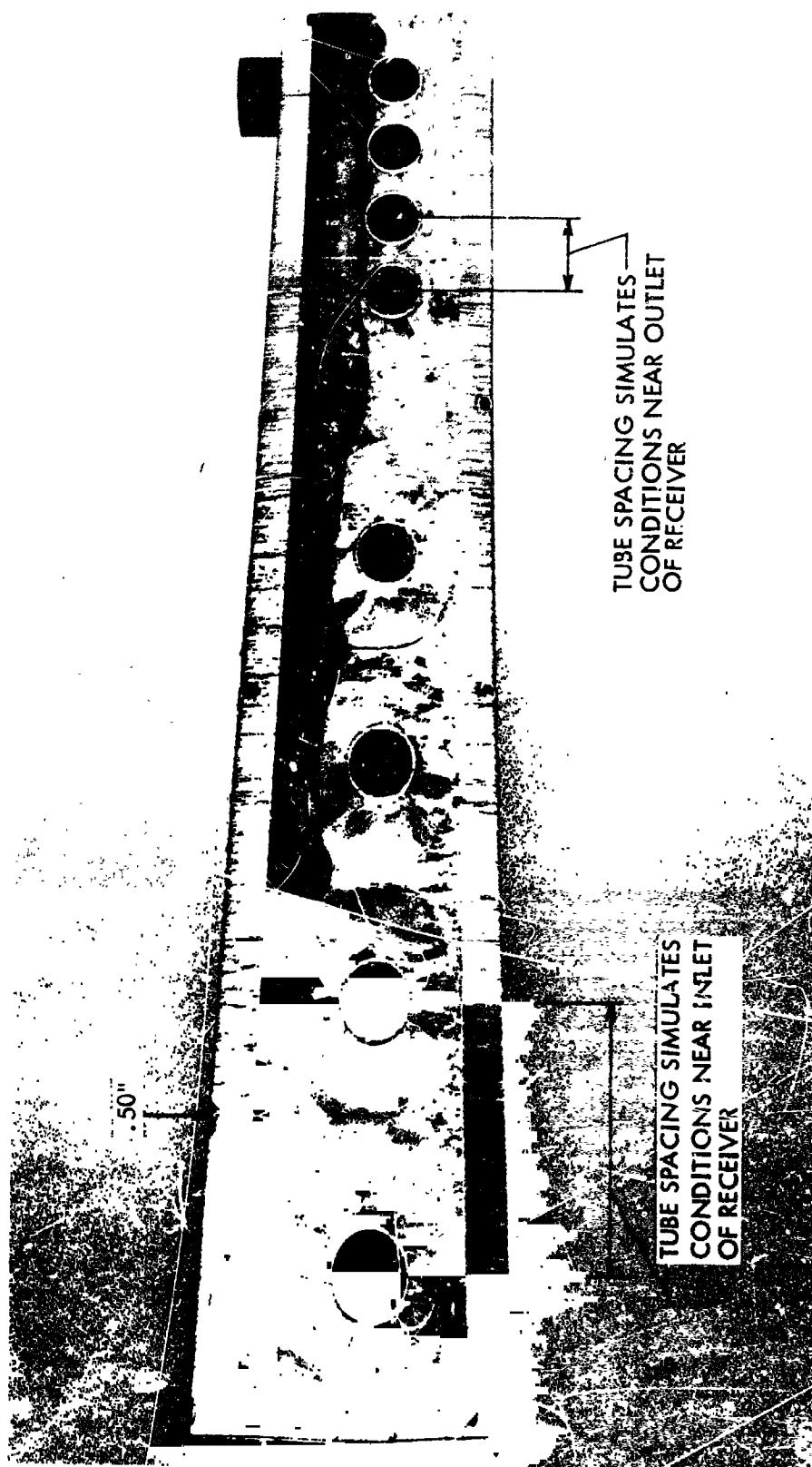
On the other hand, the emphasis in testing the dummy modules and Modules D and E was placed on obtaining a controlled freeze pattern and the experimental melting performance with the controlled freeze pattern. The two dummy modules were tested solely to demonstrate the capability to obtain a controlled freeze pattern. The test module was placed on its side by rotating the test fixture. The test plan called for the fluoride transfer tube to be at the top. The plates normally designated as top and bottom plates were in a vertical position during the freezing process. The plan was to freeze the fluoride around the top coolant tube first, with no coolant flowing through any of the other tubes. The remainder of the fluoride was to be maintained molten until the fluoride in the vicinity of the first tube was all frozen. Then coolant flow would be started through each successive tube until all the fluoride was frozen. It was hoped that placing the module on its side and freezing the fluoride in a controlled manner could result in eliminating the influence of gravity on the freezing pattern.

After the fluoride was completely frozen as evidenced by all thermocouple readings being below 1560°F, the test fixture was rotated to make the module horizontal and heating was initiated from the top in the usual manner. In the testing it was found that module heater power settings of 4500 watts or greater were required for a successful melt of the controlled freezing pattern with coolant flowing through all five tubes.

It was planned to test Modules D and E on melting by heating from the sides. In these cases, the modules were left in the vertical position after freezing was completed. Heating was then started without rotating the test fixture.

4.3.5 Experimental Results and Discussion

The major results of Module 3 are shown in Figure 44 which is a sectional view of the module after testing was completed. The type of freeze pattern normally obtained around a tube in one-g testing is clearly visible around each tube with the larger spacing. Since no coolant was flowing through the other set of tubes on the final freeze, the freezing



VIEW OF MODULE NO. 3 SECTIONED AFTER COMPLETION OF TESTING

pattern in the vicinity of the other set of tubes is controlled more by gravity than anything else. No experimental evidence is presently available to verify the type of freeze pattern obtained in zero-G, but it is believed that the same type of pattern will be obtained there too since the strontium salt appears to seek the coolest surface which should be the tube.

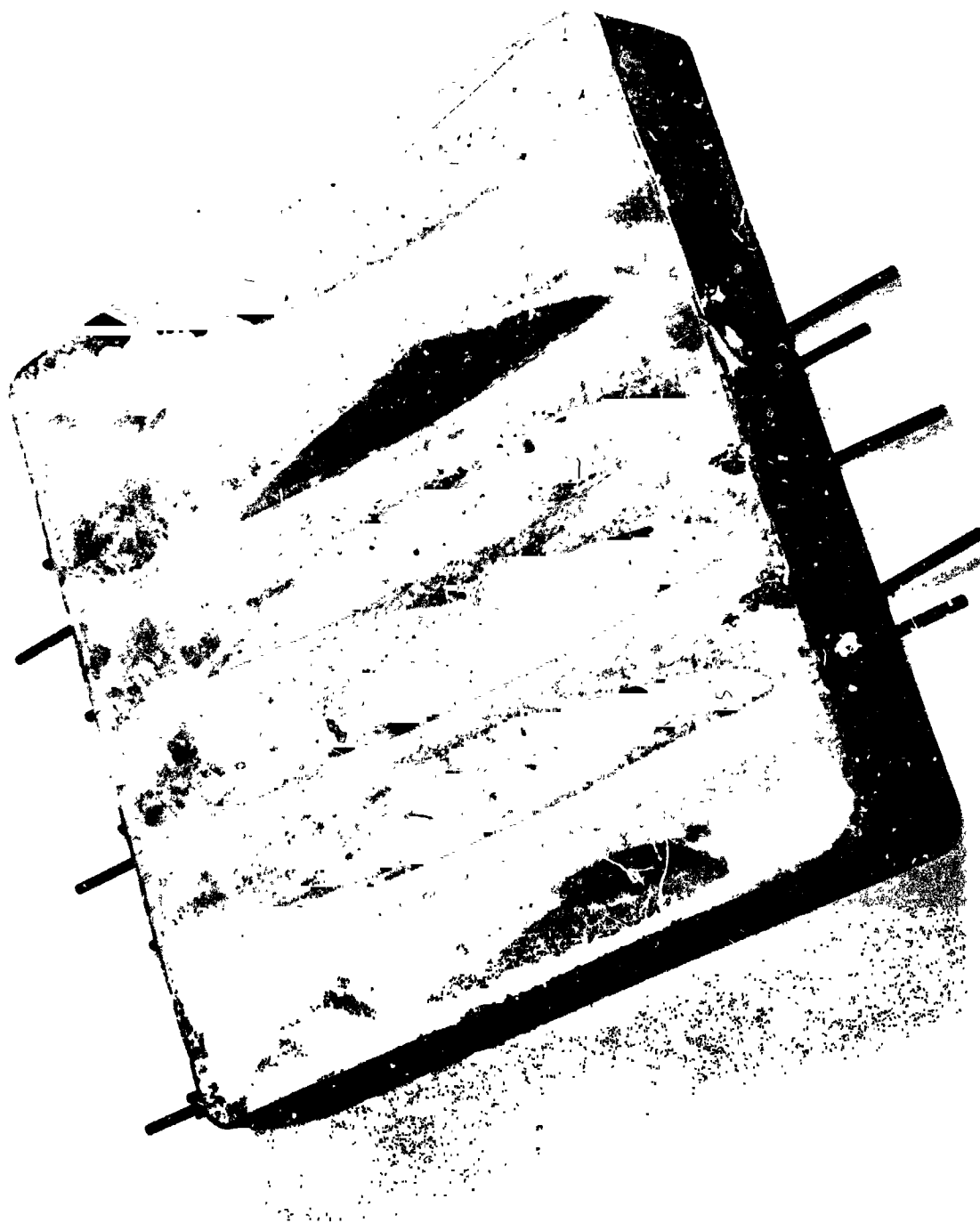
Module 8 was sectioned after completion of all tests, but the freeze pattern obtained was not clear cut and the results of the Module 8 tests were inconclusive.

The results of the first dummy module test were inclusive because the test engineer had inadvertently rotated the test fixture in such a manner that the transfer tube was at the bottom of the module. In this position, a large amount of free volume was available for the liquid fluoride to settle. On freezing, insufficient quantities of fluoride remained in the vicinity of the tubes and the test results were meaningless to point out the importance of keeping the transfer tube at the top. Experience with the new operating procedures for the controlled freezing pattern was provided, however.

X-rays taken of the second dummy module after the final freeze indicated that the fluoride was frozen in approximately the pattern desired. The module was cut open for visual examination. The cut was made so that the module could be reassembled if the results of the visual examination were unfavorable. Fortunately, the results of the visual examination were very favorable and it was concluded that a method of obtaining the desired controlled freeze pattern had been successfully demonstrated. Figure 45 is a view of dummy module number 2 after sectioning. The fluoride frozen around each of the coolant tubes can be readily observed.

Module D was loaded with fluoride and the same procedures were employed to obtain freezing patterns similar to the second dummy module. Several melt tests were made in the horizontal position and one in the vertical position. Calculation of the heat input flux indicated that one horizontal melt was at a much lower level than the others. It was postulated that possibly the module was not completely filled, and this was leading to erratic results. The fluoride in both the module and the hopper was remelted and the hopper was pressurized slightly with argon gas at 2 psig. A final horizontal melt was made after the controlled freeze pattern had been obtained. The test bed was opened to examine the module and a definite bulge of about .070-in. was observed in the top plate. Testing of Module D was terminated at this point.

During the testing of Module D, data were obtained from which the experimental geometrical resistance factor could be determined as a function of the volume frozen per unit length of tube. Only two coolant flow rates were employed during the freezing runs. Additional coolant flow rates were not specified since the prime emphasis was on obtaining the controlled freeze pattern. Each change in coolant flow rate required changes in the operating procedure. Thus, it was desired to maintain the coolant flow rate and the procedure which produced the successful demonstration in dummy module number 2. In any event, the data for both flow rates were reduced and the results are presented in Figure 46. The analytical result from the electrical analogs is shown also for comparison. The indicated performance is very similar to that illustrated in Figure 3.2-24 of Reference 1. The procedure employed



VIEW OF DUMMY MODULE 2 SECTIONED AFTER TESTING
TUBE-TO-TUBE CENTERLINE DISTANCE WAS 1-5/8 IN.

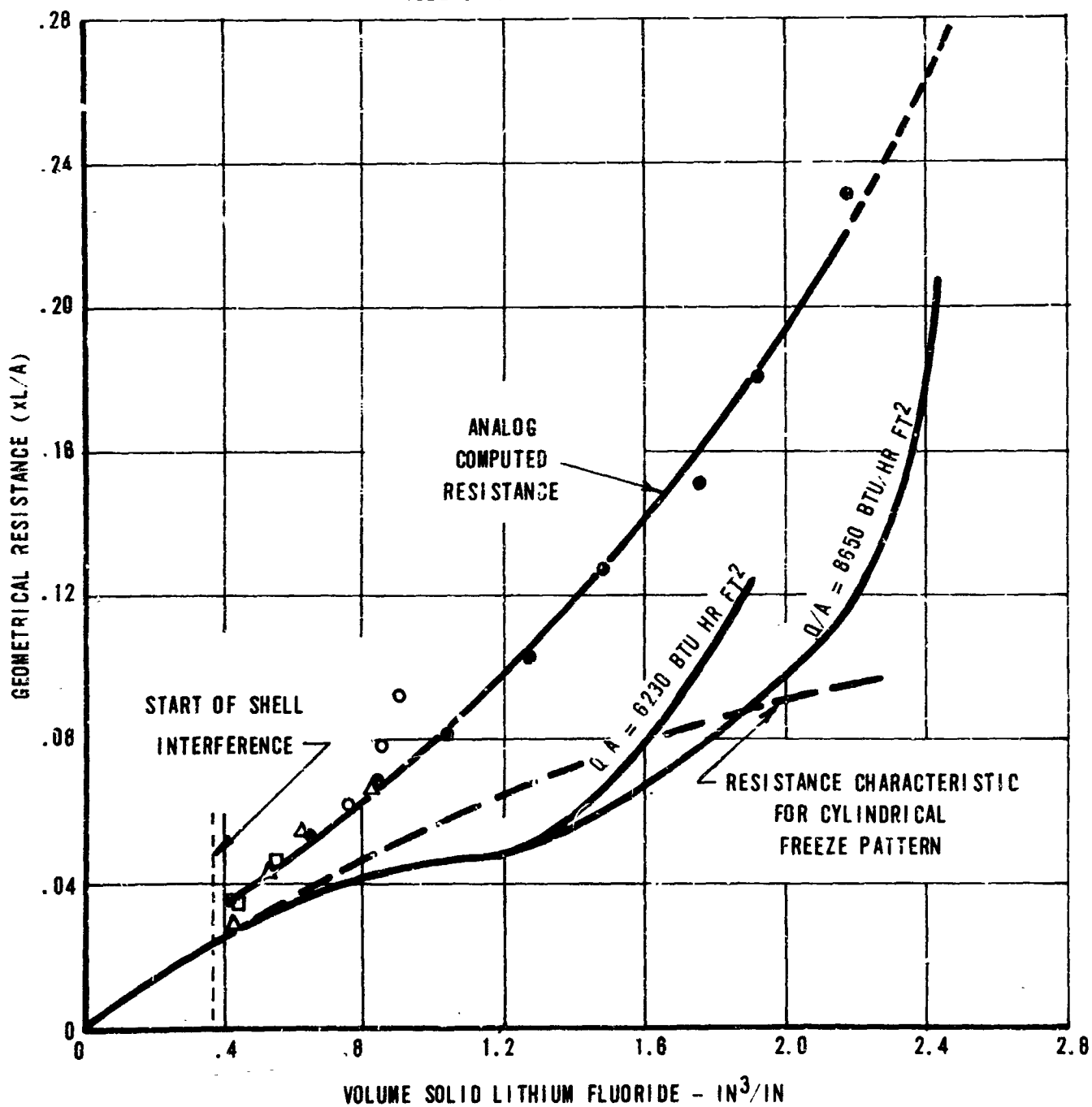
FIGURE 45

GEOMETRICAL RESISTANCE (xL/A) OF FREEZING LITHIUM FLUORIDE

TUBE DIAMETER - 1.10 IN

SHELL SPACING - 1.30 IN

- TUBE SPACING - 5.63 IN
- △ TUBE SPACING - 1.55 IN
- TUBE SPACING - 1.3 IN



in Reference 1 required results from several flow rates in order to obtain a good estimate of the experimental performance which would be directly comparable to the electric analog results. Since only two coolant flow rates were employed in testing Module D, no further estimates of the experimental performance were attempted, but nothing in the available data indicates a significant difference from the complete experiments of Reference 1. Therefore, it was concluded that the experimental performance of Module D bore a similar relationship to the electric analog prediction that the experiments of Reference 1 bore to its analog prediction. Further, it was decided that the available fluoride experimental data verified the same type of performance as the hydride in Reference 1.

The results of the heat input tests on Module D are presented in Figure 47. The analog predictions for Module A, B and C are shown for comparison. The erratic behavior of the heat input flux is clearly evident and the marked reduction in top plate temperature at the end of melting when the heating is done in the vertical position is indicative, but not conclusive, evidence of the reduction that should be possible in zero-G operation.

Module E was loaded, melted and frozen in the same manner as dummy module number 2. No hopper pressurization was attempted. The tests were conducted until essentially repeatable data were obtained for each type of test. The results of the melt tests are presented in Figure 48 and the analog predictions for Modules A, B and C are shown for comparison. Once again, melting performed with the module in the vertical position resulted in a significantly lower top plate temperature at the end of melting.

No attempts were made to reduce the freezing data since no analog predictions were calculated for the case with fins attached to the cavity surface.

The discussion on the small experiments is now complete. The results obtained were employed in the full scale flightweight unit design studies which are presented in the next section.

VARIATION OF TOP PLATE TEMPERATURE AT END OF
MELTING WITH HEAT INPUT FLUX - MODULE D

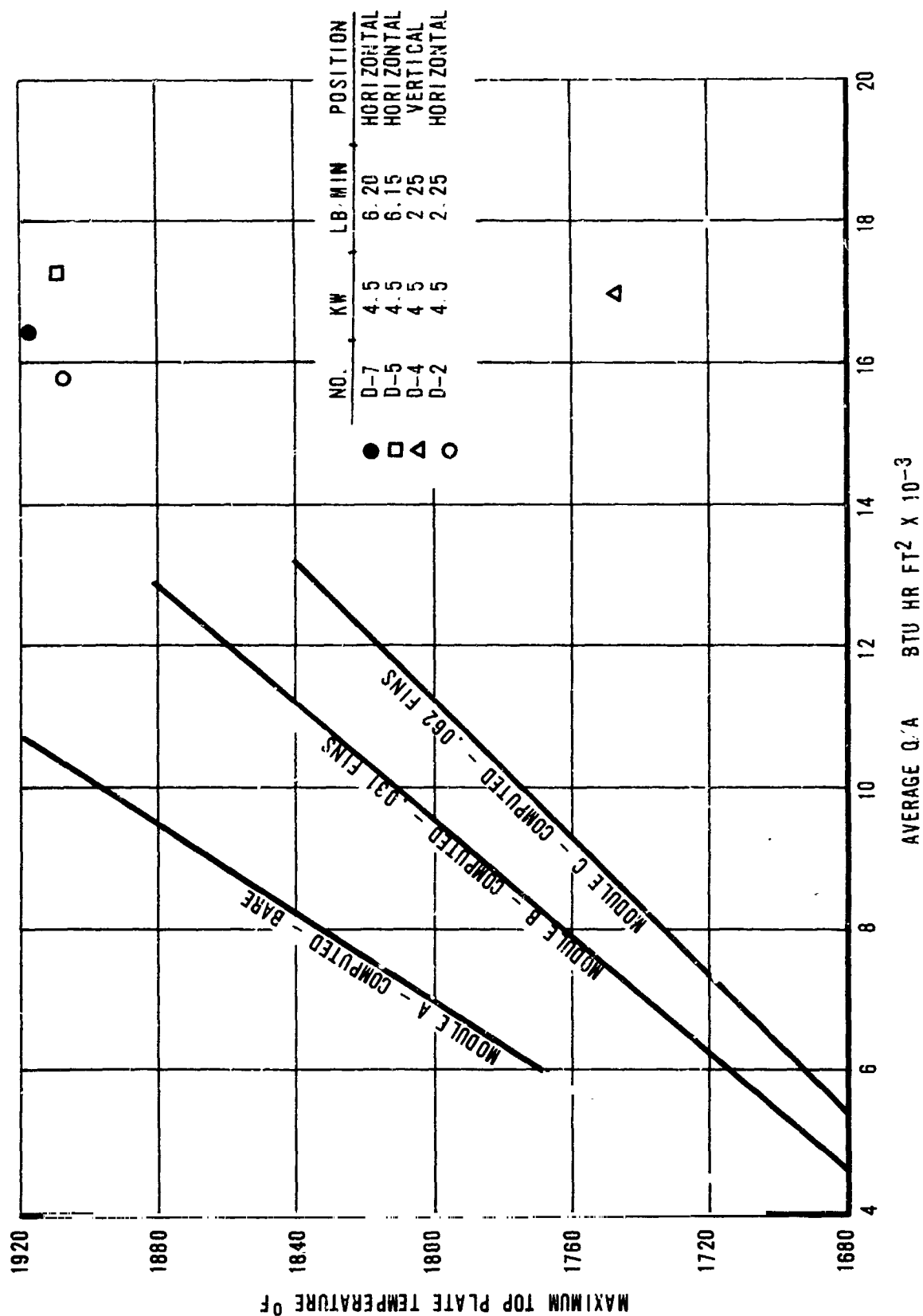
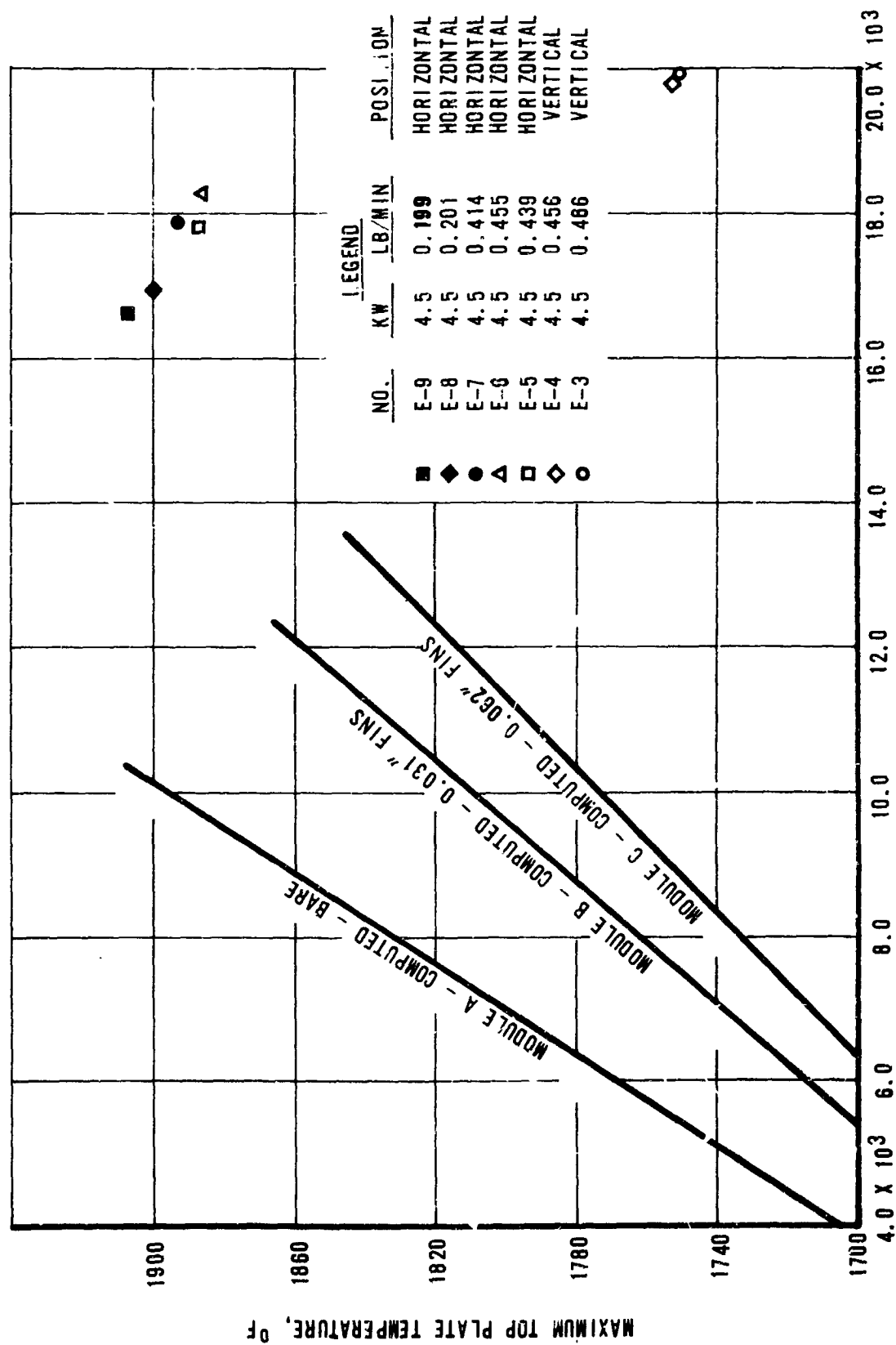


FIGURE 47

VARIATION OF TOP PLATE TEMPERATURE AT END OF
 MELTING WITH HEAT INPUT FLUX - MODULE E



LITHIUM FLUORIDE HEAT INPUT FLUX, BTU/HR-FT²

FIGURE 48

BLANK PAGE

5.0 FULL SCALE FLIGHTWEIGHT RECEIVER DESIGN STUDIES

The first major effort in the full scale flightweight receiver design studies was to evolve a concept design layout to meet the requirements of the initial receiver specifications as given in Section 2.1. As a part of this effort, it was necessary to examine in some detail the possible trade-offs between multiple-tube designs with inlet and outlet manifolds and designs with one to ten tubes which might conceivably eliminate the need for these manifolds. Receiver designs were examined for various gas pressure drops allowable in the receiver of prime interest - one designed for the nominal 300 nautical mile circular ecliptic orbit in combination with a 30-ft diameter rigid collector. Receivers were also studied for several other operating conditions which included a 300 mile orbit with a 20-ft diameter collector and the synchronous orbit for both the 20-ft and 30-ft diameter collectors.

Based on the parametric studies for the various allowable gas pressure drops, it was decided to perform a second major effort to evolve a concept design layout based on the revised specifications of Section 2.2. A series of problems were encountered which had to be overcome. These problem areas included operation at low gas Reynolds numbers with tube curvature required, inadequacy of the usual correlation employed and the influences of inert gas mixtures replacing the argon gas specified. To circumvent these problems, two concept design layouts were developed. The first one provides gas operation in turbulent flow and is adequate for helium-xenon mixtures with molecular weights near forty. The second one features gas operation in laminar flow with internally finned tubes. The latter design is intended for use with argon gas as specified in Section 2.2.

All of the receiver designs were to be considered to operate in an all sun orbit as well as the usual sun-shade orbits. Thus, some method of cavity over-temperature control must be provided. In addition, the use of aperture closure devices was to be investigated to obtain the maximum cavity energy retention. If the aperture were closed during the shade time operation, the cavity radiation losses during the shade time would be minimized. Thus, the maximum amount of energy would remain in the fluoride storage bath for transfer to the gas working fluid.

The flightweight full scale concept design studies are described in the following order:

1. Studies for the 4 per cent gas pressure drop design.
2. Studies for the 2 per cent gas pressure drop design with He-Xe mixtures.
3. Studies for the 2 per cent gas pressure drop design with argon gas.

5.1 Four Per Cent Gas Pressure Drop Design

After the hemisphere had been selected as the optimum cavity and container shape for this application, the prime effort was directed toward providing a design with fewer tubes to

improve reliability. In conjunction with this effort, preliminary designs were determined for other cavity receivers of interest to NASA. The specifications for the other cavity receivers are included in Table VI.

In addition to the preliminary design for the various cavity receivers, use of a small tube number, up to 10 tubes, was investigated to determine if elimination of the inlet and outlet manifolds was possible, practical and advantageous.

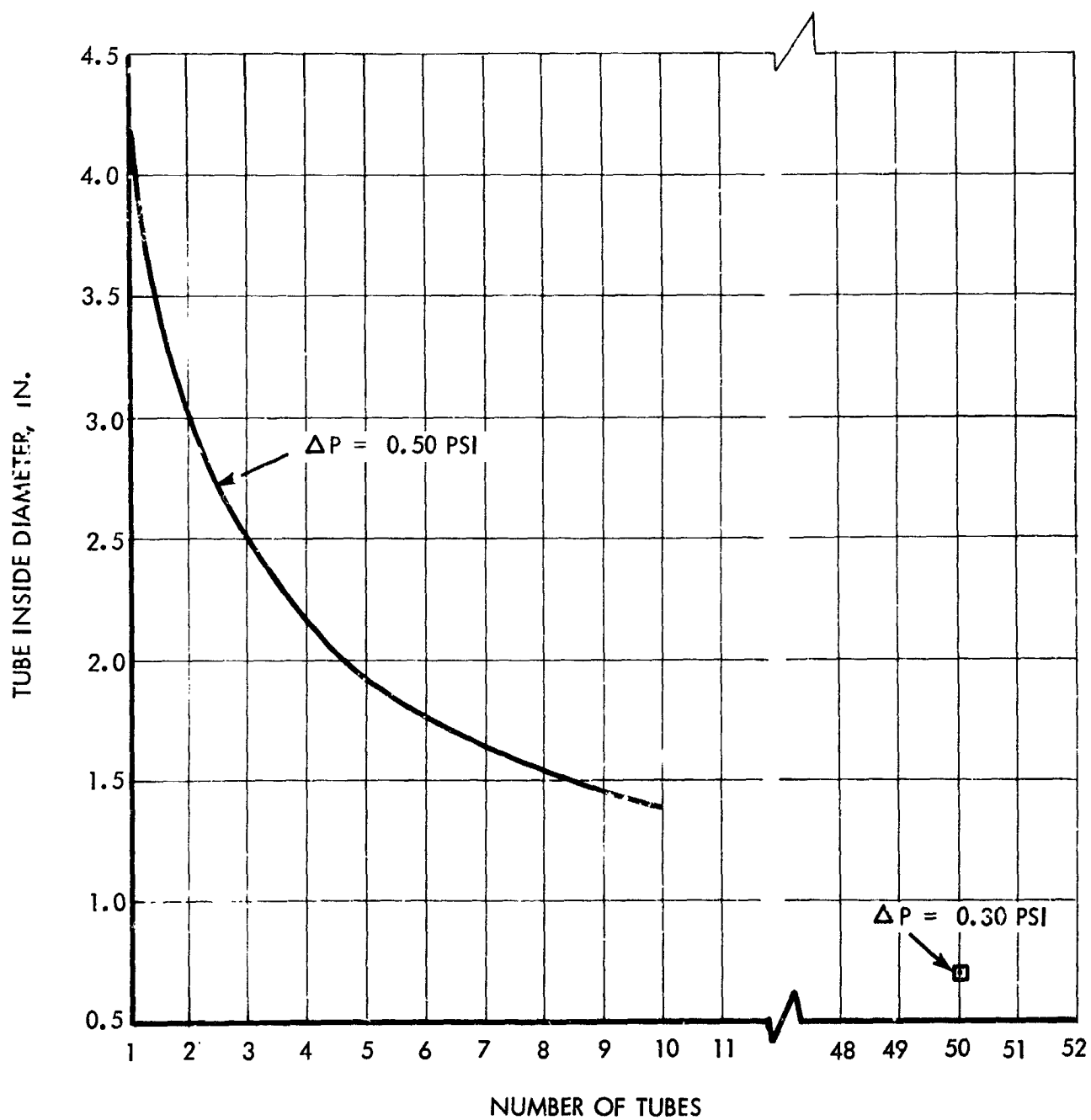
In the investigation of the use of a small number of tubes, a series of calculations was made for a gas allowable pressure drop of 0.50 psi compared to a total allowable of 0.55 psi for the four per cent design. Several calculations were made for designs at 0.45 psi and one each at 0.25 psi and 0.75 psi. The results of the calculations at 0.25, 0.45 and 0.75 psi all confirmed the results at 0.50 psi. Therefore, only the 0.50 psi results are presented, but the trends are typical of all the others. The first item of interest is the tube inside diameter required for each of the tube configurations. The variation of the tube I. D. with number of tubes is shown in Figure 49, and the multiple tube design point is illustrated for comparison. It can be observed from Figure 49 that tube bundles with less than five tubes require tube diameters greater than two inches. Even with 10 tubes a diameter of almost 1.4 inches is needed. These dimensions compare with the 0.684-inch diameter specified for the 50-tube design. The tube diameter influences the annular thickness needed in the storage bath. The larger diameters obviously required larger annuli. The larger annuli introduce more difficulties in the melting of the storage material, and this characteristic is considered a disadvantage.

A second item of interest is the heater tube surface area needed for each tube configuration. This variation is given in Figure 50 with the multiple-tube point included. It can be observed from Figure 50 that the heater surface area required decreases with tube number from one to ten tubes. At ten tubes the area needed is within one square foot of the multiple tube design area, but inlet and outlet manifolds may be required. In practice, it would be necessary to have transition pieces at least and these might require a slight pressure drop allowance. In any case, it is believed that a configuration with ten tubes is definitely marginal with regard to elimination of headers.

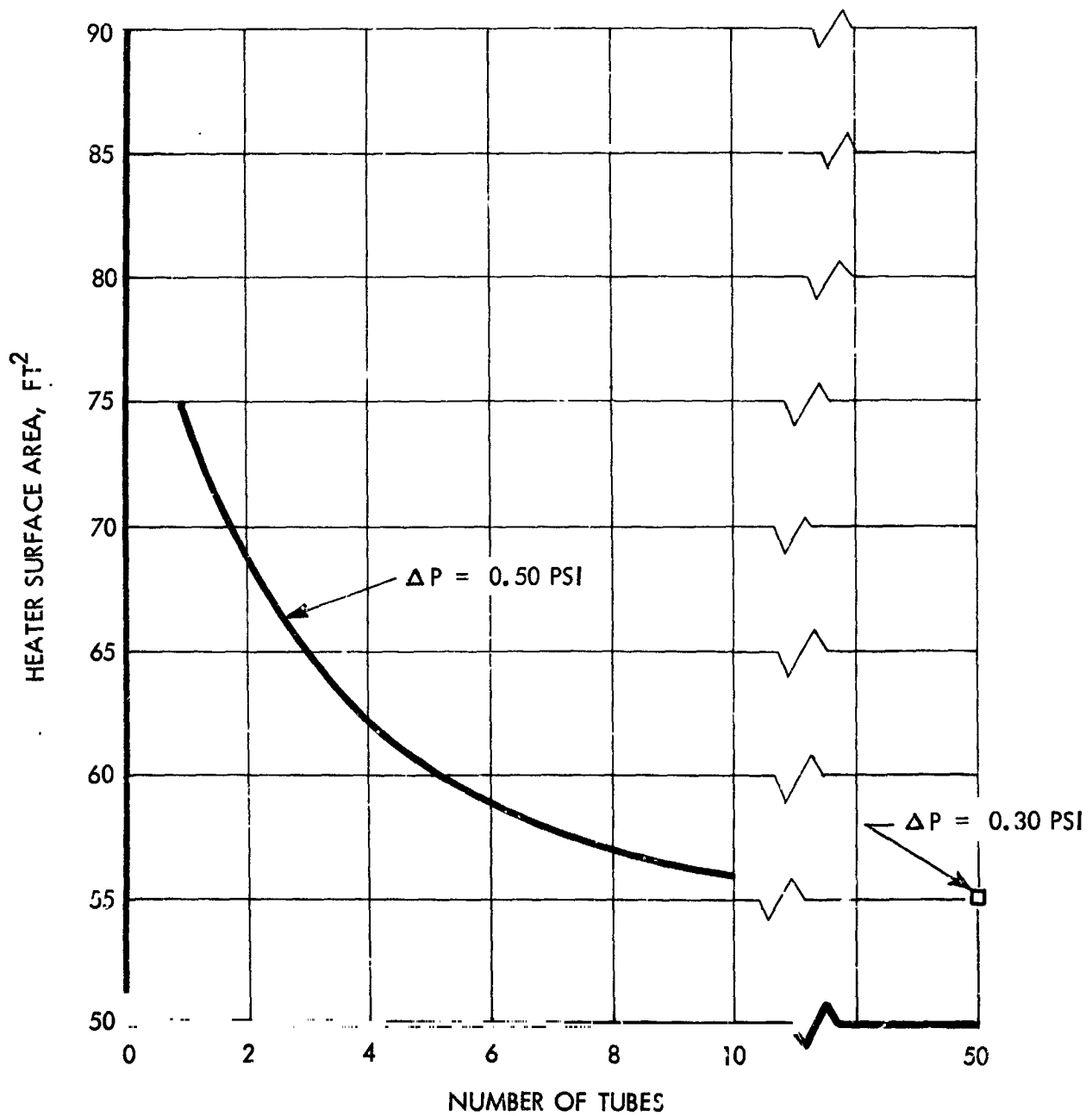
The third item of interest is the tube projected area required. The projected area is numerically equal to the surface area divided by the constant π . Thus, the variation shown in Figure 51 for the tube projected area is similar to that given in Figure 50. However, the tube projected area has added significance in that it is the minimum possible cavity surface area for any given configuration. Additional surface area must be provided for the storage salt. The added area for the salt could be held relatively constant, but the cavity surface areas for the low tube numbers would become quite large and result in a significant increase in collector blockage. The alternative is to limit the added area for the salt, but this procedure requires extended surface with its attendant complications.

After reviewing the results of this investigation, it was concluded that the use of a very few number of tubes, in the range from one to five, held little or no promise for better packaging.

VARIATION OF TUBE INSIDE DIAMETER WITH NUMBER OF TUBES



VARIATION OF HEATER TUBE SURFACE AREA
REQUIRED WITH NUMBER OF TUBES



VARIATION OF TUBE PROJECTED AREA REQUIRED
WITH NUMBER OF TUBES

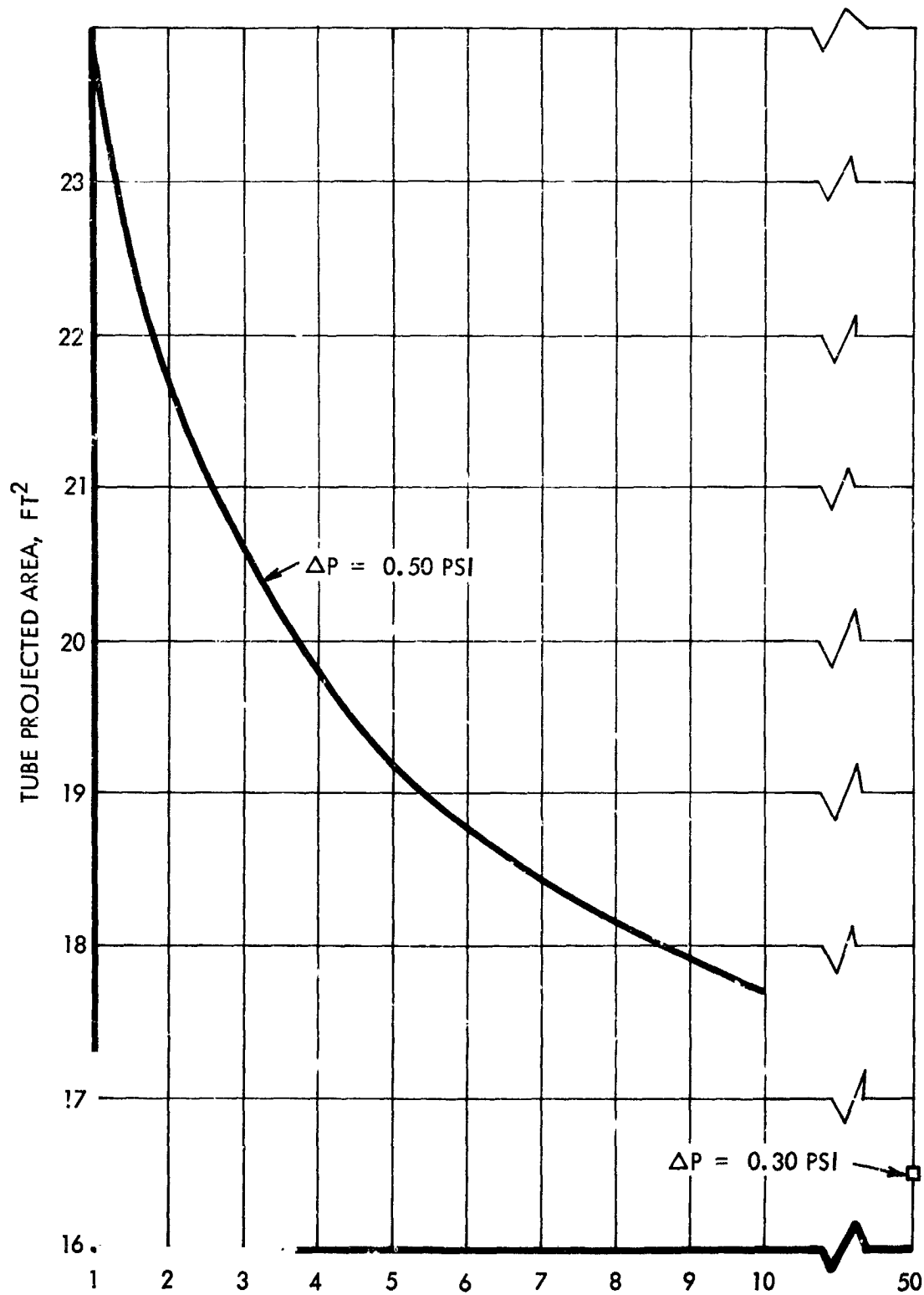


TABLE VI
SPECIFICATIONS (CAVITY RECEIVERS)

Priority	Collector Diameter (ft)	*Orbital Altitude (Nautical Miles)	Intercepted Energy (KW)	Nominal Orbit Time - Storage Time (Minutes)	Nominal Cycle Thermal Input (KW)	Total Storage (KW)
1	30	300	91.9	95.8/35.75 (1)	41.0	24.4
2	20	300	40.9	95.8/35.75 (1)	18.2	10.8
3	20	Synchronous (19, 300)	40.9	1436./71.6 (3)	27.6	32.9
4	30	Synchronous (19, 300)	91.9	1436./71.6 (3)	62.2	74.2

*Circular earth orbits in the ecliptic plane.

- (1) Calculated value of 95.80 min. orbit time with 35.465 min. of total shade and a total of 0.285 min. of varying shade to sun interval.
- (2) A. 19,300 (nautical) mile for a 23.93-hour orbit, (sidereal).
B. 19,355 (nautical) mile for 24-hour orbit.
- (3) Calculated total shade of 67.28 min. for 19,300-mile orbit and a total of 4.33 min. of varying shade to sun interval.

NOTE: Cycle thermal inputs correspond to overall collector-receiver efficiency of 75% and shadow factor of approximately 95%

In the range from five to ten, the characteristics looked more promising, but some compromises in header design might be needed. It was then decided that the multiple tube design with its inlet and outlet headers would be continued on the basis that its performance was better than the ten-tube configuration and might not have any more severe header problems. The package design possible with the multiple-tube configuration is considered superior to that with the ten-tube configuration.

The basic layout for the receiver of prime interest to NASA, condition 3, is shown in Figure 52. The characteristics for this design are as follows:

Tube Diameter	0.684 in.
Tube Length	5.8 ft (69.6 in.)
Number of Tubes	50
Cavity Diameter	51.0 in.
Receiver O. D. (including Insulation)	55.0 in.
Maximum Annular Thickness	1.4 in.
Gas Weight Flow	36.7 lb/min
Allowable Gas Pressure Drop	0.55 psi
Reynolds Number	8700

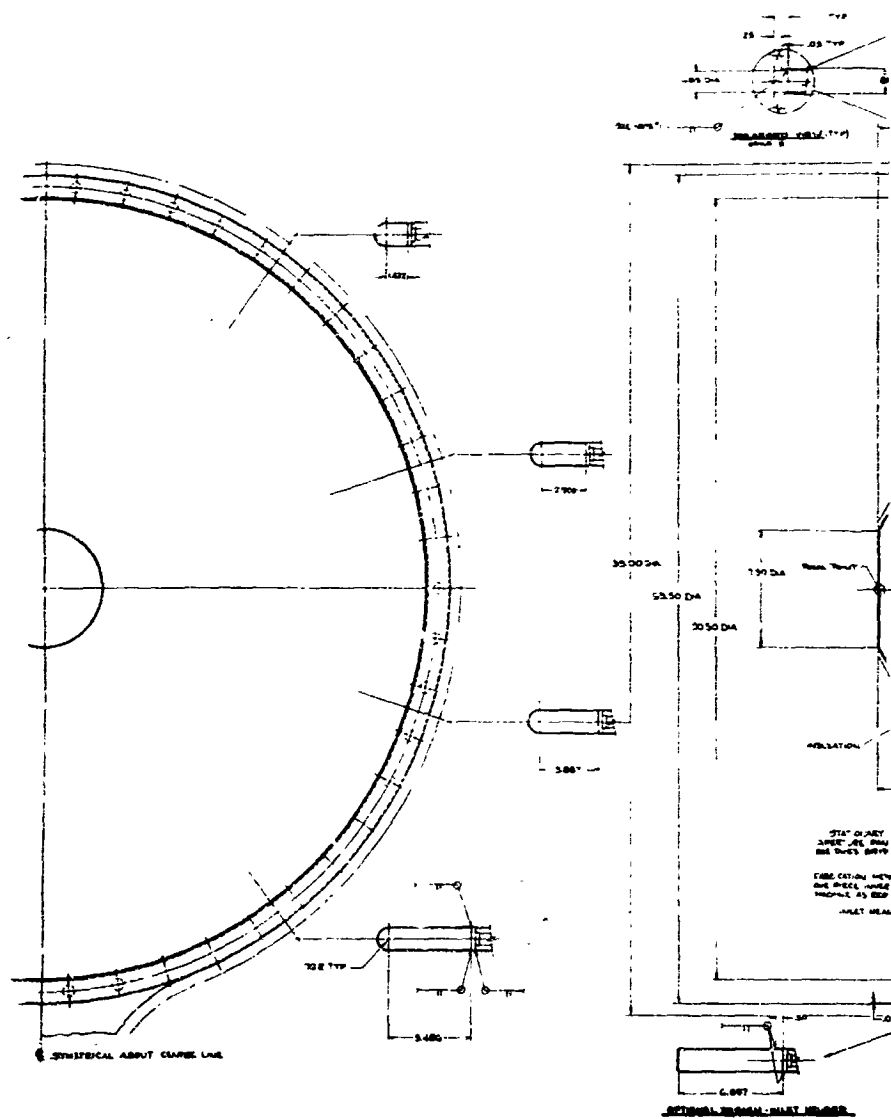
The basic container consists of inner and outer shells, an inlet and an outlet header and 50 tubes joined to each of the headers. The tubes are bent in a complex configuration to obtain the added length needed for the heat transfer. Lithium fluoride is to be loaded into the free volume between the two shells. Superinsulation is required on the outer surface of the outer shell to limit the heat lost to free space.

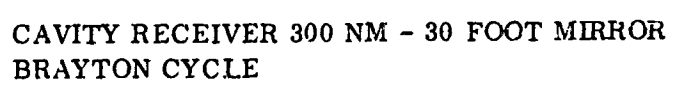
The aperture cone assembly for this receiver included both a maximum temperature control and an aperture closure device, as shown in Figure 53. Both systems were mechanical in nature and required linkage devices which tended to reduce the cavity receiver reliability. Therefore, a second look was taken in this area in conjunction with the two per cent design effort and a revised system was designed which is more reliable.

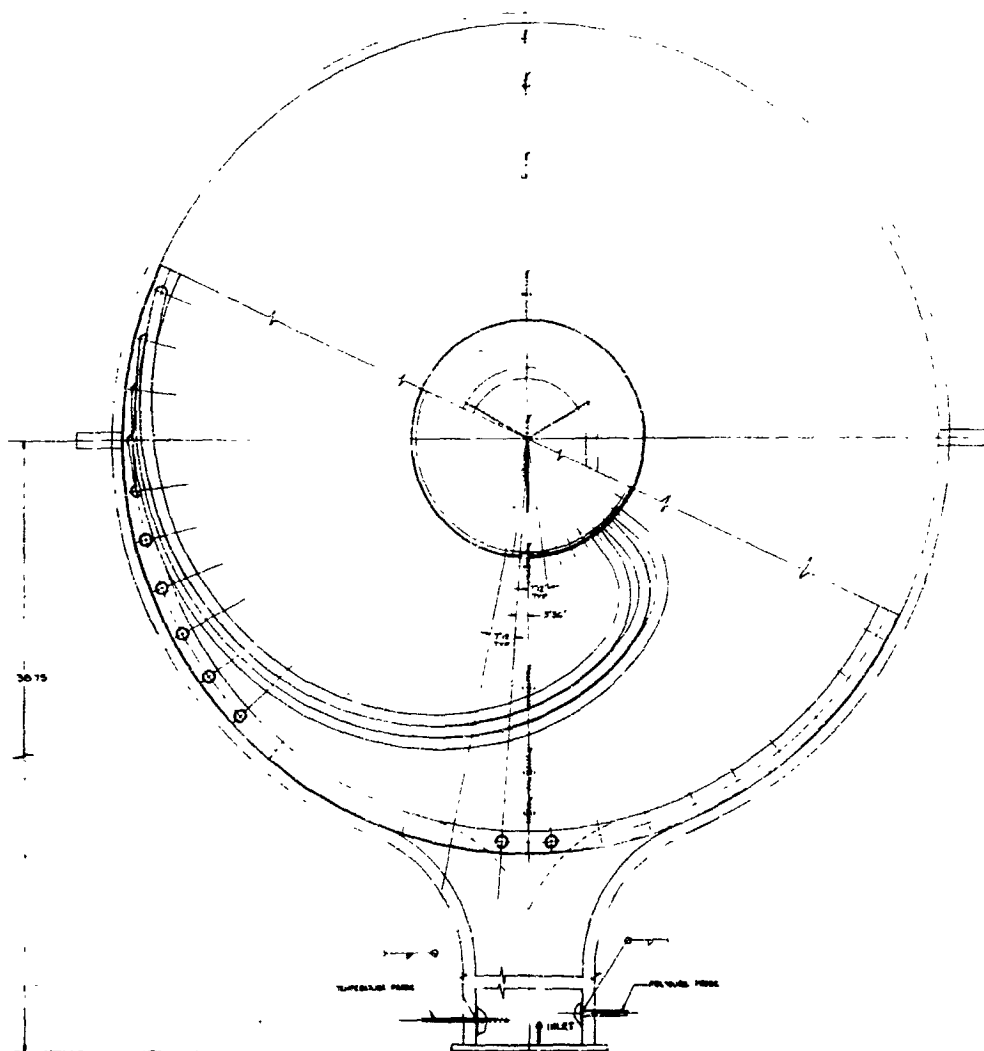
The cavity receivers designed for the other conditions in Table VI employed the same essential hemispherical concept. Their characteristics are listed below:

Item	Conditions		
	1	2	4
Number of Tubes	70	30	30
Tube Diameter, ft	0.597	0.910	0.910
Tube Length, ft	4.18	7.53	8.64
Cavity Diameter, ft	3.75	4.12	5.17
Estimated Weight, lb	236	440	830
Reynolds Number	7100	10,900	10,900

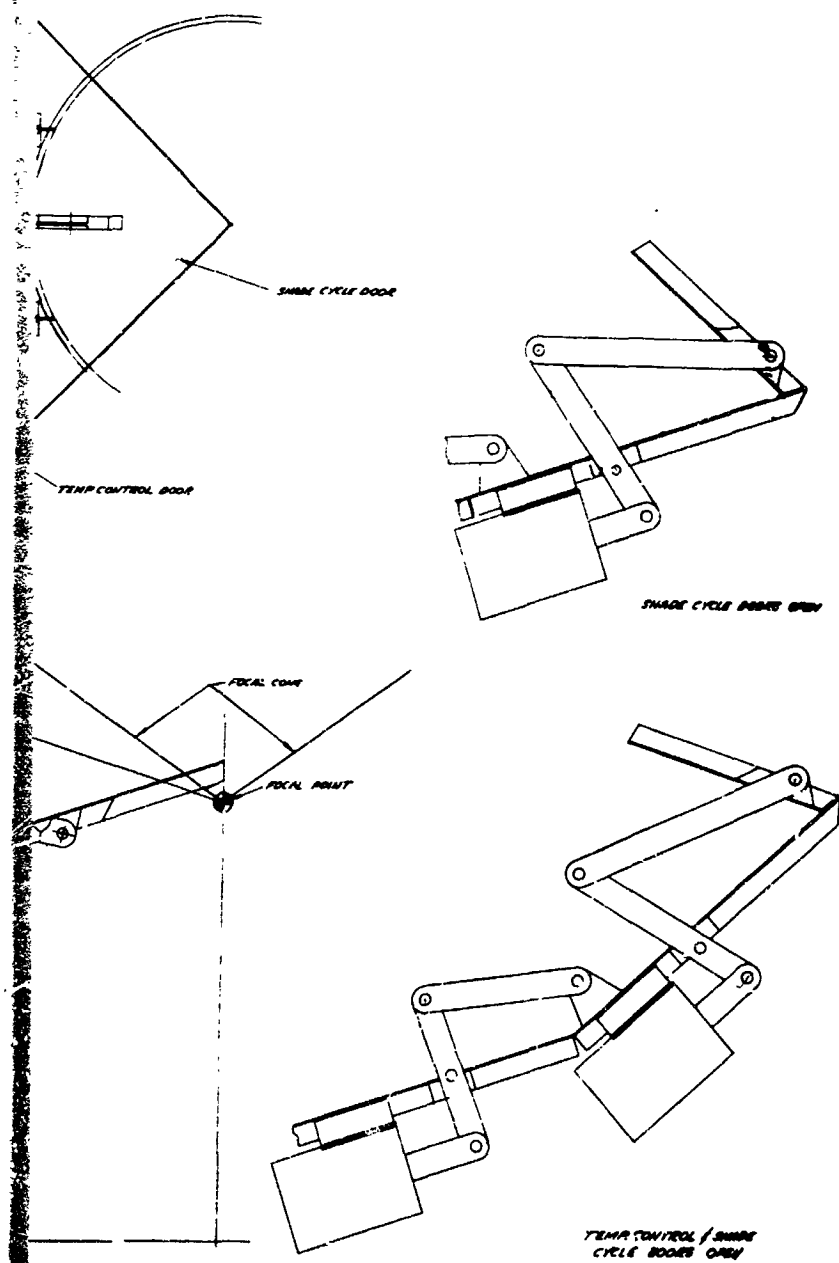
It can be observed that the practical number of tubes is reduced with the increased free lithium fluoride volume requirements of the synchronous orbit.







COMBINED CAVITY TEMPERATURE CONTROL CLOSURE DEVICE - BRAYTON CYCLE



LAND APERTURE

Typical results for the off-design performance calculations are illustrated in Figures 54 and 55. Figure 54 shows the gas temperature variation encountered with an instantaneous change of ten percent in the gas flow rate. Figure 55 shows the gas pressure variation under the same conditions.

The design investigation which had the greatest influence on system performance was an examination of the effect a change in allowable gas pressure drop might have on the cavity receiver design. It can be observed from the list of conditions above that the allowable gas pressure drop in the heater had been set at approximately four percent of the heater inlet pressure. NASA requested that designs based on allowable gas pressure drops of two, four and six percent of the heater inlet pressure be studied. The results are shown in Figure 56 for the combination of the 30-foot diameter collector and the 300 nautical mile orbit. It can be observed from Figure 56 that the estimated weight for the two percent design is about thirty pounds more than the four percent design, but no further weight reduction is achieved by the six percent design. One result of the two percent design is a larger cavity diameter and thus a larger amount of collector blockage.

The hemispherical cavity concept with multiple tube configurations was continued in the two percent gas pressure drop design studies described next. These studies were initiated after NASA's review of the parametric results summarized in Figure 56.

5.2 Two Percent Gas Pressure Drop Design - Initial

The first choice for an optimized design was a heater featuring a mean gas Reynolds number of 5500. The number of tubes corresponding to this Reynolds number was 70 with a tube inner diameter of 0.693 in. and a tube length of 69.5 in. These dimensions permitted a storage bath with a 4.5 ft diameter cavity. As a result, the maximum receiver diameter, which determines the amount of collector shadowing, was less than 5 ft.

A potential heat transfer problem area was uncovered in this design, however. In the final version of the four per cent design and in this initial version of the two per cent design, curved tubes are employed to permit use of maximum length tubes for a given cavity diameter. Although the degree of curvature is slight over most of the tube length, higher degrees of curvature are required at the inlet and outlet headers. It has been ascertained from the literature that the effect of the curvature is to increase the range of Reynolds numbers in which laminar and/or transitional flow can occur. Thus, the transitional Reynolds number from laminar to turbulent flow is increased. The potential problem area arises because the two per cent design tends to obtain optimum geometries at a lower gas Reynolds number than the four per cent design. The two per cent design optimum gas Reynolds number appears to be very close to the transitional Reynolds number, a highly undesirable situation.

The influence of tube radius on Reynolds number is illustrated in Figure 57. The transitional Reynolds number defined as RE_{CRIT} is a function of the ratio of the flow passage radius to the radius of curvature. The line shown is a plot of the equation of Reference 17, and the data are taken from References 18 and 19. Reference 17 indicates that for a Reynolds number

VARIATION OF GAS TEMPERATURE WITH
INSTANTANEOUS CHANGE OF 10% GAS FLOW RATE

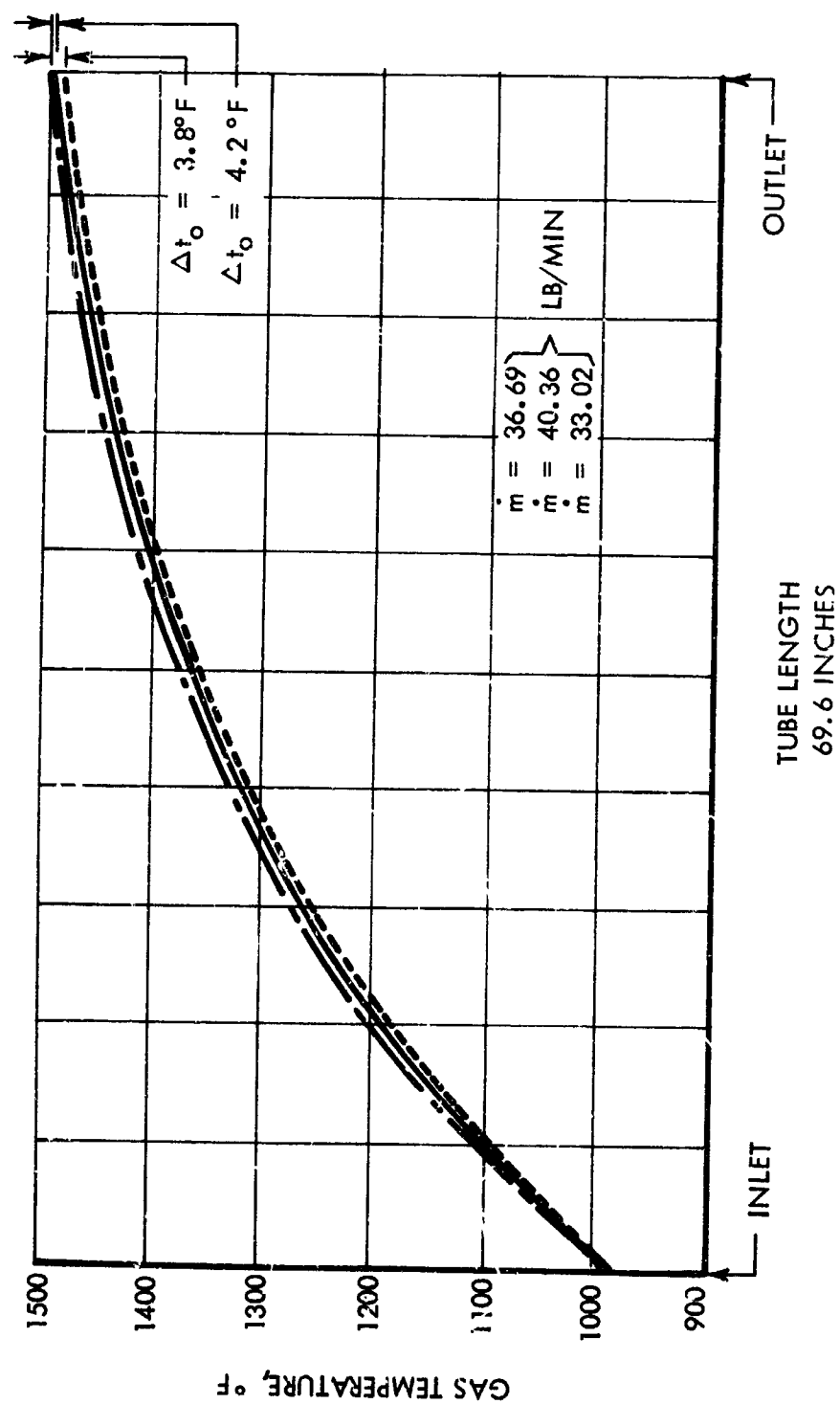


FIGURE 54

VARIATION OF GAS PRESSURE DROP WITH
INSTANTANEOUS CHANGE OF 10% IN GAS FLOW

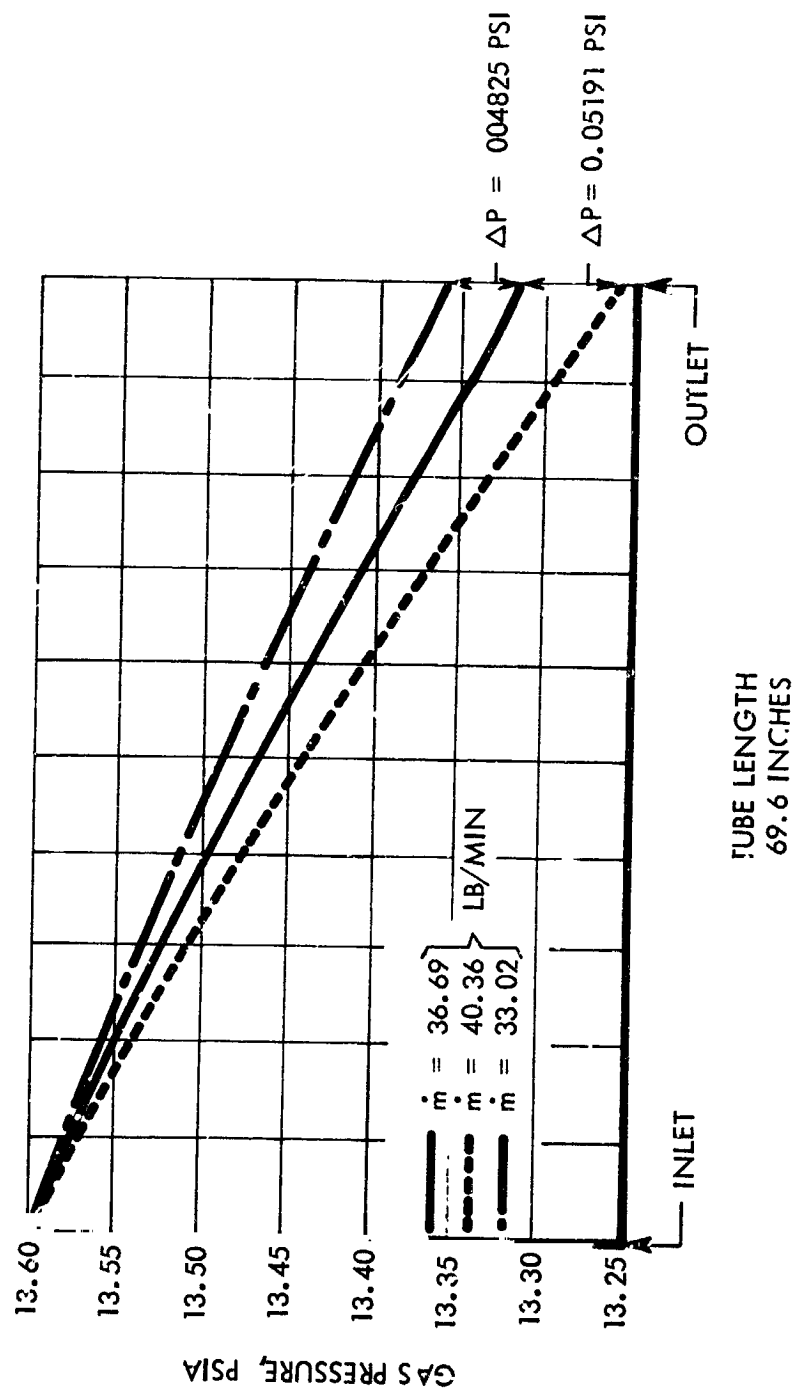


FIGURE 55

EFFECT OF $\Delta P/P_{IN}$ ON RECEIVER WEIGHT
300 N.M. ORBIT, 30 FOOT MIRROR

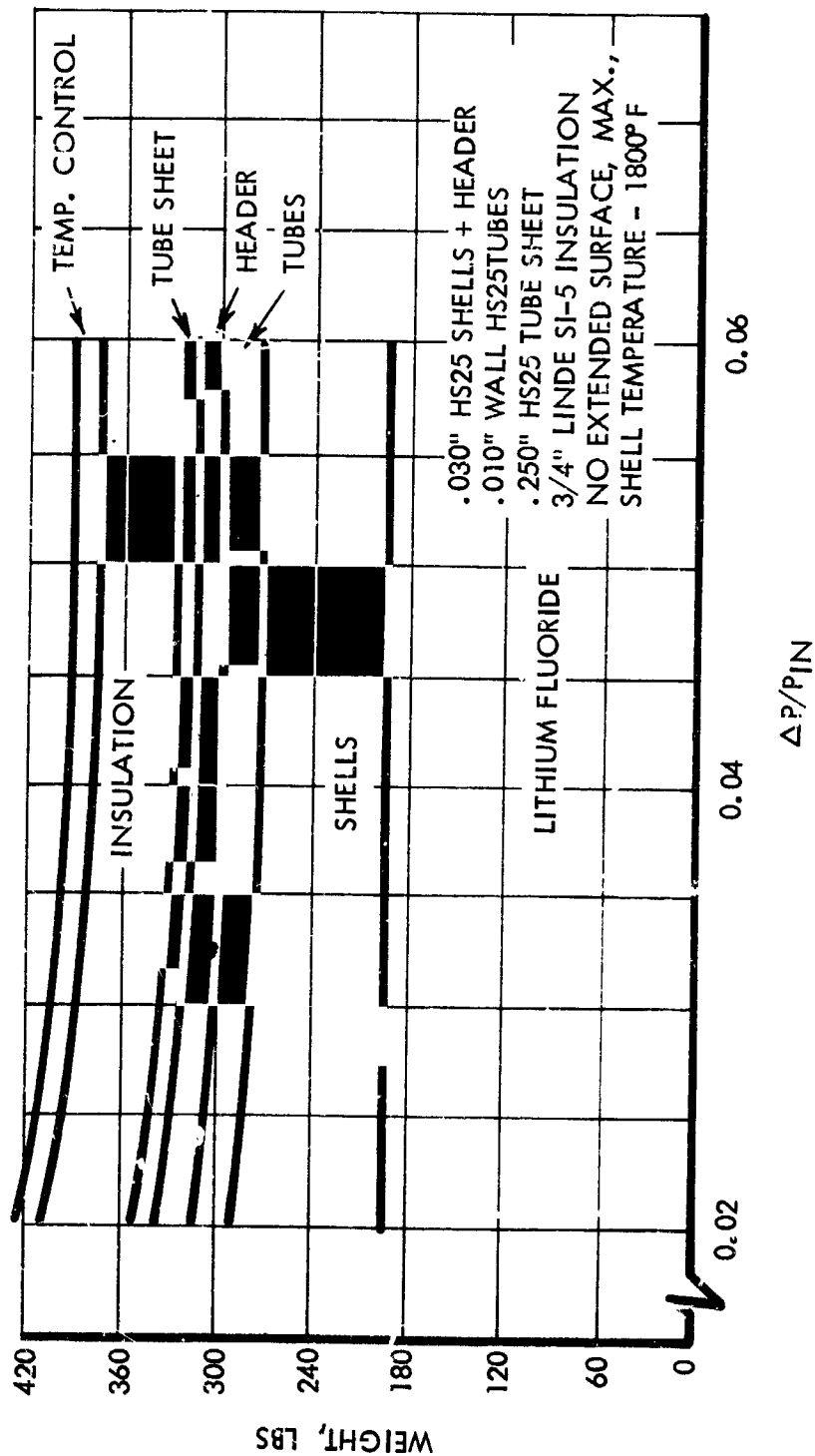


FIGURE 56

VARIATION OF THE TRANSITIONAL REYNOLDS NUMBER IN CURVED TUBES
WITH THE RATIO OF TUBE RADIUS AT RADIUS OF CURVATURE

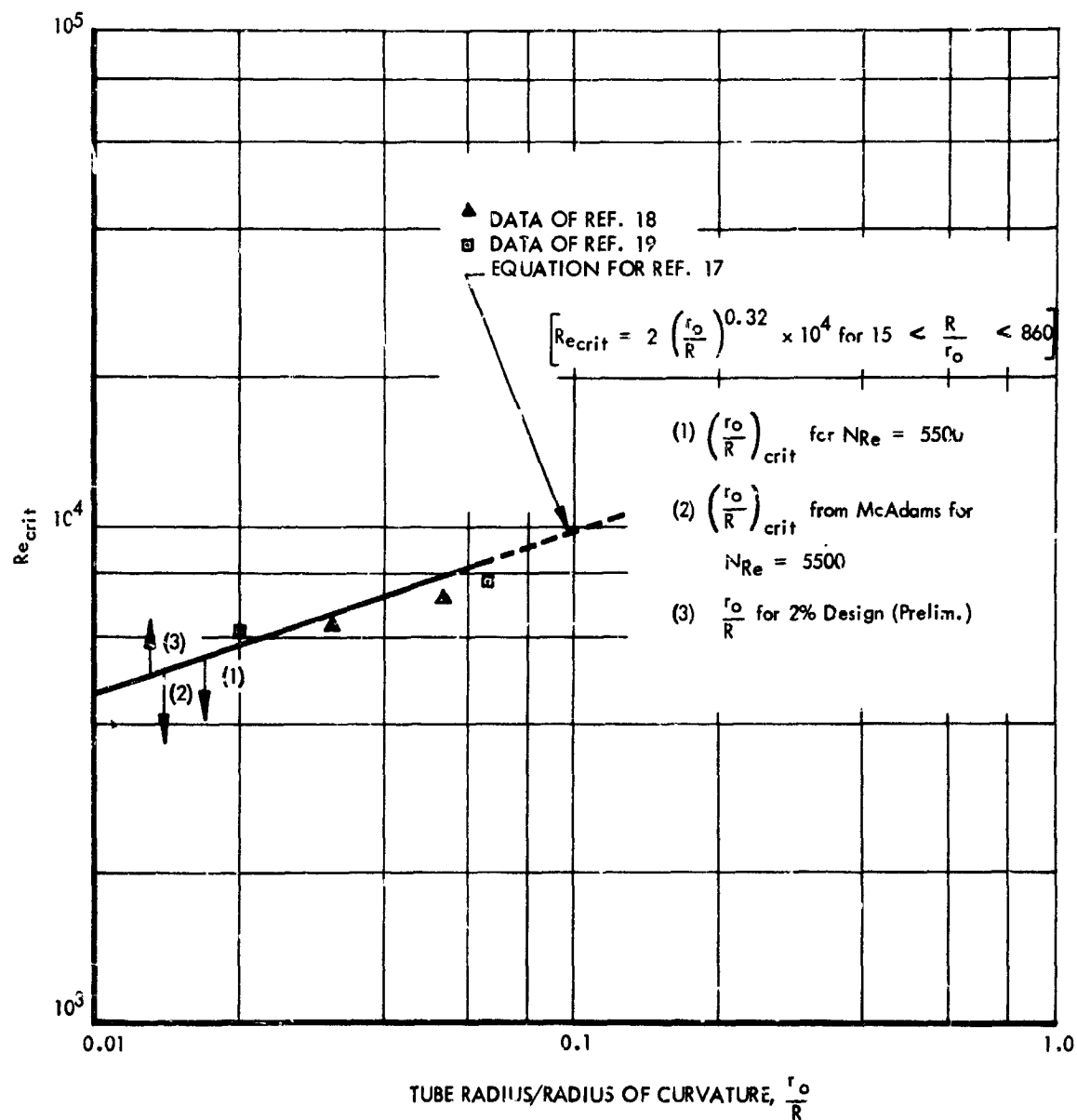


FIGURE 57

of 5500 the critical transitional radius ratio is 0.0172. Thus, for the initial two percent design, any radius ratio above 0.0172 would indicate laminar flow. However, Reference 20 indicates the critical transitional radius ratio is 0.014 for a gas Reynolds number of 5500. Since the initial two percent design indicated an actual radius ratio of 0.013, the gas flow might be marginally turbulent.

To assess the magnitude of the problem, if the initial design were operating in laminar flow, it was assumed that the heater was operating in the laminar regime and the resulting heat transfer and pressure drop calculated. As expected the pressure drop decreased from the design value to about one-third of the design value, and the outlet gas temperature dropped from 1950° R to 1716° R. These values correspond to gas temperature increases within the receiver of 504° R and 270° R. It is readily apparent that such a situation would adversely affect system performance.

Therefore, a second design was initiated. The Reynolds number was increased to a mean value of 8100. The number of tubes corresponding to this Reynolds number was 30 with a tube diameter of 1.050 inches and a tube length of 113 inches. The basic configuration for both designs was presented in Figure 52.

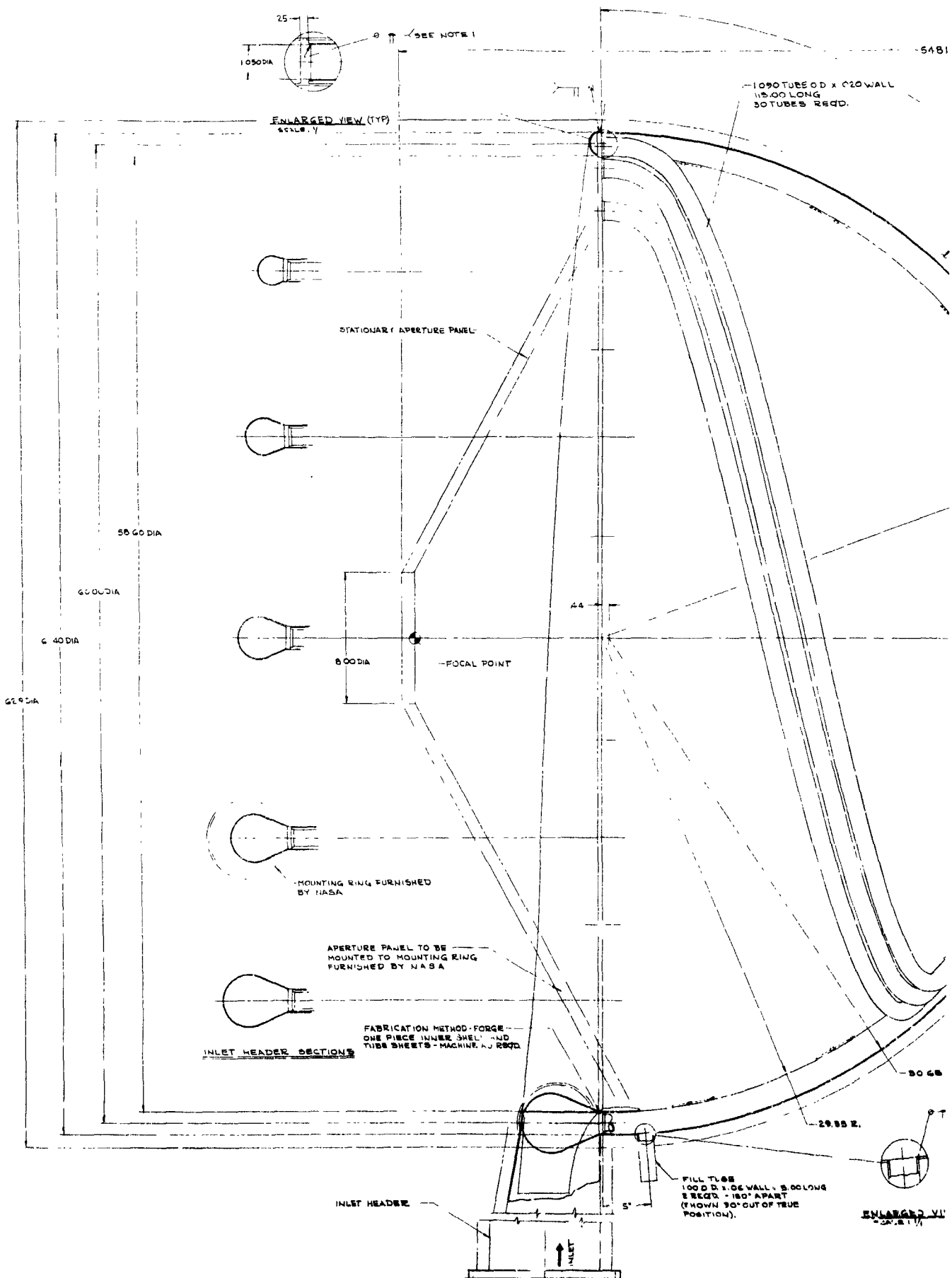
Examination and review of the resultant internal bath configuration indicated that this design was acceptable and, in fact, was more favorable than the initial design.

To determine if this trend would continue, a third design was investigated at a mean gas Reynolds number of about 10,000. This design employed 20 tubes, but the review of this one showed no additional advantages above the 30 tube design. The added void volume was considered a disadvantage, and, therefore, the 30 tube design was rated the best of the three and near optimum. The 30 tube design layout, while not completed, is shown in Figure 58.

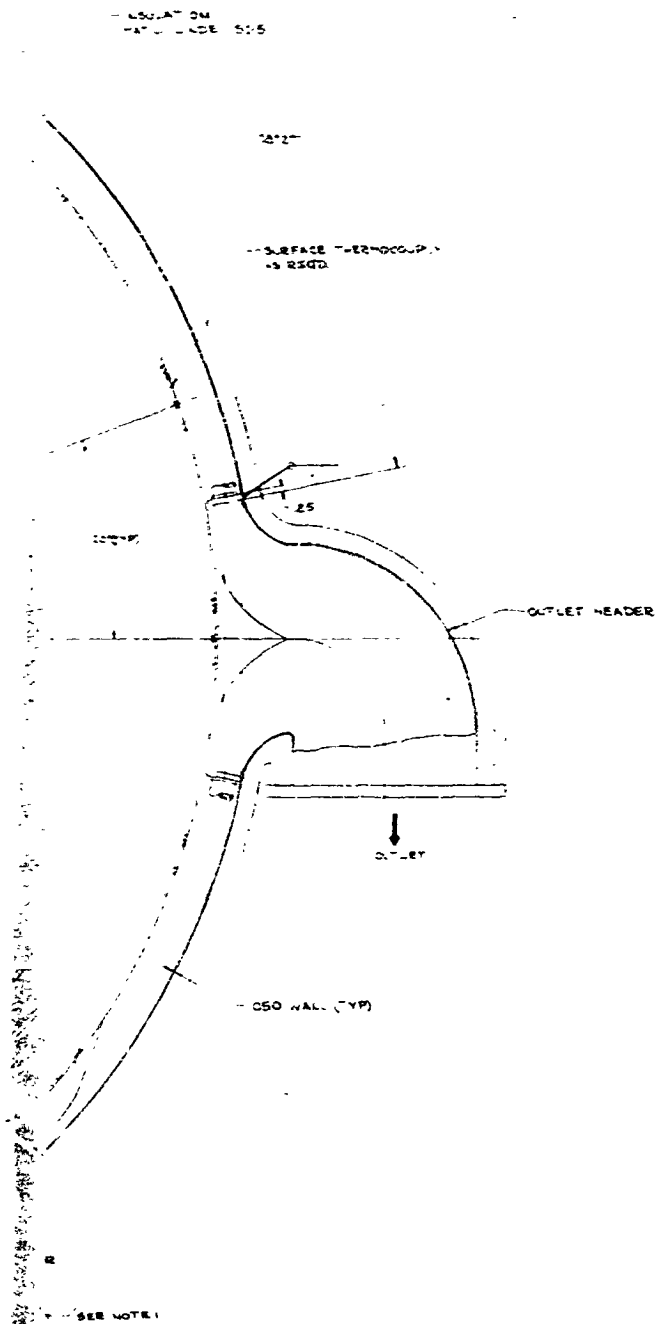
5.2.1 Stress Analysis

The stress analysis conducted on the full scale cavity receiver design was confined to the 30 tube model. The material properties were selected based on a study which is included in the Appendix, Section 8.7. The areas examined included the following:

1. Inner shell - buckling and membrane stresses
2. Outer shell - buckling and membrane stresses
3. Outer shell - to - outlet header joint
4. Outer shell - to - inlet header joint
5. Inner shell - to - inlet header joint
6. Tube membrane and thermal stresses

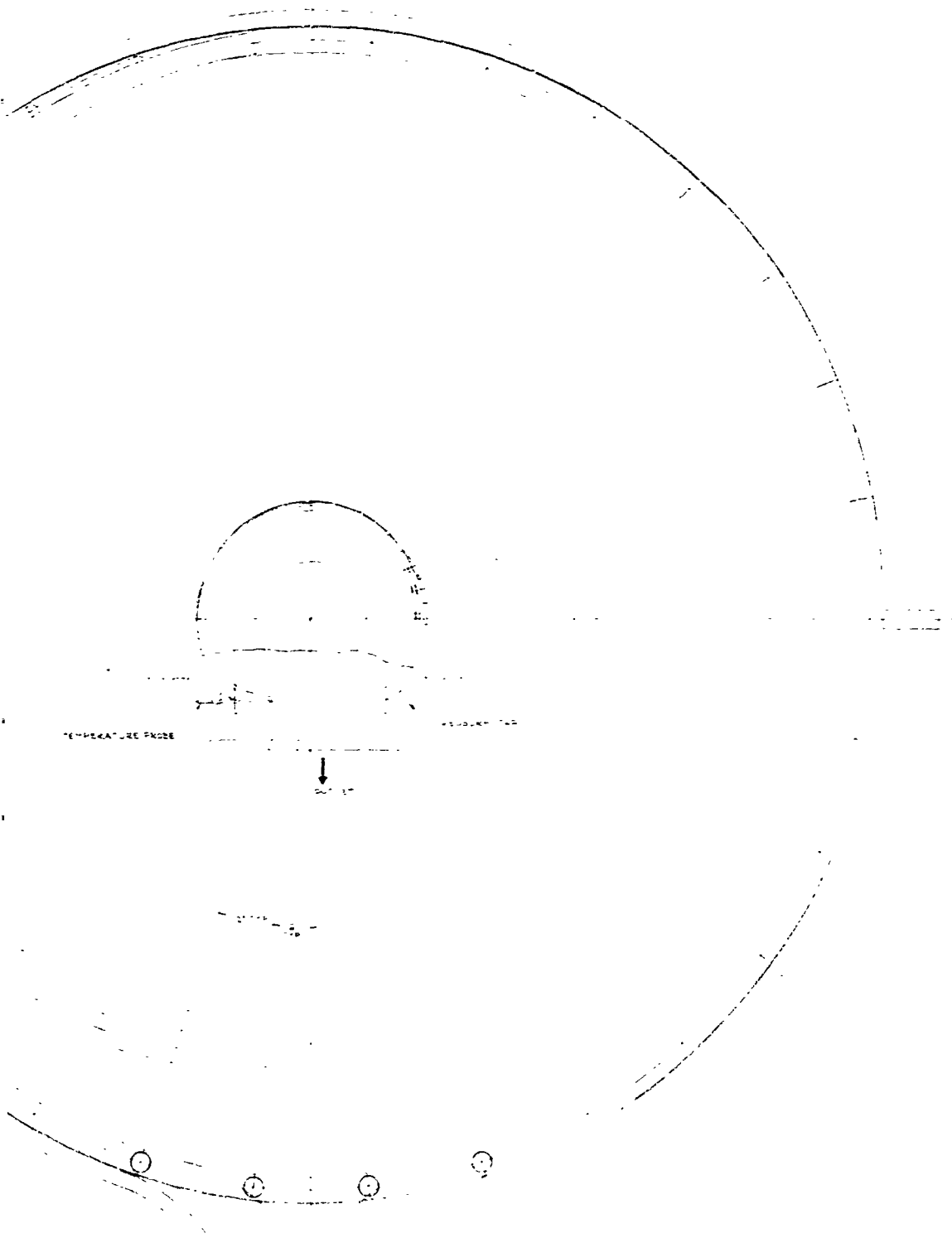


30 TUBE RECEIVER BRAYTON CYCLE



1. WALL THICKNESS SUB. 20" TO FINAL STRESS ANALYSIS
 2. ALL TUBE SHEET TO TUBE WELDS ARE INTERNAL BUTT,
 WITH SELF ALIGNMENT, 100% PENETRATION

NOTES:



TEMPERATURE PROBE

PRESSURE TAP



TEMPERATURE PROBE

PRESSURE TAP

BLANK PAGE

7. Inlet and outlet header membrane stresses

8. Aperture control mechanisms.

The inner and outer shells were approximated by cones and cylinders. The thermal stresses were based on temperature conditions assumed from earlier results on the Sunflower boiler/heat storage program. These temperature assumptions were made on the high side for conservative design. The maximum inner shell temperature was set at 1750° F with the range down to 1650° F locally.

The results showed that the outlet header pseudo-shell needed to be much thicker, approximately 1/4-inch, and that the outer shell near the outlet header should be 0.080-inch thick for a short distance from the header joint and a gradual taper to the basic shell minimum thickness of 0.050-inch. The corresponding short time classical elastic buckling pressure, based on room temperature just before launch, was calculated to be 106 psi. The ground testing was contemplated to be under space conditions. Considerable study of the conditions at the inner shell-to-inlet header joint resulted in a recommendation to move the aperture cone and, therefore, the solar concentrated incident energy, to a position three inches from the header in lieu of the present position two inches from the header. A summary of the stress investigations is included in the Appendix, Section 8.8.

The pressure required to cause instability at the tubes at 1750° F was calculated to be 309 psi. The inlet and outlet header wall thicknesses must be based on long-term steady stress levels. The inlet header must be integrated with the NASA mounting ring design. It would be desirable to determine all the resultant stresses with the STL Mark III asymmetric shell-of-revolution digital computer program.

5.2.2 Cavity Temperature Control

In conjunction with the two percent design, the cavity maximum temperature control and aperture closure mechanisms were redesigned to obtain more reliability by using simple linkage and by reducing mechanical friction pivots and contacts to an absolute minimum. The cavity maximum temperature control consists of temperature sensitive bulbs located on the cavity surface, a liquid metal working fluid, actuating bellows located on the aperture cone, lines connecting the sensors and the bellows and hinge-mounted louvers which are also located on the cone. In operation, the liquid metal is vaporized at the temperature sensitive bulb which is located in a manner which insures that the bulb is the highest temperature in the liquid metal system. The associated vapor pressure is transmitted through the liquid metal to the bellows which actuate the louvers. A spring return is provided to obtain fail-safe operation with the louvers in the closed position.

Since continued operation of the cavity receiver in the sunlight after the lithium fluoride is all melted could result in excessive cavity surface temperatures, a heat rejection system was provided to protect the cavity surface and to permit operation in all-sun orbits. Heat rejection doors permit the excess energy, which is equivalent to sixty percent of the heater duty, to be radiated to space. For a desired surface temperature of 1700° F and with an equivalent emissivity of 0.92, the open area required is 2.4 ft², or 346 in².

Heat transfer losses associated with removal of aperture closure devices were determined to be 5940 Btu/hour during the shade period which represented a 7.2% loss of energy during the shade period operation. Following a careful review of the reliability compromise associated with aperture closure devices, the small performance penalty associated with the doors was accepted to improve the cavity receiver reliability. Aperture control devices were, therefore, eliminated from further design considerations. The aperture cone assembly which resulted after the above technical direction is presented in Figure 59.

5.2.3 Heat Transfer Correlations

Following the determination of lithium fluoride conductivity and heat input and removal rates, the limiting heat transfer resistance was determined to be the cavity receiver tube to argon resistance. In the review, the following three types of correlations for heat transfer were presented:

1. Standard textbook equations.

This type was characterized by the Dittus-Boelter equation

$$\left[\frac{h D}{k} \right] = 0.023 \left[\frac{D G}{\mu} \right]^{0.8} \left[\frac{C_p \mu}{k} \right]^{0.4}$$

with all fluid properties evaluated at the bulk temperature.

Source: Reference 21

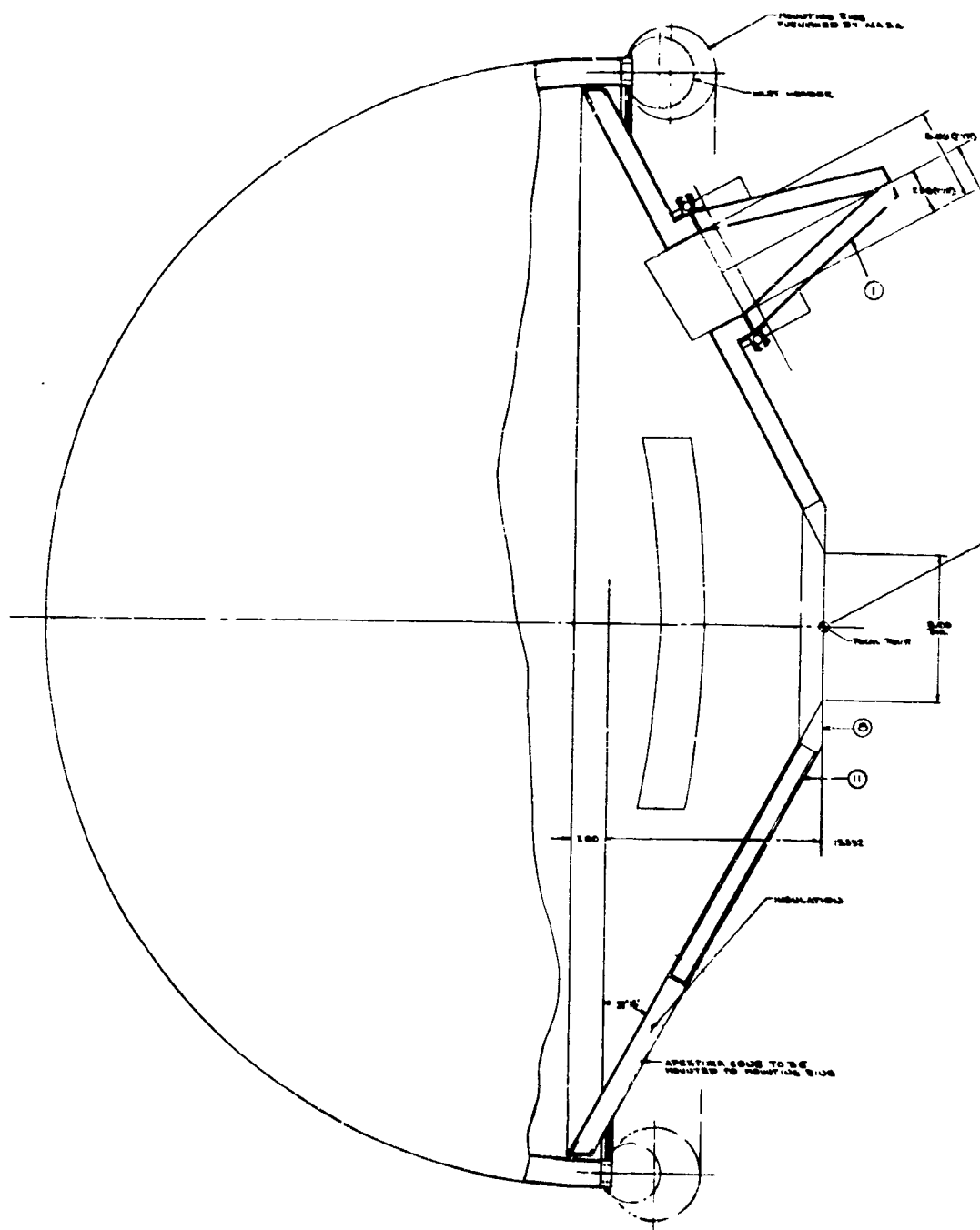
The above equation is typical of those available in heat transfer texts. It was used for the preliminary design analysis and the basic study leading to the turbulent flow design. It is valid for the Reynolds number range from 10,000 to 120,000, for L/D ratios of 60 or more and for Prandtl numbers from 0.7 to 120. The data were taken at moderate temperature differences and thus the equation is limited to the moderate range.

Another equation, taken from Reference 2, is

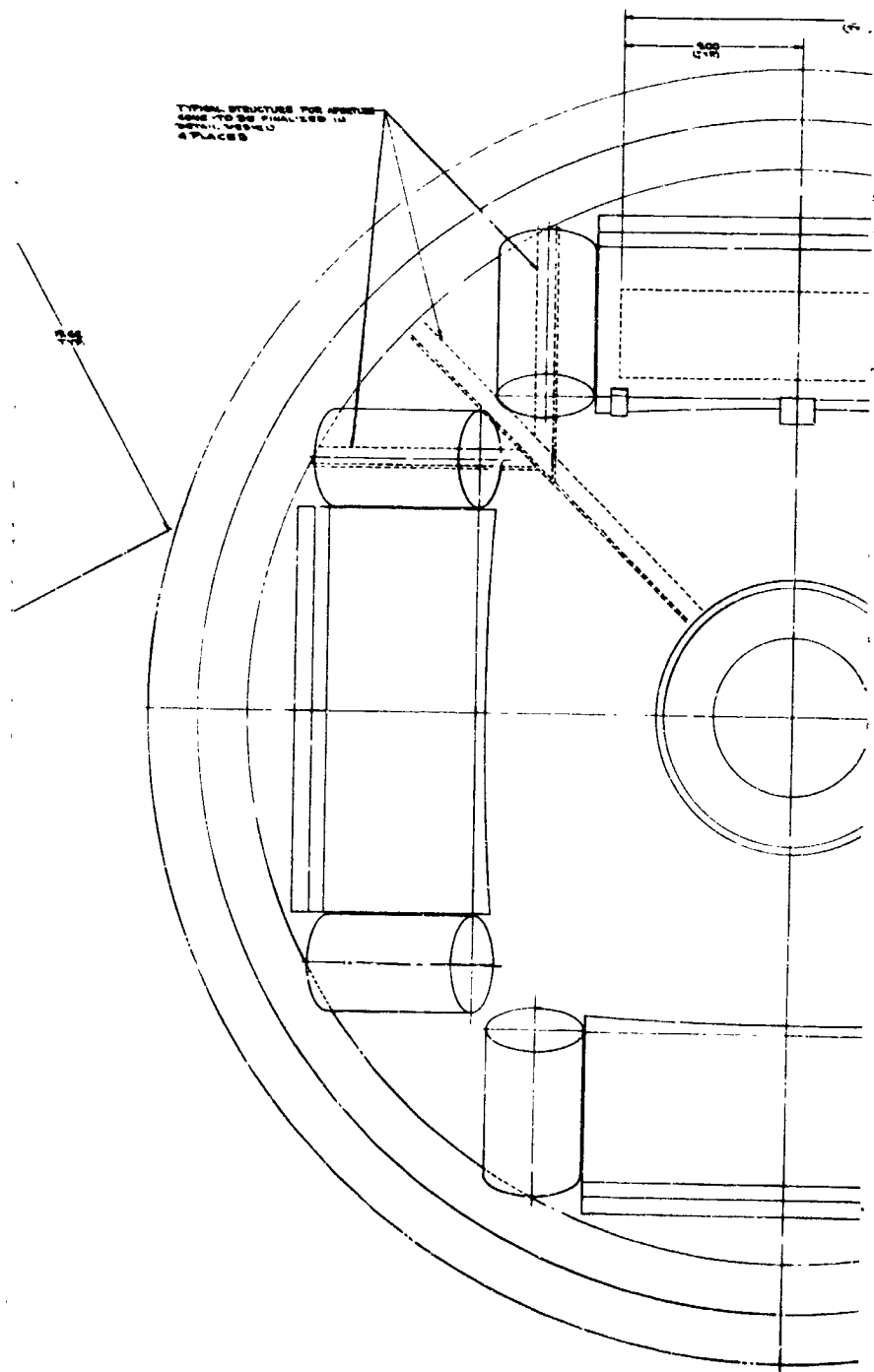
$$\frac{h}{G_{cp}} = \frac{0.0084 (D G / \mu)^{-1/4}}{1 + 1.5 P_R^{-1/6} (D G / \mu)^{-1/8} (P_R - 1)}$$

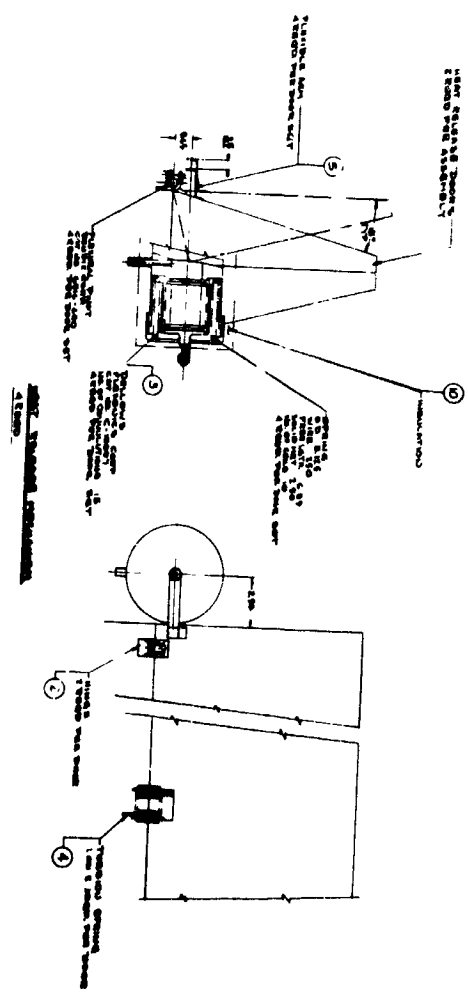
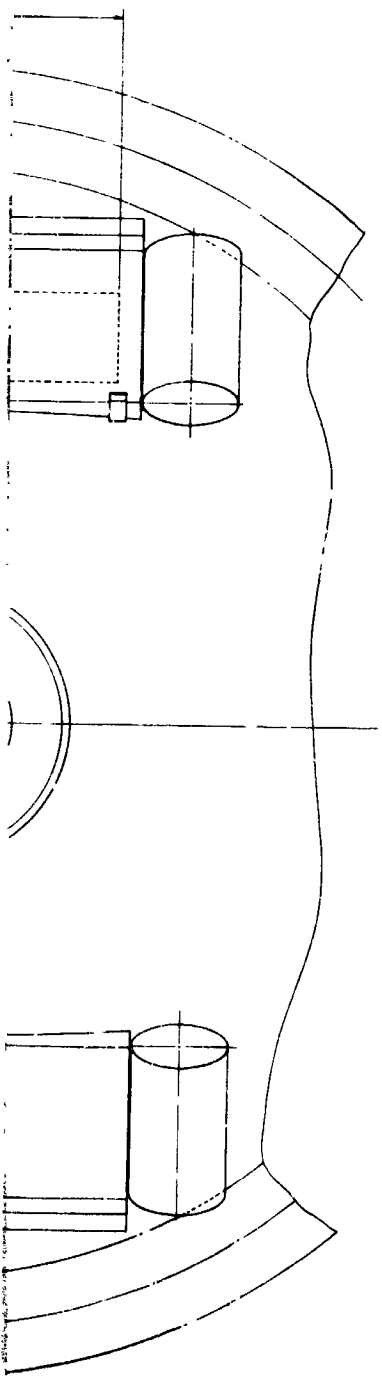
$$\text{where } P_R = \frac{C_p}{k}$$

Again, the gas properties are evaluated at the bulk temperature.



CONCEPT-BRAYTON CYCLE APERTURE CONE ASSEMBLY WITH HEAT REJECTION LOUVRES FOR ALL-SUN ORBIT





BLANK PAGE

2. British Data.

The second type of equation was typical of the correlation given in Reference 22.

$$\left[\frac{h D}{k} \right] = 0.023 \left[\frac{G D}{\mu} \right]^{0.8} \left[\frac{C_p \mu}{k} \right]^{0.4} \left[\frac{T_s}{T_b} \right]^{-0.43}$$

The gas properties are to be evaluated at the bulk temperature. This equation was obtained from data for fully developed flow, is valid for a range of Reynolds numbers from 4000 to 130,000 and applies specifically to argon. T_s in the above equation represents the surface temperature in degrees Rankine.

3. U. S. Data.

The third type of equation was taken from Reference 23.

$$\left[\frac{h D}{k} \right] = 0.034 \left[\frac{\rho V_b D}{\mu} \right]^{0.8} \left[\frac{C_p \mu}{k} \right]^{0.4} \left[\frac{L}{D} \right]^{-0.1}$$

In this equation all gas properties are to be evaluated at the average film temperature. The gas velocity is to be evaluated at the average bulk temperature.

After review of various correlations, the one shown in Reference 23 was selected for heat transfer design of the receiver.

Consideration of the friction factor showed that several forms are available. A review and comparison of the various forms is presented in Reference 24. A common equation which is credited to Drew in Reference 21 is

$$f = 0.184 \text{ Re}^{-0.2}$$

This equation is valid over the range of Reynolds numbers from 5000 to 200,000.

Another equation commonly used was suggested by Blasius:

$$f = 0.316 \text{ Re}^{-1/4}$$

Reference 24 presents equations by Nikuradse, Von Karman and Drew. A table of values is also presented therein and is reproduced here. The numerical constants in the above equations presented in Reference 24 are one fourth of the above values, and similarly the values in Table VII are one fourth of the value, calculated by the above equations.

TABLE VII
COMPARISON OF FRICTION-FACTOR VALUES
AT VARIOUS REYNOLDS NUMBERS

Re	Drew (1)	Blasius	Nikuradse	Von Karman	Drew (2)
3, 000	.00930	.0107	.0109	.0109	.0110
10, 000	.00730	.00790	.00772	.00774	.00797
100, 000	.0046	.00443	.00448	.00449	.00456
1, 000, 000	.00289	.00250	.00291	.00292	.00290
10, 000, 000	.00183	.00140	.00204	.00202	.00218

Review and consideration of their application of these various factors resulted in the selection of the basic relation by Blasius

$$f = 0.316 \text{ Re}^{-1/4}$$

The influence of the correlation on the turbulent flow design was examined, and it was found that the tube required for a 30-tube configuration on the basis of the Reference 23 correlation was significantly greater than available in the design of Figure 58. Investigation of alternate tube configurations in which the gas would operate at higher and lower Reynolds numbers indicated the packaging problem could not be solved for a cavity with reasonable collector shadowing and gas operation in turbulent flow in a bare tube.

A limited investigation was conducted of heat exchangers designed for turbulent flow operation but assisted with various forms of turbolators. An excellent summary of the increased heat transfer and the increased pressure drop encountered with typical turbolators is given in Reference 6. Preliminary analysis based on comparing the trade-off between diameter and length, with constant pressure drop, showed that there was no advantage gained in using turbolators.

The influence of the working fluid on the design was investigated. Argon gas operation was compared with helium-xenon mixtures. The properties of the helium-xenon mixture to be employed were specified by NASA. These properties and the comparable argon values are listed in Table VIII.

TABLE VIII
GAS PROPERTIES*

Gas	Viscosity (Lb/Fr-Sec)		Thermal Conductivity (Btu/Hr-Fr-°F)		Prandtl Number	
	1000° R	2000° R	1000° R	2000° R	1000° R	2000° R
Argon	2.4×10^{-5}	3.75×10^{-5}	0.018	0.0255	0.645	0.635
He - Xe (m 40)	3.1×10^{-5}	5.05×10^{-5}	0.052	0.084	0.245	0.250

It can be observed from Table VIII that the Prandtl Number from the helium-xenon mixture is considerably less than that for pure argon. The viscosity of the helium-xenon mixture is slightly higher than the viscosity of pure argon, but the thermal conductivity of the mixture is much higher than that for pure argon. It is this increase in thermal conductivity which has the most direct influence on the heat transfer coefficient. For a given Nusselt number and tube diameter, the convection heat transfer coefficient is directly proportional to the thermal conductivity. Thus, the heat transfer coefficient for the helium-xenon mixture could be expected to be much higher than the comparable coefficient for argon. While the increased viscosity does have an effect on both Reynolds number and pressure drop, the most marked change occurs in the heat transfer coefficient because of the much higher conductivity.

The mixture properties needed for the gas temperatures in the design calculations were obtained by linear interpolation between the listed values. The results of the calculations showed that the receiver design in Figure 58 would be adequate for a mixture with such properties. The tube length as shown is longer than required for this helium-xenon mixture and the pressure drop is higher than desired.

A receiver with the same concept but modified to the proper tube length, approximately 104 inches, would also operate at approximately the design pressure drop. Thus, it was concluded that turbulent flow operation would be possible for such a helium-xenon mixture and the design concept in Figure 58 would be acceptable. No effort was made to optimize a receiver design for this gas mixture. The calculations did demonstrate, however, the definite heat transfer advantages of a typical helium-xenon gas mixture as the cycle working fluid. This type of gas mixture would be helpful in reducing all of the heat exchanger requirements of the Brayton cycle power conversion system.

The next step in the evolution of the full scale flightweight unit concept design was a study of receivers with heaters intended for laminar flow operation. This study and the resulting design are described in the next section.

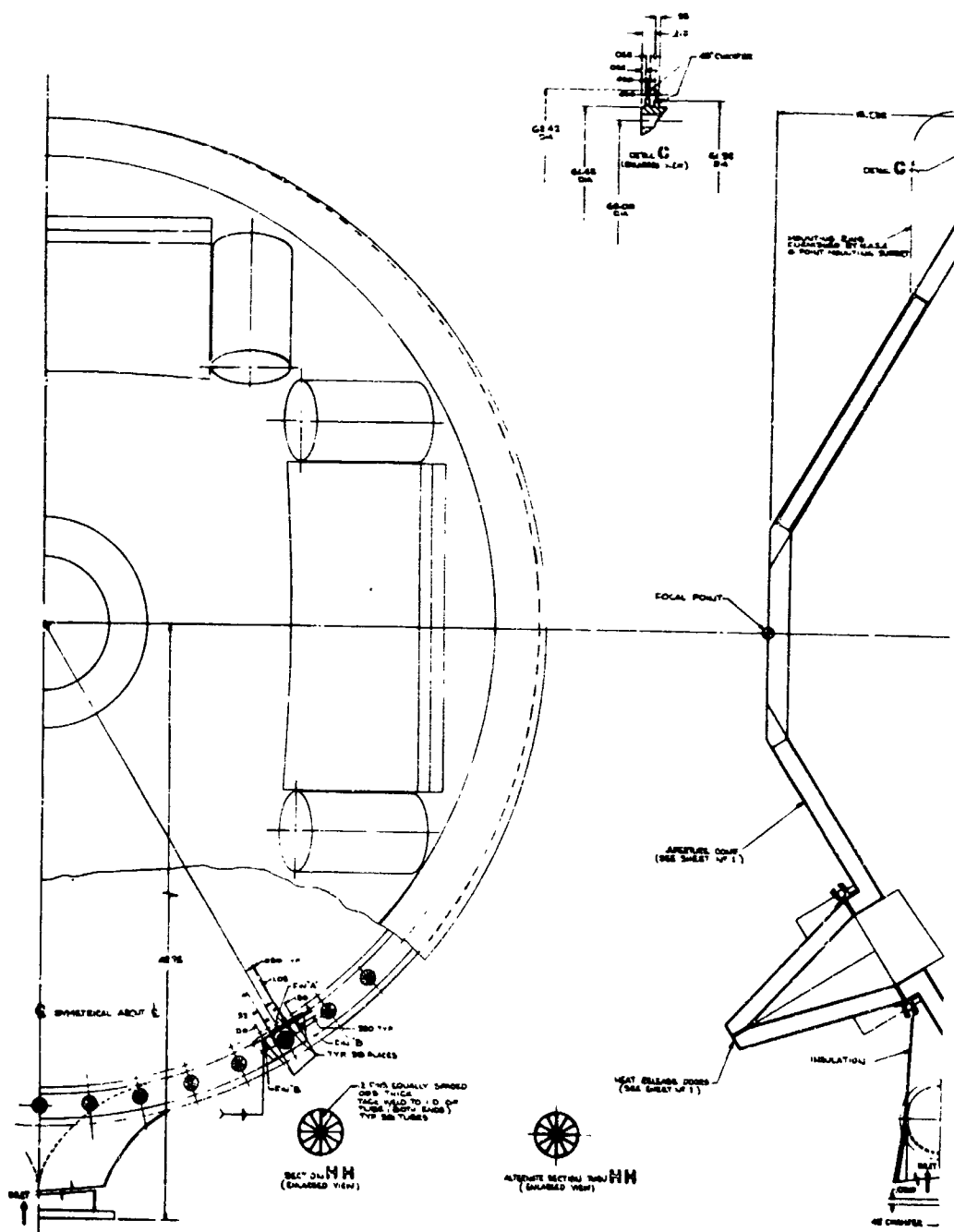
*Source: References 25 and 26.

5.3 Two Percent Gas Pressure Drop Design - Revised

The investigation of turbolators had indicated that turbulent flow operation with turbolators could not be obtained within the pressure drop limitation. Therefore, laminar flow operation, where the pressure drop per unit of heat transfer is less, was investigated. The possibility of not only turbolators but also internal fins was considered in the laminar flow case. A limited study of the potential for both turbolators and internal fins indicated that the advantage of the latter was far greater, and the investigation of designs with internal fins continued. Dr. Eckert and his associates at the University of Minnesota have published a number of papers on laminar flow in various shapes of ducts. References 27, 28, 29 and 30 are a few of the papers involved. The last reference above was considered the most suitable for the type of internal fins contemplated for this design. Two extreme conditions are noted therein, one in which the wall temperature is constant and the other in which the heat flux is constant. The conditions in the tube sector and two fins are not exactly constant wall temperature, but they are closer to constant wall temperature than to constant flux. This situation is fortunate, for the latter condition can exhibit an order of magnitude less heat transfer than the constant wall temperature case. The correlation for the constant wall temperature case was employed in the design optimization procedure. This approach can be justified on the basis of the low temperature drop in the fins caused by the low gas heat transfer coefficients.

The design concept evolved for the two percent allowable argon pressure drop is illustrated in Figure 60. This concept features the same cavity and receiver diameters as the turbulent flow design in Figure 58. The inlet and outlet header designs are also similar. The major characteristic dimensions for this receiver design are listed below:

Tube Number	58
Tube Inner Diameter	1.07 inches
Type of Tube Fin	Grade "A" Nickel, .005-in. thick
Number of Fins	12
Fin Thickness	0.005 inch
Tube Length	36.0 inches
Cavity Diameter	58.6 inches
Receiver Outer Diameter (including insulation)	62.4 inches
Reynolds Number	1000



[illegible]

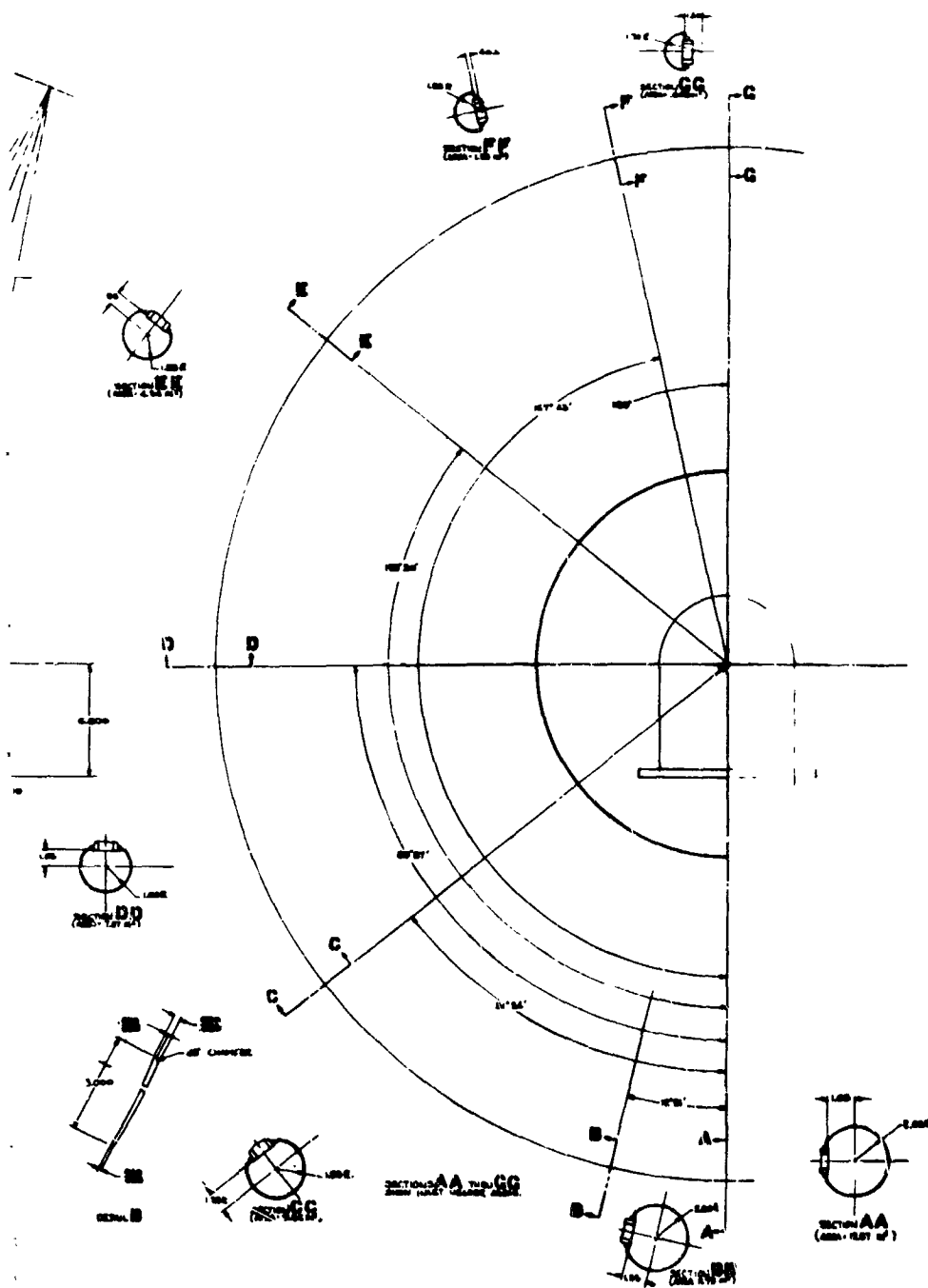


FIGURE 60

BLANK PAGE

It should be noted that the tubes are meridional in this design and do not require a compound bend. The cavity diameter could be reduced from its basic five foot bolt circle dimension to a basic four foot dimension if the cavity wall temperature levels would permit. The results of the Module D and E tests indicate that fins attached to the cavity wall are required and that the basic five foot dimension is needed to keep the flux and temperature levels low. If a four foot cavity were possible, an improved storage bath design package could be obtained and the collector shadowing reduced.

The weight estimate for the laminar flow design is shown in the following summary.

Item	Alloy	Weight lb	Volume in ³	Dimension in.
Lithium Fluoride		194		
Inner Shell Assembly				
Shell	H-25	98.08	297.21	OD - 58.70 T - .055
External Fins	Nickel	39.00	121.5	
Outer Shell Assembly				
Shell	H-25	99.5	302	ID - 61.32 T - .055
Baffles	H-25	11.05	33.54	
Tube Assembly				
Tubes	H-25	35.20	106.5	ID - 1.07 L - 36 Wall - .020
Internal Fins	Nickel	43.20	134.5	
Inlet Header Assembly	H-25	73.71	223.60	
Outlet Header Assembly	H-25	42.62	128.99	
Aperture Cone Assembly				
Aperture	Inconel X	5.6	18.73	
Inner Cone	Nickel	34.9	125.50	
Outer Cone	316 SS	16.6	57.20	
Louvers	Inconel & 316 SS	47.68	47.69	
Ring	Inconel X	7.59	25.30	
Support Structure	316 SS	10.35	35.70	
Actuating Mechanism	--	80.62	--	
Insulation (Outer Shell & Outlet Header)	Linde SIV	30.6	3127.50	T = .50
Insulation (Cone & Louvers)	Linde SIV	52.58	5287.34	
Insulation Covers	316 SS	41.78	143.98	T = .020
TOTAL		964.66		

5.4 Summary of Receiver Designs

Table IX presents a summary of the various receiver designs examined in this program. The initial group of designs featured four percent allowable gas pressure drop, with approximately one-half of the total allowed taken in the heater tubes. The remaining pressure drop was required for the inlet and outlet manifolds. The design evolved for this condition to be employed in a 300 nautical mile earth orbit in combination with a rigid 30-foot diameter solar concentrator is the third design listed. It specified 50 tubes 0.724-in. OD x .020-in. wall x 69.6 in. long. The annulus for this design was 1.40-in. with a cavity diameter of 51.0 in.

Later studies showed that the cavity diameter must be greater than the 51 in. specified. The later studies concentrated on an allowable gas pressure drop of two percent. The reduced pressure drop permitted in the heater tubes results in designs that were to operate at gas Reynolds numbers just slightly larger than 4000 which can be considered as the start of the turbulent region. The effects of tube curvature in stabilizing the gas flow and use of recent turbulent heat transfer correlations in the design analysis indicated that the turbulent flow designs were marginal even with the insertion of turbulators. At the very end of the design study, a switch was made to a design based on laminar flow with internal fins within the tubes. The design evolved in this last minute effort specified 58 tubes 1.11-in. OD x 0.020-in. wall x 36.0 in. long with twelve internal, continuous fins 0.005-in. thick. The cavity diameter for this design is 58.7 in.

The fins should be fabricated from Grade "A" nickel to achieve the conductivity required. All structural parts of the receiver exposed to lithium fluoride should be fabricated with Haynes alloy 25 or its equivalent, L-605. This recommendation is based on the results of the material corrosion investigation reported in TRW ER-6561.

TABLE IX
SUMMARY OF RECEIVER DESIGNS ATTEMPTED WITH PERTINENT NOTES

Pressure Drop Design %	No. of Tubes	I. D. of Tube inches	Tube Wall Thickness inches	Tube Length inches	O. D. of Receiver inches	I. D. of Receiver inches	Annular Thickness Receiver inches	Remarks
4	130	0.422	0.020	130	60.0	57.36	1.32	Initial design attempt (p. 18) 130 tubes undesirable because of manufacturing problems and long term reliability of joints
4	10	1.38	0.020	186.0	55.2	52.2	1.50	Non-manifold design.
4	50	0.684	0.020	69.6	53.8	51.0	1.40	For 30 ft dia. collector and 300 n.m. orbit, tubes bent in complex configuration to achieve the desired heat transfer as based on Boelter Equation.
4	70	0.597	0.020	50.16	46.74	45.0	0.872	For 20 ft dia. collector and 300 n.m. orbit.
4	30	0.910	0.020	90.36	53.48	49.44	2.02	For 20 ft dia. collector and synchronous orbit.
4	30	0.910	0.020	103.68	67.08	62.04	2.52	For 30 ft dia. collector and synchronous orbit.
2	70	0.693	0.020	69.5	57.40	54.0	1.70	Possible (p. 60) transitional flow at Re. 5500, some uncertainty in design.
2	30	1.05	0.020	118.3	61.3	58.7	1.30	Mean Reynolds Number at 8100.
2	20	1.29	0.020	143.8	61.57	58.43	1.57	Mean Reynolds Number at 10,000.
2.45	30	1.13	0.020	191.0	77.14	74.40	1.37	Use of NACA 1020 correlation.
2	30	1.05	0.020	104.0	61.3	58.7	1.3	Helium-Xenon Mixture.
2	58	1.07	0.020	36.0	62.4*	58.7*	1.30	Laminar flow at Re 880 - 12 fins of .005 in. "A" Ni in each tube (p. 70).

*Drawings for shell fabrication have following dimensions.

I. D. of outer shell = 30.660 R = 61.32 in. with .05 in. shell wall thickness, O. D. of outer shell = 61.42 in.

O. D. of inner shell = 29.35 R = 58.70 in. with .05 in. shell wall thickness; I. D. of inner shell = 58.60 in.

6.0 CAVITY TEMPERATURE DISTRIBUTION

The object of the cavity temperature distribution analysis for a 2% design was to apply the latest analytical tools available to calculate the cavity temperature distribution. The techniques employed had been demonstrated on the Sunflower program earlier and reported in Reference 1. Since that time, more advanced techniques have become available, particularly in the area of the calculation of the incident flux on the cavity wall. The analysis may be broken into five elements:

1. Incident flux distributions
2. Cavity radiation solutions
3. Lithium fluoride resistance determinations
4. Program integration
5. Shade time calculations
6. Sun time results.

6.1 Incident Flux Distributions

In the Sunflower program, the incident flux was determined by a laborious hand calculation using an adaptation of the Hukuo-Mii method, Reference 30. The incident flux was obtained in this manner for the proposed cavity, and it was extended to the revised cavity based on Lambert's Cosine Law. Recently, two important computer programs have been made available by the Air Force via Aerospace Corporation. These programs are designated I-74A and I-74B. The calculation with the I-74A program obtains the flux distribution on the focal plane and any parallel plane in front or in back of the focal plane. Calculations with the I-74B program produce the incident flux distribution on any arbitrary surface behind the focal plane. The program includes provisions for the effect of "vignetting" which is the blockage exhibited by a fixed aperture.

Incident flux distributions were obtained with the I-74B program for perfect collector orientation to the sun and for two levels of misorientation, $1/4$ and $1/2$ degrees. The results obtained are shown in Figures 61, 62 and 63 for zero, $1/4$ and $1/2$ degree misorientation, respectively. The abscissa in these figures is cosine θ where θ is the angle formed by a line drawn from the point on the surface to the center of the cavity and a line representing the collector-cavity optic axis. The collector characteristics employed in these calculations were taken from the results of the Brayton cycle collector design study reported in Reference 12. The aperture was sized to afford optimum conditions for the $1/4$ degree misorientation case. The collector characteristics are listed below:

RADIAL VARIATION IN SOLAR INCIDENT FLUX WITH COLLECTOR PERFECTLY ORIENTED

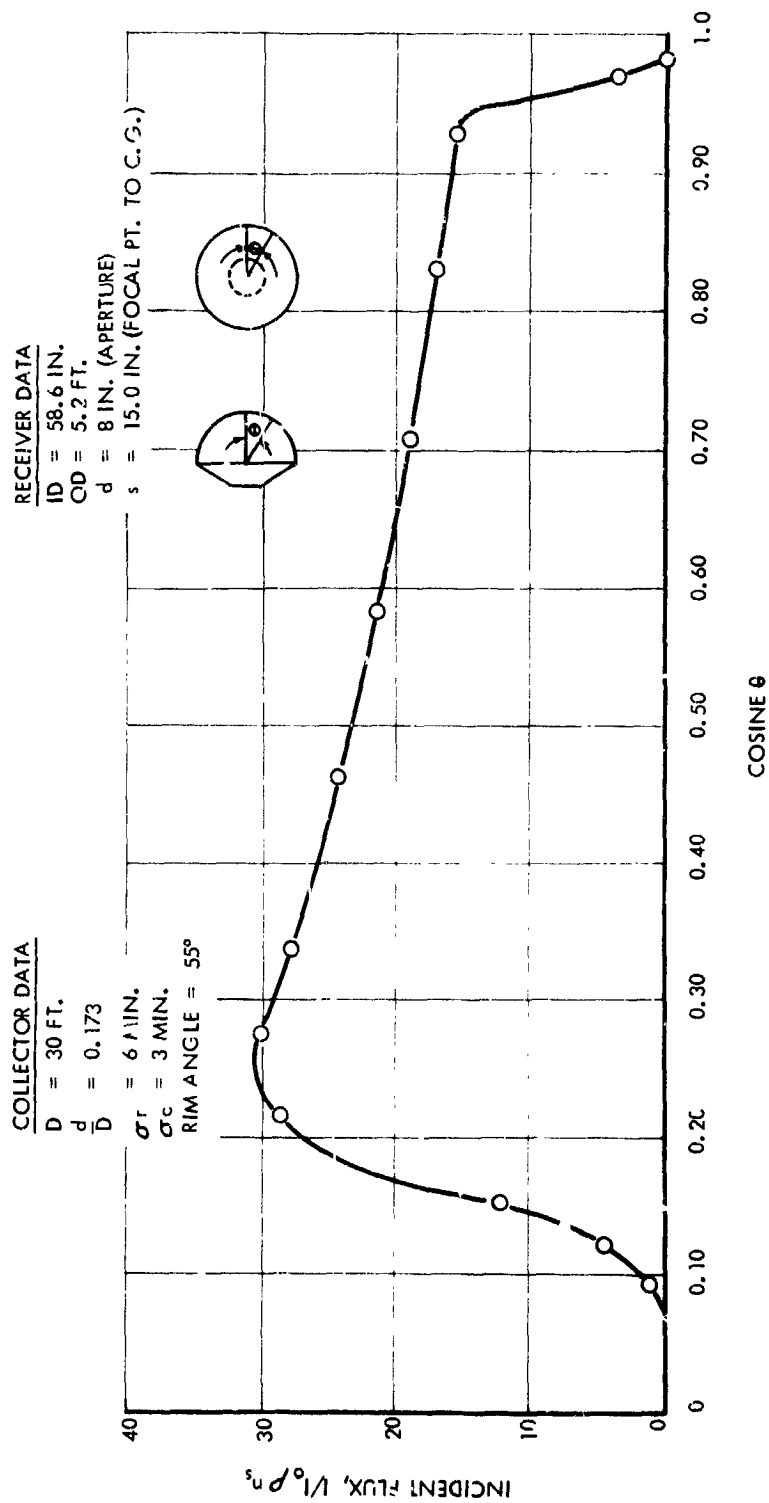


FIGURE 61

RADIAL AND CIRCUMFERENTIAL VARIATION IN CAVITY INCIDENT FLUX
WITH COLLECTOR MISORIENTED 1/4 DEGREE IN DIRECTION OF MAJOR AXIS

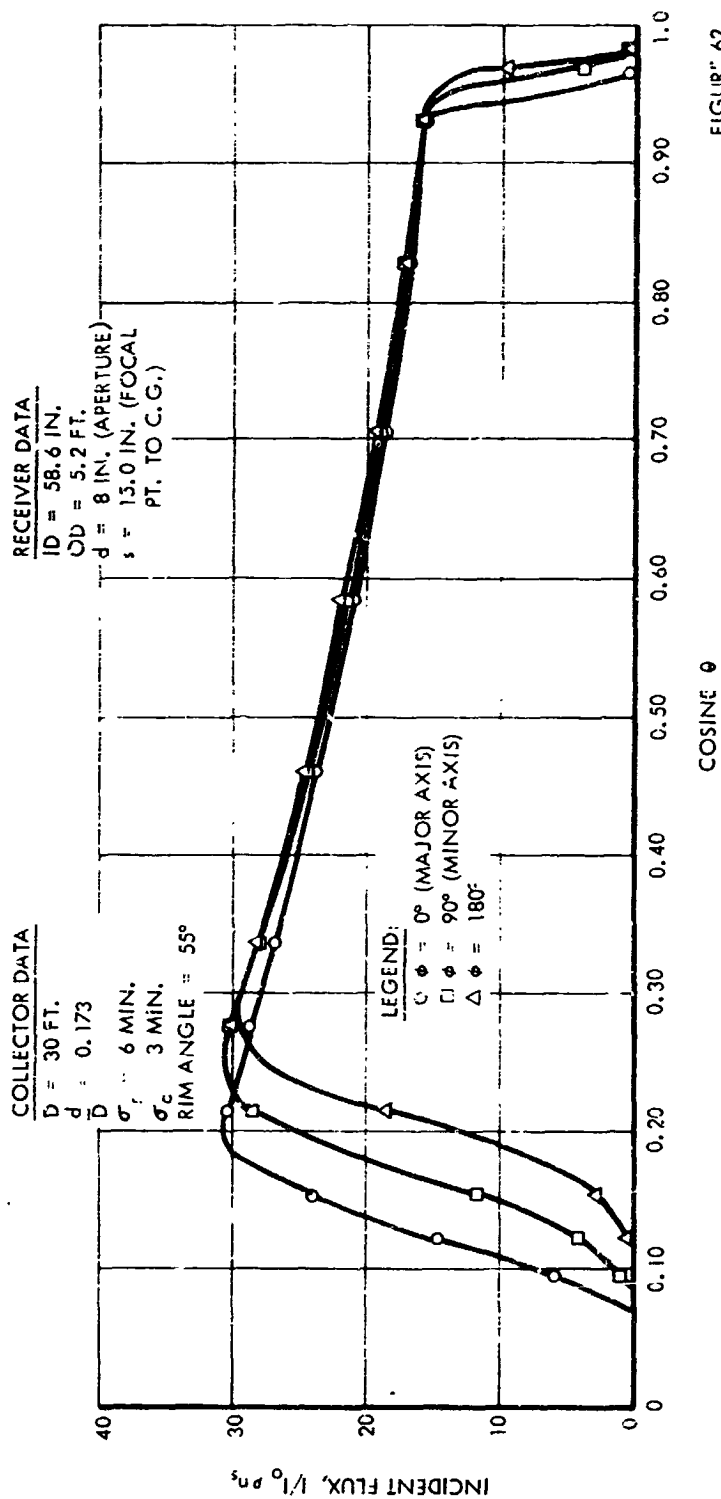


FIGURE 62

RADIAL AND CIRCUMFERENTIAL VARIATION IN CAVITY INCIDENT FLUX
WITH COLLECTOR MISORIENTED 1/2 DEGREE IN DIRECTION OF MAJOR AXIS

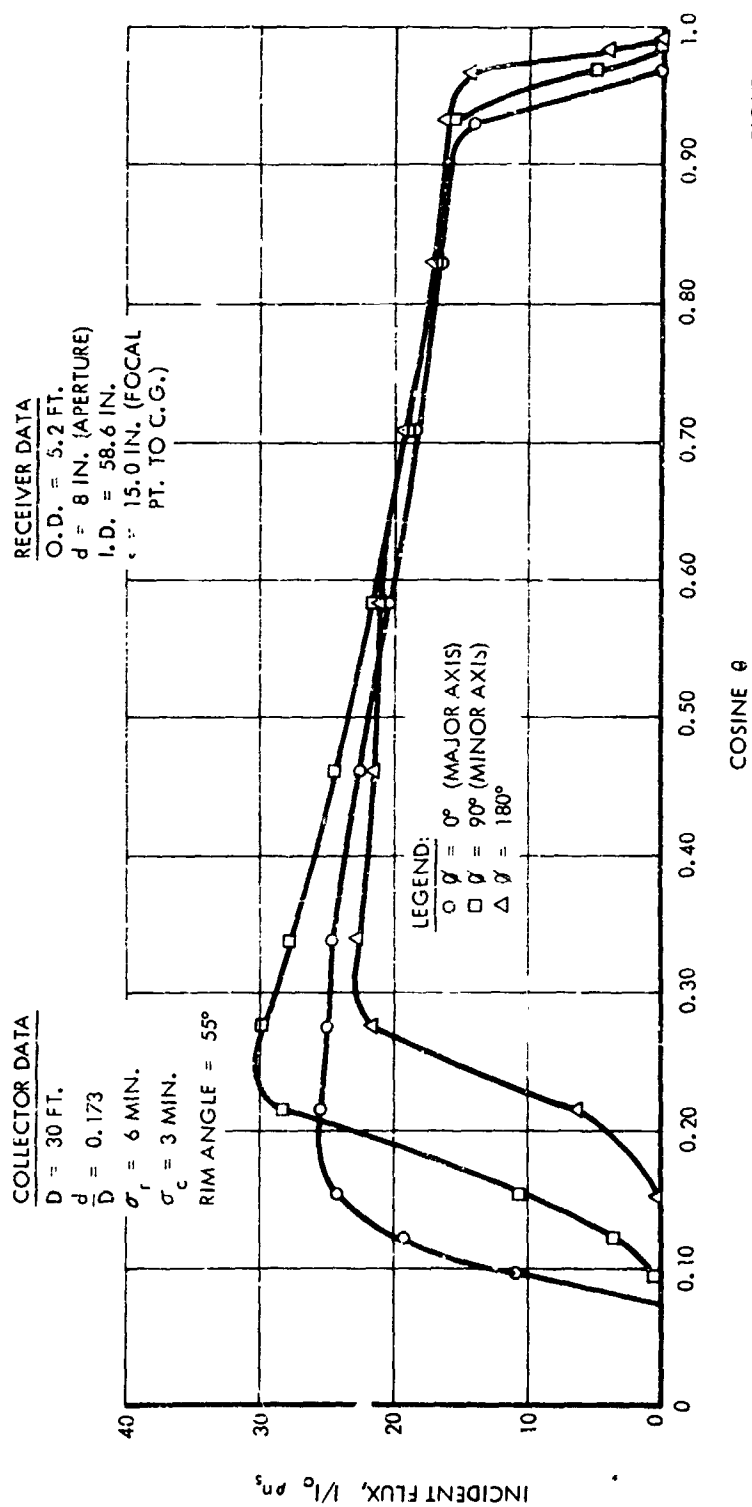


FIGURE 63

Diameter	30 Feet
Rim Angle	55 degrees
Focal Length	172.89 inches
Surface Error, Radial	6 minutes
Surface Error, Circumferential	3 minutes
Center Shadow (Receiver O.D.)	5.2 feet
Reflectivity	90 percent

The total energy into the cavity and the local flux levels were determined for a system structural blockage of 6 percent. This blockage is in addition to the receiver shadowing. Later estimates by NASA may show that a total blockage of 6 percent for the structure plus 3 percent for the receiver is greater than the system needs. In that case, both the total energy and the local flux would increase since the computer program results are listed as $I/I_0 \rho n_s$ where I is the incident flux, I_0 is the solar constant, ρ is the collector reflectivity and n_s is one minus the fractional structural blockage, or 0.94 in this case. The value of the above ratio is set by the computer program results, but it is apparent that an increase in the denominator will increase the numerator also.

An analysis of the flux distribution shown in Figures 61, 62 and 63 was conducted to achieve a physical understanding of the results. The incident flux distribution for the perfectly oriented case, Figure 61, was as anticipated. In the case of the 1/4 degree misorientation, Figure 62, radial slices were taken on both halves of the major axis in the direction of misorientation and on one half of the minor axis. The flux distribution was known to be symmetric about the major axis. It can be observed from Figure 62 that the incident flux over most of the cavity surface is almost independent of the direction of the radial slice. It is only at the open end (low values of cosine θ) and at the dome end where significant differences occur. Study of this result led to a modification of the computer program for this case. The modification simplified the cavity portion of the program by reducing it to a symmetrical flux distribution as in the perfectly oriented case.

Examination of Figure 63 revealed another result which had not been fully anticipated. It can be observed from Figure 63 that the radial flux distributions for the two halves of the major axis are significantly lower than that for the minor axis. In Figure 62 the major axis distribution achieved the highest energy level as expected. Thus, the question about the Figure 63 immediately arose as to what had caused this apparent change. It was postulated that the shift was caused by the fixed aperture. Further, a cavity with a larger fixed aperture would exhibit a more normal flux distribution similar to Figure 62. A computer run was made for the 1/2 degree misorientation case with a 10-inch fixed aperture.

The results of this run are shown in Figure 64. It can be observed from Figure 64 that the peak levels for the major axis distributions are higher than in Figure 63 and are more nearly normal, or what would be expected. These results illustrate clearly the fact that orientation errors greater than the aperture design value should be avoided. Not only is the energy level within the cavity reduced under the conditions of Figure 63, but considerable energy is directed on the outside of the aperture cone where provisions for heat dissipation must be made.

6.2 Cavity Radiation Solutions

The cavity radiation flux and the resultant surface temperature distribution were solved based on the method presented in Reference 15. The decision to employ this method rather than that of Reference 1 was based on the ability to adapt the approach of Reference 15 more readily to the cases of misorientation. In Reference 15, the temperature distribution was assumed and the resultant flux calculated. In this case, however, neither the temperature distribution nor the radiant flux can be assumed. In addition, the heat absorbed by the wall and transferred to the fluoride must be evaluated. (The fluoride resistance to heat flow is a variable and is described in Section 6.3.2.) Thus, the surface temperatures can be expected to be variable and the distribution could change also.

Another term was added to the cavity flux equations presented in Reference 15 to account for the heat transferred from the wall to the fluoride. This term had the form of

$$\frac{-k_1 \Delta l}{R_{w-m}} [T(x) - T_m]$$

Thus, the unknowns in the equation are the surface temperature, $T(x)$, and the flux, $v(x)$.

The details of the equations and the calculation procedure are presented in the Appendix, Section 8.10.

6.3 Lithium Fluoride Resistance Determinations

The basic analog technique employed to determine the lithium fluoride resistance during shade time operations was postulated and confirmed on the Sunflower program, Reference 1. The method to be employed in the case of simultaneous heat addition and extraction, representing the sun time operations, was defined on the Sunflower program but was not reported. In the current program, the analog techniques were extended in the case of simultaneous heat addition and extraction. Each of these two areas are described in turn below.

6.3.1 Fluoride Resistance During Freezing

The analytical procedure employed to obtain the fluoride resistance during freezing has been presented in Section 4.3.1. To summarize the procedure, a series of electric analogs

VARIATION OF CAVITY INCIDENT FLUX IN RADIAL AND CIRCUMFERENTIAL DIRECTIONS WITH COLLECTOR MISORIENTED 1/2 DEGREE ALONG CAVITY MAJOR AXIS

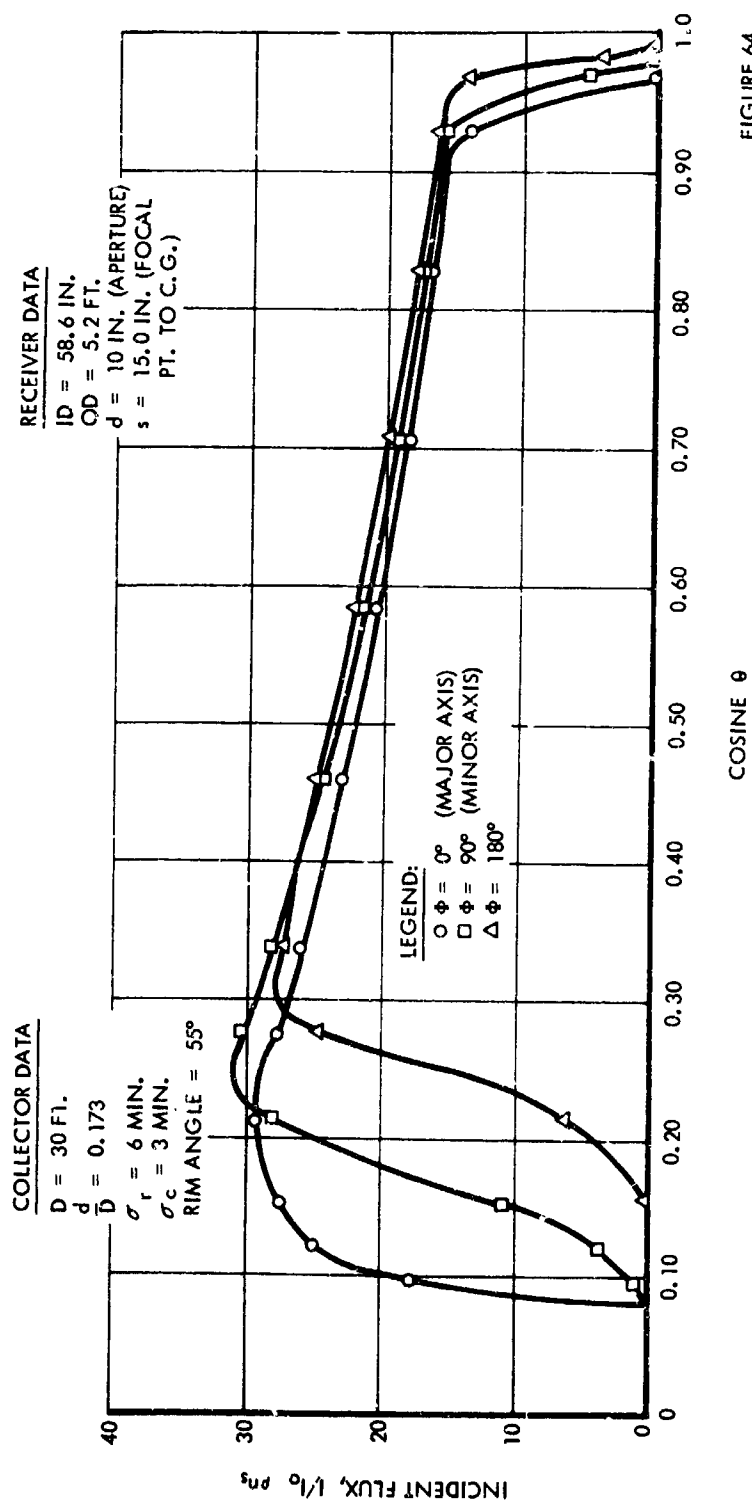


FIGURE 64

are constructed in which the physical model is reproduced on "Teledeltos" electrical conducting papers. A voltage potential is applied between the source and sink, and lines of constant potential, corresponding to isotherms, can be identified. With knowledge of location of an isotherm relative to the melt line, the position of the melt line at some later time can be determined because it can be shown that the distance which the melt line moves is inversely proportional to the local distance from the melt line to the isotherm.

Several melt line positions were determined as illustrated in Figures 41 and 65. At each melt line position, the electrical resistance from the melt line to the tube wall and the amount of lithium fluoride frozen were measured. The electrical resistance can be readily converted to a geometrical resistance factor. The results are shown in Figure 43.

The final freeze pattern and lithium fluoride volume distribution of solid and liquid provide the starting point for the electric analog simulation of heat addition through the inner shell, corresponding to the sun portion of the orbit.

The procedure for determining the resistance during melting is presented next.

6.3.2 Fluoride Resistance During Melting

The basic procedure for each of the electric analogs representing the melting process is essentially the same as that during freezing in that isotherms are located in both the liquid and the solid. These isotherms are taken as close as possible to the melt line to improve the accuracy. Again, the local movement of the melt line is inversely proportional to the local distance between the melt line and the isotherm. As shown in Appendix B of Reference 1, the local distance, Δ , is proportional to

$$\left[\frac{q_L}{q_S} \quad \frac{1}{\delta_L} - \frac{1}{\delta_S} \right]$$

where q_L/q_S is the ratio of the heat flow through the liquid to the heat flow through the solid and δ_L and δ_S are the local distances between the melt line and the liquid isotherm and the melt line and the solid isotherm, respectively. The heat ratio is a variable, of course, and is equivalent to

$$\frac{k_L}{k_S} \frac{\Delta T_L}{\Delta T_S}$$

Since the thermal conductivity in the liquid and the solid are known constants, the variability enters in the temperature difference ratio. The temperature difference in each instance is between the melt line and the isotherm.

A series of analogs was constructed to determine the melt line motion with sun time at each of two tube locations. It was hoped to perform this simulation at additional tube locations, but time and funding restrictions prevented this.

ADDITIONAL MELT LINE PATTERN

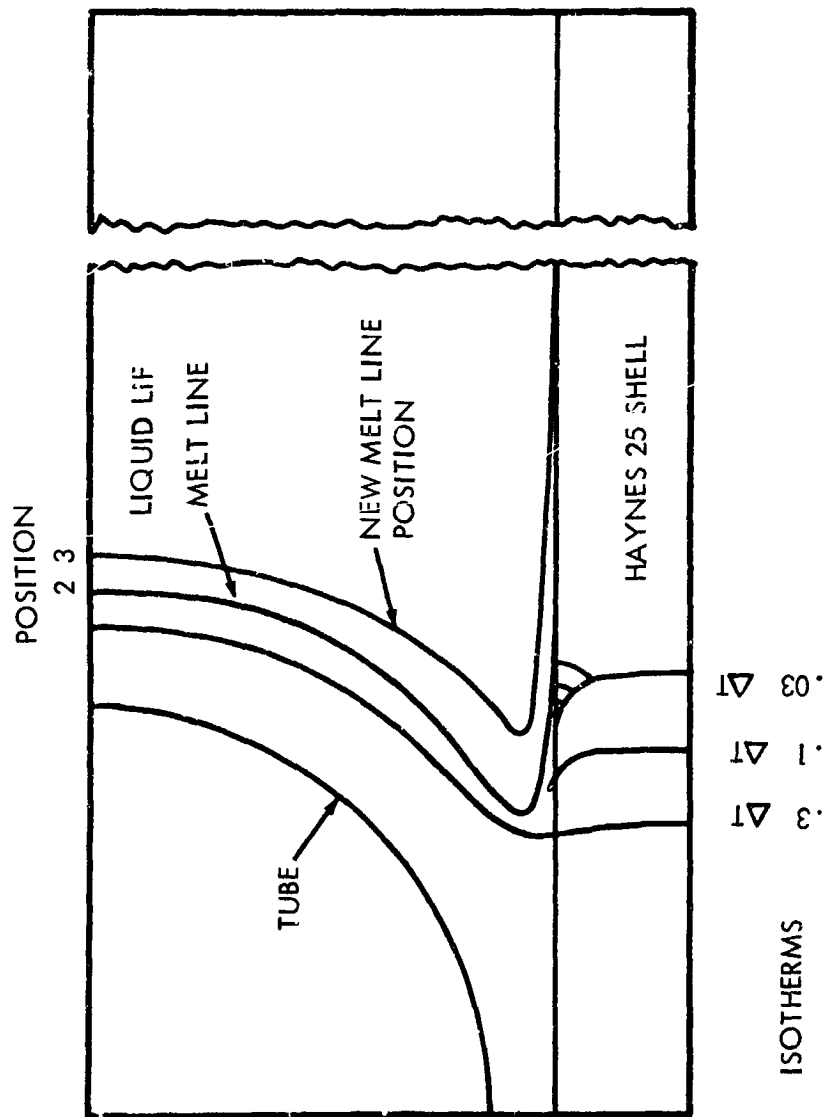


FIGURE 65

The melt line motions obtained on the analogs indicated that the melt line approaches the tube rapidly. As the melt line touches the tube, the simulation discussed above breaks down because the local distance between the melt line and the tube, which is an isotherm, is zero. Therefore, a new technique was required.

The new technique is based on the fact that the local gas temperature within the tube is much lower than the melt line temperature. Thus, even though a section of the tube wall reaches the melt line temperature and the lithium fluoride solid resistance is zero, the gas film resistance is still effective and controls the rate of heat transfer at the local tube section. The modified procedure consists of establishing a potential difference between the cavity surface and a lower level representing the gas temperature as illustrated in Figure 66. Electrical resistances representing the gas film resistance are inserted as shown. Thus, the voltage differential between the cavity wall and the tube is proportional to the temperature difference. Similarly, by inserting the resistance r , the voltage difference between the cavity wall and the melt line becomes proportional to the actual temperature differential. With a potentiometer and a microammeter, lines of constant potential can be located in the liquid and solid regions. Once the equal potential lines have been defined, the local movement of the melt line was obtained by methods similar to the determination of the resistance during freezing.

The results obtained for the two tube sections are shown in Figures 67 and 68. Figure 67 gives the variation of the wall-to-melt line geometrical resistance factor with the amount of lithium fluoride melted. Figure 69 presents the similar variation for the melt line-to-tube resistance factor.

6.4 Computer Program Integration

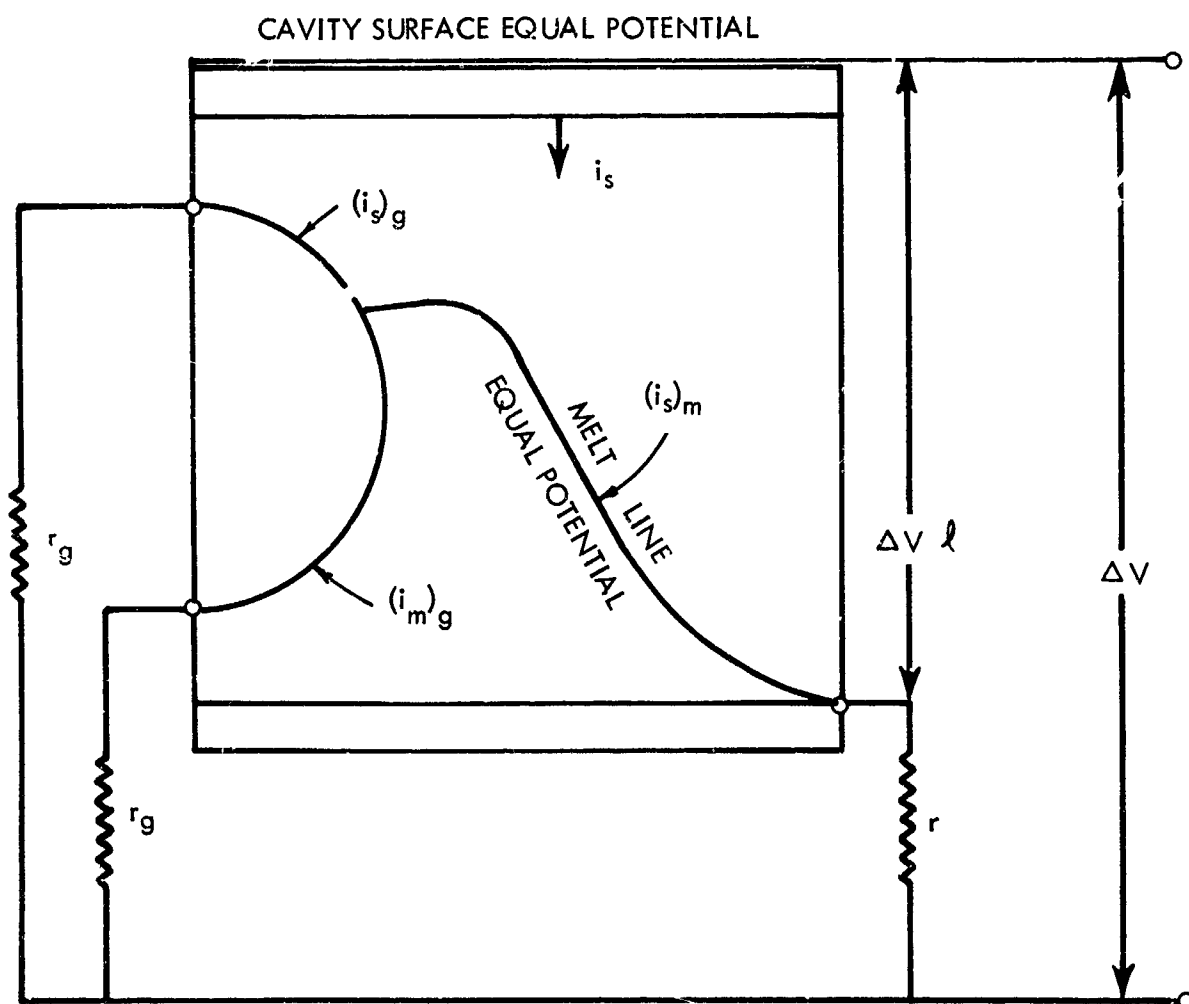
The computer program written for the cavity temperature distribution calculations considers the problem in three major parts:

1. Cavity surface to melt line
2. Melt line to gas
3. Time dependency

6.4.1 Cavity Surface to Melt Line Heat Transfer

The basic governing equations for this part of the program are described in Section 6.2. The surface temperatures and the flux levels are determined for twenty-one sections on the cavity surface corresponding to definite sections along the tube. Several sections on the aperture cone and in the dome are included in the cavity calculations. The fluoride resistance from the cavity wall to the melt line is determined from Figure 68. Printed results from this part of the program include the cavity surface temperature and the net flux into the fluoride for each section.

ELECTRIC ANALOG SIMULATION HEAT ADDITION



VARIATION OF WALL-TO-MELT LINE GEOMETRICAL RESISTANCE FACTOR
WITH AMOUNT OF FLUORIDE MELTED

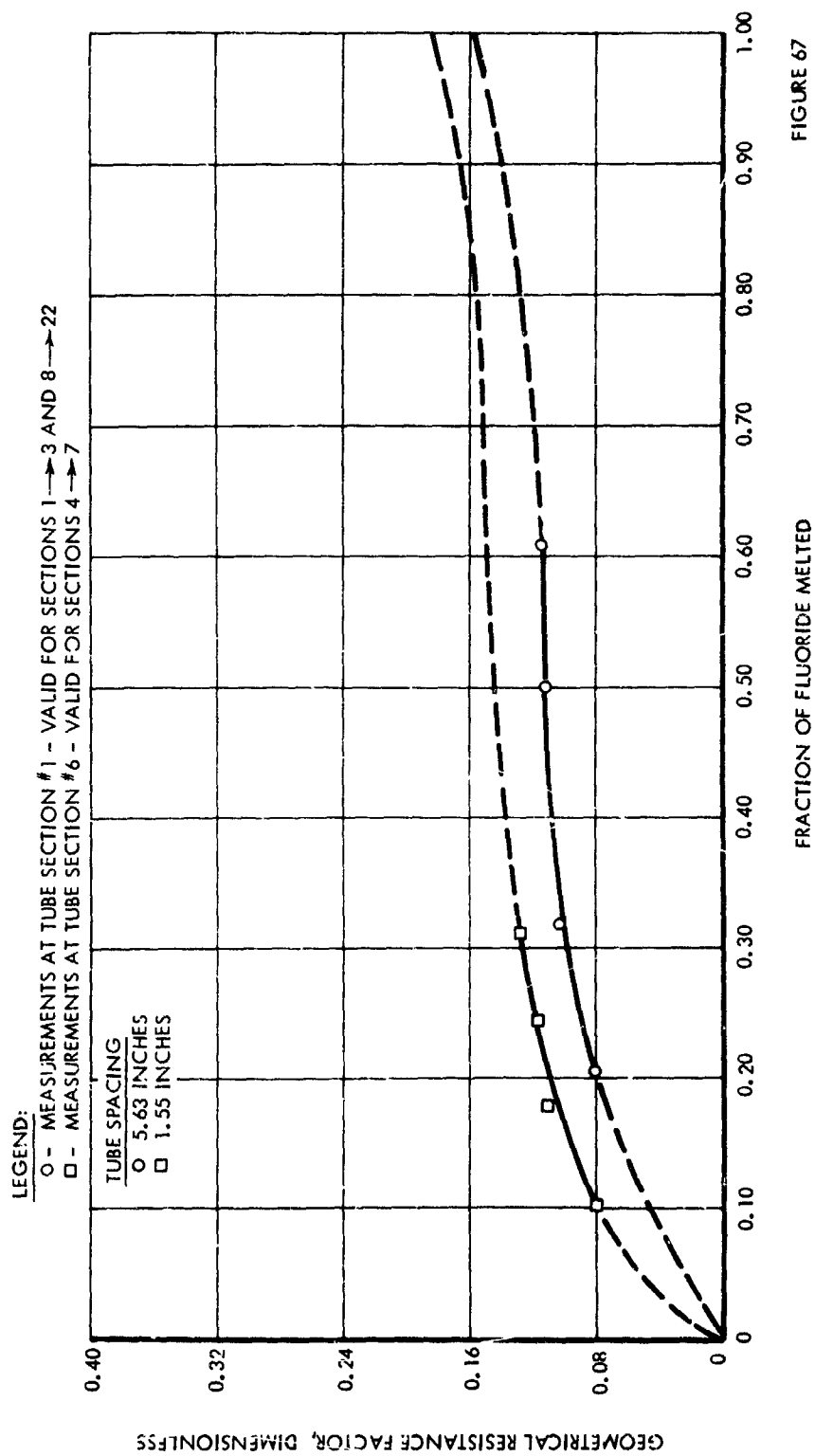


FIGURE 67

VARIATION OF MELT LINE-TO-TUBE GEOMETRICAL RESISTANCE FACTOR
WITH AMOUNT OF FLUORIDE MELTED

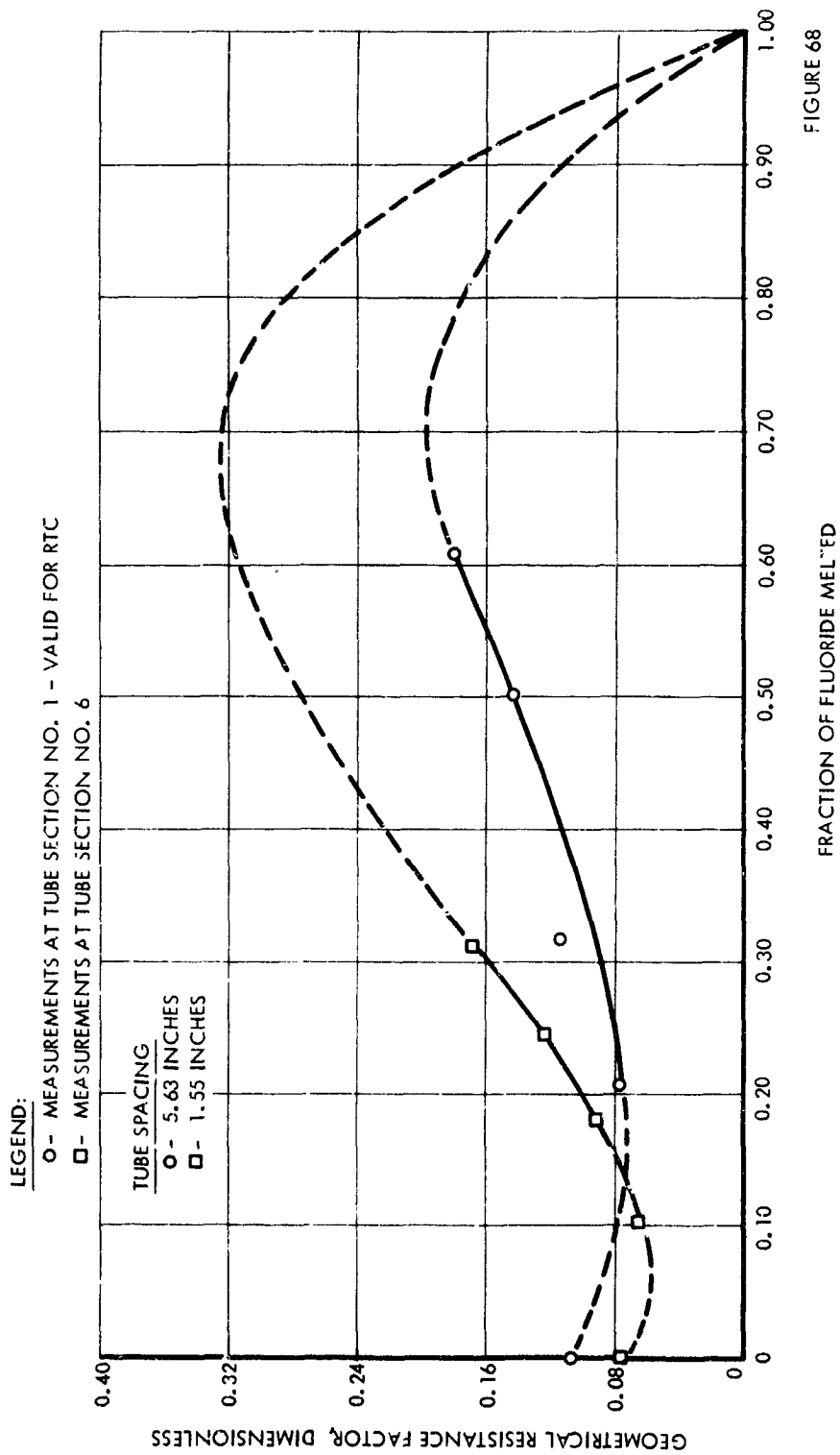
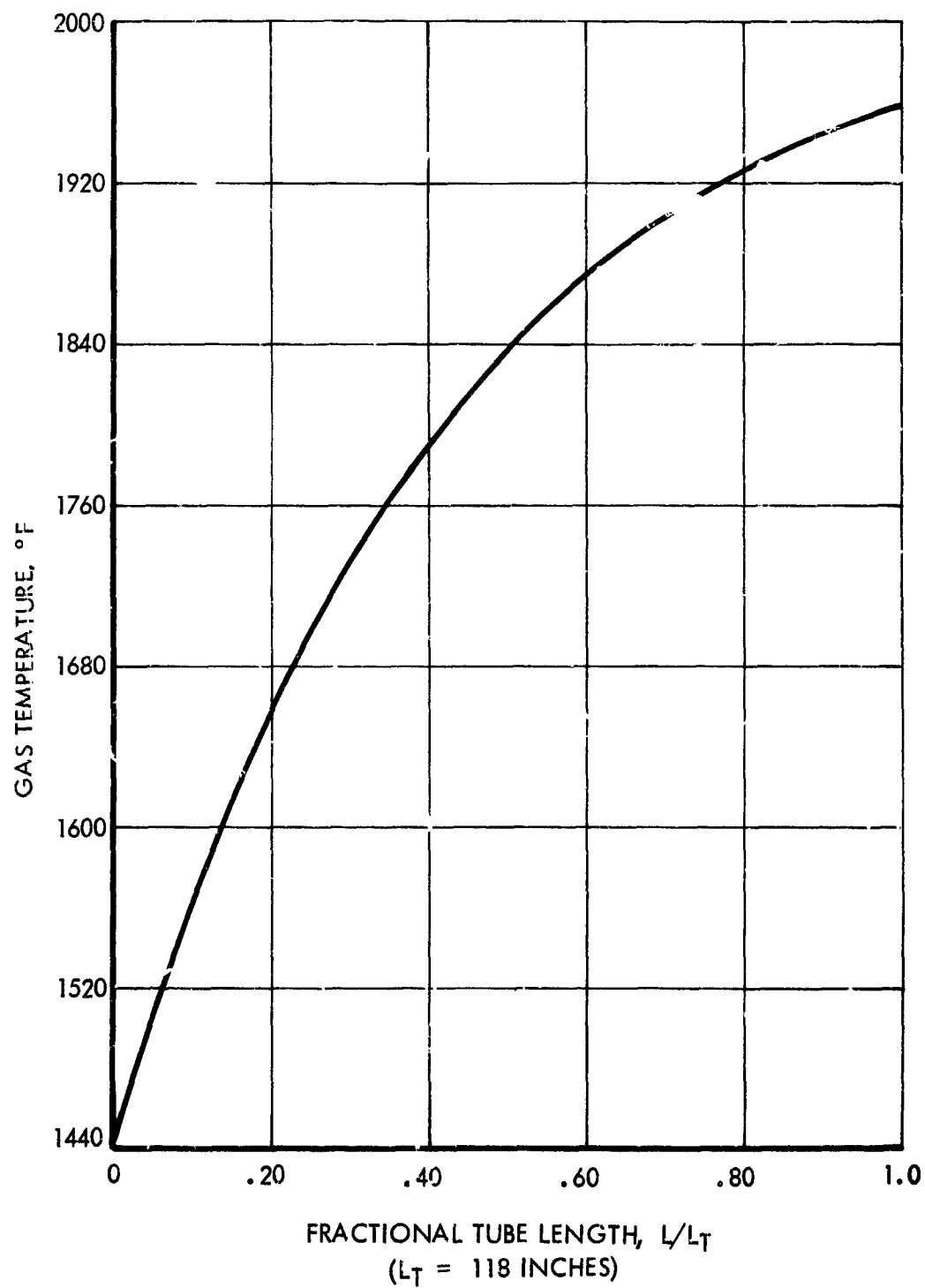


FIGURE 68

TYPICAL GAS TEMPERATURE VARIATION ALONG
HEATER TUBE DURING SHADE TIME OPERATION



6.4.2 Melt Line to Gas Heat Transfer

The second part of the computer program calculates the heat transfer from the melt line to the gas working fluid. The fluoride resistance is determined from Figure 68. Tube sections 4 through 7 employed the variation shown for section 6. Tube sections 1, 2, 3 and 8 through 22 employed the variation shown for tube section 1. For each section the level was determined by the starting value, which was the resistance at the end of the shade time. The fluoride thermal resistance is numerically equal to the geometrical resistance factor divided by the thermal conductivity of the solid.

The gas thermal resistance is the reciprocal of $\pi D h$. The heat transfer coefficient was calculated from the correlation taken from Reference 21 as described in Section 5.2. The sum of the two thermal resistances is taken as the total thermal resistance. The heat exchanger per unit of tube length is the temperature difference between the melt line and the gas divided by the total thermal resistance.

In the cases where the melt line touches part of the tube, the local heat transfer for that part of the tube is based on the gas thermal resistance only since the resistance of the solid fluoride is zero. The measurements for tube sections 1 and 6 indicated that the variation of the tube angle touched by the melt line increased with the amount of fluoride approximately linearly. Therefore, a linear variation was employed. For tube section 1, the melt line touched the tube at 15 percent melted. For tube section 6, the melt line touched the tube at 5 percent melted. In both cases, it was assumed that the melt line touched all of the tube at the all melted condition.

The gas pressure drop within the tube was determined with the Blasius friction factor discussed in Section 5.2 and the conventional equation

$$\Delta P = f \frac{L}{D} \frac{G^2}{\rho^2 g_c}$$

The gas density in the above equation was taken as the average for each tube section.

6.4.3 Time Dependency

The third part of the program keeps track of the amount of lithium fluoride melted at each tube section as sun time increases. The fluoride resistances are evaluated based on the amount of fluoride melted and are determined in this part of the program for the next temperature calculation. Thus, the calculation procedure determines quasi-steady-state temperature distributions for a series of time increments during the sun time. The procedure employed for the shade time portion of the orbit is discussed next.

6.5 Shade Time Calculations

The basic procedure utilized by a previous program written specifically for the shade time operating conditions is similar to that described in Section 6.4.2. In this case, losses through the outer shell wall and the cavity wall were assumed negligible. This assumption is considered valid for a cavity with an aperture closure device. In the future, it is intended to modify the program to properly reflect the cavity losses.

The fluoride resistance variation during shade time is based on Figure 43. Again, the fluoride resistance is numerically equal to the geometric resistance divided by the solid thermal conductivity. The total thermal resistance is the sum of the fluoride thermal resistance and the gas thermal resistance. The heat transfer per unit of tube length is the temperature difference between the melt line and the gas divided by the total thermal resistance.

The results obtained for the shade time are shown in Figures 69 and 70. Figure 69 gives the gas temperature variation along the tube with shade time, and Figure 70 gives a similar variation for the gas pressure.

One item of interest was noted in the results for the shade time calculations. The amount of lithium fluoride available for tube sections 4, 5, 6 and 7 was less than that required to operate for 36 minutes. (Refer to Table XII in Appendix.) If the 30-tube turbulent flow design was intended for fabrication, the annular spacing in the vicinity of these tube sections would be increased to provide space for the additional fluoride volume required. No changes were made since this design is not scheduled to be fabricated.

A typical heat flux variation with tube length during shade time is presented in Figure 71.

6.6 Sun Time Results

The solution for the solar flux distribution on the cavity surface produced results shown in Figure 72 for the perfectly oriented collector. The incident flux distribution from Figure 61 is also shown for comparison. It can be observed that the solar flux radiation distribution is generally at a lower level than the incident flux distribution.

A typical net flux distribution available for heat transfer into the storage bath is presented in Figure 73 for the perfectly oriented case. The incident flux distribution is again presented for comparison.

The influence of thermal emissivity of the cavity walls is illustrated by Figures 73, 74 and 75. Figure 73 has a wall thermal emissivity of 0.4. Figure 74 represents a wall emissivity of 0.6, and Figure 75 is for a wall emissivity of 0.2. While these graphs give flux results, the wall temperature variation follows the flux and is similar.

The wall temperature distribution corresponding to the flux distribution of Figure 73 is given in Figure 76.

TYPICAL VARIATION OF GAS PRESSURE ALONG HEATER
TUBE DURING SHADE TIME OPERATION

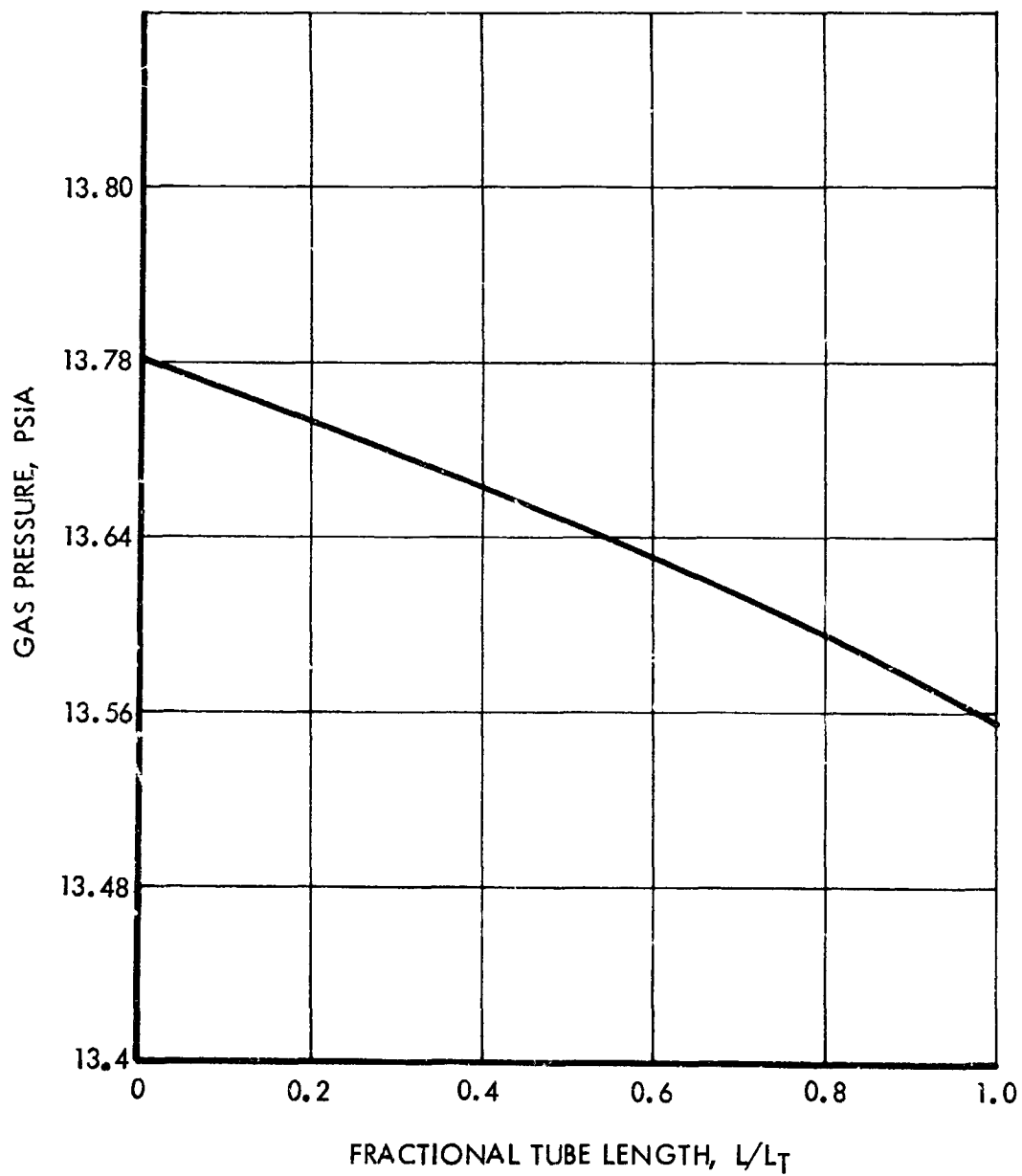


FIGURE 70

VARIATION OF HEATER TUBE FLUX ALONG TUBE DURING SHADE TIME

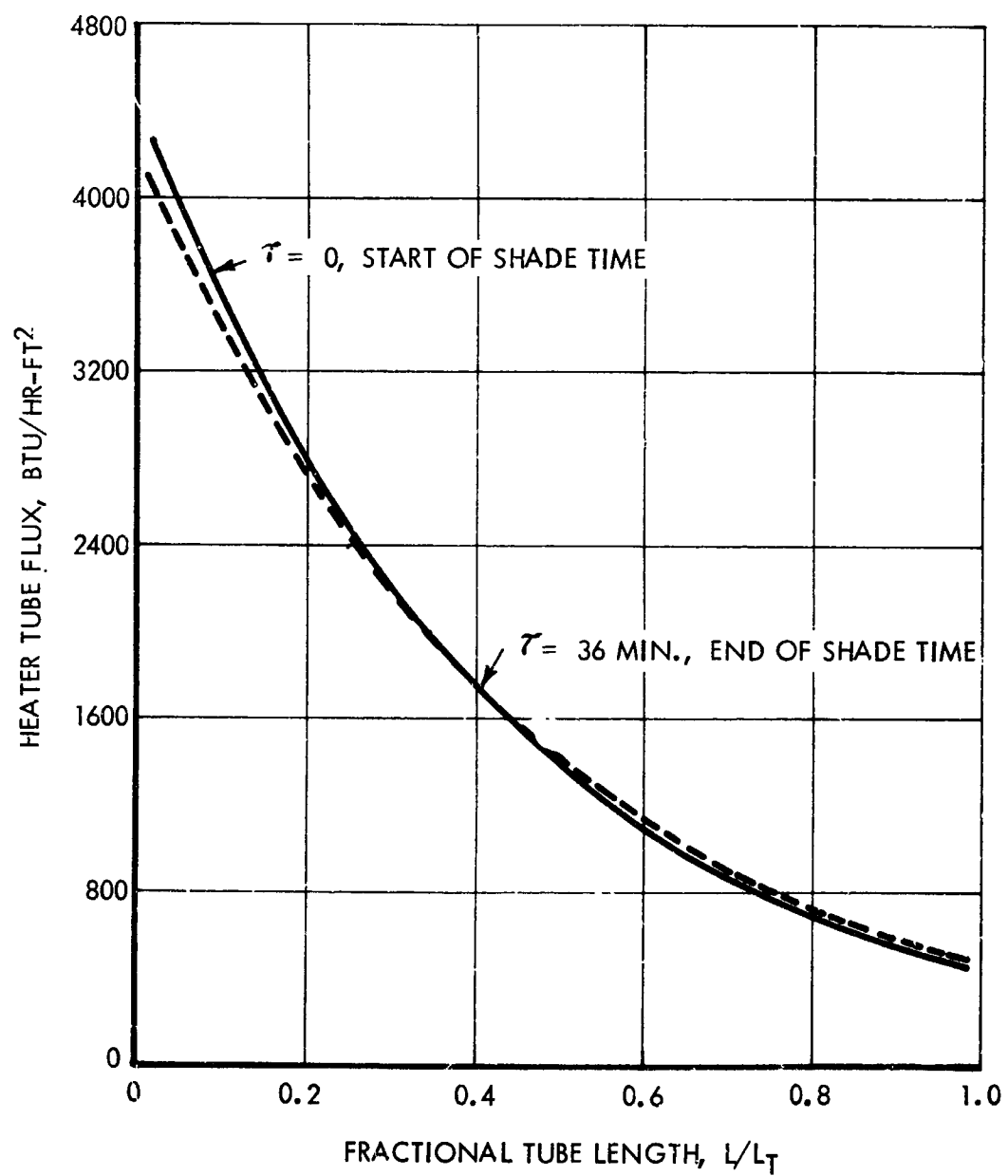
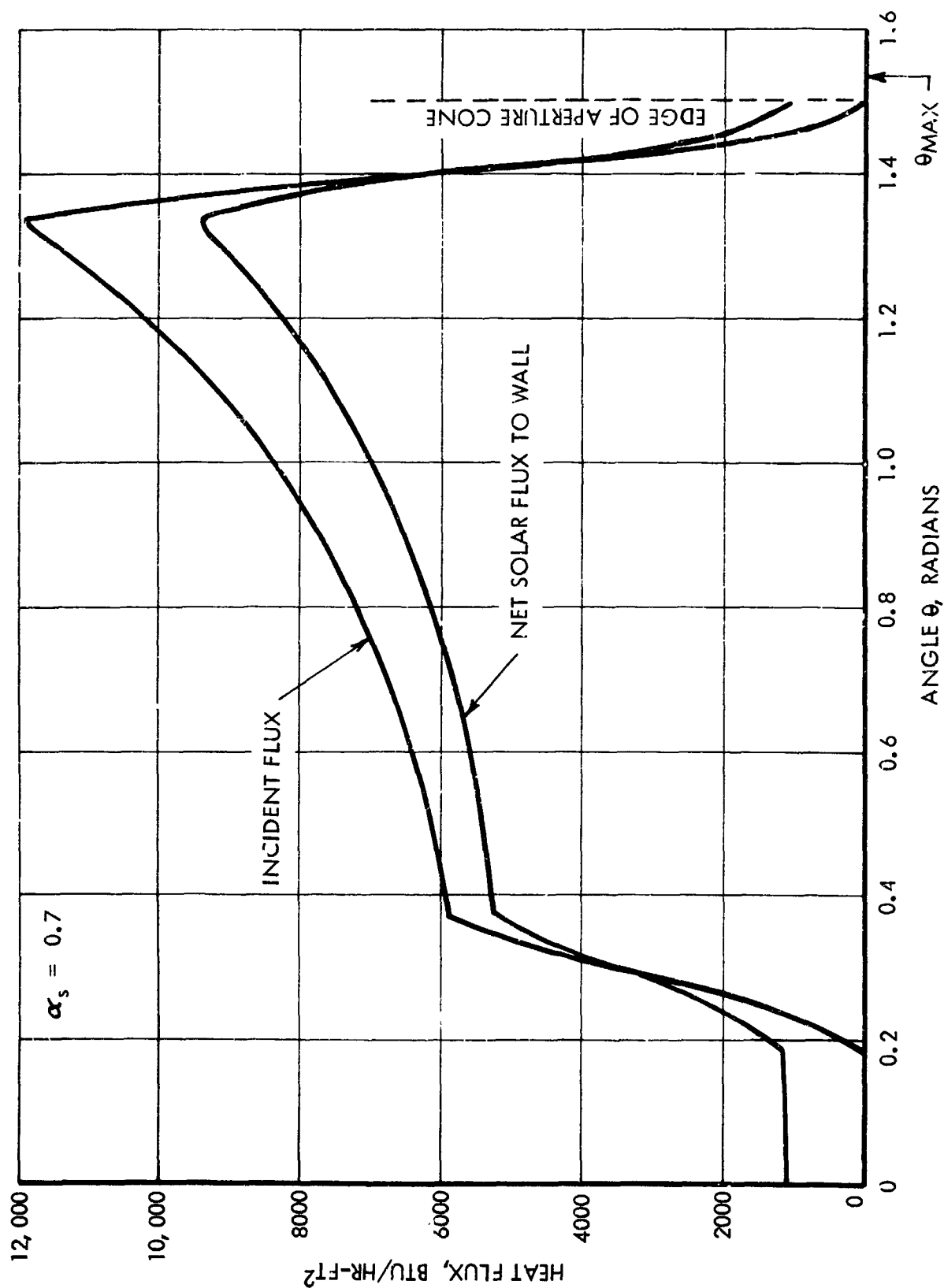


FIGURE 71

VARIATION OF SOLAR FLUX ON CAVITY WALL FOR PERFECTLY ORIENTED COLLECTOR ($\beta = 0^\circ$)



TYPICAL VARIATION OF TOTAL CAVITY WALL FLUX FOR THE PERFECTLY ORIENTED COLLECTOR ($\beta = 0^\circ$)

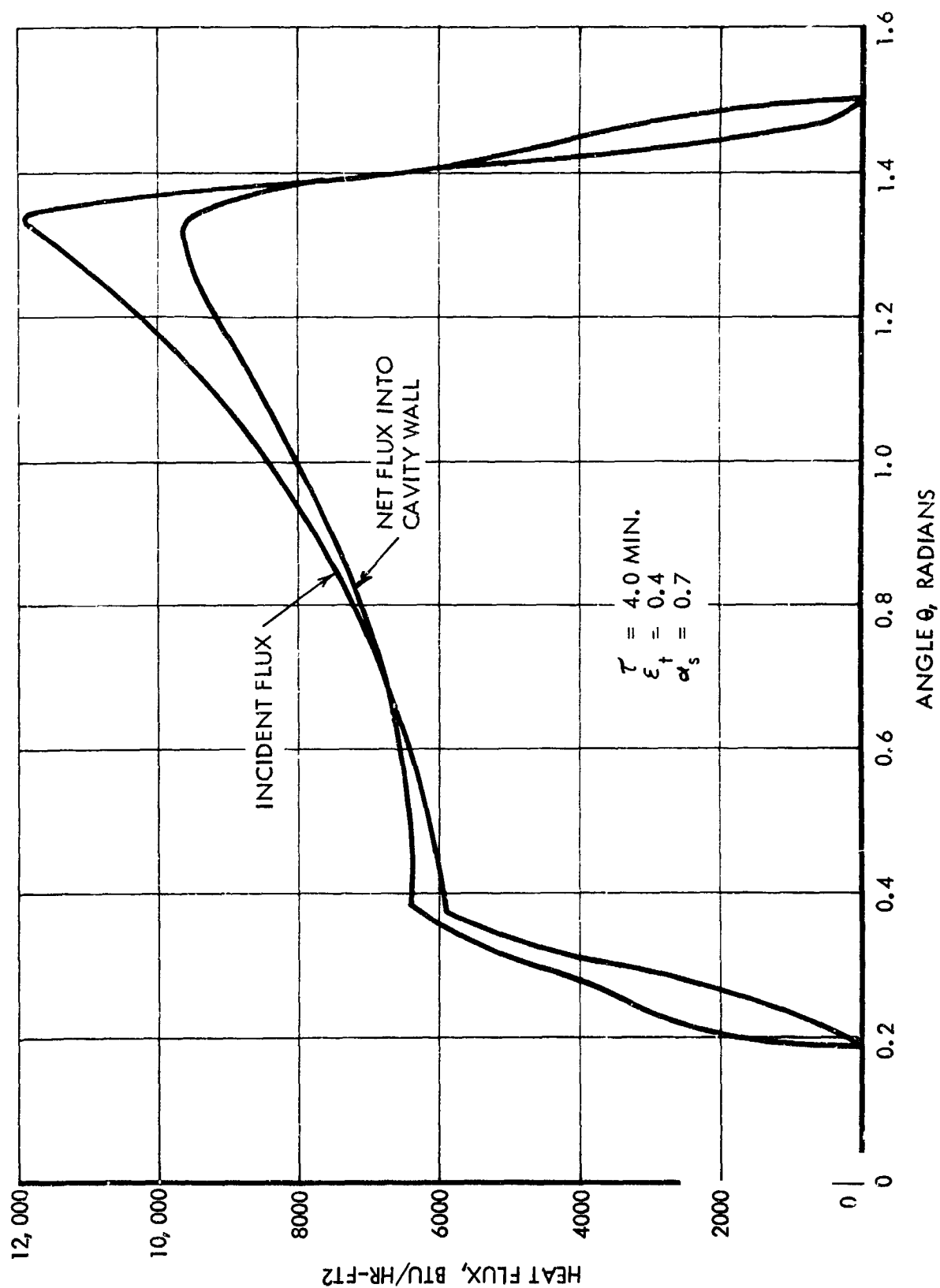
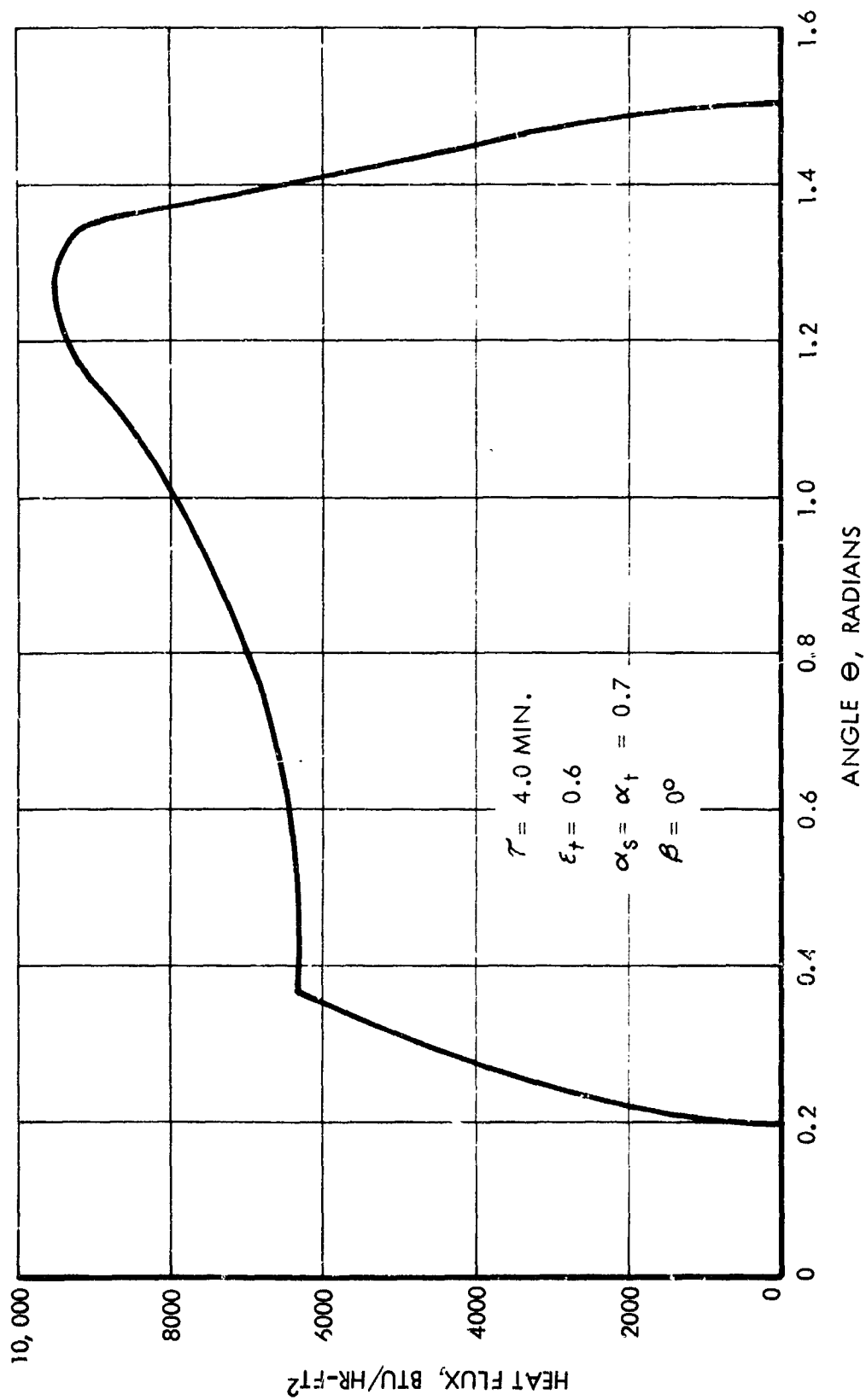
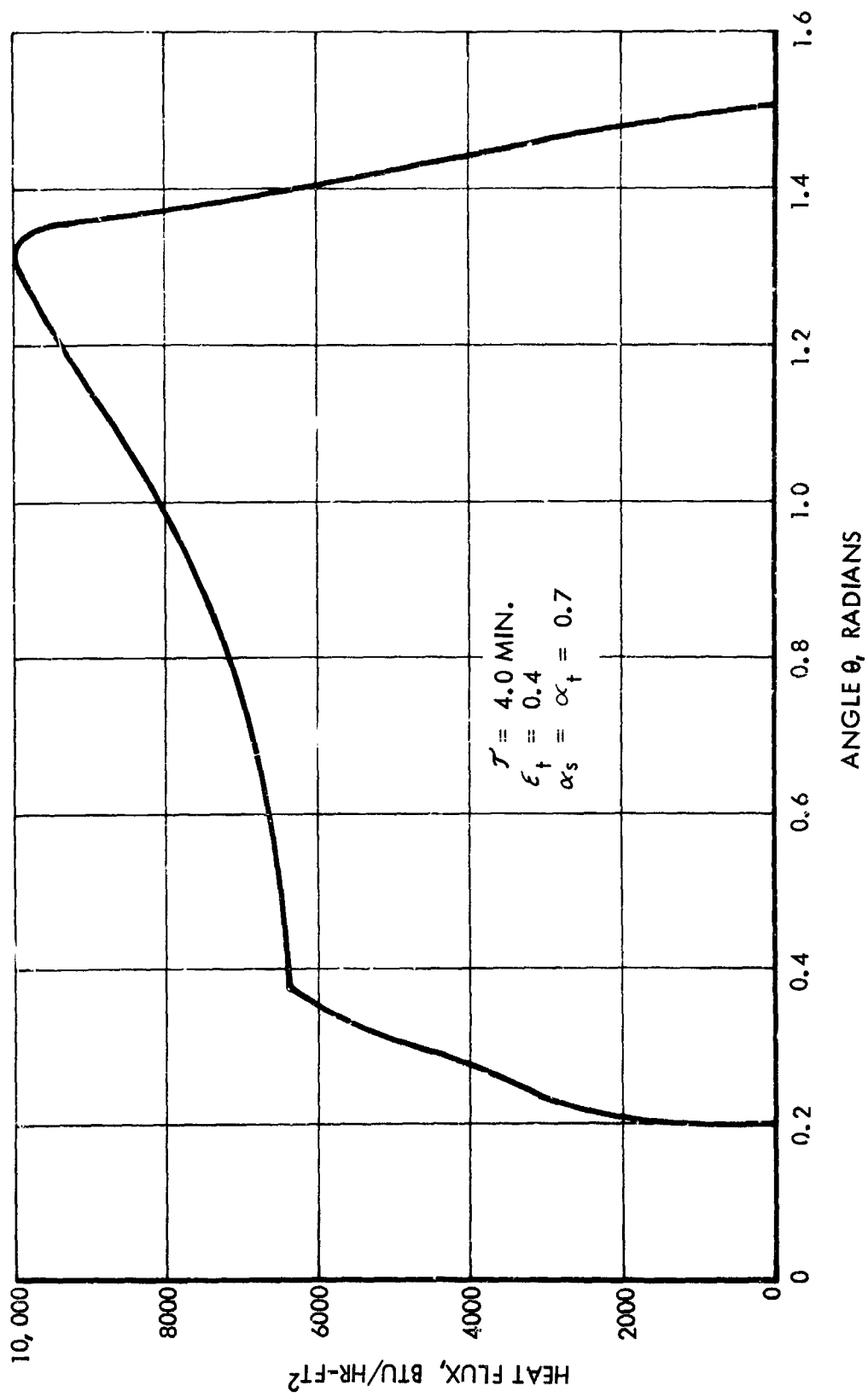


FIGURE 73

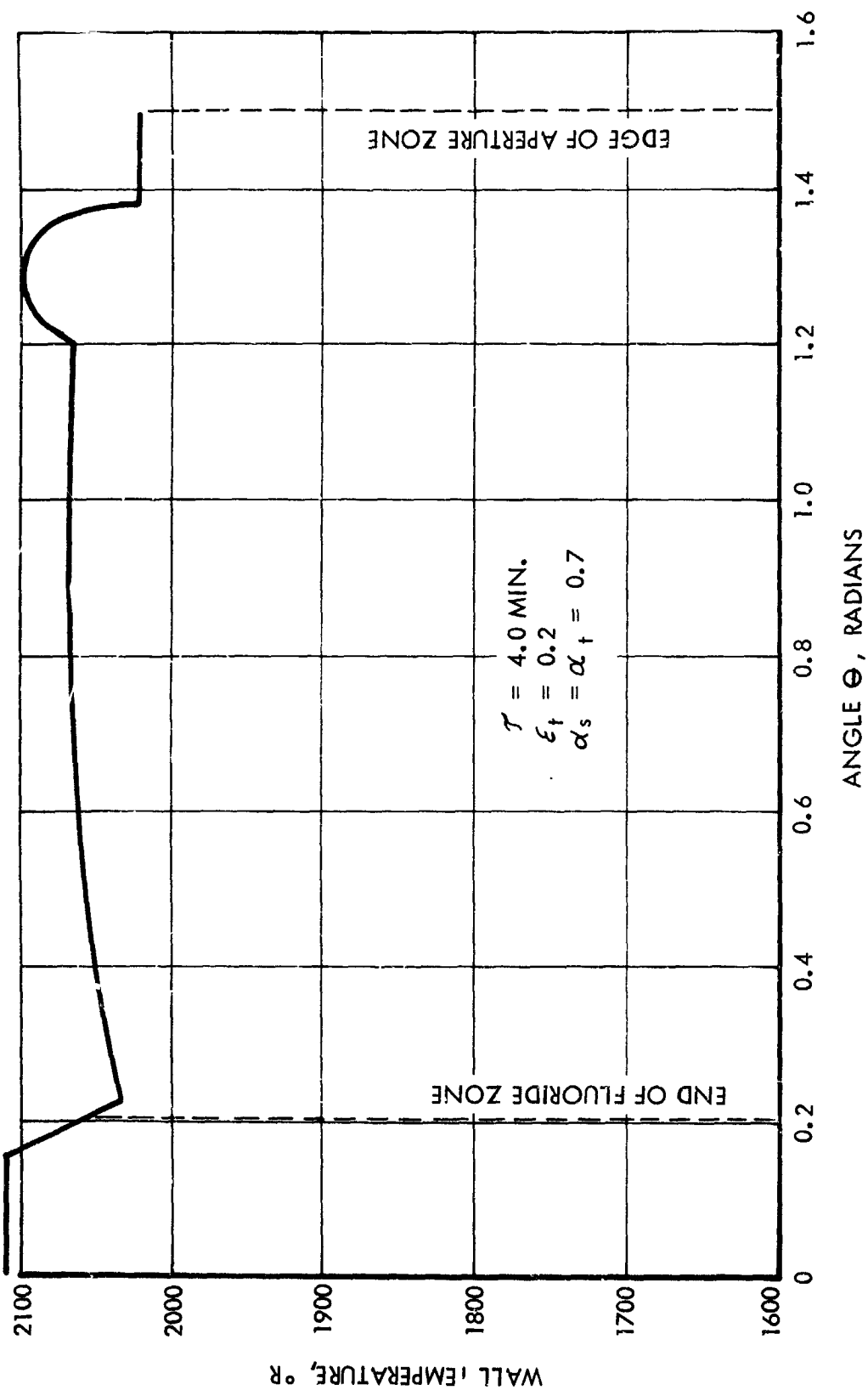
TYPICAL VARIATION OF TOTAL CAVITY WALL FLUX FOR THE PERFECTLY ORIENTED COLLECTOR WITH HIGH WALL EMISSIVITY



TYPICAL VARIATION OF TOTAL CAVITY WALL FLUX FOR THE PERFECTLY ORIENTED COLLECTOR ($\beta = 0^\circ$) WITH LOW EMISSIVITY



TYPICAL CAVITY WALL TEMPERATURE DISTRIBUTION FOR PERFECTLY ORIENTED COLLECTOR ($\beta = 0^\circ$)



The heat flux distribution along the heater tube for the case of Figure 73 is shown in Figure 77. This distribution in the sun time can be compared with Figure 71 which gives the shade time results. It can be observed that some sections of the tube near the inlet are at lower levels in the sun time than in the shade time. This situation is caused by insufficient heat coming from the cavity in this region. Gas temperature and pressure distributions along the tube are presented in Figures 78 and 79 for the case of Figure 73. The tube wall temperature is also shown in Figure 78. The strong heat rate control by the high gas thermal resistance is indicated by the large temperature difference between the tube wall and the gas mean.

Two instantaneous variations in gas flow rate were studied. The flow rate was increased from 36.7 lb/min to 40.37 lb/min and decreased to 33.03 lb/min. Heat flux, mean gas temperature and pressure distributions along the tube are given in Figures 80, 81, and 82, respectively, for the higher flow rate and in Figures 83, 84 and 85, respectively, for the lower flow rate. In both cases, the cavity conditions are the same as in Figure 73. The cavity wall temperature distribution is very insensitive to the gas flow rate changes.

The cavity wall temperature distribution for the 1/4 degree misorientation corresponding to the other conditions of Figure 73 is given in Figure 86. A range of temperatures can be expected in the circumferential direction and the two extremes are shown.

Figure 87 illustrates the similar temperature distributions for the 1/2-degree misorientation.

6.7 Comparison of Analog, Experimental and Computed Cavity Wall Temperature Variations

The data obtained from the analog study presented in Appendix 5 (Section 8.5) and from the experimental results on Module D were reviewed for comparison with the computed values. The cavity wall location of prime interest is that region which exhibits the highest local flux going into the cavity walls for transfer to the lithium fluoride. Examination of the computer program results revealed that the maximum local cavity wall flux occurred at a value of θ equal to 1.277 radians. The variation of the local cavity wall flux at this location with time in the sun is shown in Figure 89. It can be observed from Figure 89 that the initial flux level is over 10,000 Btu/hr-ft² and drops steadily to a value approaching 8600 Btu/hr-ft².

The computed cavity wall temperature variation with melting time corresponding to the flux variation of Figure 88 is presented in Figure 89. The initial value, 1560°F, is equivalent to the melting temperature of lithium fluoride.

Examination of the experimental results with Module D indicated that run D-7 was a typical one. Figure 47 was employed for this purpose. The top plate temperature variation corrected to the bottom surface of the top plate is given for run D-7 in Figure 90. It can be observed from Figure 47 that run D-7 was performed at a heat input flux level of about 16,500 Btu/hr-ft². Further, it can be observed from Figure 47 that runs D-2 and D-7 are about on a line with the analog results for heat input with 0.062-inch fins. On this basis, it was postulated that the experimental performance in run D-7 was equivalent to the analog

TYPICAL VARIATION OF HEATER TUBE FLUX
ALONG TUBE LENGTH DURING SUN TIME

$\beta = 0^\circ$ (PERFECT ORIENTATION)

$\tau = 4.0$ MIN

$\epsilon_t = 0.4$

$\mathcal{L}_s = \mathcal{L}_t = 0.7$

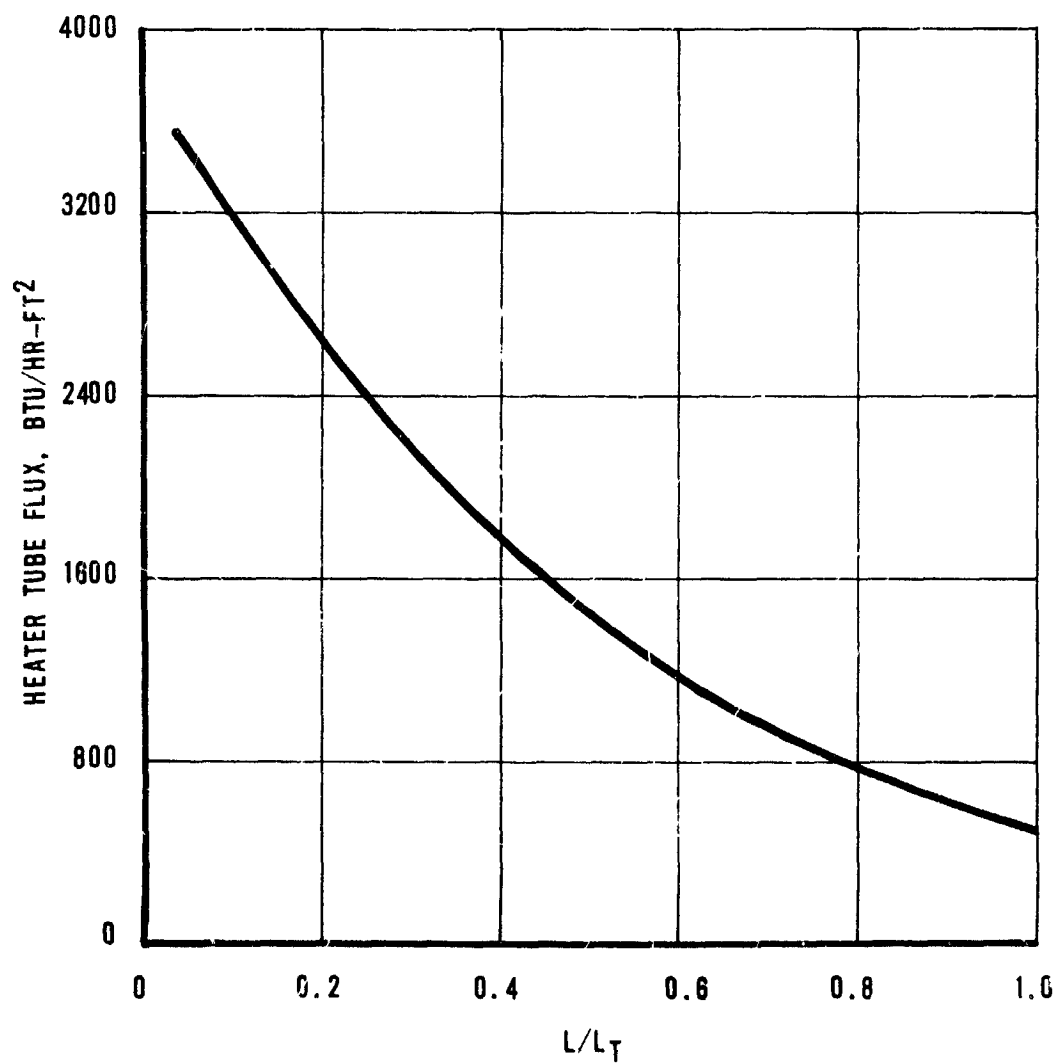
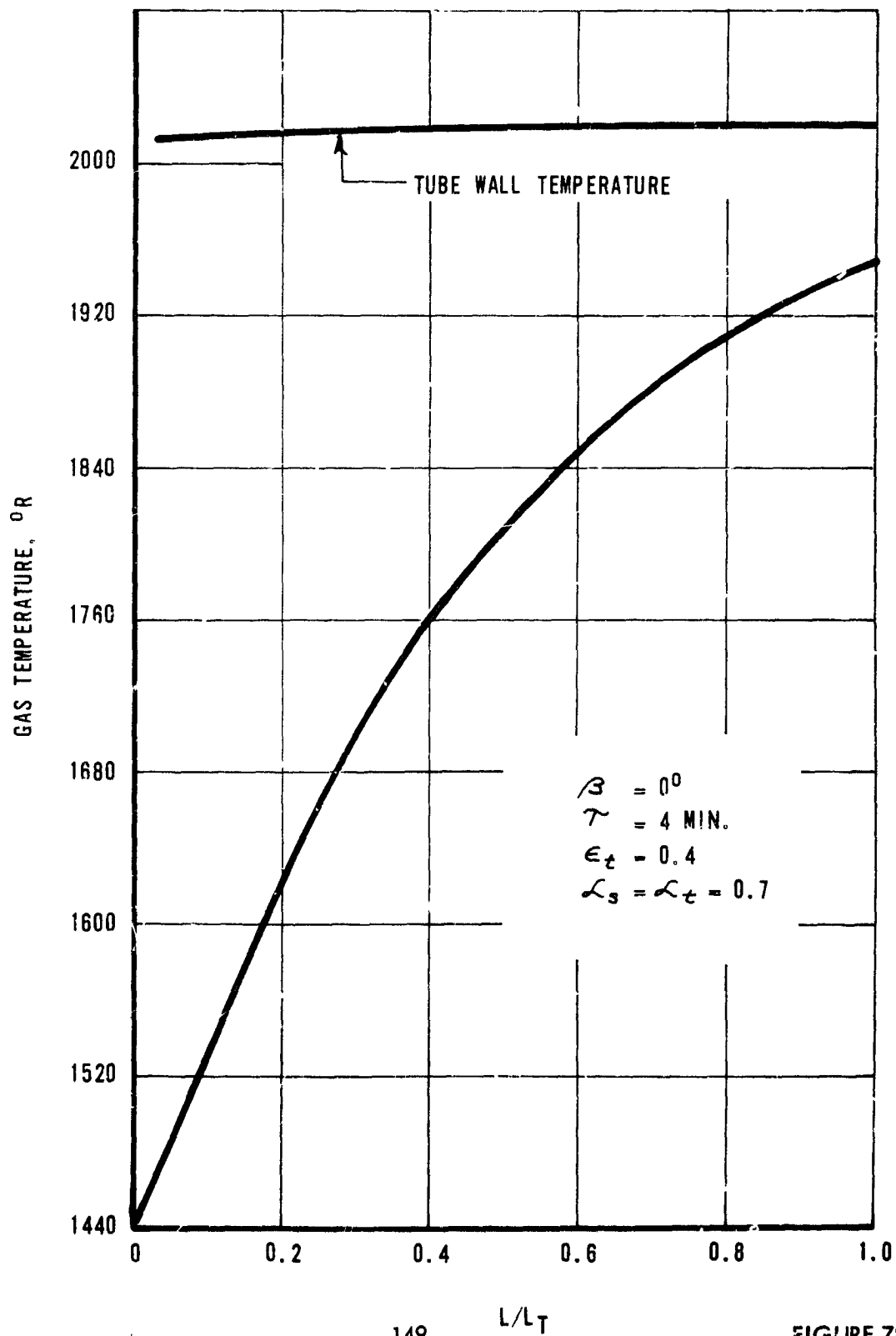


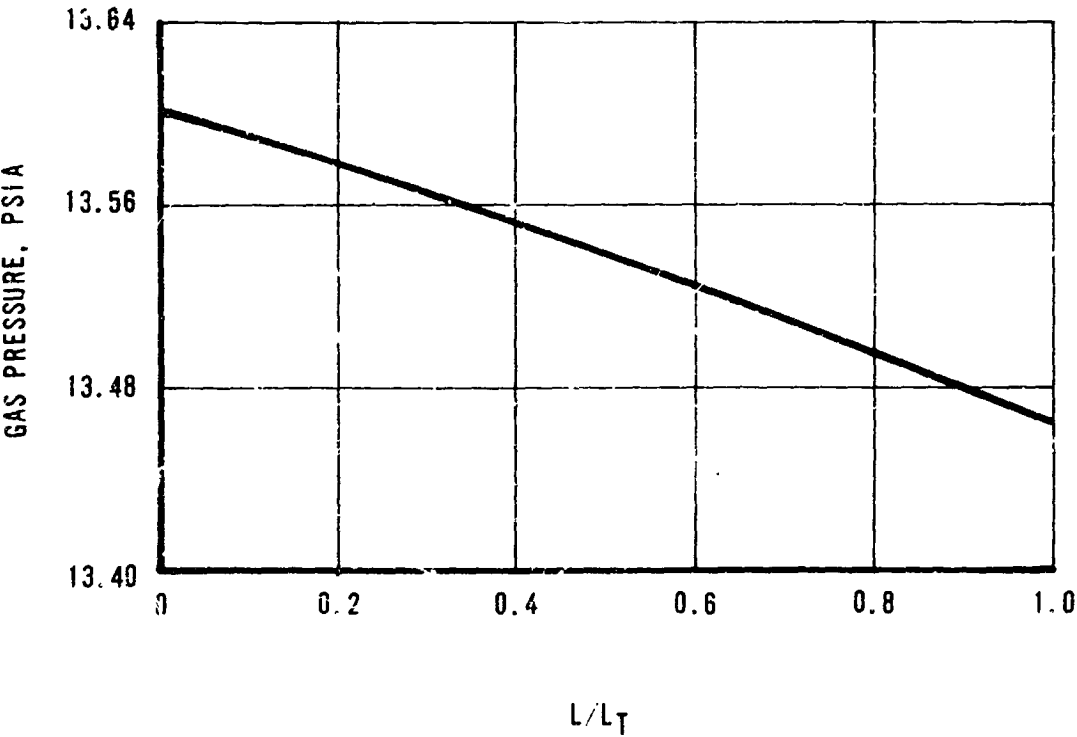
FIGURE 77

TYPICAL VARIATION OF GAS AND TUBE WALL TEMPERATURES
ALONG TUBE LENGTH DURING SUN TIME



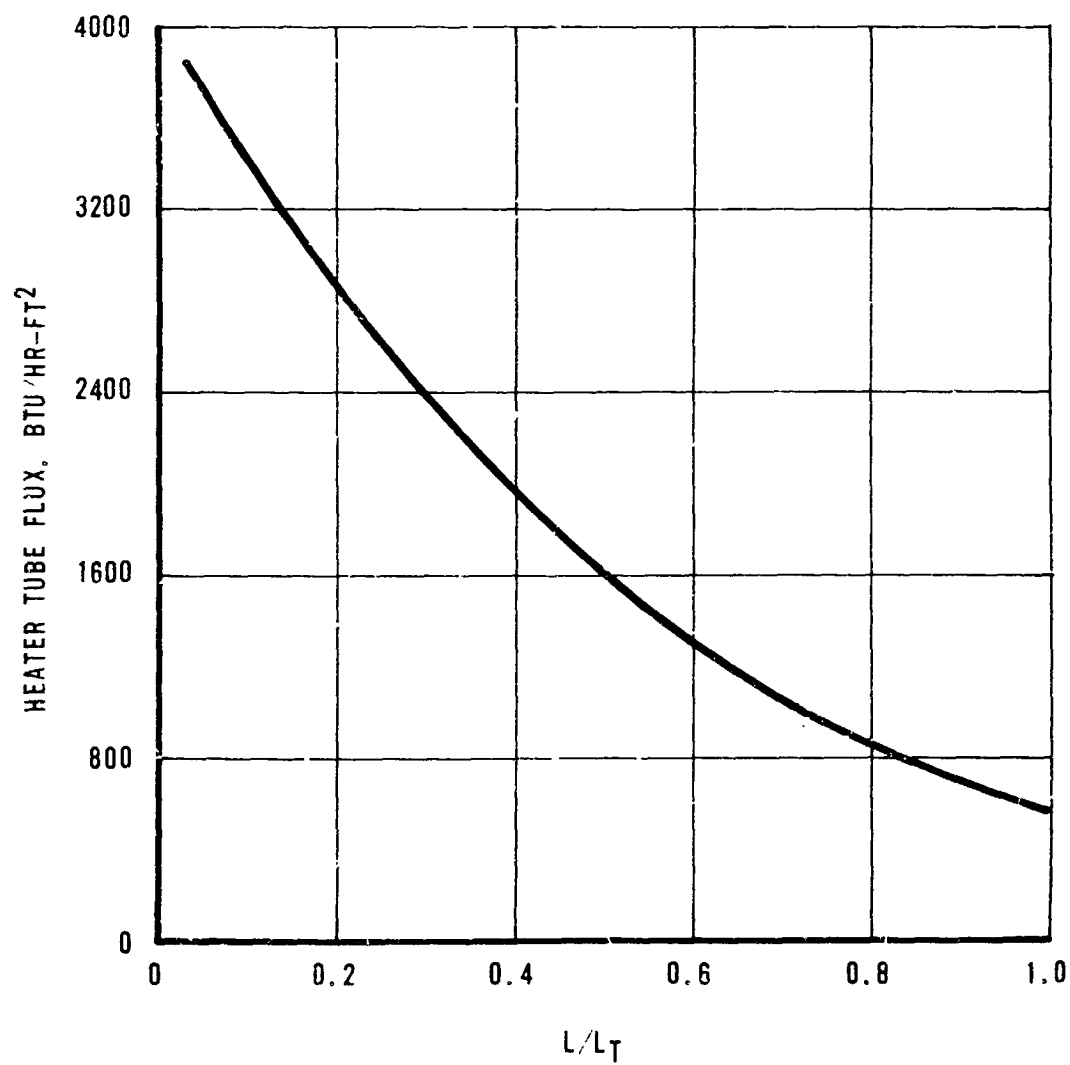
TYPICAL VARIATION OF GAS PRESSURE
ALONG TUBE LENGTH DURING SUN TIME

$\beta = 0^\circ$
 $\tau = 4.0 \text{ MIN.}$
 $\epsilon_t = 0.4$
 $\alpha_s = \alpha_t = 0.7$



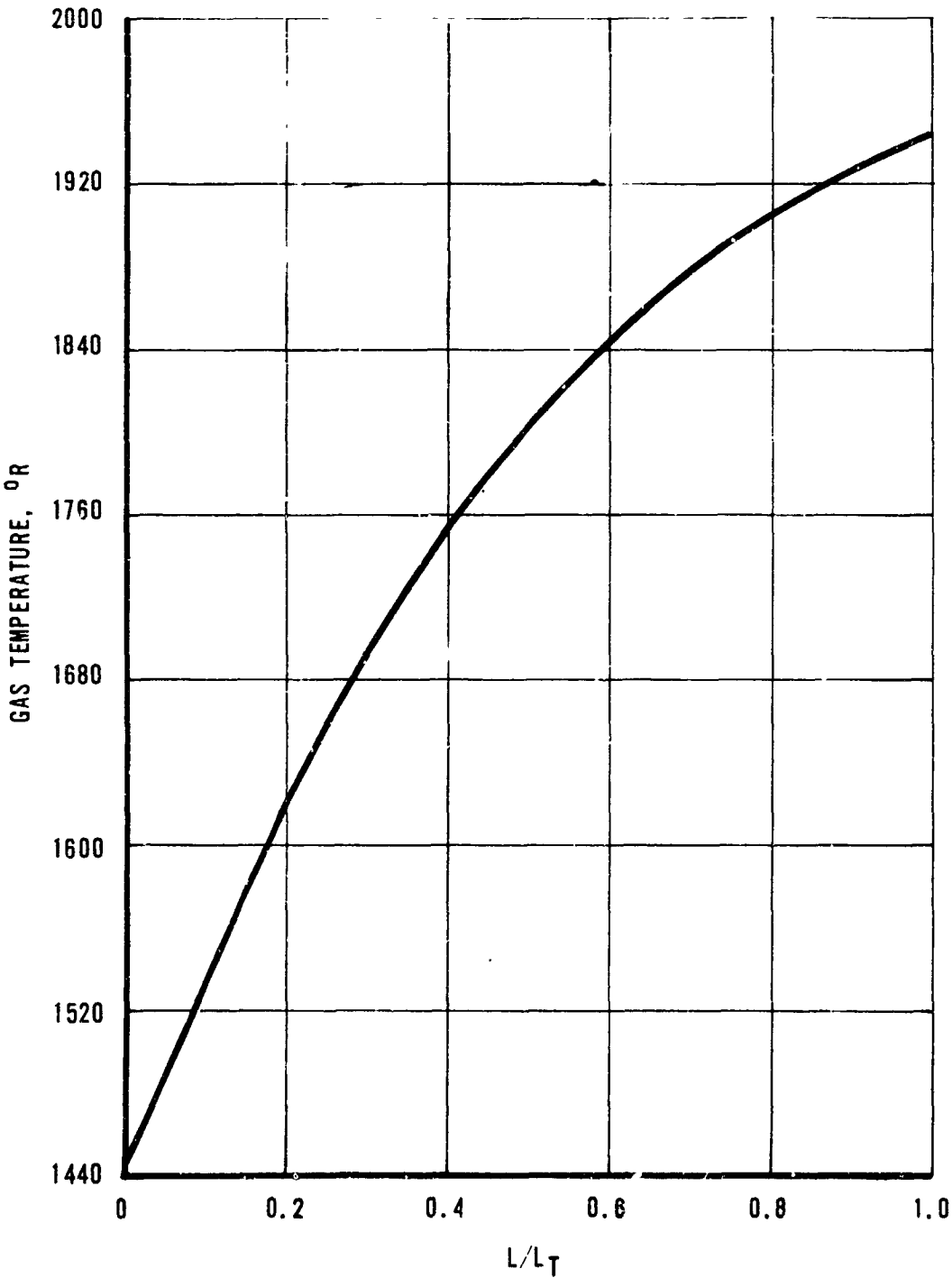
TYPICAL VARIATION OF HEATER TUBE FLUX ALONG TUBE LENGTH DURING
SUN TIME WITH GAS FLOW RATE 10 PERCENT ABOVE DESIGN FLOW RATE

$\beta = 0^\circ$
 $\gamma = 4.0 \text{ MIN}$
 $\epsilon_t = 0.4$
 $L_s = L_t = 0.7$
 $w = 40.37 \text{ LB/MIN}$



TYPICAL VARIATION OF GAS TEMPERATURE ALONG TUBE LENGTH DURING SUN
TIME WITH FLOW RATE 10 PERCENT ABOVE DESIGN FLOW RATE

$\beta = 0^\circ$
 $\tau = 4.0 \text{ MIN.}$
 $\epsilon_t = 0.4$
 $\alpha_s = \alpha_c = 0.7$
 $w = 40.37 \text{ LB/MIN.}$



TYPICAL VARIATION OF GAS PRESSURE ALONG TUBE LENGTH DURING SUN
TIME WITH FLOW RATE 10 PERCENT ABOVE DESIGN FLOW RATE

$$\begin{aligned}\beta &= 0^\circ \\ \tau &= 4.0 \text{ MIN.} \\ E_t &= 0.4 \\ L_s = L_t &= 0.7 \\ w &= 40.37 \text{ LB/MIN}\end{aligned}$$

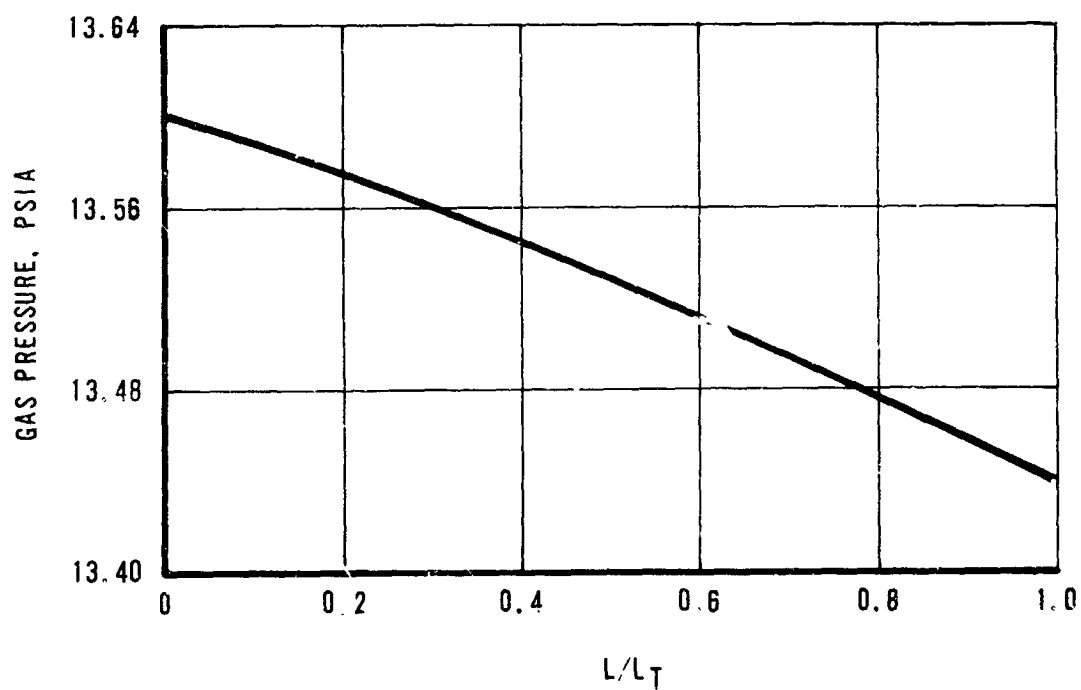


FIGURE 82

TYPICAL VARIATION OF HEATER TUBE FLUX ALONG TUBE LENGTH DURING
SUN TIME WITH FLOW RATE 10 PERCENT BELOW DESIGN FLOW RATE

$$\begin{aligned}\beta &= 0^\circ \\ \gamma &= 4.0 \text{ MIN} \\ \epsilon_t &= 0.4 \\ \alpha_s = \alpha_t &= 0.7 \\ w &= 33.03 \text{ LB/MIN}\end{aligned}$$

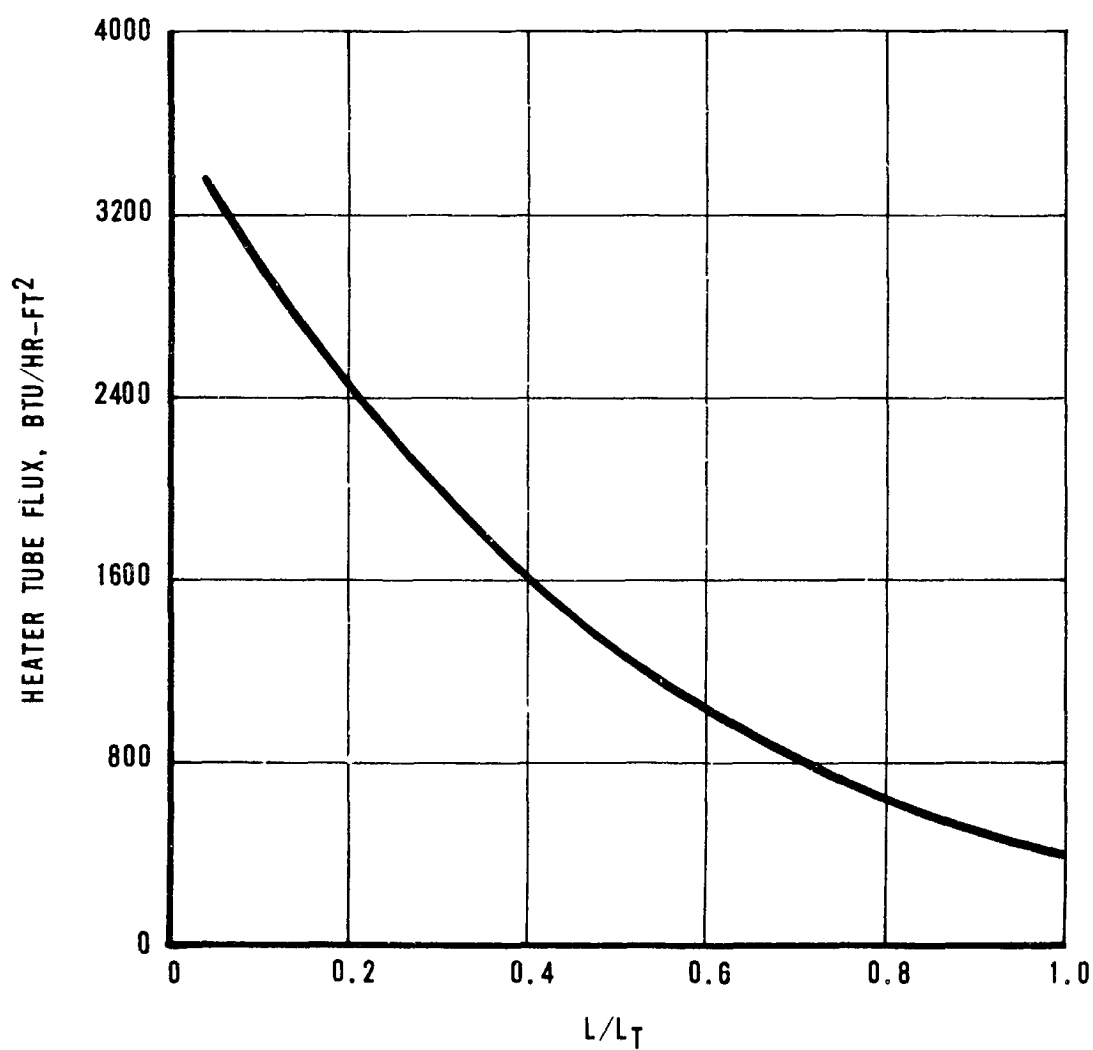


FIGURE 83

TYPICAL VARIATION OF GAS TEMPERATURE ALONG TUBE LENGTH DURING
SUN TIME WITH FLOW RATE 10 PERCENT BELOW DESIGN FLOW RATE

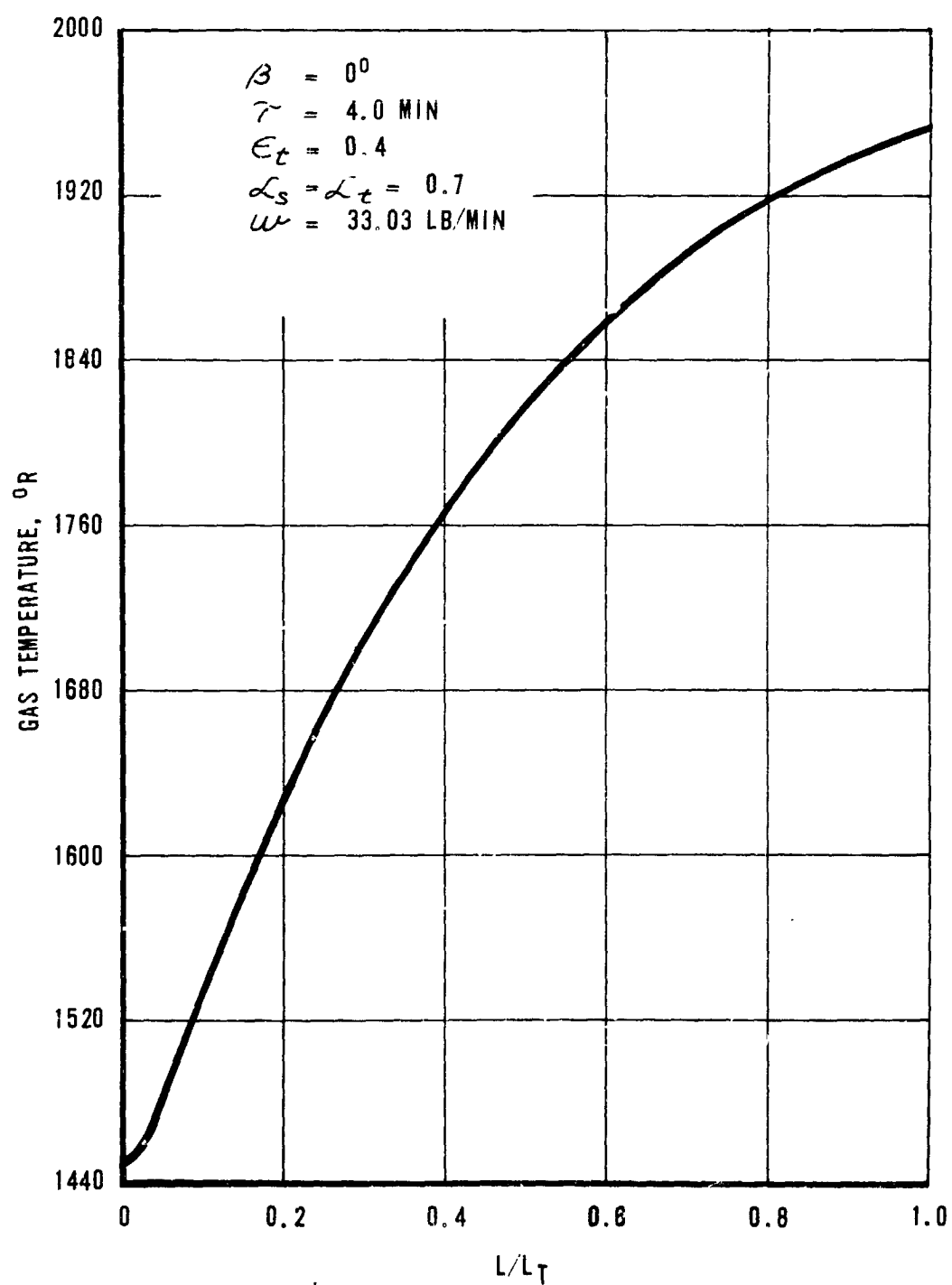


FIGURE 84

TYPICAL VARIATION OF GAS PRESSURE ALONG TUBE LENGTH DURING
SUN TIME WITH FLOW RATE 10 PERCENT BELOW DESIGN FLOW RATE

$$\begin{aligned}\beta &= 0^\circ \\ \tau &= 4.0 \text{ MIN} \\ \epsilon_t &= 0.4 \\ \mathcal{L}_s = \mathcal{L}_t &= 0.7 \\ w &= 33.03 \text{ LB/MIN}\end{aligned}$$

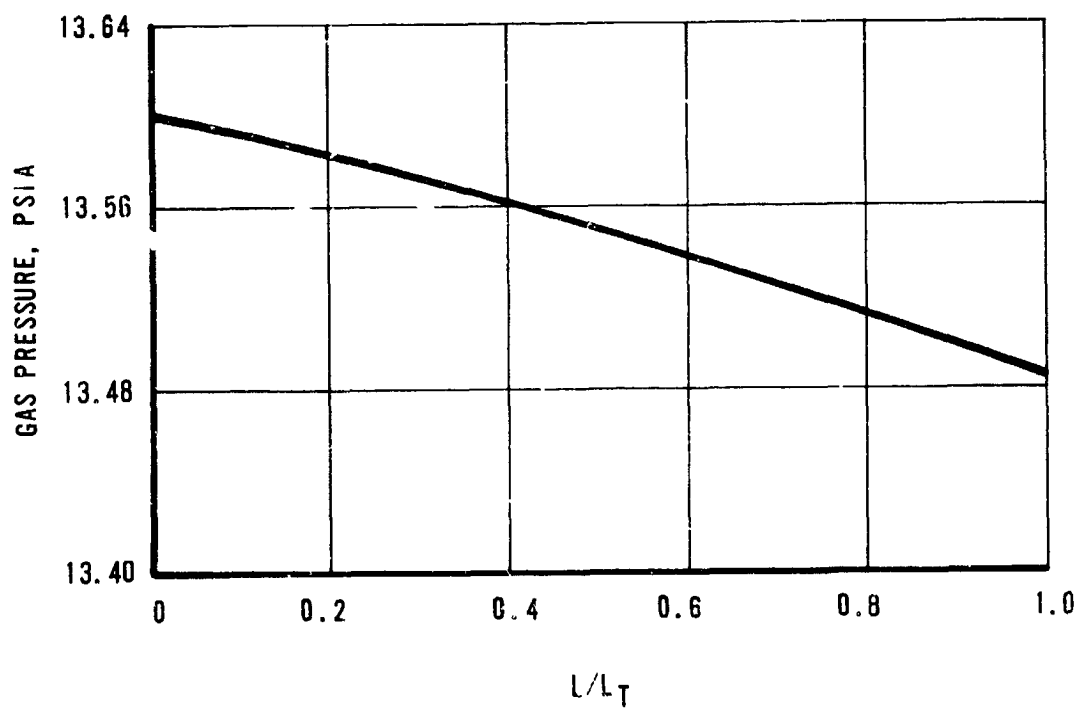
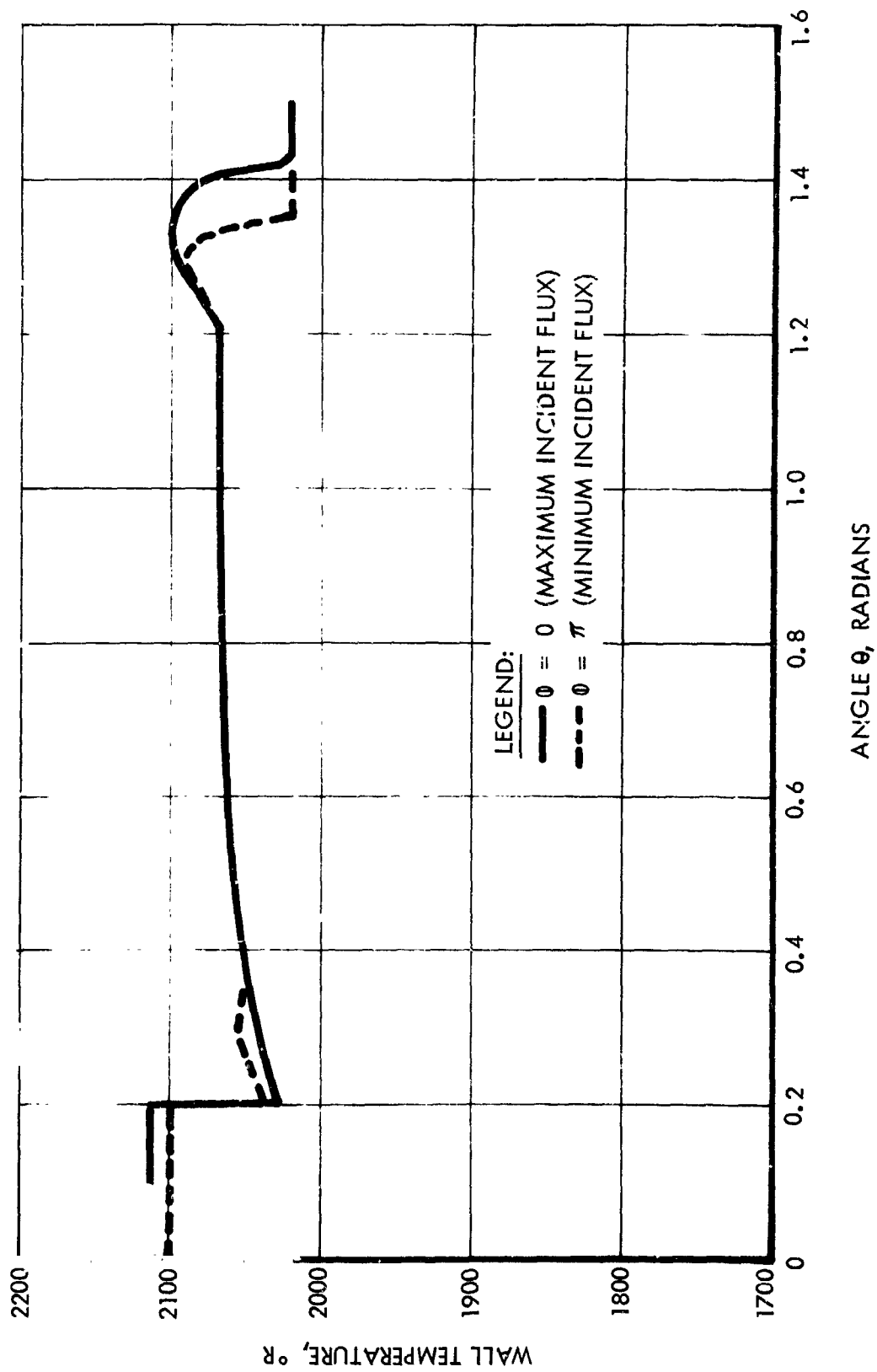


FIGURE 85

TYPICAL WALL TEMPERATURE DISTRIBUTION DURING SUN TIME
FOR COLLECTOR MISORIENTED 1/4 DEGREE FROM THE SUN

$$\begin{aligned} \beta &= 1/4 \text{ DEGREE} \\ \tau &= 4.0 \text{ MIN.} \\ \xi_t &= 0.4 \\ \alpha_s = \alpha_t &= 0.7 \end{aligned}$$



TYPICAL WALL TEMPERATURE DISTRIBUTION DURING SUN TIME
FOR COLLECTOR MISORIENTED 1/2-DEGREE FROM THE SUN

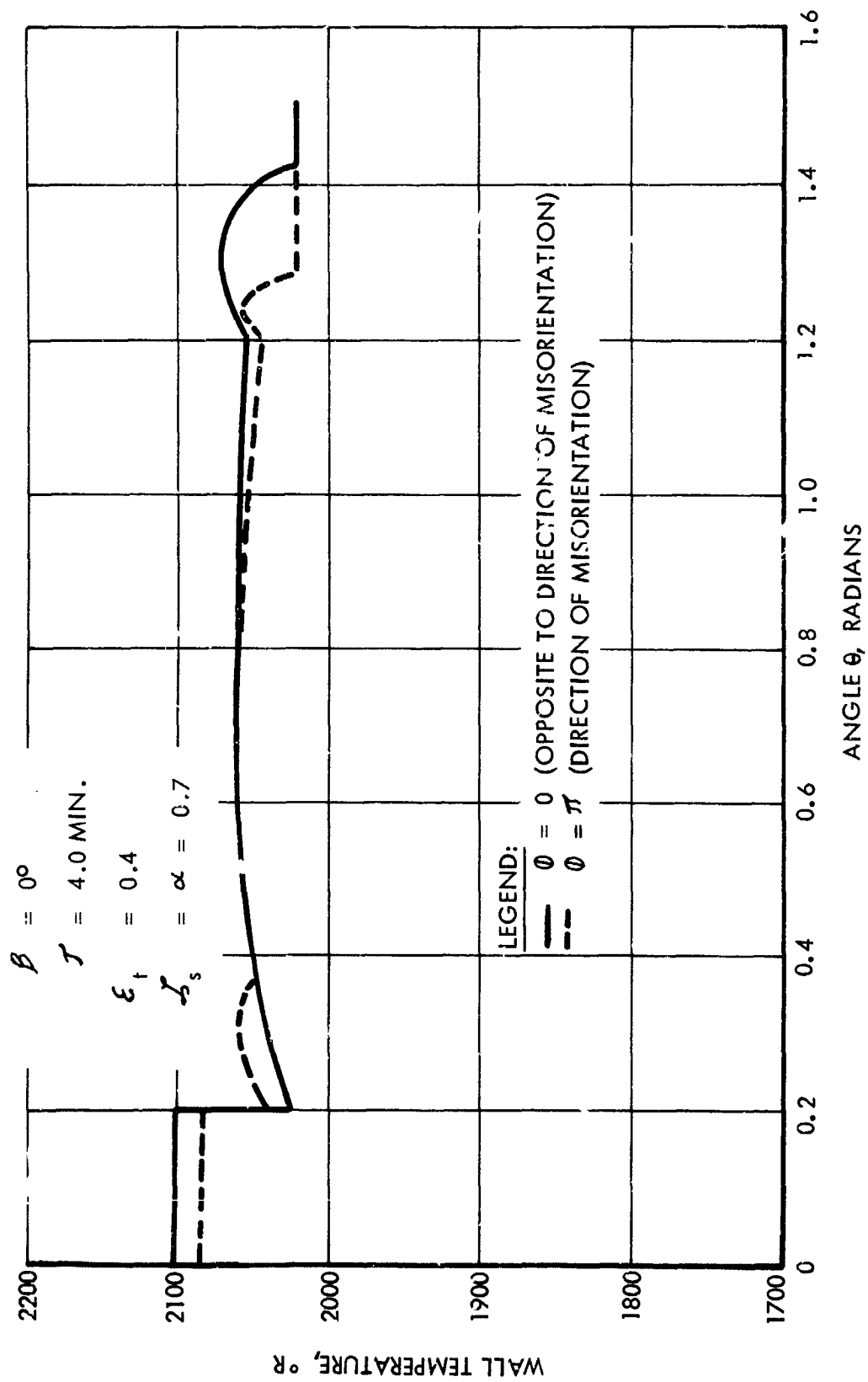
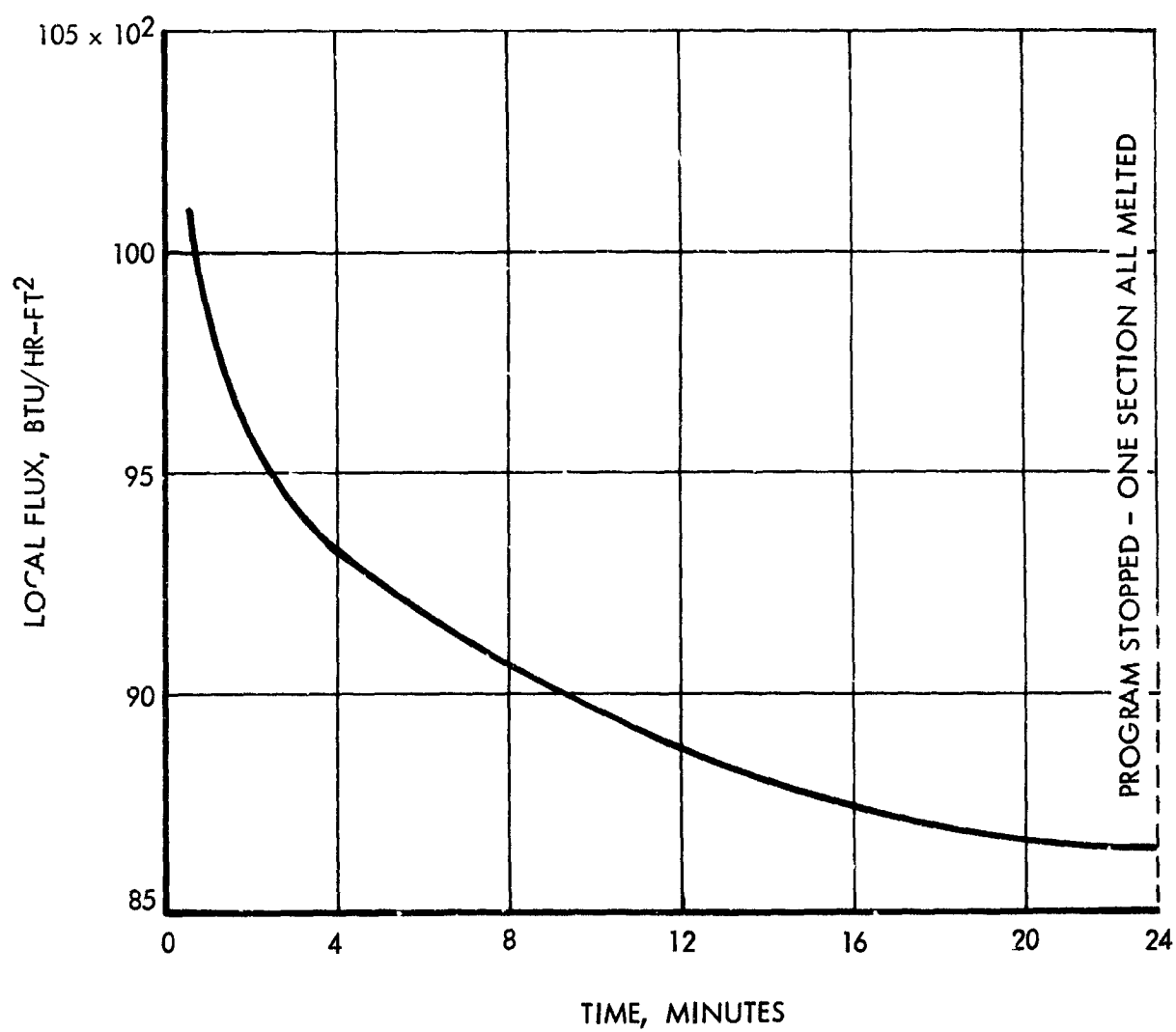


FIGURE 87

VARIATION OF MAXIMUM CAVITY WALL FLUX WITH MELTING TIME

$$\begin{aligned} \beta &= 0^\circ \\ \alpha_s &= \alpha_T = 0.7 \\ \epsilon_T &= 0.4 \end{aligned}$$



VARIATION OF CAVITY WALL TEMPERATURE WITH MELTING TIME
AT CAVITY LOCATION WHERE MAXIMUM CAVITY WALL FLUX OCCURS

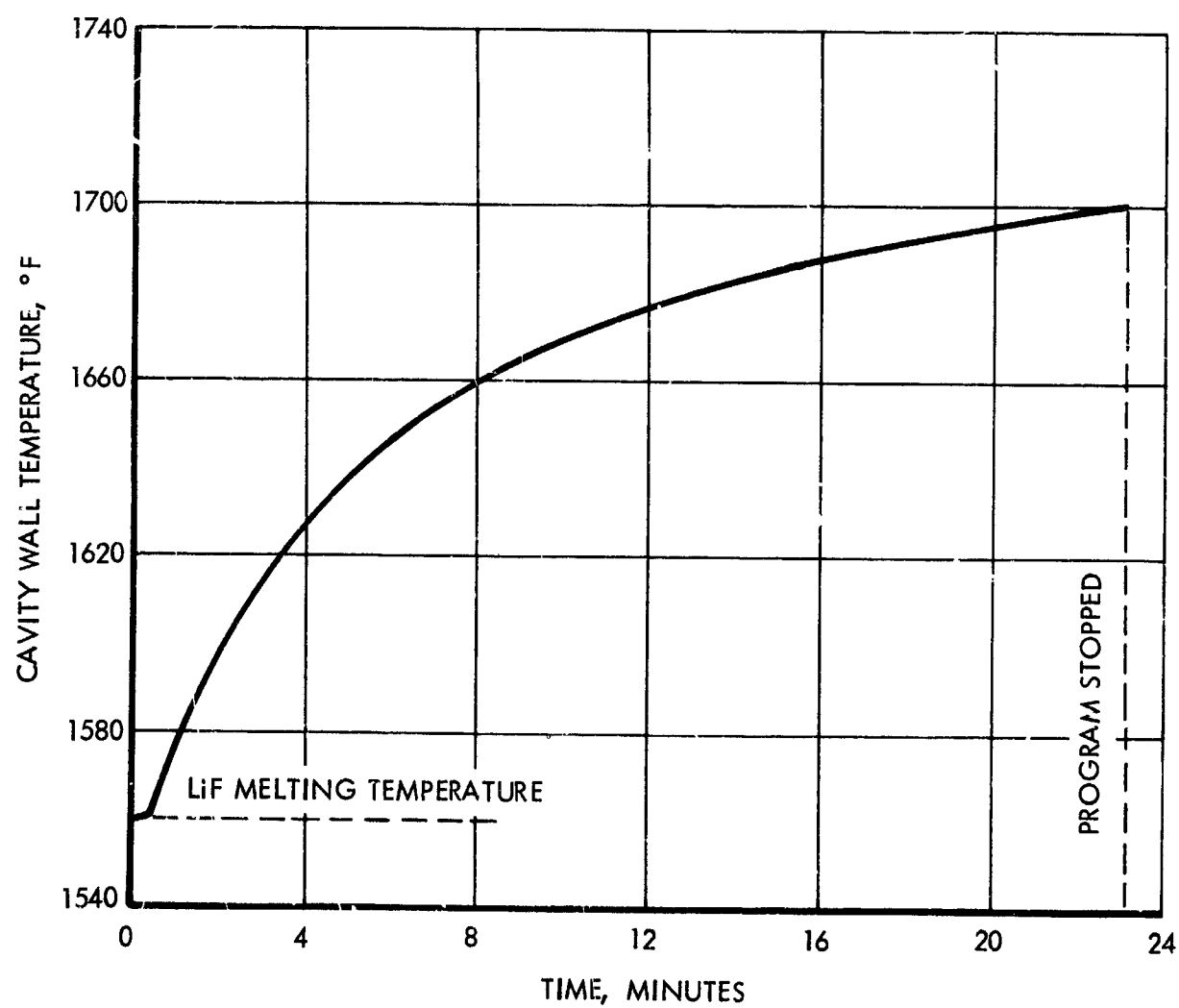


FIGURE 89

results predicted for Module C, and, therefore, the analog results obtained for Module C at a flux level of 10,000 Btu/hr-ft² could be considered equivalent to the Module Experimental results at 10,000 Btu/hr-ft². Hence, the analog results for the case of Module C at 10,000 Btu/hr-ft² are also given in Figure 90.

Finally, a comparison of the analog results without fins at a flux level of 10,000 Btu/hr-ft² of the projected experimental performance of Module D at the same flux level and the computed results for the maximum flux location is shown in Figure 90. The reduction in wall temperature achieved by the controlled freezing patterns of Module D is clearly illustrated for the 1-G testing condition. The projected additional temperature reduction which should be possible in zero-G operation is also indicated. Based on the temperature pattern shown, it is estimated that the maximum cavity wall temperature in zero-G operation will occur in the all melted condition at $1725 \pm 5^\circ \text{F}$. This temperature would be the control temperature for opening of the heat rejection doors.

VARIATION OF TOP PLATE TEMPERATURE OF MODULE D
IN RUN NO. 7 WITH MELTING TIME

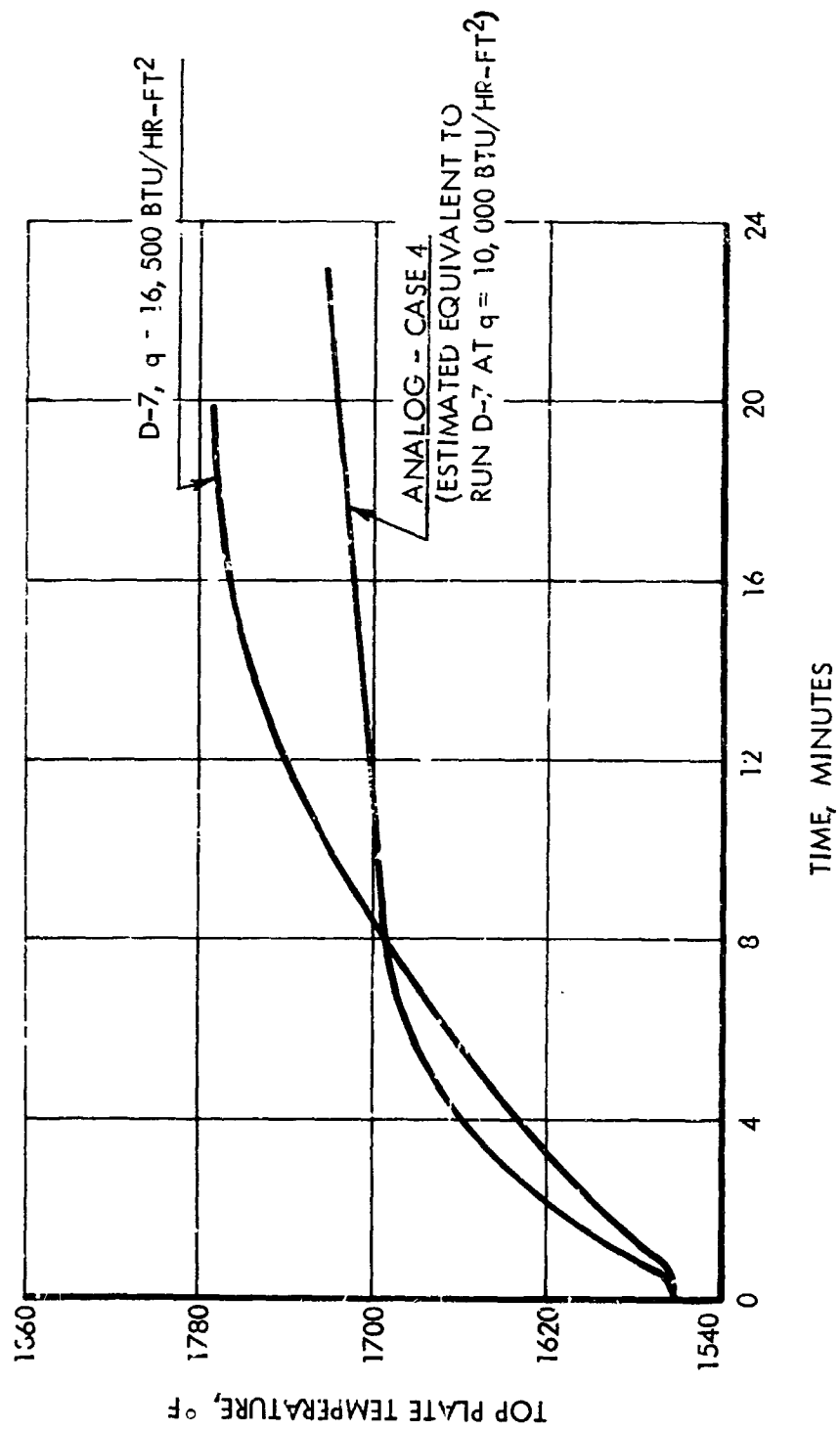


FIGURE 90

COMPARISON OF ANALOG, EXPERIMENTAL AND COMPUTED CAVITY WALL
TEMPERATURE VARIATIONS WITH MELTING TIME

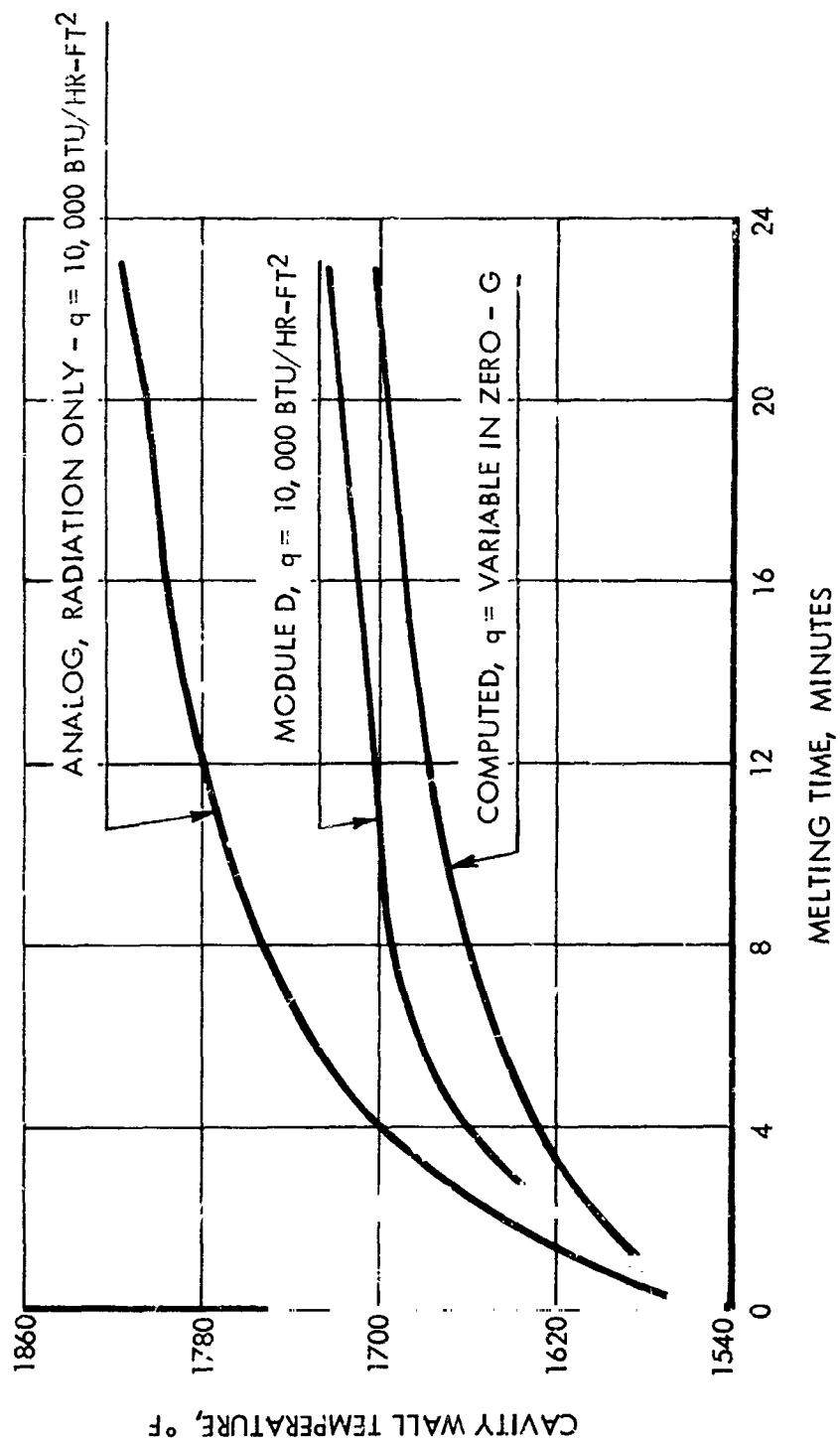


FIGURE 91

7.0 RECOMMENDATIONS FOR FUTURE WORK

The following recommendations for future work are made on the basis of the results obtained under contract NAS 3-2779.

1. Single tube heat transfer and pressure drop tests should be conducted with the full scale, curved, internally-finned tube immersed in a lithium fluoride storage bath. The inlet and outlet header conditions should be simulated as closely as possible.
2. The receiver design layout should be reduced to detail drawings preparatory to fabrication of full scale units.
3. Special tooling required for the fabrication of full scale units should be designed and built.
4. Process development needed for the fabrication of full scale inner and outer shells should be started.
5. The freezing and melting characteristics of lithium fluoride in zero-G operation should be determined. This type of experiment would require operation in orbit to obtain the complete data.
6. A structural test of a prototype configuration should be initiated at the earliest possible date.

Appendices

BLANK PAGE

8.0 APPENDICES

The following items are presented as Appendices to this report:

1. References
2. Nomenclature
3. Lithium Fluoride Properties Summary
4. Heat Input Analysis
5. Radiation Analog Investigation
6. Top Plate Buckling Analysis
7. Materials Properties Selection
8. Structural Analysis
9. Aperture Control Design Analysis
10. Cavity Temperature Distribution Analysis
11. Reliability Estimates

Appendices 1 and 2 give the references and nomenclature, respectively, for the main body of the report. In cases where the other Appendices employ nomenclature or references, it is defined and they are listed within that Appendix.

8.1 References

1. "Sunflower Boiler/Heat Storage Topical Report," TRW, Inc., ER-4869, April 1963.
2. Eckert, E.R.G. and Drake, R.M., Jr., Heat and Mass Transfer, Second Edition, McGraw-Hill Book Co., New York, N.Y., 1959.
3. "Brayton Cycle Cavity Receiver Development - Quarterly Report - July 1963 to September 1963," TRW, Inc., ER-5579, October 1963.
4. Wilson, H.W., Callery Chemical Co., Private Communication.
5. McKinnon, R.A., Vild, T.J. and Milko, J.A., "Design Study of Solar Brayton Cycle Cavity Receivers with Lithium Fluoride Heat Storage," Third Biennial Aerospace Power Systems Conference of the AIAA, Paper No. 64-727, Philadelphia, Pa., September 1-4, 1964.
6. Sams, E.W., "Heat Transfer and Pressure Drop Characteristics of Wire Coil Type Turbulence Promoters," Reactor Heat Transfer Conference, New York, N.Y., November 1 and 2, 1956.
7. "Tables of Thermal Properties of Gases," National Bureau of Standards Circular 564, U.S. Department of Commerce, November 1, 1955.
8. "Lithium Fluoride," Lithium Corporation of America, Inc., Product Data Bulletin 123-762, New York, N.Y., February 6, 1964.
9. Kelley, K.K., "Contributions to the Data on Theoretical Metallurgy - XIII. High Temperature Heat-Content, Heat-Capacity, and Entropy Data for the Elements and Inorganic Compounds," Bureau of Mines Circular 584, U.S. Government Printing Office, Washington, D.C., 1960.
10. Douglas, T.B. and Dever, J.L., "Lithium Fluoride: Heat Content from 0 to 900°F, the Melting Point and Heat of Fusion," Journal of the American Chemical Society, Vol. 76, pp. 4826-29, 1954.
11. "Annual Progress Report for Period Ending January 31, 1963," Reactor Chemistry Division, Oak Ridge National Laboratory, ORNL-3417, Oak Ridge, Tenn., May 1, 1963.
12. "Brayton Cycle Solar Collector Design Study - Final Report," TRW, Inc., ER-5838, March 1964.
13. "Brayton Cycle Cavity Receiver Development - Quarterly Report - October 1963 to December 1963," TRW, Inc., ER-5736, January 1964.

14. Stephens, C.W. and Haire, A.M., Jr., "Internal Design Consideration for Cavity-Type Solar Absorbers," *Journal of the American Rocket Society*, July 1961, pp. 896-901.
15. Schrenk, G.L., "Solar Collection Limitations for Dynamic Converters - Simulation of Solar-Thermal Energy Power Systems," *Proceedings of the Sixth AGARD Conference*, Cannes, France, March 16-20, 1964.
16. Schwartz, H.W., Tarter, J.H. and Wille, D.J., "Research on Thermal Storage for Advanced Solar Powered Dynamic Space Power Plants - Final Report," *Research Laboratories Division, Bendix Corporation, Report No. 2656*, 24 July 1964.
17. Ito, H., "Friction Factors for Turbulent Flow in Curved Pipes," *Journal of Basic Engineering*, June 1959. ASME Paper No. 58 - SA-14.
18. Taylor - Data as found in McAdams, *Heat Transmission*, Third Edition, McGraw-Hill Book Co., 1954, p. 151.
19. White - Data as found in IBID.
20. Drew - Formula as given in IBID.
21. McAdams, W.H., *Heat Transmission*, Third Edition, McGraw-Hill Book Co., New York, N.Y., 1954.
22. Barnes, J.F., "An Experimental Investigation of Heat Transfer from the Inside Surface of a Hot Smooth Tube to Air, Helium and Carbon Dioxide," *Ministry of Aviation, Reports and Memoranda No. 3246*, Her Majesty's Stationery Office, London, England, 1961.
23. Humble, L.V., Lowdermilk, W.H. and Desmon, L.G., "Measurements of Average Heat-Transfer and Friction Coefficients for Subsonic Flow of Air in Smooth Tubes at High Surface and Fluid Temperatures," *National Advisory Committee for Aeronautics Report 1020*, 1951.
24. Knudsen, J.G. and Katz, D.L., *Fluid Dynamics and Heat Transfer*, Second Edition, McGraw-Hill Book Co., New York, N.Y., 1958.
25. Svehla, Roger A., "Estimated Viscosities and Thermal Conductivities of Gases at High Temperatures," *NASA TR-R-132*.
26. Brokaw, Richard S., "Alignment Charts for Transport Properties, Thermal Conductivity, and Diffusion Coefficients for Non-polar Gases and Gas Mixtures at Low Density," *NASA TR-T-81*, 1961.

27. Eckert, E.R.G. and Irvine, T.F., Jr., "Flow in Corners of Passages with Non-circular Cross Sections," Transactions of the American Society of Mechanical Engineers, Vol. 78, May 1956.
28. Eckert, E.R.G. and Irvine, T.F., Jr., "Pressure Drop and Heat Transfer in a Duct with Triangular Cross Section," Journal of Heat Transfer, May 1960, p. 125.
29. Eckert, E.R.G. and Irvine, T.F., Jr., "Analysis of Laminar Heat Transfer in Wedge-Shaped Ducts," WADD Report 56-98, April 1956.
30. Eckert, E.R.G., Irvine, T.F., Jr., and Yen, J.T., "Local Laminar Heat Transfer in Wedge-Shaped Passages," Transactions of the American Society of Mechanical Engineers, Vol. 80, October 1958.
31. Hukuo, N. and Mii, H., "Design Problems of a Solar Furnace," Solar Energy, Vol. 1, No. 203 (1957), pp. 108-114.

9.1.1 Reference - Definitions - Trade Names

1. "Min-K" Insulation: A thermal insulating material marketed by Johns-Manville under this trade name.
2. Marinite: A sheet type insulating marketed by Johns-Manville under this trade name.
3. "Teledeltos": An electrical conducting paper marketed by General Electric Co. under this trade name.
4. "Schmidt Plot": A graphical approximation method originally proposed by E. Schmidt for determining unsteady heat flow through a semi-infinite body. Refer to:

E. Schmidt, "Einführung in Die Technische Thermodynamik," P. 262, Springer-Verlag, Berlin, 1936.

8.2 Nomenclature

The following nomenclature is employed in the main body of the report:

- A - Heat exchange surface area, sq. ft
- A_{bath} - Area of test module storage bath normal to heat flow, sq. ft
- A_c - Cross-sectional flow area, sq. ft
- c_p - Specific heat at constant pressure, Btu/lb-°F
- c_v - Specific heat at constant volume, Btu/lb-°F
- D - Tube inner diameter, ft
- f - Friction factor, dimensionless
- G - Mass velocity, lb-sec-sq. ft
- g_c - Gravitational constant, 32.2 ft/sq. sec.
- h - Convection heat transfer coefficient, Btu/hr-°F-sq. ft
- h_f - Heat of fusion, 449 Btu/lb
- I - Incident flux on cavity walls, Btu/hr-sq. ft
- I_o - Solar energy constant, 433 Btu/hr-sq. ft
- K - Pressure drop factor
- K_L - Pressure drop factor for laminar flow
- K_T - Pressure drop factor for turbulent flow
- k - Thermal conductivity, Btu/hr-ft-°F
- k_f - Thermal conductivity of fin, Btu/hr-ft-°F
- k_l - Thermal conductivity of liquid lithium fluoride, Btu/hr-ft-°F
- k_{LiF} - Thermal conductivity of lithium fluoride, Btu/hr-ft-°F
- k_s - Thermal conductivity of solid lithium fluoride, Btu/hr-ft-°F

k_w	- Wall thermal conductivity, BTU/hr-ft/°F
L	- Tube length, ft
Δl	- Incremental tube length, ft
m	- Mass, lb
\dot{m}	- Mass flow rate, lb/sec
N	- Tube number, dimensionless
N_u	- Nusselt number, dimensionless
P_1	- Pressure at compressor inlet, lb/sq. in. abs.
P_2	- Pressure at compressor outlet, lb/sq. in. abs.
P_3	- Pressure at heater inlet, lb/sq. in. abs.
P_4	- Pressure at heater outlet, lb/sq. in. abs.
P_5	- Pressure at recuperator inlet, lb/sq. in. abs.
P_6	- Pressure at recuperator outlet, lb/sq. in. abs.
Pr	- Prandtl number, dimensionless
ΔP	- Gas pressure drop, lb/sq. ft.
Q	- Heat flow, BTU/hr
Q_{air}	- Heat flow to the air, BTU/hr
Q_{bath}	- Heat flow to the bath, BTU/hr
Q_{cond}	- Heat flow conducted along the sides of the module, BTU/hr
Q_H	- Heat flow to the heater, BTU/hr
Q_{loss}	- Heat flow lost, BTU/hr
Q_{in}	- Heat flow into the module, BTU/hr
Q_{out}	- Heat flow out of the module, BTU/hr

Q_n	- Heat flow to the elemental areas, BTU/hr
q_l	- Heat flow to the liquid, BTU/hr
q_s	- Heat flow to the solid, BTU/hr
R	- Gas constant, 38.7 ft ³ /°R
R_f	- Thermal resistance of fluoride, hr-ft ² -°F/BTU
R_g	- Thermal resistance of gas, hr-ft ² -°F/BTU
R_t	- Total thermal resistance, hr-ft ² -°F/BTU
R_w	- Wall thermal resistance, hr-ft ² -°F/BTU
R_{w-m}	- Geometric resistance from wall to melt line, dimensionless
Re	- Reynolds number, dimensionless
Re_{crit}	- Critical Reynolds number, dimensionless
r_i	- Inside radius of tube, ft
r_m	- Radius to melt line, ft
r_o	- Outside tube radius, ft
St	- Stanton number, dimensionless
T_b	- Bulk temperature, °F
$T_{i, fin}$	- Initial temperature of fin, °F
$T_{i, LiF}$	- Initial temperature of lithium fluoride, °F
$T_{i, plate}$	- Initial temperature of plate, °F
T_m	- Melt line temperature, °F or °R
T_{p1}	- Temperature of top third of upper plate, °F
T_{p2}	- Temperature of bottom third of upper plate, °F
T_{p3}	- Temperature of top third of lower plate, °F

T_{p4}	- Temperature of bottom third of lower plate, °F
$T_{LiF, S, Max}$	- Maximum temperature of top surface of lithium fluoride bath, °F
T_s	- Temperature of solid, °F
$T_{(x)}$	- Temperature of point X, °R
ΔT	- Temperature difference, °F
ΔT_{air}	- Increase in air temperature, °F
ΔT_L	- Temperature difference in liquid, °F
ΔT_{LiF}	- Lithium fluoride temperature difference, °F
ΔT_s	- Temperature difference in solid, °F
t	- Temperature, °F
t_f	- Fin temperature, °F
t_g	- Gas temperature, °F
t_{gi}	- Inlet gas temperature, °F
t_{go}	- Outlet gas temperature, °F
t_m	- Melt temperature, or mean, °F
Δt_g	- Gas temperature difference, °F
Δt_m	- Log mean temperature difference, °F
Δt_w	- Wall temperature difference, °F
V_b	- Bulk velocity, ft/sec
w	- Weight flow rate, lb/sec
x	- Distance, ft
δ_l	- Small distance in liquid, ft
δ_h	- Small distance in fluoride, ft

δ_s	- Small distance in solid, ft
δ_n	- Small distance in fluoride, ft
ρ	- Reflectivity, dimensionless
$\bar{\rho}$	- Mean density, lb/cu. ft
ρ_l	- Density of liquid, lb/cu. ft
ρ_s	- Density of solid, lb/cu. ft
τ	- Time, hr
μ	- Viscosity, lb/ft-sec
$\bar{\mu}$	- Mean viscosity, lb/ft-sec
η_s	- Structural blockage ratio, dimensionless
θ	- The angle whose origin is at the center of geometry of the hemisphere and is formed by a line drawn from a point on the cavity wall to the origin and a line representing the collector-receiver optic axis, radians

3.3 Lithium Fluoride Properties

Source: Reference 8

Appearance: White Powder

Bulk Density: 50 lb/ft³ (approximate)

Analysis:

	<u>Typical</u>	<u>Guaranteed</u>
Lithium Fluoride	99.6%	99.5%
Ignition Loss	0.4	0.5
Loss at 110° C	0.02	0.05
SO ₄	0.01	0.02
Fe ₂ O ₃	0.01	0.02
Acidity (as HF)	None	0.01
Alkalinity (as Li ₂ CO ₃)	0.005	0.02

Particle Size:

	<u>Typical</u>
minus 200 U. S. Std. Sieve	99%
minus 325 U. S. Std. Sieve	95%

Packaging:

Fiber drums with polyethylene liner

5, 25, 100, 200 lbs net

Shipping Regulations:

ICC - Classified as a Class B Poison requiring a white label on each shipping container. Railway Express shipments limited to 200 lbs in one container.

Postal - Not acceptable for mailing.

Handling Precautions:

Avoid breathing dust, prolonged contact with skin, or ingestion.

Physical Properties:

Molecular Weight	25.94	
Crystal Structure	Face-centered cubic; NaCl type	
	$a_{25^\circ\text{C}} = 4.01732 \text{ \AA}$	(1)
Color and Form	White Powder	
Density	(solid: 25°C) $2.63905 \pm 0.0001 \text{ gm/cm}^3$	(2)
	(liquid: 870°C) 1.789 gm/cm^3	
	(liquid: $887^\circ - 1058^\circ\text{C}$)	
	$d_4^{25} = 2.201 - 0.000474t \text{ gm/cm}^3$	(3)
Melting Point	$348^\circ\text{C} \pm 1^\circ$	(4)
	(ΔV on melting = + 29.4%)	(4a)
Boiling Point	1681°C	(5)
Heat Capacity	C_p (solid: 25°C) = 10.015 cal/degree/mole	
	C_p (liquid: $848^\circ - 896^\circ\text{C}$) = 15.51 cal/degree/mole	(4)
Heat of Formation	$\Delta H_{25^\circ\text{C}}^\circ = 146.3 \text{ kcal/mole}$	(5)
Heat of Fusion	$\Delta H_{848^\circ\text{C}} = 6.470 \text{ kcal/mole}$	(4)
Heat of Vaporization	$\Delta H_{1681^\circ\text{C}} = 51.0 \text{ kcal/mole}$	(5)
Free Energy of Formation	$\Delta F_{25^\circ\text{C}}^\circ = 139.6 \text{ kcal/mole}$	(5)
Entropy	$S_{25^\circ\text{C}}^\circ = 8.52 \text{ cal/degree/mole}$	(4)

(For further data on thermodynamic functions of LiF, from 298°K to 1200°K , see Reference 4.)

Surface Tension of Fused Salt
(LiF-nitrogen)

Temp. °C	γ (dynes/cm)	(6)
868.5	249.5	
944	242.3	
1029	233.5	
1156	217.4	
1270	201.1	

Electrical Conductivity of
Fused Salt

Temp. °C	Specific Conductance (ohm ⁻¹ cm ⁻¹)	(7)
860	3.30	
890	8.39	
920	8.55	
950	8.77	
980	9.01	

Vapor Pressure of Fused Salt

Temp. °C	mm of Hg	(8)
1047	1	
1211	10	
1333	40	
1425	100	
1591	400	
1681	760	

Solubility in Water

Temp. °C	Weight % LiF	(9)
0°	0.1204	
25°	0.1331	
35°	0.1354	

Insoluble in organic solvents such as
alcohol, acetone, ether, and THF.

Uses:

Lithium fluoride is used extensively as an ingredient in brazing and soldering fluxes and in welding rod coatings. Various salt combinations are suitable for hard soldering (10) and for brazing steel (11), aluminum (12), titanium and other metals (13).

Lithium fluoride is used as a flux and an opacifier in ceramics. It also imparts toughness, brilliance, harder surface, resistance to devitrification, and lower coefficient of expansion to glass and ceramic bodies.

Illustrative of unusual properties contributed by lithium fluoride in glass and ceramics are:

Electrically conductive glass includes LiF and suboxides of titanium (14).

Mullite formation from kaolin at temperatures below 900° C is made possible by LiF additions (15).

A formed, fired dielectric ceramic consists chiefly of a double fluoride of lithium and iron, manganese, lead, or zinc (16).

Ductile ceramics employing LiF have been prepared (17).

Lithium fluoride is a component of special quality fluoborate glass (18).

A reflection reducing coating is applied to glass as a sol of LiF (19).

In the preparation of high-density periclase from magnesia, the required firing temperature is lowered by the addition of lithium fluoride (20).

Lithium fluoride crystals are used in optics and prisms for infrared and X-ray spectroscopy (21), and as windows in monochromators for ultraviolet transmission (22). Ultraviolet reflector coatings of high performance, good stability, and precision application on aluminum mirrors are made with lithium fluoride (23).

Fuel cells for space vehicles may use an LiF-LiCl eutectic as an electrolyte (24).

Extraction of aluminum is improved by the addition of LiF to the cryolite in the pot lines. The addition lowers the melting point and density of the electrolyte and increases the electrical conductivity. Cell output may be increased by as much as 12% (25).

N.B. The information in this bulletin is presented in good faith, but no warranty is given, nor is freedom from any patent to be inferred.

References: Lithium Fluoride Only

1. Straumanis, Ievens and Karlsons, Z. physik, Chem., B42, 143 (1939).
2. Hutchison and Johnston, J. Am. Chem. Soc., 62, 3165 (1940).
3. "International Critical Tables," McGraw-Hill Book Co., Inc., New York, N. Y., 1, 149.
4. Douglas and Dever, J. Am. Chem. Soc., 76, 4826 (1954).
- 4a. Schinke, H., and Sauerwald, F., Z. anorg. u. allgem Chem. 287, 313-24 (1956).
5. "Selected Values of Chemical Thermodynamic Properties," Circular 500, U. S. National Bureau of Standards, U. S. Government Printing Office, Washington, D. C. (1952).
6. "International Critical Tables," McGraw-Hill Book Co., Inc., New York 4, 442.
7. Yim, E. W., and Feinleib, M., J. Electrochemical Soc. 104, 622-30 (1957).
8. Kelley, U. S. Bureau of Mines, Bulletin 383 (1935).
9. Payne, J. Am. Chem. Soc., 59, 947 (1937).
10. Coleman, J. D. and Ewing, C. W., U. S. Patent 2, 322, 416 (to General Motors) June 22, 1943.
11. Harvey, G. W., U. S. Patent 2, 442, 892 (to Solar Aircraft) June 8, 1948.
12. Miller, M. A. and Haupin, W. E., U. S. Patents 2, 552, 104-6 (to Alcoa), May 8, 1951.
13. Marlub-Sobel, M. and Weigart, K. M., U. S. Patent 2, 882, 593, (to Curtiss-Wright Corp.), June 10, 1957.
14. King, B. W. and Tripp, H. P., U. S. Patent 2, 933, 458 (to Diamond Alkali), April 19, 1960.
15. Okuda, Hiroshi; Kato Shuzo; and Iga, Takeo, Yogyo Kyokai Shi 69 (785): 150-60, May 1961.
16. Mockrin, Isidore, U. S. Patent 2, 899, 321 (to Pennsalt), August 11, 1959.
17. Hazlett, T. H., Univ. of California, Inst. of Eng. Res. Program, NP-19066, 1961. (Nuc. Sci. Abs. 15(14): 2391, July 31, 1961.)

18. De Paolis, P.F., U.S. Patent 2,933,404 (to Eastman), April 19, 1960.
19. Moulton, H.R., U.S. Patent 2,432,484 (to American Optical Co.) December 9, 1947.
20. Atlas, Leon M., U.S. Patent 2,823,134 (to Armour Research Foundation of Illinois) February 11, 1958.
21. a) Birks, L.S., *Revue Universelle Mines* 15(5): 526-30, May 1959.
b) Prugger, Hans, et al, *Z. angew. Phys.* 11(12): 467-70, December 1959.
c) Rabillon, R., et al, *Revue Universelle Mines* 15(5): 536-8, May 1959.
d) Wright, N., *Rev. Sci. Instr.* 15, 22-27 (1944).
22. Eby, J.E., et al, *Phys. Rev.* 116(5): 1099-1105, December 1, 1959.
23. Angel, D.W., et al, *J. Opt. Soc. Am.* 51(8): 913-4, August 1961.
24. a) Del Duca, M.G., Fuscoe, J.M., and Johnston, T.A., *Astronautics* 5(3): 36-8, 40, 42, 44, March 1960.
b) Snoke, D.R. and Fuscoe, J.M., *SAE Journal* 69(9) 68-9, June 1961.
25. a) Ransley, C.E., *J. Metals* 14(2): 129-35, February 1962.
b) Lewis, R.A., U.S. Patent 3,034,972 (to Kaiser Aluminum), May 15, 1962.
c) Yim, E.W., and Feinleib, M., *J. Electrochem. Soc.* 104, No. 10, 626-30, October 1957.
d) I-An Chu and A. I. Belvaev., *Isvest. Vysshikli Ucheb. Zavedenil. Tsvetnays Mat.* 2. No. 2, 69-79 (1959). (*Chem. Abs.* 53, 1959, p. 186836).

Price List:

Lithium Fluoride - 99.5% Guaranteed

<u>Quantity</u>	<u>Delivered</u>	<u>Per Pound</u>
10, 000 lbs and up	50 x 200 lb drums	\$1.50
	100 x 100 lb drums	1.50
2, 000 lbs through 9, 900 lbs		1.55
1, 000 lbs through 1, 900 lbs		1.60
200 lbs through 500 lbs		1.65

Delivered in continental United States (Alaska excepted) and f. a. s. eastern U. S. ports by rail or truck.

<u>F. O. B. Plant</u>	<u>Per Pound</u>
100 lb drums	\$1.65
25 lb drums	1.80
5 lb drums	2.00
1 lb bottle	2.50

F. O. B. Bessemer City, North Carolina

Prices are subject to change without prior notice.

Minimum order \$10.00.

Terms - Net 30 days.

Containers and Shipping Information:

	<u>1 lb</u>	<u>5 lb</u>	<u>25 lb</u>	<u>100 lb</u>	<u>200 lb</u>
	glass in carton	poly. lined fiber drum	poly. lined fiber drum	poly. lined fiber drum	poly. lined fiber drum
Rated capacity	16 oz	1 gal	5 gal	16.5 gal	36 gal
Width, in.	5 x 5	9	12	16	21
Height, in.	8.5	5	13	21	28
Ocean cube	-	0.234 (0/3)	1.083 (1/0)	3.111 (3/1)	7.146 (7/2)
Gross wt. lbs	5	6	28	109	214
Ship by	exp.	exp.	exp.	frt.	frt.
Label	noi	noi	noi	noi	noi

Schedule B 83990. Export license required over \$25.00.

8.4 Heat Input Analysis

The heat-conduction problem in the Brayton cycle cavity receiver or modules is nonlinear because the change in phase of the lithium fluoride involves a moving boundary (the melt line) whose location is unknown. Since there are at present no analytical techniques available for solving this nonlinear problem, recourse has been taken to approximate methods. These approximate methods fall under the categories of finite differences, variational principles and heat balance integral. In this Appendix use is made of the heat balance integral method to predict the heat transfer performance of the Brayton cycle modules.

8.4.1 Results

The results of the analysis show that by the use of the heat balance integral the problem can be expressed in form of an integro-differential equation which can be solved by laplace transform or the differential analog computer. Using an additional approximation, namely, a linear relationship between melt line position and the boundary temperatures θ and θ_2 , the problem reduces to a single differential equation which can be solved also on the differential analog computer or by graphic integration.

8.4.2 Discussion and Recommendations

Because of the assumed quadratic temperature distribution in the lithium fluoride, it is not possible to evaluate the accuracy of the methods used except by experimental means or by the use of analog methods like the Columbia University analog computer. In essence, then, the researcher has three tools (experimental, by analogs and by analysis) available to solve this particular heat transfer problem. It is probably wise to make use of all three methods for a complete understanding of the problem.

5.4.3 Nomenclature

A	Area
a	Constant
B	Distance between top plate and top of lithium fluoride
b	Constant
C	Constant
C_l	Specific heat of liquid lithium fluoride
C_s	Specific heat of solid lithium fluoride
f	Function
k_l	Thermal conductivity of liquid lithium fluoride
k_s	Thermal conductivity of solid lithium fluoride
L	Distance between top and bottom plate
l_l	Width of liquid
l_s	Width of solid
l_{si}	Initial width of solid
q_1	Heat transferred to lithium fluoride
q_2	Heat removed from lithium fluoride
S	Distance of melt line from top plate
t_1	Temperature of lithium fluoride at top
t_2	Temperature of lithium fluoride at bottom
t_f	Temperature of cooling fluid
t_m	Lithium fluoride melting temperature
U	Overall heat transfer coefficient of cooling fluid

W	Inventory of lithium fluoride
V	Volume of lithium fluoride
X	Distance from top plate
α	Thermal diffusivity k/c
θ_1	Temperature excess over melting point at top
θ_2	Temperature deficiency from melting point at bottom
θ_{\max}	Maximum temperature excess
λ	Heat of fusion
ρ_e	Density of liquid
ρ_s	Density of solid
T	Time

SPECIAL RELATIONS

$$\alpha_1 = \frac{\rho_s}{\rho_e}$$

$$\alpha_8 = \alpha_7 \nu \theta_5$$

$$\alpha_2 = \frac{L_{si}}{L}$$

$$\alpha_9 = \alpha_6 q_1$$

$$\alpha_3 = 1 - \frac{L_{si}}{L} = 1 - \alpha_2$$

$$\alpha_9' = \frac{L_{sf} q_1}{K_e}$$

$$\alpha_4 = 1 - \rho_s/\rho_e = 1 - \alpha_1$$

$$\beta_1 = \alpha_5 + \alpha_4 S/L$$

$$\alpha_5 = \rho_s/\rho_e (1 - \frac{L_{si}}{L}) = \alpha_1 \alpha_3$$

$$\beta_2 = \alpha_5 + S/L (\alpha_4 - 1)$$

$$\alpha_6 = \frac{L}{K_e}$$

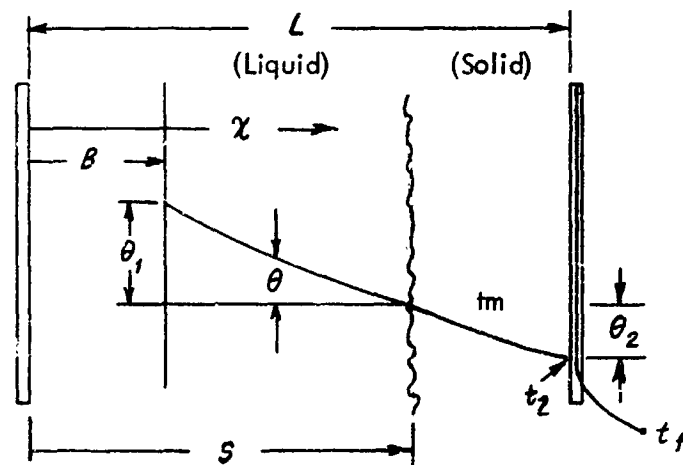
$$\beta_3 = 1 - S/L$$

$$\alpha_7 = L/K_s$$

$$\beta_4 = \frac{\theta_2}{\theta_f} - 1$$

ANALYSIS

The heat conduction problem of the Brayton cycle modules shall be considered as a one dimensional problem, and the effect of any fins is accounted for as an equivalent conductivity. Schematically, the problem appears as below*



The governing equation in each region is:

$$\alpha \frac{\partial^2 \theta}{\partial x^2} = \frac{\partial \theta}{\partial \tau} = \theta$$

Following the usual procedure θ is expressed as a polynomial in x , i.e.

$$\theta(x, \tau) = \alpha(\tau) + b(\tau)x + c(\tau)x^2$$

For the liquid section:

$$\text{At } x = B \quad -K_e \left(\frac{\partial \theta}{\partial x} \right)_B = q_1$$

*Note: For explanation of the symbols see nomenclature.

$$\frac{\partial \theta}{\partial x} = b + 2cx$$

$$\left(\frac{\partial \theta}{\partial x}\right) = b + 2cB$$

$$-\frac{g_1}{K_e} = b + 2cB \text{-----} 1$$

$$\text{at } x=B \quad \theta = \theta_1$$

$$\theta_1 = a + bB + cB^2 \text{-----} 2$$

$$\text{at } x=S \quad \theta = 0$$

$$0 = a + bS + cS^2 \text{-----} 3$$

Combine 2 & 3

$$\theta_1 = bB - bS + cB^2 - cS^2$$

$$\theta_1 = b(B-S) + c(B^2 - S^2)$$

Combine with 1

$$\theta_1 = \left(-\frac{g_1}{K_e} - 2cB\right)(B-S) + c(B^2 - S^2)$$

$$\theta_1 = -\frac{g_1}{K_e} (B-S) + c[(B^2 - S^2) - (B-S)2B]$$

$$c = \frac{\theta_1 + \frac{g_1}{K_e} (B-S)}{(B^2 - S^2) - (B-S)2B}$$

$$= \frac{\theta_1 + \frac{g_1}{K_e} (B-S)}{-(B^2 - 2BS + S^2)} = \frac{\theta_1 + \frac{g_1}{K_e} (B-S)}{-(B-S)^2}$$

$$c = \frac{-\theta_1}{(B-S)^2} - \frac{g_1}{K_e(B-S)}$$

Solving for b by Equation 1

$$-\frac{g_1}{K_e} = b + 2B \left[\frac{-\theta_1}{(B-S)^2} - \frac{g_1}{K_e(B-S)} \right]$$

$$b = -\frac{g_1}{K_e} + \frac{2B\theta_1}{(B-S)^2} + \frac{2Bg_1}{K_e(B-S)}$$

Solving for a by Equation 3

$$a = \frac{S^2\theta_1}{(B-S)^2} + \frac{g_1 S^2}{K_e(B-S)} + \frac{g_1 S}{K_e} - \frac{2B\theta_1 S}{(B-S)^2} - \frac{2Bg_1 S}{K_e(B-S)}$$

$$\theta = \frac{S^2\theta_1}{(B-S)^2} + \frac{g_1 S^2}{K_e(B-S)} + \frac{g_1 S}{K_e} - \frac{2B\theta_1 S}{(B-S)^2} - \frac{2Bg_1 S}{K_e(B-S)}$$

$$+ \left[-\frac{g_1}{K_e} + \frac{2B\theta_1}{(B-S)^2} + \frac{2Bg_1}{K_e(B-S)} \right] K + \left[\frac{-\theta_1}{(B-S)^2} - \frac{g_1}{K_e(B-S)} \right] \chi^2$$

Regrouping, we obtain

$$\theta = \left(\frac{g_1}{K_e(B-S)} + \frac{\theta_1}{(B-S)^2} \right) S^2 \left[1 - \left(\frac{\chi}{S} \right)^2 \right] + \left(\frac{g_1}{K_e} - \frac{2B\theta_1}{(B-S)^2} - \frac{2Bg_1}{K_e(B-S)} \right) S \left(1 - \frac{\chi}{S} \right)$$

Note that θ , b and s are functions of time τ and B and S are related

$$\theta = E_e(\tau) \left(1 - \frac{\chi}{S} \right) + F_2(\tau) \left[1 - \left(\frac{\chi}{S} \right)^2 \right]$$

Similarly, for the solid section:

$$\theta(\chi, \tau) = a(\tau) + b(\tau)\chi + c(\tau)\chi^2$$

$$\text{at } \chi = L \quad -K_s \left(\frac{\partial \theta}{\partial \chi} \right)_2 = g_2 = v(f_2 - t_f)$$

$$\frac{\partial \theta}{\partial \chi} = b + 2c\chi$$

$$\left(\frac{\partial \theta}{\partial \chi} \right)_1 = b + 2cL$$

$$-\frac{g_2}{K_s} = b + 2cL \quad 4$$

$$\text{at } x = S \quad \theta = 0$$

$$0 = a + bS + cS^2 \quad 5$$

$$\text{at } x = L \quad \theta = \theta_2$$

$$\theta_2 = a + bL + cL^2 \quad 6$$

Combining 5 & 6

$$\theta_2 = bL - bS + cL^2 - cS^2$$

$$\theta_2 = b(L-S) + c(L^2 - S^2)$$

Combine with 4

$$\theta_2 = \left(\frac{-g_2}{K_s} - 2cL \right) (L-S) + c(L^2 - S^2)$$

And after regrouping

$$c = \frac{-\theta_2}{(L-S)^2} - \frac{g_2}{K_s(L-S)}$$

Combine with 3

$$b = \frac{-g_2}{K_s} + 2L \left[\frac{\theta_2}{(L-S)^2} + \frac{g_2}{K_s(L-S)} \right]$$

Solve for a by Equation 5

$$\begin{aligned} a &= \frac{\theta_2 S^2}{(L-S)^2} + \frac{g_2 S^2}{K_s(L-S)} + \frac{Sg_2}{K_s} - \frac{2L\theta_2 S}{(L-S)^2} - \frac{2Lg_2 S}{K_s(L-S)} \\ \theta &= \frac{\theta_2 S^2}{(L-S)^2} + \frac{g_2 S^2}{K_s(L-S)} + \frac{Sg_2}{K_s} - \frac{2L\theta_2 S}{(L-S)^2} - \frac{2Lg_2 S}{K_s(L-S)} \\ &+ \left[-\frac{g_2}{K_s} + \frac{2L\theta_2}{(L-S)^2} + \frac{2Lg_2}{K_s(L-S)} \right] x + \left[\frac{-\theta_2}{(L-S)^2} - \frac{g_2}{K_s(L-S)} \right] x^2 \end{aligned}$$

$$\theta = \left(\frac{\theta_2}{(L-S)^2} + \frac{f_2}{K_S(L-S)} \right) S^2 \left[S - \left(\frac{\chi}{S} \right)^2 \right] + \left(\frac{f_2}{K_S} - \frac{2L\theta_2}{(L-S)^2} - \frac{2L f_2}{K_S(L-S)} \right) S \left(1 - \frac{K}{S} \right)$$

$$\theta = E_S(\tau) \left(1 - \frac{\chi}{S} \right) + F_S(\tau) \left(1 - \frac{\chi^2}{S^2} \right)$$

Note: f_2 , S and θ_2 are functions of time

$$\begin{aligned} \text{but } f_2 &= V(t_2 - t_f) \\ &= V(t_2 - t_m - \tau_s + t_m) \\ &= V(\theta_2 - \theta_f) \end{aligned}$$

$\therefore \theta_2$ and S are functions of time.

Find B from conservation of mass

$$l_e A \rho_e + l_s A \rho_s = W = \text{const} \quad 7$$

$$\text{Also, } B + l_e + l_s = L = \text{const} \quad 8$$

$$S + l_s = L \quad 9$$

Combine 7 & 8 to eliminate l_e

$$(L - B - l_s) \rho + l_s \rho_s = \frac{W}{A}$$

Combine with 9 eliminating l_s

$$(L - S) \rho_s + \rho_e (S - B) = \frac{W}{A} = \frac{A l_s \rho_s}{A}$$

$$\therefore B = L \left[\frac{\rho_s}{\rho_e} \left(1 - \frac{l_s \rho_s}{L} \right) + \frac{S}{L} \left(1 - \frac{\rho_s}{\rho_e} \right) \right]$$

$$\text{Let } \omega_1 = \frac{\rho_s}{\rho_e} \quad \alpha_1 = 1 - \frac{\rho_s}{\rho_e} = -\alpha_1$$

$$\alpha_2 = \frac{l_s \rho_s}{L} \quad \alpha_3 = \frac{\rho_s}{\rho_e} \left(1 - \frac{l_s \rho_s}{L} \right) = \alpha_1 \alpha_2$$

$$\alpha_3 = 1 - \frac{l_s \rho_s}{L} = 1 - \alpha_2 \quad \alpha_2 = \frac{L}{K_e}$$

Also,

$$\begin{aligned} \beta_1 &= \alpha_5 + \alpha_4 \frac{s}{L} & \dot{\beta}_1 &= \alpha_4 \frac{\dot{s}}{L} \\ \beta_2 &= \alpha_5 + \frac{s}{L} (\alpha_4 - 1) & \dot{\beta}_2 &= \frac{\dot{s}}{L} (\alpha_4 - 1) \end{aligned}$$

$$\therefore \underline{B = L\beta_1}$$

Now, the conduction equation must be solved with the following boundary conditions:

For the Liquid

$$q_{in} - q_{out} = \int \frac{\delta}{\delta T} (E) dV$$

where $E = \rho_e C_e (t_e - t_m) = \rho_e C_e \theta_e$

$$dV = A dx$$

$$q_{out} = -K_e \left(\frac{\partial \theta_e}{\partial x} \right)_s A$$

and $q_{in} = \text{CONST.} = q_1 A$

$$A q_1 + K_e \left(\frac{\partial \theta_e}{\partial x} \right)_s A = \int_{\frac{\delta}{\delta T}}^{T_1(T)} (\rho_e C_e \theta_e) A dx$$

$$q_1 + K_e \left(\frac{\partial \theta_e}{\partial x} \right)_s = \rho_e C_e \int_{\frac{\delta}{\delta T}}^{s(T)} (\theta_e) dx \dots\dots\dots 10$$

Similarly, for the solid

$$-A K_s \left(\frac{\partial \theta_s}{\partial x} \right)_s - q_2 A = \int_{\frac{\delta}{\delta T}}^{T_1(T)} (\rho_s C_s \theta_s) dV$$

$$-K_s \left(\frac{\partial \theta_s}{\partial x} \right)_s - q_2 = \rho_s C_s \int_{\frac{\delta}{\delta T}}^{LH \text{ CONT}} (\theta_s) dx \dots\dots\dots 11$$

At the melt line

$$K_s \left(\frac{\partial \theta_s}{\partial x} \right)_s - K_e \left(\frac{\partial \theta_e}{\partial x} \right)_s = \lambda \rho_e \frac{\delta s}{\delta T} \dots\dots\dots 12$$

Add equation 10 & 11

$$q_1 + K_e \left(\frac{\partial \theta_e}{\partial x} \right)_s - K_s \left(\frac{\partial \theta_s}{\partial x} \right)_s - q_2 = \rho_e C_e \int_{b(\tau)}^{s(\tau)} \frac{\partial}{\partial \tau} (\theta_e) dx + \rho_s C_s \int_{s(\tau)}^L \frac{\partial}{\partial \tau} (\theta_s) dx \dots 13$$

Combine Equations 12 & 13

$$q_1 - q_2 - \lambda \rho_e \frac{\partial s}{\partial \tau} = \rho_e C_e \int_{b(\tau)}^{s(\tau)} \frac{\partial}{\partial \tau} (\theta_e) dx + \rho_s C_s \int_{s(\tau)}^L \frac{\partial}{\partial \tau} (\theta_s) dx \dots \dots \dots 14$$

*Changing the order of integration - differentiation by the Leibnitz rule yields
(see pg. 233 Advanced Mathematics for Engineers by Reddick & Miller)

Let $\theta_e = f_e(x, \tau) = E_e(\tau) \left(1 - \frac{x}{s}\right) + F_e(\tau) \left[1 - \left(\frac{x}{s}\right)^2\right]$

$\theta_s = f_s(x, \tau) = E_s(\tau) \left(1 - \frac{x}{s}\right) + F_s(\tau) \left[1 - \left(\frac{x}{s}\right)^2\right]$

$$\therefore \frac{d}{d\tau} \int_{b(\tau)}^{s(\tau)} f_e(x, \tau) dx = \int_{b(\tau)}^{s(\tau)} \frac{\partial}{\partial \tau} f_e(x, \tau) dx - f_e(b, \tau) \frac{db}{d\tau} + f_e(s, \tau) \frac{ds}{d\tau}$$

And

$$\frac{d}{d\tau} \int_{s(\tau)}^L f_s(x, \tau) dx = \int_{s(\tau)}^L \frac{\partial}{\partial \tau} f_s(x, \tau) dx - f_s(s, \tau) \frac{ds}{d\tau} + \underbrace{f_s(L, \tau) \frac{dL}{d\tau}}$$

Equation 14 becomes

$$q_1 - q_2 - \lambda \rho_e \frac{\partial s}{\partial \tau} = \rho_e C_e \left[\frac{d}{d\tau} \int_{b(\tau)}^{s(\tau)} f_e(x, \tau) dx + f_e(b, \tau) \frac{db}{d\tau} - f_e(s, \tau) \frac{ds}{d\tau} \right] \\ + \rho_s C_s \left[\frac{d}{d\tau} \int_{s(\tau)}^L f_s(x, \tau) dx + f_s(s, \tau) \frac{ds}{d\tau} \right]$$

*Using an averaging technique the differential with respect to time may be taken outside of the integral as is done in References 1 and 2. This possibility should be checked out for the present problem if more work is to be done with it.

SUBSTITUTING:

$$g_1 - g_2 - \lambda \beta_2 \frac{\partial s}{\partial T} = \rho_c c_e \left[\frac{d}{dT} \int_B^s \left[E_e \left(1 - \frac{\lambda}{s} \right) + F_e \left(1 - \frac{\lambda^2}{s^2} \right) \right] ds \right]$$

INTEGRATING AND INSERTING THE LIMITS YIELDS:

$$15... \quad g_1 - g_2 - \lambda \beta_2 \frac{ds}{dT} = \rho_c c_e \left\{ \frac{d}{dT} \left[E_e \left(s - \frac{s^2}{2s} \right) + F_e \left(s - \frac{s^3}{3s^2} \right) - E_e (B - \frac{B^2}{2B}) - F_e (B - \frac{B^3}{3B^2}) \right] \right\}$$

IT WILL BE RECALLED THAT

$$B = L/\beta_1 \text{ AND}$$

ALSO,

$$E_e = \left(g_1 / K_e - \frac{2B\theta_1}{(B-s)^2} - \frac{2B g_1}{K_e (B-s)} \right) s = d_6$$

AND

$$\dot{E}_e = d_6 g_1 \dot{s} / L - \frac{2L [\beta_2^2 (\dot{s} / L \theta_1 \beta_1 + \dot{s} / L \theta_1 \beta_1 + \dot{s} / L)]}{\beta_2^4}$$

$$F_e = \frac{(\dot{s} / L)^2}{d_5 + d_4 \dot{s} / L - \dot{s} / L} \left(d_6 g_1 + \frac{c}{d_5 + d_4} \right)$$

$$\dot{F}_e = \frac{d_6 g_1 (\beta_1 - \dot{s} / L \dot{\beta}_1 - (\dot{s} / L)^2 \dot{\beta}_2)}{(\beta_2)^2} + \frac{\dot{\beta}_2 (\beta_2)}{(\beta_2)^2}$$

$$E_s = \frac{s}{L} \left(\frac{(\theta_2 - 1)}{K_3} \right) - \frac{2\theta_2}{(1 - \dot{s} / L)^2}$$

∴

$$E_s = \frac{1}{L} U \theta_2 \beta_4 - \frac{2\theta_2 \dot{s} / L}{\beta_3^2}$$

$$\dot{E}_s = \frac{\dot{s} / L}{L} U \theta_2 \beta_4 + \frac{\dot{s} / L}{L} U \theta_2 \beta_4 -$$

$$F_s = \frac{\theta_2 (\dot{s} / L)^2}{\beta_3^2} + \frac{(\dot{s} / L) d_7 U \theta_2 \beta_4}{\beta_3} =$$

$$\dot{F}_s = \frac{\beta_3^2 [\dot{\theta}_2 (\dot{s} / L)^2 + \theta_2 2 \dot{s} / L \times \dot{s} / L] - \theta_2 c}{\beta_3^4}$$

DIFFERENTIATING EQ. 15 AND SUBSTITUTING FOR E_e , F_e , E_s , F_s AND

$$g_1 - g_2 - \lambda \beta_2 \frac{ds}{dT} = \rho_c c_e \left\{ E_e \dot{s} - E_e \dot{\beta} - \frac{\beta^2}{2} \frac{E_e}{\beta} \dot{s} + E_e \frac{\beta}{\beta} \dot{\beta} + \left(\frac{\beta}{2} - B + \frac{B^2}{2s} \right) \dot{E}_e \right\}$$

$$+ \left[E_c \left(1 - \frac{B}{S} \right) + F_c \left(1 - \frac{B^2}{S^2} \right) \right] \frac{dB}{d\tau} - \underbrace{\left[E_c \left(1 - \frac{S}{S} \right) + F_c \left(1 - \frac{B^2}{S^2} \right) \right]}_{\text{THIS TERM IS ZERO}}$$

$$- \frac{B^2}{2S} - F_c \left(B - \frac{B^2}{3S^2} \right) + \left[E_c \left(1 - \frac{B}{S} \right) + F_c \left(1 - \frac{B^2}{S^2} \right) \right] \frac{dB}{d\tau}$$

$$\dot{B} = L \alpha_4 \frac{\dot{S}}{L} = \alpha_4 \dot{S}$$

$$\frac{\dot{S}}{L} = \frac{2L \frac{1}{2} \theta_1 \dot{\beta}_1}{\beta_2^2} - \frac{2\alpha_6 g_1 \frac{1}{2} L \beta_1}{\beta_2}$$

$$\frac{\dot{\beta}_1 - \frac{1}{2} \theta_1 \beta_1 \dot{\beta}_2}{\beta_2^2} - \frac{2\alpha_6 g_1 [\beta_2 (\frac{1}{2} L \beta_1 + \frac{1}{2} L \dot{\beta}_1) - \frac{1}{2} L \beta_1 \dot{\beta}_2]}{\beta_2^2}$$

$$\frac{1}{L - \frac{1}{2} L} = \frac{\alpha_6 g_1 (\frac{1}{2} L)^2}{\beta_2} + \frac{\theta_1 (\frac{1}{2} L)^2}{(\beta_2)^2}$$

$$\frac{\dot{\theta}_1 (\frac{1}{2} L)^2 + \theta_1 2 \frac{1}{2} L \dot{\beta}_1 - \dot{\theta}_1 (\frac{1}{2} L)^2 2 \beta_2 \dot{\beta}_2}{\beta_2^4}$$

$$- \frac{2L \nu \theta_f (\frac{\theta_2}{\theta_1} - 1)}{K_3 (1 - \frac{1}{2} L)}$$

IF WE LET

$$\alpha_7 = \cdot$$

$$\beta_3 = 1$$

$$\frac{2\alpha_7 \nu \theta_f \beta_4 \frac{1}{2} L}{\beta_3}$$

$$\frac{2\beta_3^2 (\dot{\theta}_2 \frac{1}{2} L + \theta_2 \frac{1}{2} L) - 2\theta_2 \frac{1}{2} L 2\beta_3 \dot{\beta}_3}{\beta_3^4} - \frac{2\alpha_7 \nu \theta_f [\beta_3^2]}{\beta_3^4}$$

$$\frac{\theta_2 (\frac{1}{2} L)^2}{\beta_3^2} + \frac{\alpha_8 (\frac{1}{2} L)^2 \beta_4}{\beta_3}$$

$$\text{LET } \alpha_8 = \alpha_7 \nu \theta_f$$

$$\frac{2\beta_3 \dot{\beta}_2}{\beta_3^2} + \frac{\alpha_8 [\beta_3 (2 \frac{1}{2} L \cdot \frac{1}{2} L \beta_4 + (\frac{1}{2} L)^2 \dot{\beta}_4 - (\frac{1}{2} L)^2 \beta_4 \dot{\beta}_3)]}{\beta_3^2}$$

THEIR DERIVATIVES YIELDS

$$\frac{2}{3} F_c \dot{S} - E_c \dot{B} - \frac{2}{3} \frac{B^3}{S^3} F_c \dot{S} + F_c \frac{B^2}{S^2} \dot{B} + \left(\frac{2}{3} S - B + \frac{B^3}{3S^2} \right) \dot{F}_c + E_c \dot{B} - E_c$$

$$\frac{s^2}{s^2} \left] \frac{ds}{dT} \right] + \beta_3 C_s \left[\frac{d}{dT} \int_s^L \left[E_s \left(1 - \frac{x}{s} \right) + F_s \left(1 - \frac{x^2}{s^2} \right) \right] dx + \underbrace{\left[E_s \left(1 - \frac{s}{s} \right) + F_s \left(1 - \frac{s^2}{s^2} \right) \right] \frac{ds}{dT}}_{\text{THIS TERM IS ZERO}} \right]$$

$$\left. \right] + \beta_3 C_s \left\{ \frac{d}{dT} \left[E_s \left(L - \frac{L^2}{2s} \right) + F_s \left(L - \frac{L^3}{3s^2} \right) - E_s \left(s - \frac{s^2}{2s} \right) - F_s \left(s - \frac{s^3}{3s^2} \right) \right] \right\}$$

1

$$\frac{L}{s} \quad \beta_4 = \frac{\theta_2}{\theta_1} - 1 ; \quad \dot{\beta}_4 = \frac{\dot{\theta}_2}{\theta_1}$$

$$- \frac{s}{L} \quad \dot{\beta}_3 = - \frac{\dot{s}}{L}$$

$$\frac{\beta_3 (\dot{\beta}_4 \frac{s}{L} + \dot{\beta}_4 \frac{s}{L}) - \dot{\beta}_4 \frac{s}{L} \beta_3}{\beta_3^2}$$

$$\left\{ \frac{E_s}{s} \dot{\theta} + E_s \dot{\theta} - E_s \frac{\theta^2}{s^2} \dot{\theta} \right\} + \beta_3 C_s \left\{ - \frac{1}{2} \dot{s} + \frac{E_s}{2} \frac{L^2}{s^2} \dot{s} + \left(L - \frac{s}{2} - \frac{L^2}{2s} \right) \dot{E}_s \right. \\ \left. + F_s \left(- \frac{1}{3} \dot{s} + \frac{2}{3} \frac{L^3}{s^3} \dot{s} \right) + \left(L - \frac{s}{3} - \frac{1}{3} \frac{L^3}{s^2} \right) \dot{F}_s \right\}$$

$$\begin{aligned}
\theta_1 - \frac{d\theta}{dx} \left(\frac{\theta_2}{\theta_1} - 1 \right) - \lambda \rho c \dot{s} = \rho C_p \left\{ L \frac{\dot{s}}{L} \left[\frac{d_1 \beta_2^2 - 2L \theta_1 \beta_1 - 2d_1 \beta_1 \beta_2}{\beta_2^2} \right] \right. \\
- \frac{2d_1 [\beta_2 (\dot{s}/L \beta_1 + \dot{s}'/L) - \dot{s}/L \beta_1 \dot{s}/L (d_1 \beta_2^2)}{\beta_2^2} \\
\left. + \frac{L \dot{s}/L}{3 \dot{s}/L} \left[2(\dot{s}/L)^3 - 3\beta_1 (\dot{s}/L)^2 + \beta_1^3 \right] \right\} + \\
- \frac{2d_2 (\dot{s}/L \beta_3 + \dot{s}'/L)}{\beta_3} - \frac{2d_2 \beta_3 \dot{s}/L}{\beta_3^2} \\
- \frac{L \dot{s}/L}{3 (\dot{s}/L)^2} \left(-(\dot{s}/L)^3 + 2(\dot{s}/L)^2 + 1 \right)
\end{aligned}$$

ALSO, ACCORDING TO THE CONDUCTION EQUATION

$$\dot{\theta} = \alpha \frac{\partial^2 \theta}{\partial x^2} \quad \text{ASSUMING, AS BEFORE}$$

$$\dot{\theta} = 2\alpha c$$

$$x = B$$

$$\dot{\theta}_1 = 2\alpha c \left[-\frac{\theta_1}{(B-s)^2} - \frac{\theta_1'}{K_2(B-s)} \right]$$

$$\dot{\theta}_1 = -2\alpha c \left[\frac{\theta_1}{(L\beta_1 - s)^2} - \frac{\theta_1'}{K_2(L\beta_1 - s)} \right] =$$

$$\dot{\theta}_1 = -\frac{2\alpha c}{L^2 \beta_2^2} \left[\theta_1 + d_1 \beta_2 \right]$$

AT $x = L$

$$\dot{\theta}_2 = -2\alpha c \left[\frac{\theta_2}{(L-s)^2} + \frac{\theta_2'}{K_3(L-s)} \right]$$

$$\dot{\theta}_2 = -\frac{2\alpha c}{L^2 \beta_3^2} \left[\theta_2 + d_2 \beta_3 \left(\frac{\theta_2}{\theta_1} - 1 \right) \right]$$

NOTE: EQUATION 16 CAN BE PUT INTO THE FOLLOWING FORM

$$f_1(\dot{s}/L, \theta_3, \theta_2) \dot{s} = -f_2(\dot{s}/L, \theta_1, \theta_2)$$

ALSO, THE MELTING PROBLEM IS NOW EXPRESSED WITH THE USE OF TWO DIFFERENTIAL ANALOG COMPUTER OR WITH THE USE OF LA EQUATIONS 1, 2 AND 3 REDUCES THE PROBLEM TO ONE DIFFERENTIAL EQUATION

$$\begin{aligned}
 & 2(\dot{s}/L)^2 - \beta_1^2 \frac{\dot{s}/L}{2(\dot{s}/L)^2} + \frac{L}{2(\dot{s}/L)} [(\dot{s}/L)^2 - 2\dot{s}/L\beta_1 + \beta_1^2] \left\{ d_9 \dot{s}/L - \frac{2L[\beta_2^2(\dot{s}/L - 1)]}{\beta_2^2} \right. \\
 & \left. + L \dot{s}/L \frac{2}{3} \frac{(\dot{s}/L)^2}{\beta_2^2} [d_9 \beta_2 + d_1] [(\dot{s}/L)^3 - (\beta_1)^3] + \frac{\dot{s}/L}{\beta_2^2} [d_9 (2\beta_2 \dot{s}/L - \right. \\
 & \left. \beta_2^2) \left\{ \left(\frac{\dot{s}}{2} \frac{\dot{s}/L}{(\dot{s}/L)^2} (1 - (\dot{s}/L)^2) (d_8 \beta_4 - \frac{2\theta_2}{\beta_3^2} - \frac{2d_8 \beta_4}{\beta_3}) - \left\{ d_8 \right. \right. \right. \\
 & \left. \left. \frac{\dot{s}/L}{2\dot{s}/L} \right\} \frac{L}{2\dot{s}/L} (-2\dot{s}/L + (\dot{s}/L)^2 + 1) + \frac{2\dot{s} \times (\dot{s}/L)^2}{3\beta_3^2 (\dot{s}/L)^2} (1 - (\dot{s}/L)^3) \right\} \right. \\
 & \left. \left(\frac{\theta_2 \dot{s}/L + 2\theta_3 \dot{s}/L}{\beta_3^3} + \frac{2\theta_2 \dot{s}/L \dot{s}/L}{\beta_3^3} + \frac{d_8 (2\dot{s}/L \beta_4 + \dot{s}/L \frac{\theta_2}{\beta_3})}{\beta_3} \right) \right\}
 \end{aligned}$$

$$\theta = q + lx + cx^2 \text{ THEN } \frac{\partial \theta}{\partial x} = l + 2cx \text{ AND}$$

$$\text{BUT } B = L\beta_1$$

$$-2d_e \left[\frac{\theta_1}{L^2(\beta_1 - \dot{s}/L)^2} - \frac{\theta_1}{K_e L(\beta_1 - \dot{s}/L)} \right] = -\frac{2d_e}{L^2} \left[\frac{\theta_1}{\beta_2^2} + \frac{d_6}{r} \right]$$

$$\begin{aligned}
 & = -2d_s \left[\frac{\theta_2}{L^2(1 - \dot{s}/L)^2} + \frac{2\theta_2(\frac{\theta_2}{\theta_2} - 1)}{K_s L(1 - \dot{s}/L)} \right] = -\frac{2d_s}{\beta_3^2 L^2} \left[\theta_2 + \frac{d_6}{d_7} \right. \\
 & \left. - 1) \right]
 \end{aligned}$$

FORM

θ_1, θ_2)

OF 3 SIMULTANEOUS DIFFERENTIAL EQUATIONS WHICH CAN BE SOLVED BY LAPLACE TRANSFORMATIONS. ASSUMING A LINEAR RELATIONSHIP BETWEEN θ AND x AS SHOWN BELOW

$$\begin{aligned}
 & \frac{\dot{\theta}_1 \beta_1 + \frac{s}{L} \dot{\theta}_1 \beta_1 + \frac{s}{L} \dot{\theta}_1 \frac{s}{L} - \frac{s}{L} \dot{\theta}_1 \beta_1 2 \beta_2 \frac{s}{L} (d_4 - 1)}{\beta_2^4} \\
 & \left[\frac{s}{L} \frac{s}{L} (d_4 - 1) \right] + (\dot{\theta}_1 \frac{s}{L} + 2 \dot{\theta}_1 \frac{s}{L}) - \frac{2 \dot{\theta}_1 \frac{s}{L} \frac{s}{L} (d_4 - 1)}{\beta_2} \Big] \\
 & \left(\frac{s}{L} \beta_4 + \frac{s}{L} \frac{\dot{\theta}_2}{\theta_3} \right) - \frac{2 (\dot{\theta}_2 \frac{s}{L} + \dot{\theta}_2 \frac{s}{L})}{\beta_3^2} - \frac{4 \dot{\theta}_2 \frac{s}{L} \times \frac{s}{L}}{\beta_3^3} \\
 & (2 + d_8 \beta_4 \beta_3) \\
 & \left. \left. \left. \left. \right) + \frac{d_8 \frac{s}{L} \beta_4 \frac{s}{L}}{\beta_3^2} \right) \right\} \right\} \dots \dots \dots 16
 \end{aligned}$$

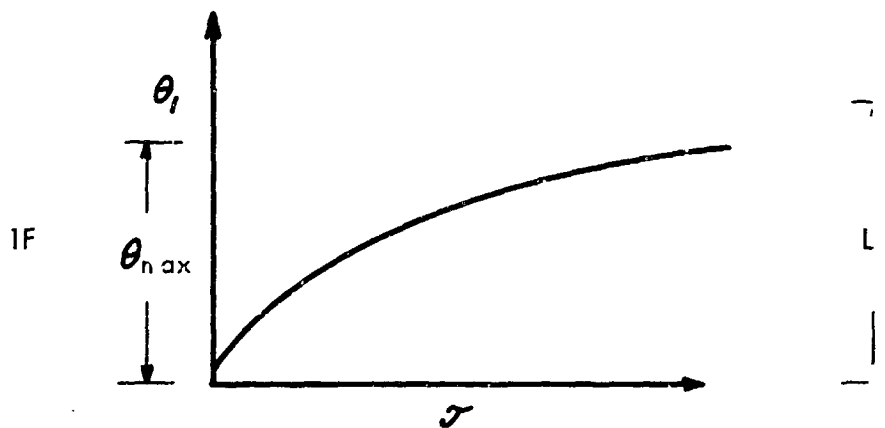
$$\frac{\partial^2 \theta}{\partial x^2} = 2c$$

$$\left[\frac{a_1}{2} \right]$$

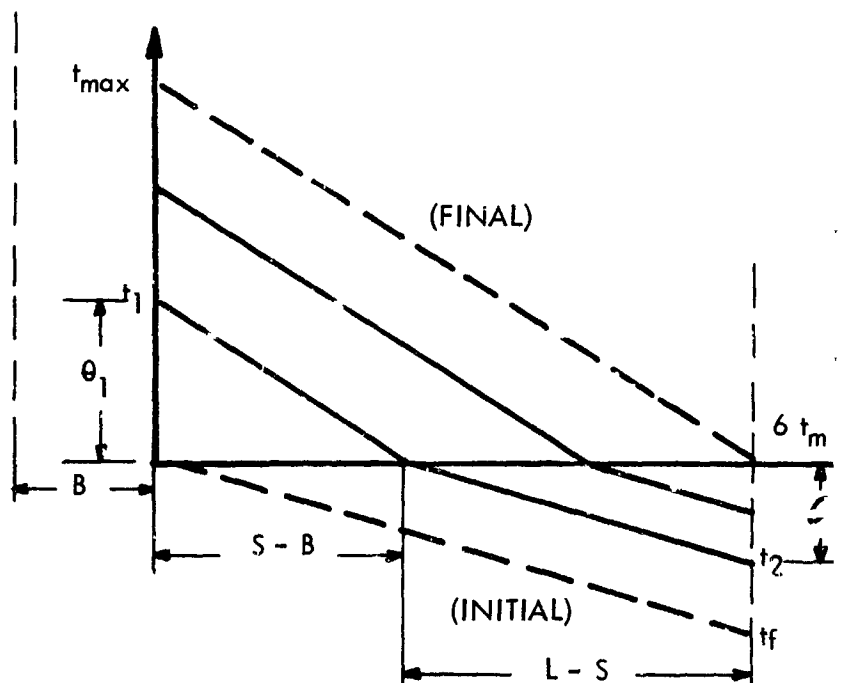
$$\left(\frac{\theta_2}{\theta_3} - 1 \right) \beta_3$$

OLVED ON THE
ETWEEN

CONSIDER THE FOLLOWING RELATIONSHIPS:

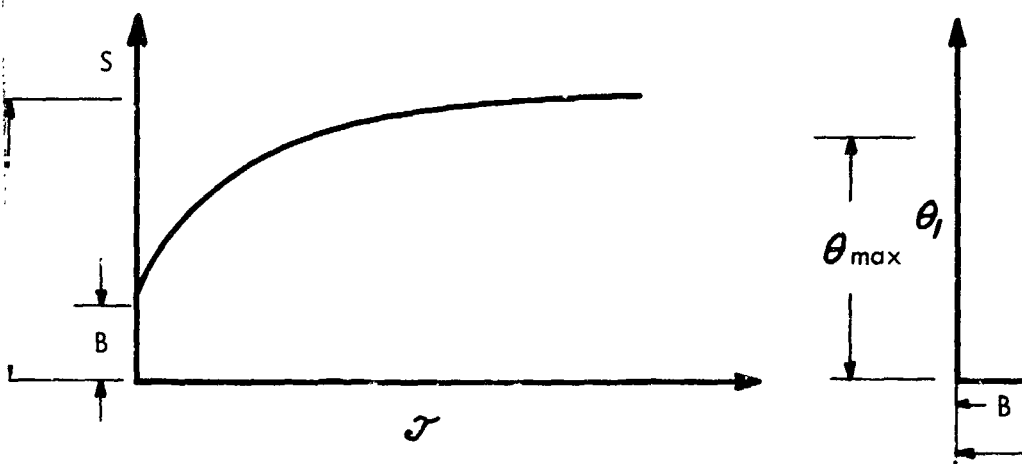


ASSUMING THE LINEAR RELATIONSHIP IS ADEQUATE



INTRODUCING θ_1 , θ_2 , θ_3 , AND θ_2 INTO EQUATION REDUCES THE PHYSICAL PROBLEM TO A DIFFERENTIAL EXPRESSION OF THE FORM

$$S = f(S/L)$$



ATE, ONE OBTAINS

$$\frac{\theta_1}{s-B} = \frac{\theta_{\max}}{L-B}$$

ALSO, $\theta \propto \frac{K_e}{L_e}$

$$\theta_1 = \frac{s-B}{L-B} \theta_{\max} \quad \therefore \theta_1 = \frac{(s-B)}{(L-B)}$$

OR

$$\theta_1 = \frac{(s-L\beta_1)}{(L-L\beta_1)} \frac{g_1 l_{sf}}{K_e} = \frac{(s/L-\beta_1)}{(1-\beta_1)}$$

BUT $\dot{\theta}_1 = -\frac{2de}{L^2\beta_2^2} [\theta_1 + d_9\beta_2] =$

$$\dot{\theta}_1 = -\frac{2de}{L^2\beta_2} \left[\frac{d\theta_1}{\beta_1-1} + d_9 \right]$$

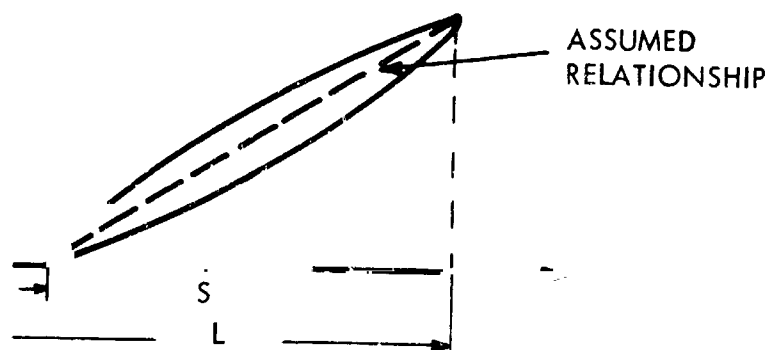
AND $\frac{\theta_2}{L-S} = \frac{\theta_f}{L-B}$

$$\theta_2 = \frac{L-S}{L-B} \theta_f = \frac{L(1-\beta_1)}{L(1-\beta_2)}$$

FINALLY,

$$\theta_2 = -\frac{2ds}{L^2\beta_3^2} [\theta_2 + d_8\beta_3] =$$

$$\dot{\theta}_2 = -\frac{2ds}{L^2\beta_3} \left[\frac{\theta_f}{\beta_1-1} + d_8 \right]$$



$$= g_1$$

$$\frac{g_1 L \alpha}{K_e} \quad \text{BUT } B = L \beta_1$$

$$) dq' \quad \theta_1 = \frac{dq' \beta_2}{(\beta_1 - 1)}$$

$$= - \frac{2 d e}{L^2 \beta_2^2} \left[\frac{dq' \beta_2}{(\beta_1 - 1)} + dq \beta_2 \right]$$

$$\frac{\theta_2 - 1}{\theta_1} \theta_1 = \frac{\theta_1 \beta_3}{(\beta_1 - 1)}$$

$$\frac{\theta_2 - 1}{\theta_1} \theta_1 = - \frac{2 d_3}{L^2 \beta_3^2} \left[\frac{\theta_1 \beta_3}{(\beta_1 - 1)} + d_3 \beta_3 \left(\frac{\theta_2 - 1}{\theta_1} - 1 \right) \right]$$

$$\frac{\theta_2 - 1}{\theta_1} \theta_1$$

8.5 Radiation Analog Investigation

8.5.1 Description of the Problem

The interstices between two parallel plates and fins which are attached to the top plate are partially filled with lithium fluoride (See Figure 92). The lithium fluoride is in contact with the bottom plate, leaving a void space between the surface of the lithium fluoride and the underside of the top plate. The fins are perpendicular to both plates and their tips are kept $1/8$ inch away from the lower plate.

The top side of the upper plate receives heat at a uniform and constant rate. Some of this received heat is removed from the system at the underside of the lower plate at a uniform and constant rate. The lithium fluoride is initially solid at a uniform temperature and melts due to the heat received by radiation through the void from the top plate and by conduction through the fins, while it loses heat to the lower plate. During the process of melting, the lithium fluoride expands by 29% and, therefore, the initial void space gradually decreases.

It is desired to compute for several different heat input rates and fin thickness values, the top and bottom surface temperatures of both plates, the melting front location of lithium fluoride versus time, and lithium fluoride temperature versus time at a number of locations based on which the temperature distribution of the lithium fluoride at any instance can be found. The computations are to be terminated when the total mass of lithium fluoride is molten.

8.5.2 Data and Property Values

For the computations the following values were used:

1. Geometry; see also Figure 92

Top and bottom plate thickness	0.5 in.
Distance between plates	1.5 in.
Fin spacing from center to center	0.75 in.
Distance between tip of fins and the bottom plate	0.125 in.
Initial void space between LiF surface and top plate	0.535 in.
Fin thickness	0; 0.031 in.; 0.062 in.

2. Properties of Lithium Fluoride

Thermal conductivity; solid	5.1 Btu/ft, hr, °F
Thermal conductivity; liquid	11.3 Btu/ft, hr, °F
Specific heat; solid	0.55 Btu/lb, °F
Specific heat; liquid	0.6 Btu/lb, °F
Density; solid	0.084 lb/in ³
Density; liquid	0.065 lb/in ³
Melting temperature	1560°F
Heat of fusion	450 Btu/lb
3. Properties of Top and Bottom Plates

Thermal conductivity	15 Btu/ft, hr, °F
Specific heat	0.13 Btu/lb °F
Density	0.33 lb/in ³
4. Properties of Fins

Thermal conductivity	29 Btu/ft, hr, °F
Specific heat	0.105 Btu/lb, °F
Density	0.322 lb/in ³
5. Radiation interchange factor (emissivity x shape factor) between LiF surface and plate

	0.674
--	-------
6. Heat Input Rates

	$5 \times 10^3, 7.5 \times 10^3, 10 \times 10^3$ Btu/ft ² , hr
--	---
7. Heat Removal Rate

	1.5×10^3 Btu/ft ² , hr
--	--

SECTION OF MODULE EMPLOYED IN ANALOG COMPUTATIONS

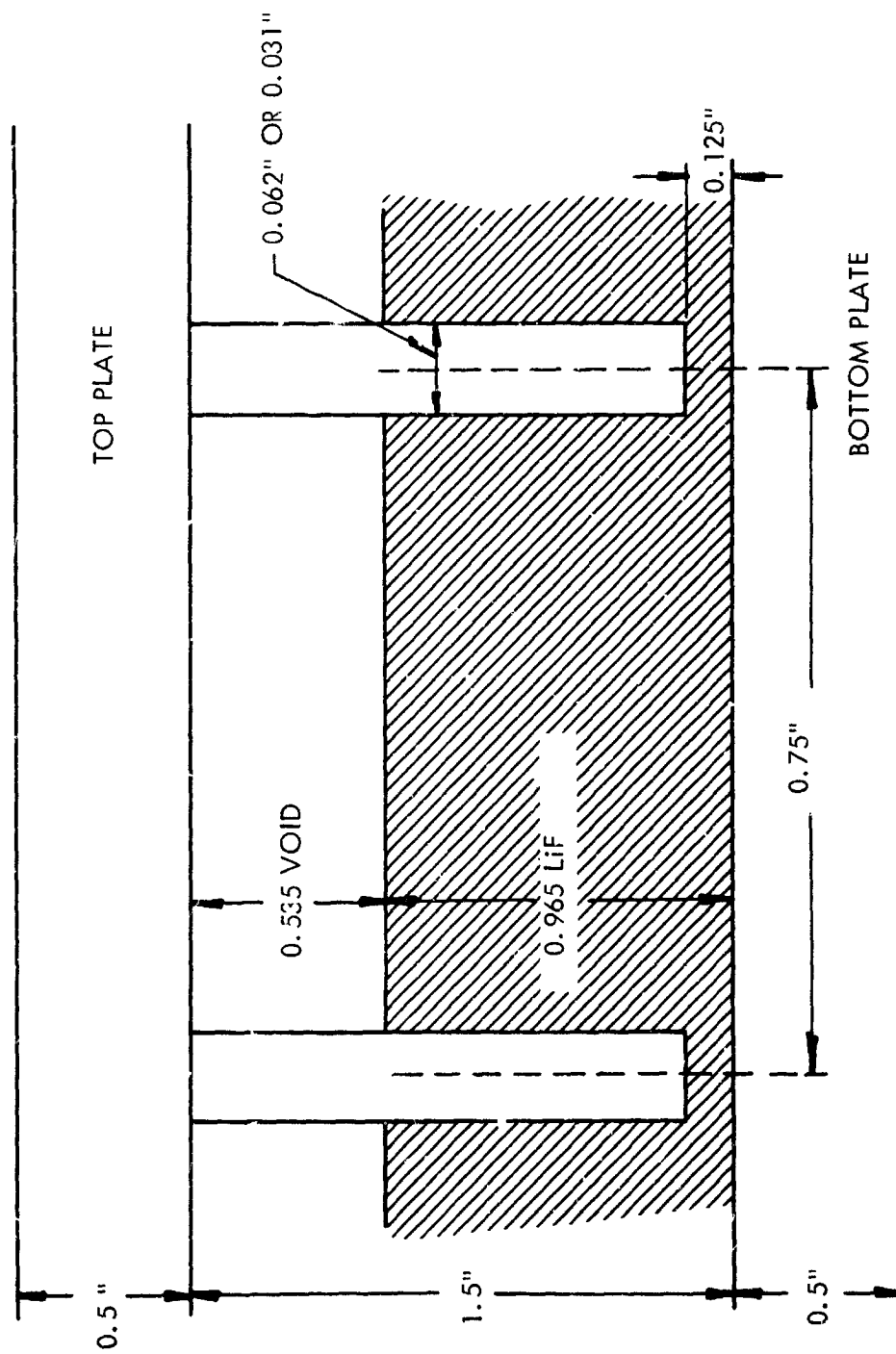


FIGURE 92

8. Initial Temperatures:

In the first three computations (0 fin thickness, $Q_{in} = 5 \times 10^3, 7.5 \times 10^3, 10 \times 10^3$ Btu/ft², hr) the initial temperatures were as follows:

$$\text{plates } T_{i \text{ plate}} = 1400^\circ \text{F}$$

$$\text{LiF } T_{i \text{ LiF}} = 1560^\circ \text{F}$$

In the rest of the computations the initial temperatures were

$$\text{plate } T_{i \text{ plate}} = 1500^\circ \text{F}$$

$$\text{fin } T_{i \text{ fin}} = 1500^\circ \text{F}$$

$$\text{LiF } T_{i \text{ LiF}} = 1500^\circ \text{F}$$

8.5.3 Cases Considered

A total of 13 cases were computed as listed below:

Case No.	Q_{in} Btu/ft ² , hr	Fin Thick- ness in.	LiF Lateral Conductivity	Initial Temperatures		
				$T_{i \text{ LiF}}$ °F	$T_{i \text{ plate}}$ °F	$T_{i \text{ fin}}$ °F
1	5000	0	---	1560	1400	---
2	7500	0	---	1560	1400	---
3	10,000	0	---	1560	1400	---
4	10,000	.062	real	1500	1500	1500
5	10,000	.062		1500	1500	1500
6	7500	.062	real	1500	1500	1500
7	5000	.062	real	1500	1500	1500
8	5000	.031	real	1500	1500	1500
9	7500	.031	real	1500	1500	1500
10	10,000	.031	real	1500	1500	1500
11	10,000	.031		1500	1500	1500
12	5000	0	---	1500	1500	1500
13	10,000	0	---	1500	1500	1500

The rate of heat removal was 1500 Btu/ft², hr in all cases.

8.5.4 Assumptions

In solving the problem, the following assumptions were made:

There is no contact resistance between lithium fluoride and the bottom plate.

There is no contact resistance between the fin and lithium fluoride.

There is no contact resistance between fin and top plate.

8.5.5 Method of Solution

The computations were carried out on the Heat and Mass Flow Analyzer, a passive element analog computer, representing the thermal resistance by electrical resistance, heat capacitance by electric capacitance, heat flow by current, temperature by voltage and heat (real) time by electric time.

In the case of no fin (Cases 1, 2, 3, 12, 13), the one-dimensional heat flow was studied on a one-dimensional electric analog circuit having eight sections to represent the lithium fluoride perpendicular to the plates and four sections for each of the plates.

In the case of fins, the problem involves two-dimensional heat flow. Because of the complexity of the two-dimensional heat flow involving varying geometry (expansion of lithium fluoride while undergoing change of phase), only eight lithium fluoride sections perpendicular to the plates were used and the entire heat capacity of each section was considered to be concentrated in the center line between two fins. When representing the real two-dimensional system in the present simplified way, it is not known what single equivalent thermal resistance value is to be used in the computations with regard to the heat flow in the lateral (parallel to plates) direction. To overcome this difficulty, two limits were explored:

1. One limit is obtained by using the real conductivity of the lithium fluoride which results in the maximum thermal resistance value since the heat capacitance is concentrated in the center line.
2. The second limit is given by assuming infinite lateral conductivity.

The change of properties (specific heat, thermal conductivity, volumetric expansion) of lithium fluoride was made at the instance when half of the heat of fusion necessary to melt the section had been introduced.

Due to the expansion of the lithium fluoride when melting, the location of contact between the latter and the fin changes continuously, which change was approximated by a number of finite steps.

The fin itself was represented by a large number of sections to facilitate the simulation of the above contact location change.

The thermal resistance to radiation across the void space was considered in two discrete steps:

1. One constant mean value was used from the beginning of the computation until the uppermost lithium fluoride section reached the melting temperature.
2. During the rest of the computation another constant mean value was introduced.

The computations were continued until all the lithium fluoride became molten.

8.5.6 Presentation of Results

The results are presented partly in Table X - where the final plate and lithium fluoride surface temperatures, the time required to melt all the lithium fluoride and finally the total heat introduced to the system are listed - and partly in graphs.

Graphs are available showing for each case:

top plate upper and lower surface temperature vs time:	T_{p1}, T_{p2}
bottom plate upper and lower surface temperature vs time:	T_{p3}, T_{p4}
lithium fluoride surface temperature vs time:	$T_{LiF, s}$
lithium fluoride temperatures vs time at 0.6633" and 0.3015" from bottom plate in solid state (note that as the LiF melts, the distance from bottom plate changes):	$T_{LiF} (.6633),$ $T_{LiF} (.3015)$
location of melting front vs time.	

8.5.7 Results

A comparison of cases 1-2-3, 4-6-7, 8-9-10 and 12-13 (See Table X) indicates that for identical geometrics and initial conditions, an increase in the heat input rate results in an increase in the quantity of heat necessary to melt some amounts of lithium fluoride (Figure 93), while the melting time shortens (Figure 21).

Comparing the final top plate surface temperatures, it is interesting to note that they vary linearly with the heat input rate (Figure 22), higher heat input rates resulting in higher temperatures.

TABLE X
SUMMARY OF ANALOG RESULTS

Case Number	Q_{in} Btu/ft ² , hr	Q_{out} Btu/ft ² , hr	Fin Thickness, in.	L/F Lateral Conductivity	Initial Temperature			Final Plate Surface Temperature				$T_{L/F, s, max}$	Total Time, minutes	Total Heat into Module During Melting, Btu/ft ²
					$T_{L/F}$	T_{plate}	T_{fin}	T_{101}	T_{102}	T_{103}	T_{104}			
1	5000	1500	0	---	1560	1400	---	1732	1715	1560	1555	1603	115.5	6738
2	7500	1500	0	---	1560	1400	---	1810	1785	1560	1555	1620	72	7200
3	10000	1500	0	---	1560	1400	---	1885	1860	1560	1555	1640	53	7508
4	10000	1500	.062	real	1500	1500	1500	1775	1750	1560	1555	1637	45.0	6375
5	10000	1500	.062	∞	1500	1500	1500	1770	1742	1560	1555	1638	45.5	6446
6	7500	1500	.062	real	1500	1500	1500	1723	1705	1560	1555	1620	62.8	6280
7	5000	1500	.062	real	1500	1500	1500	1673	1660	1560	1555	1600	103.3	6025
8	5000	1500	.031	real	1500	1500	1500	1690	1678	1560	1555	1605	104	6067
9	7500	1500	.031	real	1500	1500	1500	1750	1730	1560	1555	1623	63	6300
10	10000	1500	.031	real	1500	1500	1500	1810	1780	1560	1555	1645	46.5	6587
11	10000	1500	.031	∞	1500	1500	1500	1805	1775	1560	1555	1642	47.0	6658
12	5000	1500	0	real	1500	1500	1500	1735	1720	1560	1555	1605	111.6	6452
13	10000	1500	0	real	1500	1500	1500	1895	1865	1560	1555	1643	50.1	7098

TOTAL HEAT INPUT VS HEAT INPUT RATE
OF MODULE SECTION

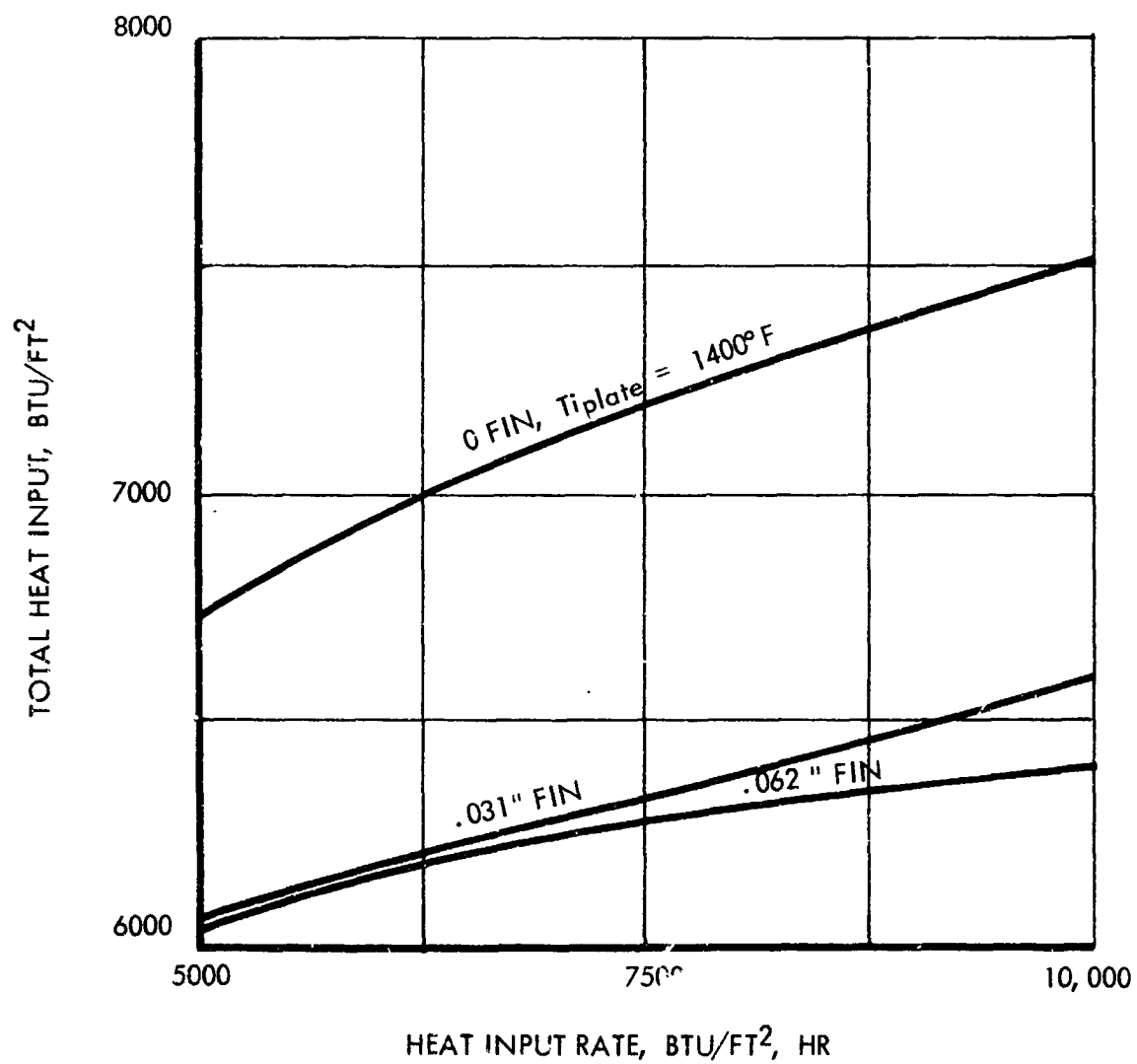


FIGURE 93

The bottom plate final surface temperatures were identical in all cases.

Comparing cases 4-5 and 10-11, one finds that the assumption of infinite lateral conductivity for the lithium fluoride has a negligible influence on the results.

Investigating the influence of fin thickness on the top surface temperatures (Figure 94), on the total melting time (Figure 95) and on the total heat input (Figure 93 and Table V), it is found that the increase in the value of the above quantities is minor when decreasing the fin thickness from 0.062 in. to 0.031 in. The changes become significant when the fin thickness is further decreased all the way to zero. The value of the total heat input into the system in the case of no fin is so much different from the other two values that the available three values do not permit the prediction of the heat input for a fin thickness between 0 and 0.031 in.

On the computed lithium fluoride temperature-time curves (recorder sheets; Figures 100 to 102) for each lithium fluoride point a constant temperature is shown at the melting point for a finite period of time although in reality the temperature changes continuously with time at each location. The reason for this deviation lies in the fact that in the computations, finite sections were used to represent the lithium fluoride; as the number of sections is increased (decreasing the section size), the computed curve approaches the real one more closely.

On Figures 96 to 99, presenting the progress of melting front, the melting time shows a linear variation with location. On these graphs at any time-reading the ordinate (y_1) below the curve shows the layer thickness of lithium fluoride being solid. (For illustration see Figure 96.) When the ordinate reading above the line y_2 is multiplied by $.084/.065$, the lithium fluoride layer thickness in liquid phase is obtained. The total layer thickness then is given by $y_1 + .084/.065 y_2$.

8.6 Test Module Stress Analysis

8.6.1 Introduction

This report presents stress analyses of the top, bottom and side plates of the subject test module. The analyses were performed in order to determine plate thicknesses sufficient to prevent any measurable module deformation.

The limiting stresses were based on a .2% creep in 1000 hours. These time and creep values were selected to provide some conservatism to the elementary methods used and to the limited available creep data.

8.6.2 Results

The required plate thicknesses for various temperatures and pressures are shown in Figures 105 and 108. For the maximum temperature and pressure of 1900°F and 14.7 psi,

TOP PLATE FINAL SURFACE TEMPERATURES
VS. FIN THICKNESS OF MODULE SECTION

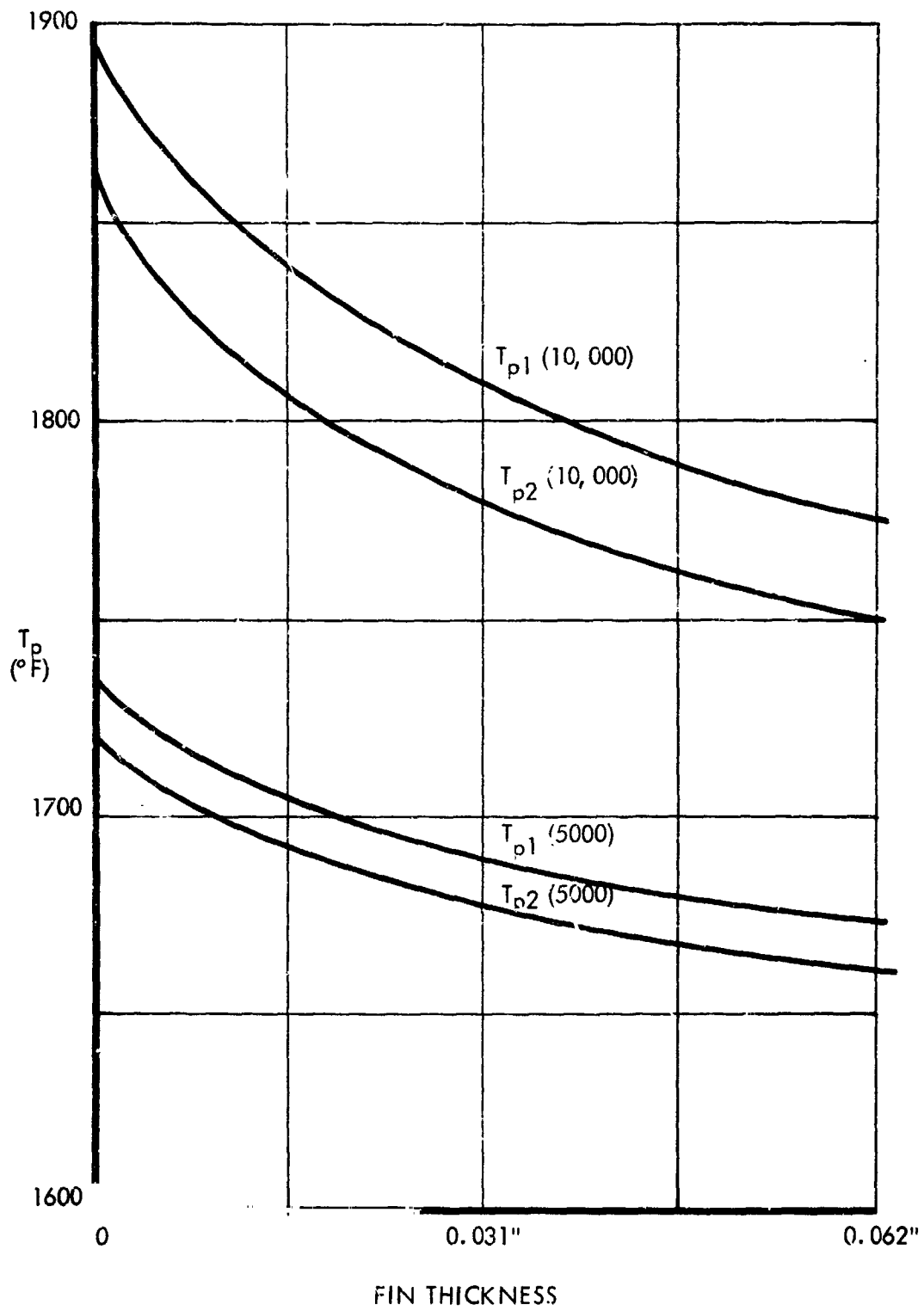


FIGURE 94

MELTING TIME VS FIN THICKNESS OF MODULE SECTION

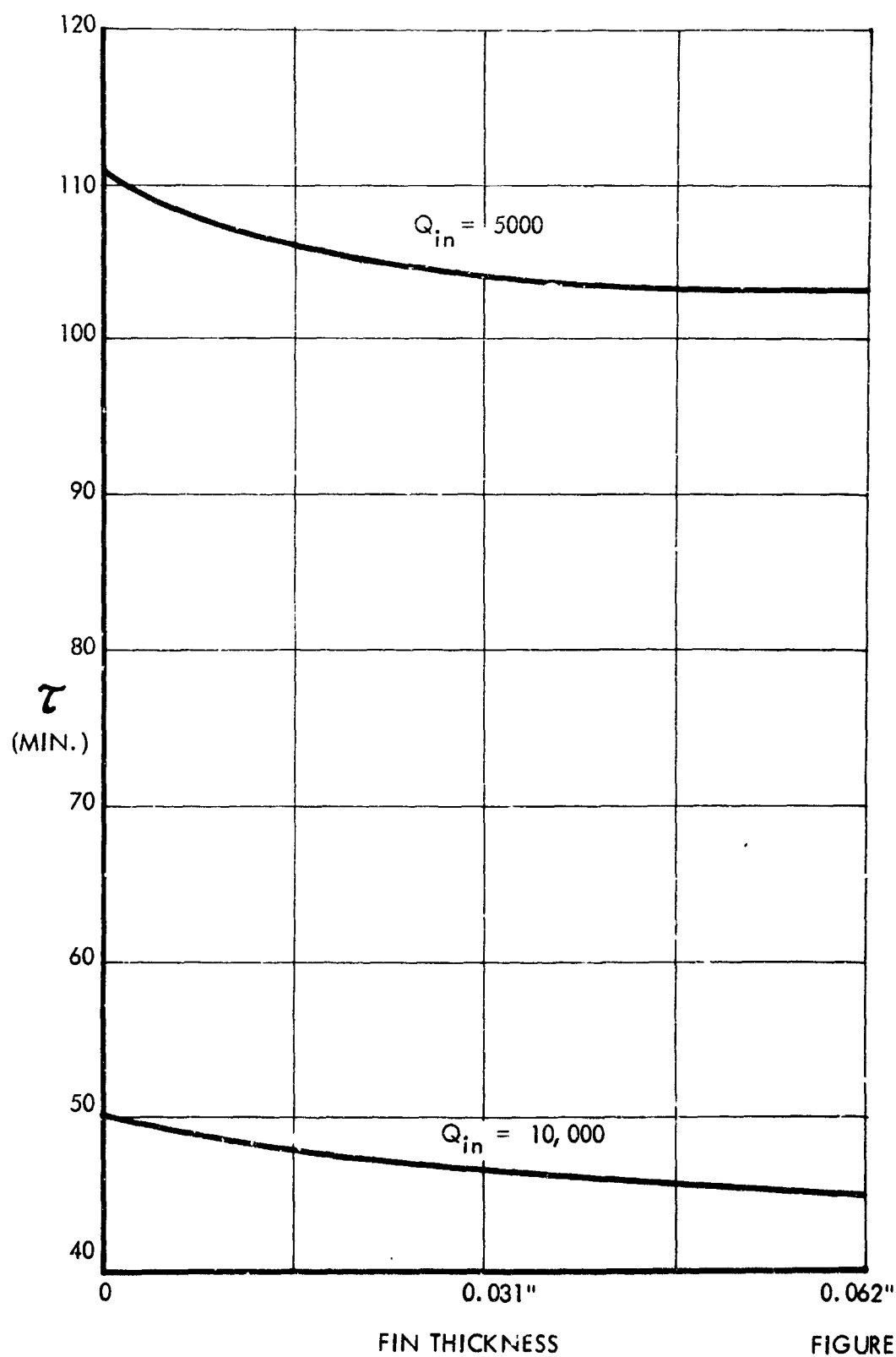


FIGURE 95

PROGRESS OF MELTING FRONT IN MODULE SECTION

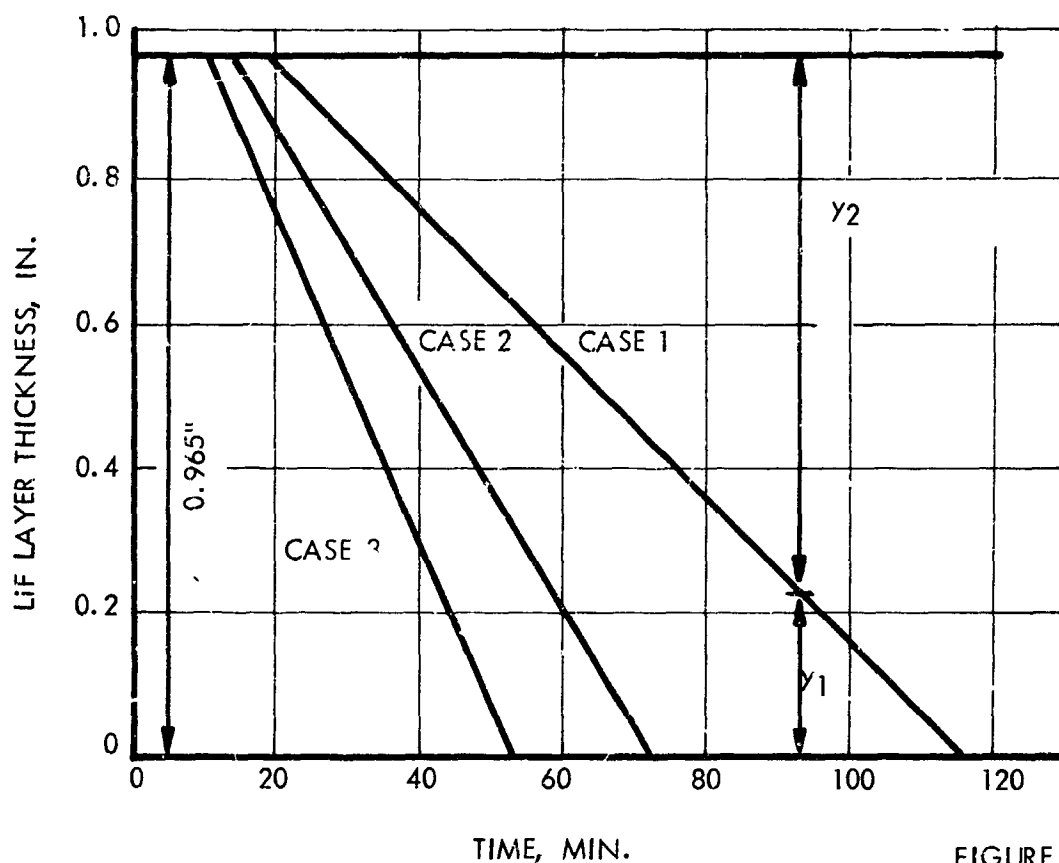


FIGURE 96

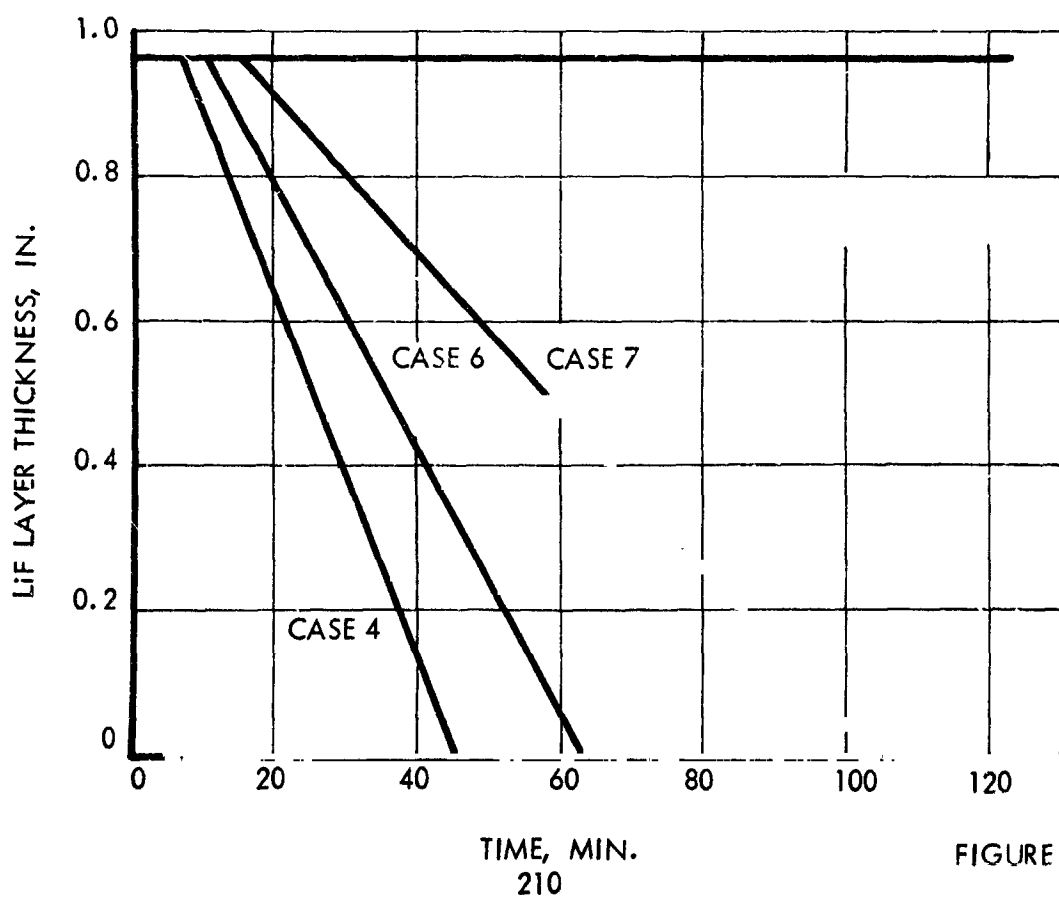


FIGURE 97

PROGRESS OF MELTING FRONT IN MODULE SECTION

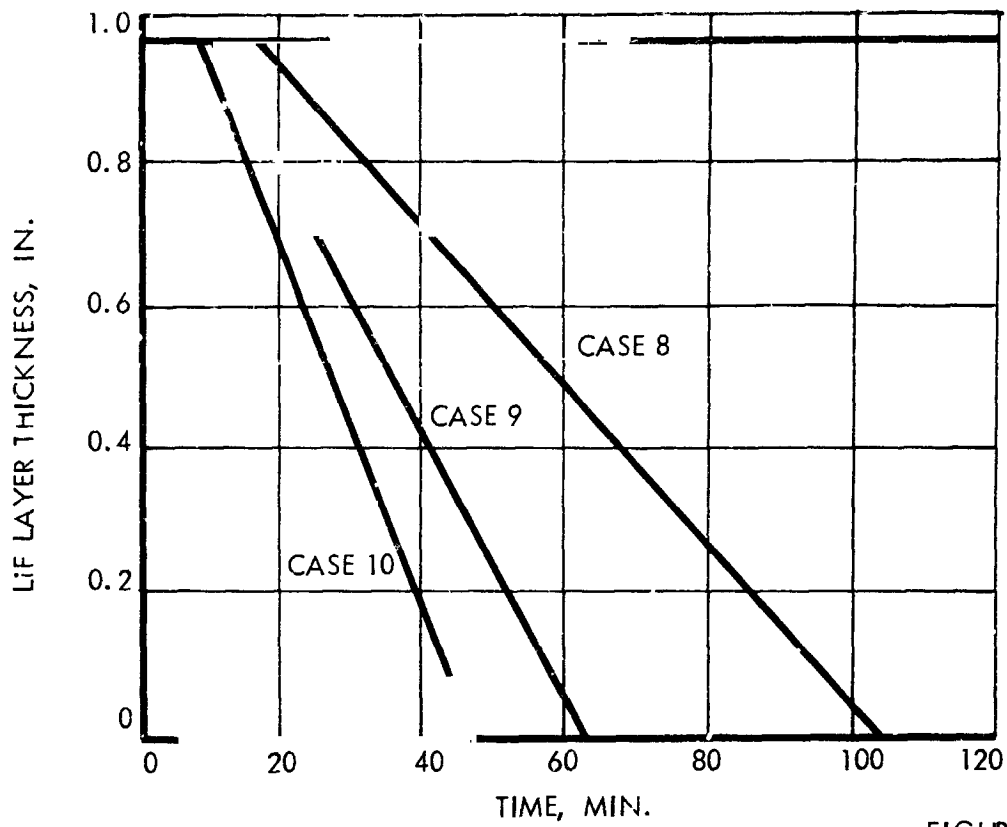


FIGURE 98

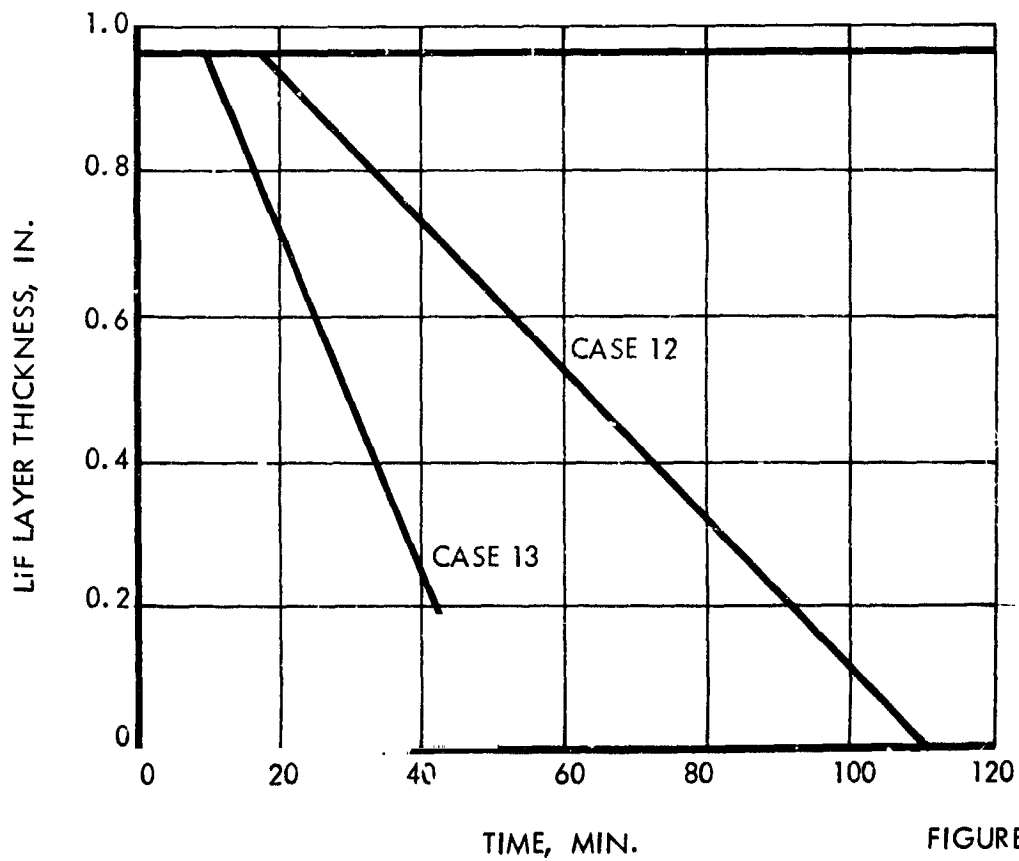


FIGURE 99

COMPUTER RECORDER SHEETS

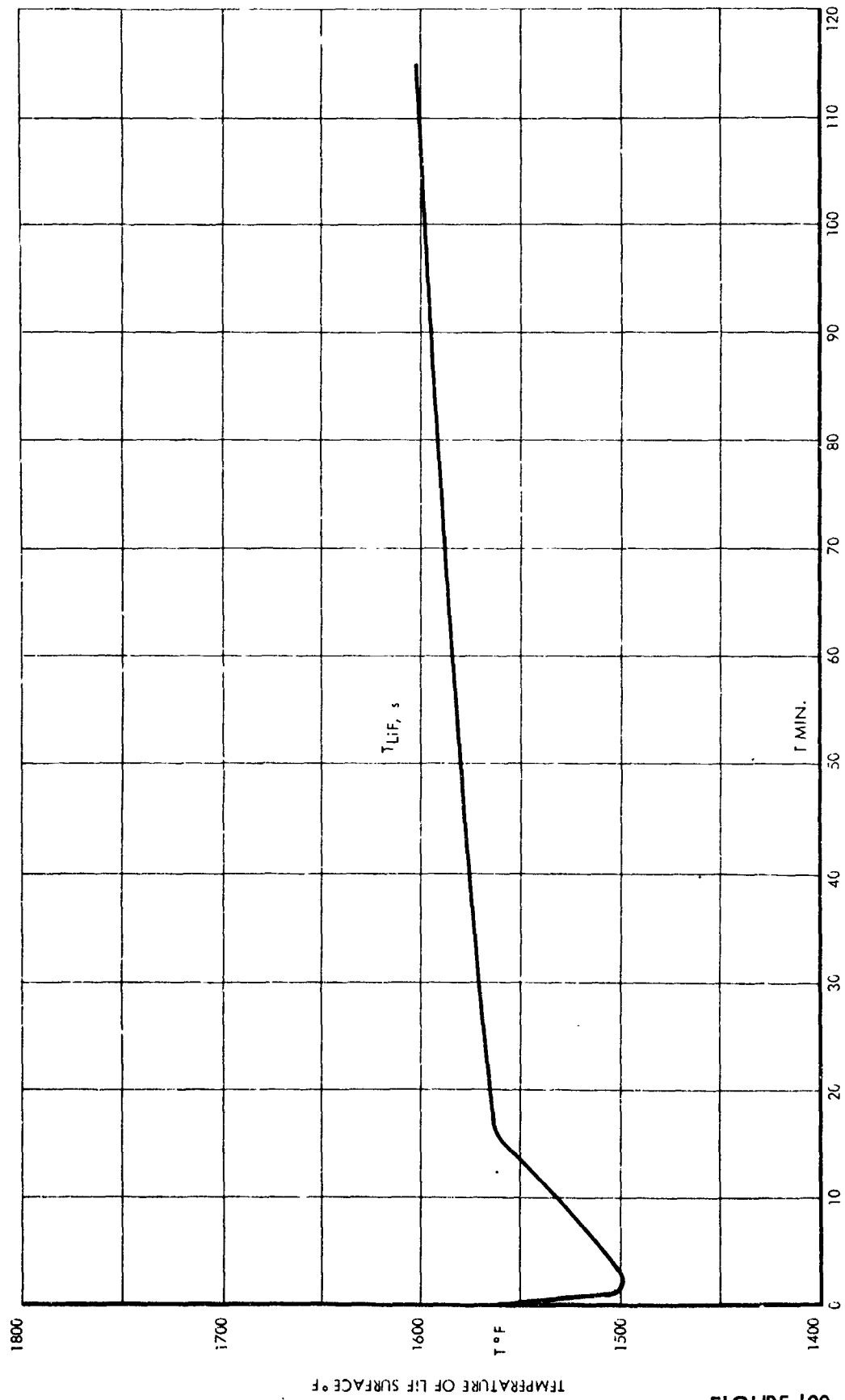


FIGURE 100

PRECEDING PAGES BLANK NOT FILMED

COMPUTER RECORDER SHEETS

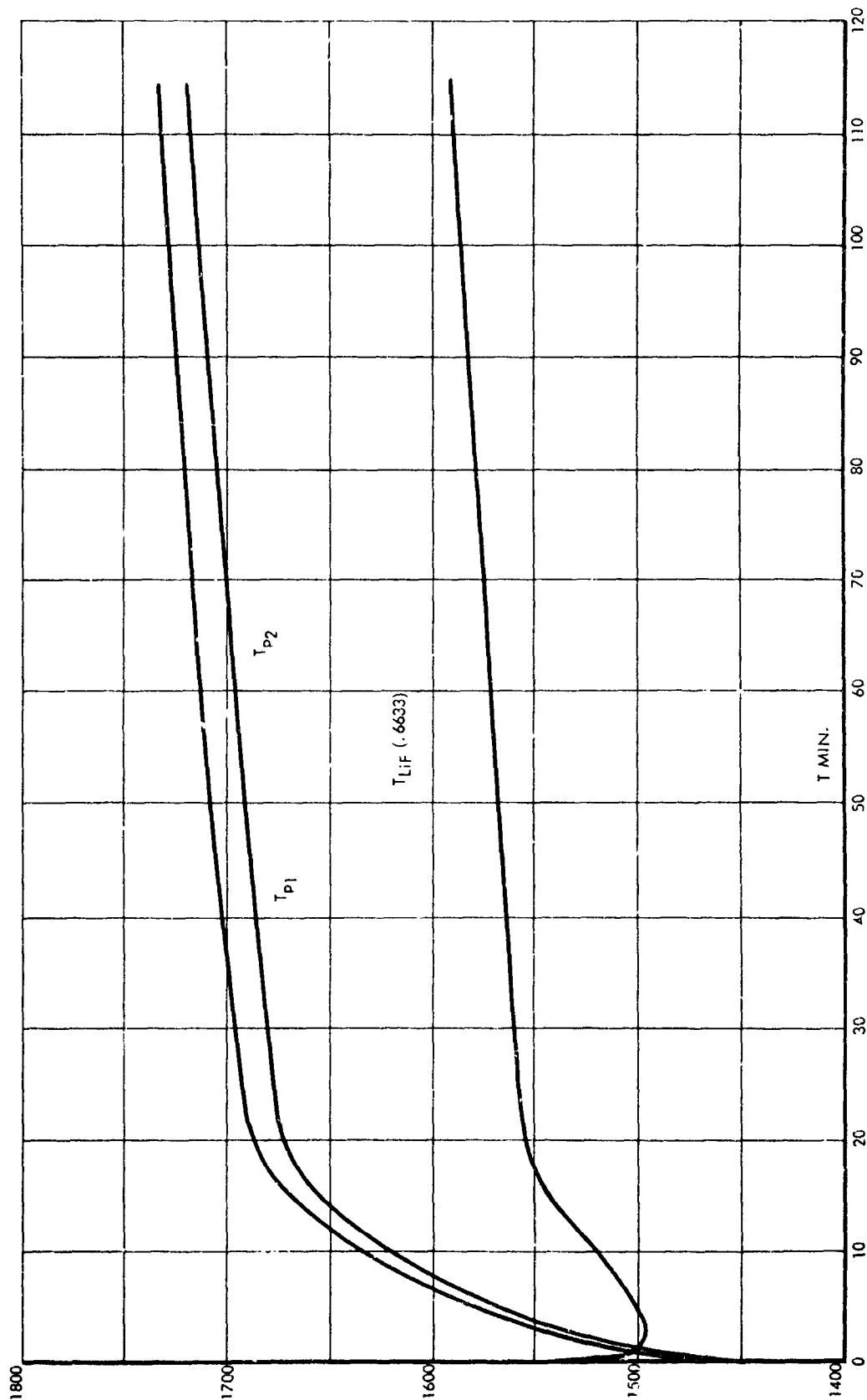


FIGURE 101

COMPUTER RECORDER SHEETS

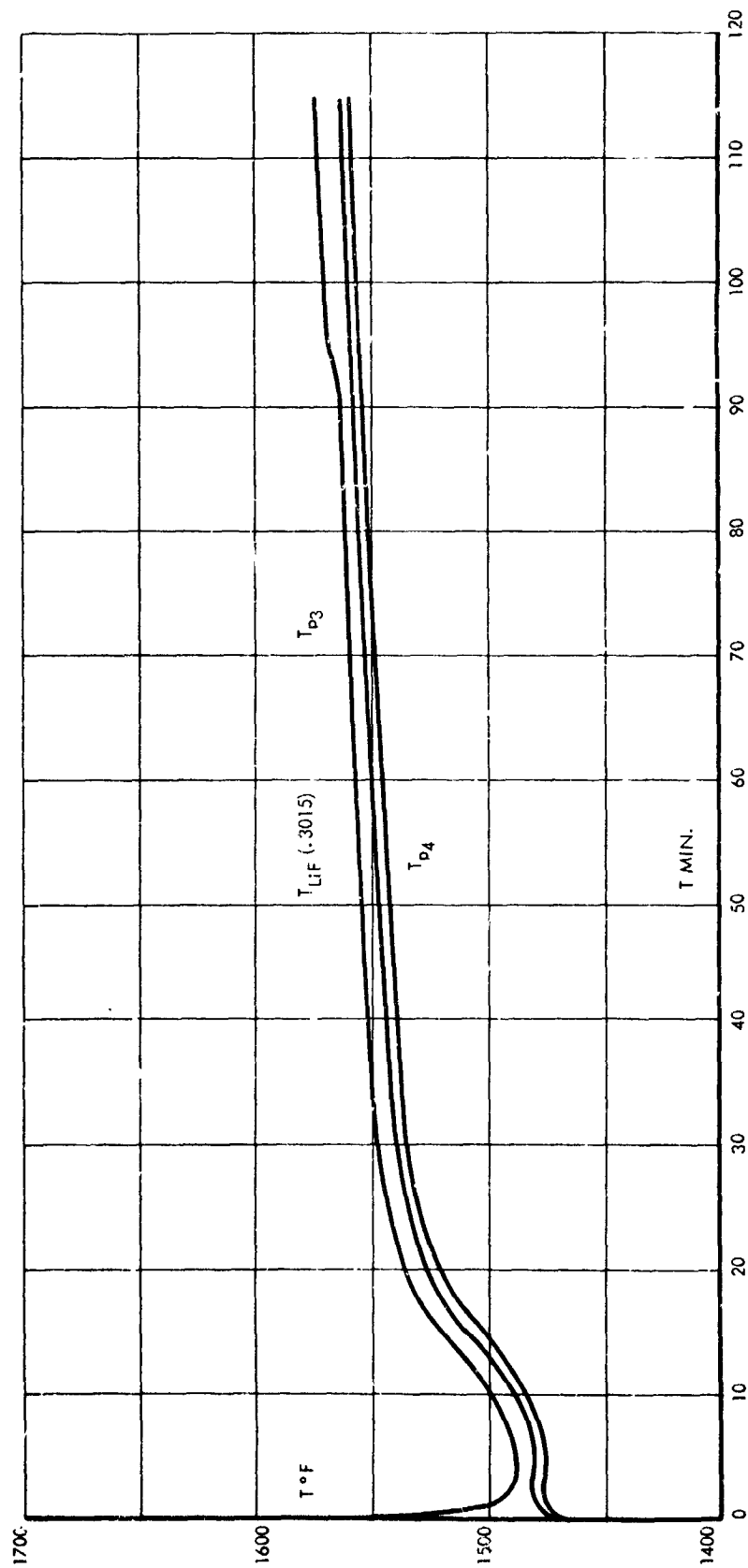


FIGURE 102

PRECEDING PAGES BLANK NOT FILMED

a top plate thickness of .438 inches and a side plate thickness of .088 inches are required. Since the bottom plate is at the temperature of the lithium fluoride (1600°F) a thickness of .291 inches will be sufficient for that plate.

3.6.3 Recommendations

The curves given in Figure 105 and Figure 108 should be used to determine the required plate thicknesses. The figures show that a substantial reduction in plate thickness, with accompanying reductions in cost and weight, can be obtained by a reduction in pressure or temperature or both.

The thicknesses given in the above referenced figures result in a minimum section stiffness. Any alternations, such as slots or holes, which reduce the plate cross sectional bending stiffness must be compensated for by an increase in plate thickness of an amount sufficient to restore the original solid plate stiffness.

8.6.4 References

1. Roark, R.J., Formulas for Stress and Strain, 3rd Edition, McGraw-Hill Book Company, Inc., New York, Toronto, London, 1954.
2. Aerospace Structural Metals handbook, Volume II, March 1963, V. Weiss, Editor.
3. Timoshenko, S. and Woinowsky-Krieger, S., Theory of Plates and Sheels, 2nd Edition, McGraw-Hill Book Company, Inc., New York, Toronto, London, 1959.
4. Universal Cyclops Steel Corporation, High Temperature Metals Bulletin, HTM 300 1-59-5M, page 33.
5. Timoshenko, S., Strength of Materials Part II, 3rd Edition, D. Van Nostrand Company, Inc., Princeton, New Jersey, 1956.

8.6.5 Detailed Analysis

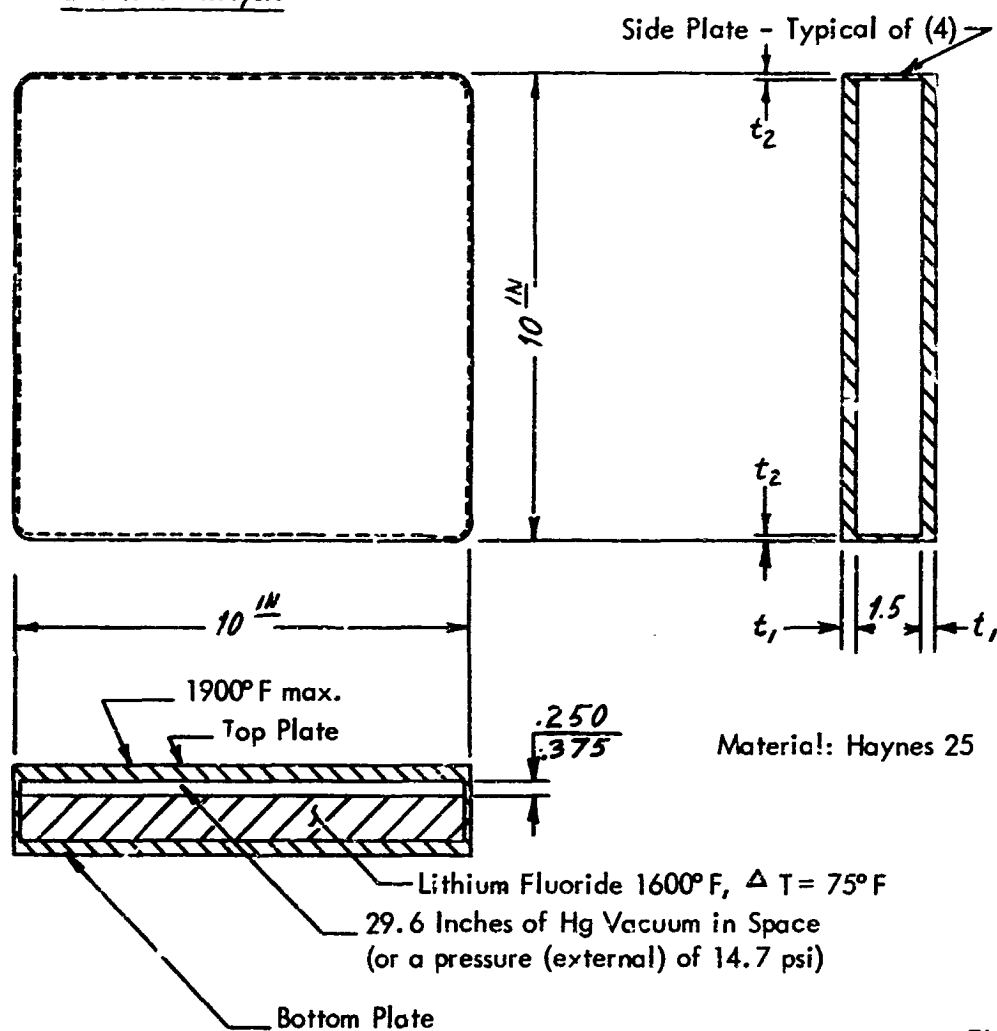


FIGURE 103

TEST MODEL BASIC DIMENSIONS

Ref. TRW Dwg 81299-18

For Haynes 25 (also known as Unitemp L-605) a .2% creep will take place after 1000 hours if the stress level equals or exceeds:

2200 psi at 1900° F
3200 psi at 1800° F
4400 psi at 1700° F
5000 psi at 1600° F

Based on a Larson-Miller
Conversion of Information
Contained in Reference (4)

8.6.5.1 Analysis of Top and Bottom Plates

Since the side plates shown in Figure 103, are relatively thin compared to the top and bottom plates, they were assumed to offer no rotational resistance to the top and bottom plates. The analytical model consisting of a simply supported square plate with a uniform load over it's entire surface is shown in Figure 104 below.

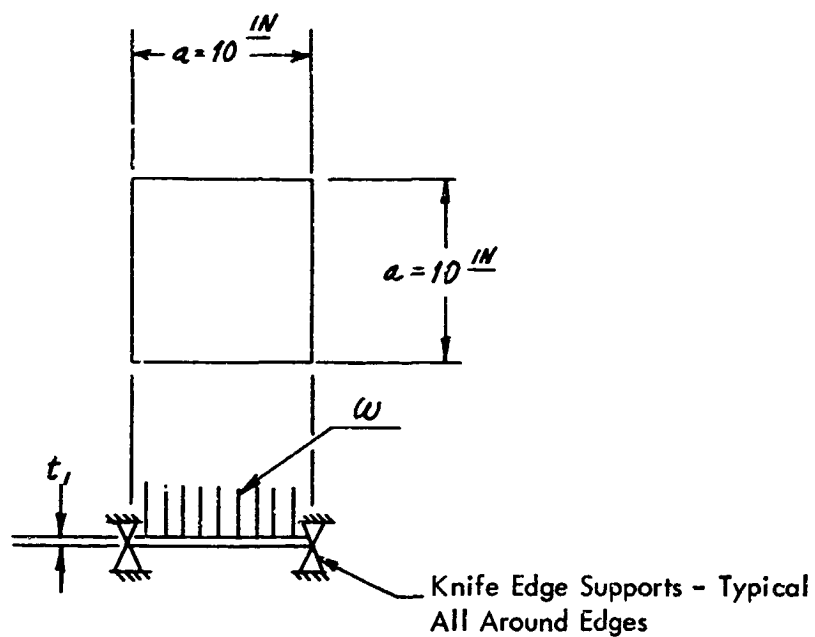


FIGURE 104

ANALYTICAL MODEL OF TOP AND
BOTTOM PLATE

The maximum bending moment (M) in the plate shown in Figure 104, occurs at the center and may be expressed by:

$$M = \beta w a^2$$

where: $\beta = .0479$ for a square plate

(a & w as shown in Figure 104)

The maximum bending stress (σ_B) in the plate is:

$$\sigma_B = \frac{6 M}{t_i^2}$$

$$\text{or } t_i^2 = \frac{6 M}{\sigma_B}$$

$$t_i^2 = \frac{6 \times .0479 \times w \times 10^{-2}}{\sigma_B}$$

$$\underline{\underline{t_i^2 = 2 B .74 \frac{w}{\sigma_B}}}$$

From this equation and for the limiting stress values, the required plate thicknesses were determined for various values of w . These thicknesses are tabulated in Table XI, and are plotted in Figure 105.

REQUIRED TOP & BOTTOM PLATE
THICKNESS
VS
TEMPERATURE

(Based on .2% Creep in 1000 Hrs)

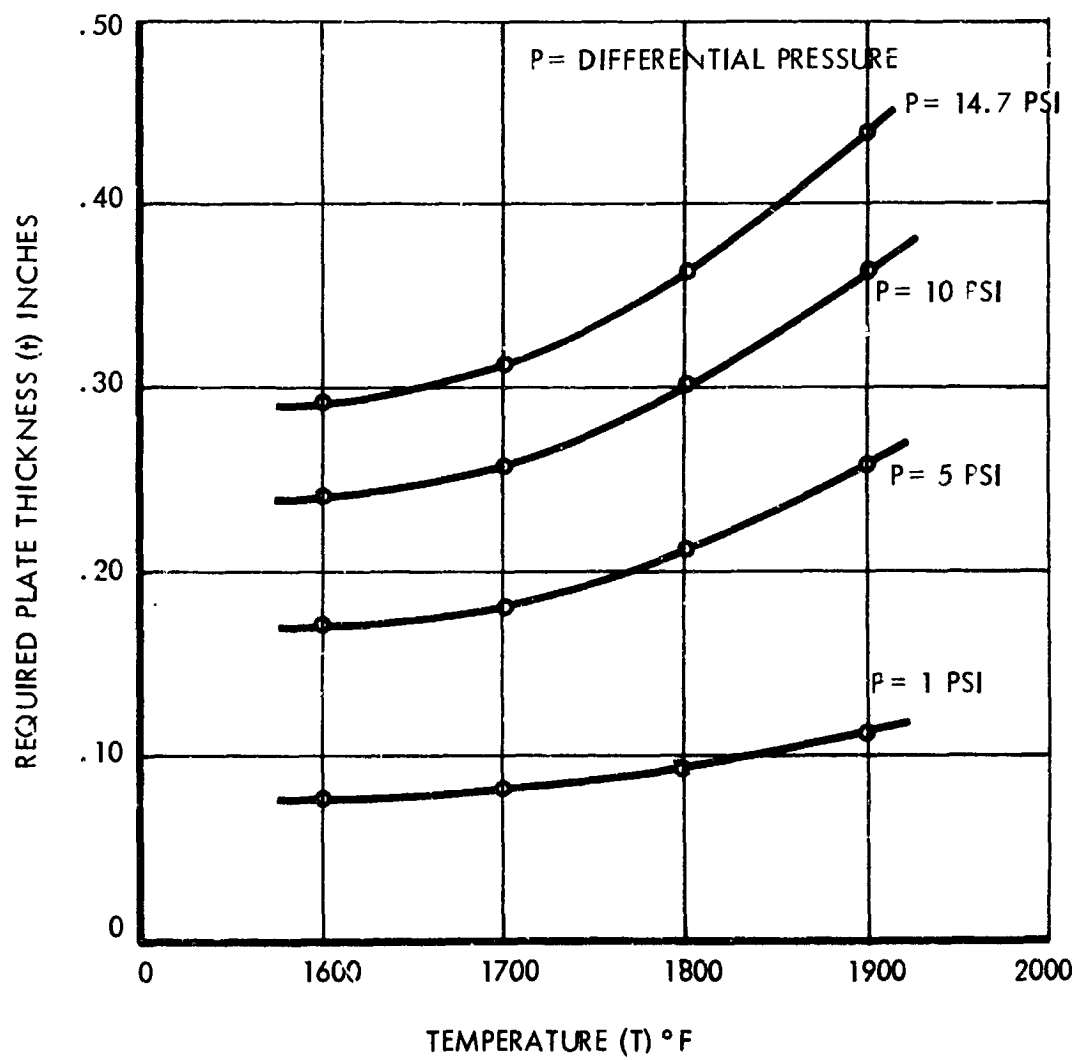


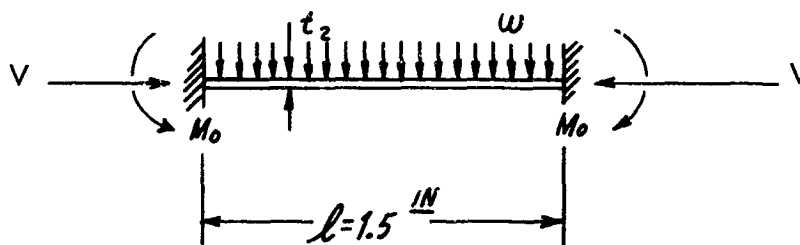
FIGURE 103

TABLE XI
TOP AND BOTTOM PLATE THICKNESSES

Temperature °F	Allowable Stress (σ_B) PSI	Plate Pressure (PSI)			
		14.7	10	5	1
1900	2200	.4382	.3614	.2556	.1143
1800	3200	.3633	.2997	.2119	.0948
1700	4400	.3099	.2556	.1807	.0808
1600	5000	.2907	.2397	.1695	.0758

8.6.5.2 Analysis of Side Plates

Since the side plates are long (10 inches) compared to their width (1.5 inches), it may be assumed that near the center, where the maximum stresses and deflections occur, the influence of the boundary conditions at the short edges are negligible. The 1 inch wide beam shown in Figure 106 below was used as the analytical model.



ANALYTICAL MODEL OF SIDE PLATES

FIGURE 106

The maximum reactive forces (V) of the side plates on the top and bottom plates occur at the center of each 10 inch edge and may be expressed by:

$$V = \delta w a$$

where: $\delta = .420$ for a square plate

For $a = 10$ inches:
$$V = \underline{\underline{4.20 w \text{ lb/in}}}$$
 Eq. (1)

The bending moments (M_o) may be expressed by:

$$M_o = \frac{w l^2}{12} \times \frac{\tan u - u}{\frac{1}{3} u^2 \tan u}$$

For $l = 1.5$ inches

$$M_o = \underline{\underline{.5625 w \frac{\tan u - u}{u^2 \tan u}}}$$
 Eq. (2)

$$\underline{\underline{u^2 = \frac{V l^2}{4EI}}}$$
 Eq. (3)

$$\text{Maximum Stresses} = \underline{\underline{\sigma = \frac{V}{t} + \frac{6 M}{t^2}}}$$
 Eq. (4)

Sample Calculation

For 1900° F, $w = 14.7$ psi, $t = .125$ in.

At 1900° F $E = 19.5 \times 10^{-6}$ psi

Eq. (1)
$$V = 4.20 \times 14.7 = \underline{61.74 \text{ lb/in}}$$

Eq. (3)
$$u^2 = \frac{61.74 \times 2.25 \times 12}{4 \times 19.5 \times 10^{-6} \times .125^3}$$

$$\underline{u^2 = .01094} \quad \underline{u = .10459}$$

$$\underline{\tan u = .10497}$$

$$\text{Eq. (2)} \quad M_o = .5625 \times 14.7 \times \frac{.10497 - .10459}{.01094 \times .10497}$$

$$\underline{M_o = 2.73572}$$

$$\text{Eq. (4)} \quad \sigma = \frac{61.74}{.125} + \frac{6 \times 2.73572}{.125^2}$$

$$\underline{\underline{\sigma = 1544 \text{ psi}}}$$

Similar calculations were performed for the 4 values of temperature (1600, 1700, 1800 and 1900°F) and three values of pressure (14.7, 10 and 5 psia). The maximum stress levels determined from these calculations are plotted in Figure 107.

The intersection points of the stress versus thickness curves and the limiting stress lines in Figure 107 produced points of required plate thickness for the respective temperatures. These thicknesses are plotted in Figure 108.

STRESS IN SIDE PLATES VS THICKNESS

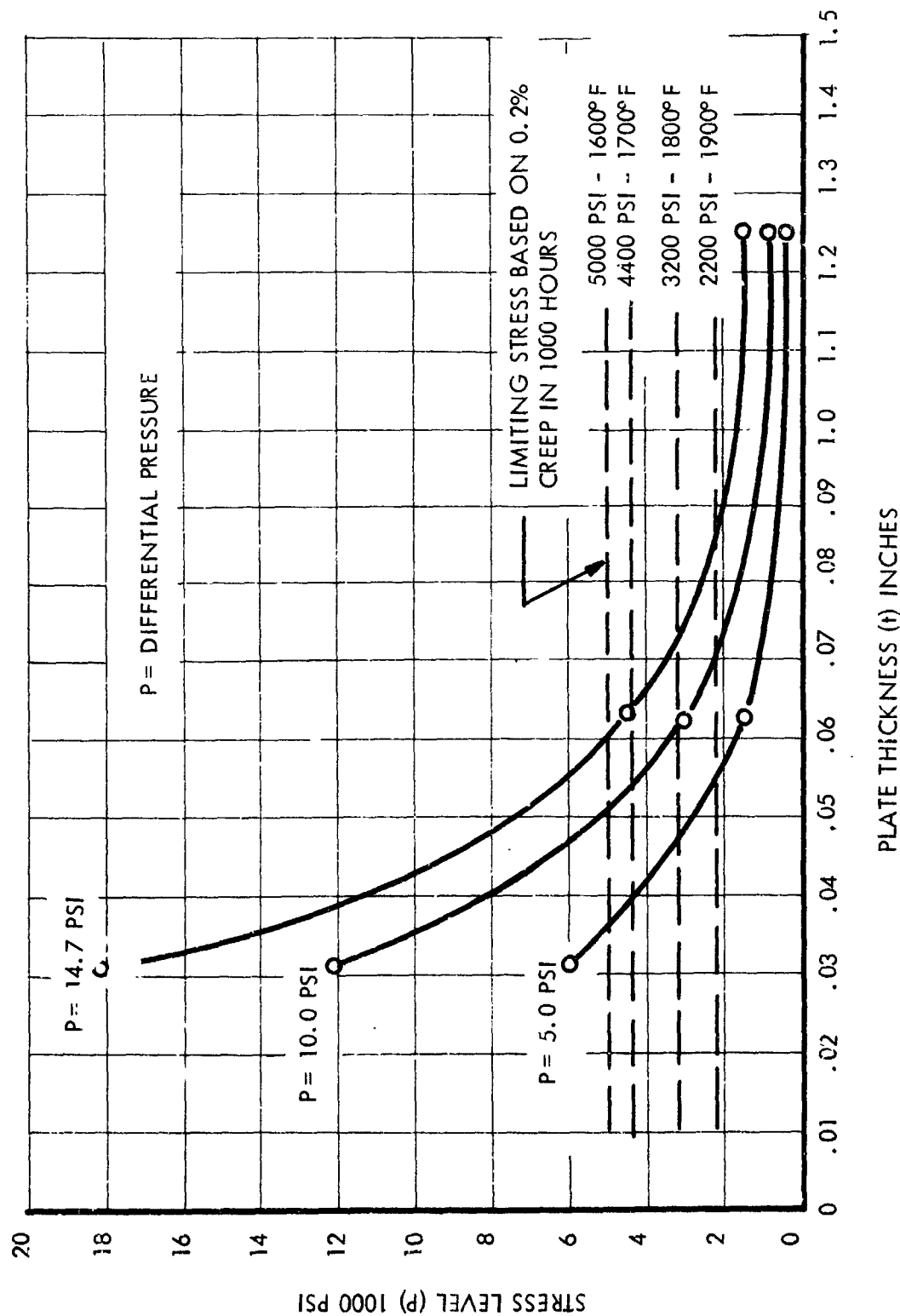


FIGURE 107

REQUIRED SIDE PLATE THICKNESS
VS
TEMPERATURE

(Based on .8% Creep in 1000 Hrs)

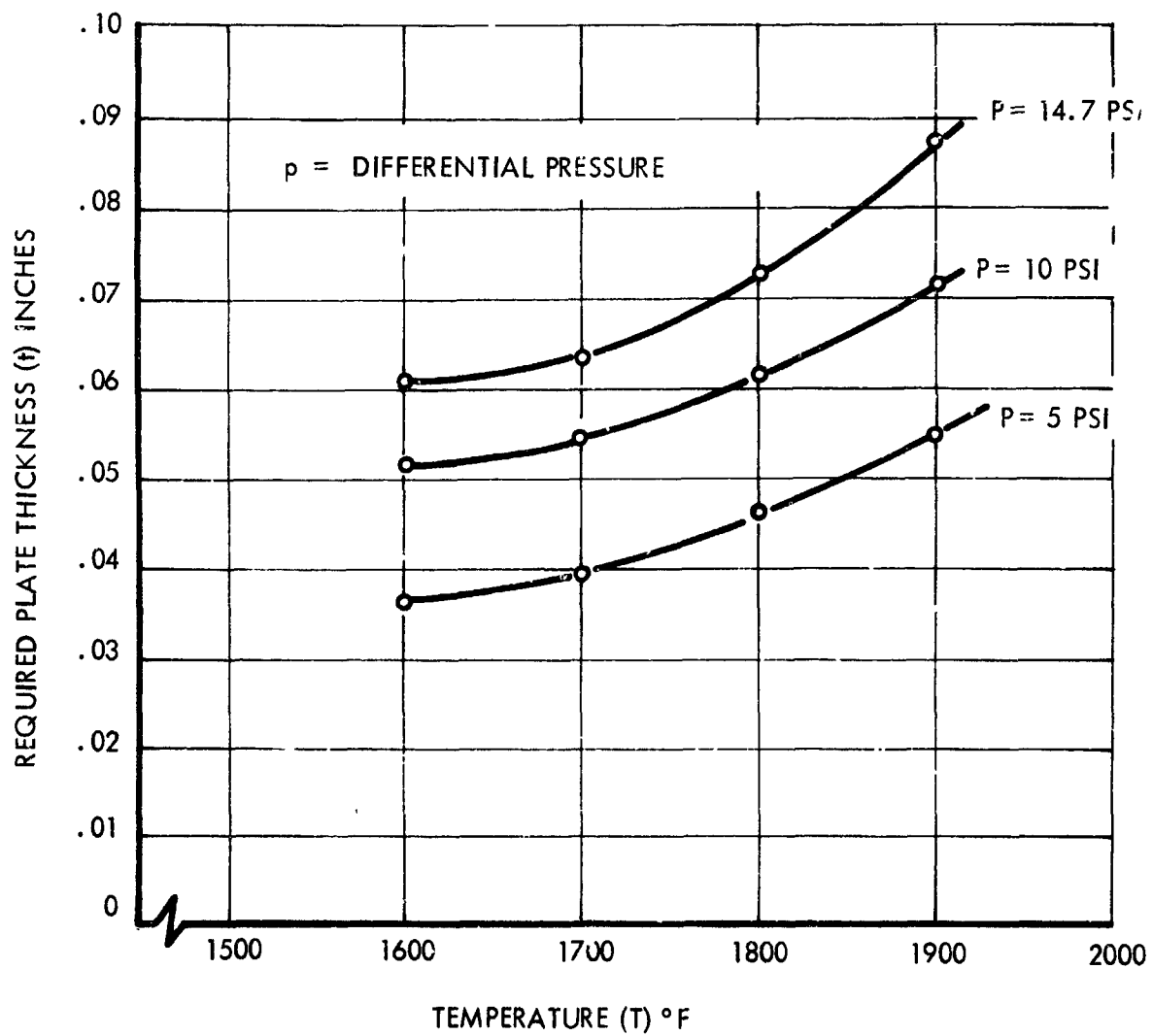


FIGURE 108

8.7 High Temperature Properties of Haynes 25 and Waspaloy

The high temperatures of Haynes 25 and Waspaloy which are pertinent to the stress analysis of the Brayton cycle cavity receiver have been abstracted from literature and prepared in graphical form. The following figures are submitted for review.

Haynes 25

Modulus of elasticity vs. temperature Figure 109

Coefficient of thermal expansion vs. temperature Figure 109

Creep rupture stress vs. Larson Miller parameter Figure 110

Waspaloy

Modulus of elasticity vs. temperature Figure 111

Coefficient of thermal expansion vs. temperature Figure 112

Creep rupture stress vs. Larson Miller parameter Figure 113

Hastelloy X

Creep rupture stress vs. Larson Miller parameter Figure 114

For the case of Haynes 25, it is intended that the data presented by Haynes Stellite Company⁽¹⁾ will be used. In the case of Waspaloy, the data presented by Cyclops Corporation⁽²⁾ and the Carpenter Steel Company⁽³⁾ will be used. Poisson's ratio for Waspaloy has not been found in available literature.

Poisson's ratio will be taken as .30 and constant over the range of temperatures expected. The density of Waspaloy will be taken as .296 pounds per cubic inch.

The time-temperature relation in the Larson Miller parameter is found to be 54, 200 for 10, 000 hours at 1800° F.

$$\begin{aligned} P &= (T + 460) (20 + \log t) \\ &= (1800 + 460) (20 + 4.0) = 54, 200 \end{aligned}$$

Based on a mean square curvilinear regression study of Haynes 25 creep rupture data, the design stress for Haynes 25 at 1800° F for 10, 000 hours will be taken as 1900 psi. Stress rupture of sheet was experimentally observed at 3, 600 psi in 1000 hours at 1800° F and at 2800 psi after 100 hours at 2000° F.

A similar mean square study of Waspaloy data showed that the design stress for this material at 1800° F for 10,000 hours could be about 2100 psi. It should be pointed out that only a single test of Waspaloy was made at 1800° F from which it was concluded that creep rupture could occur in 100 hours at 6500 psi⁽⁵⁾. The location of this point on the Larson-Miller master creep curve suggests that this data point is either a "sport" or a suggestion that serious physical changes take place in Waspaloy at temperatures greater than 1600° F.

8.7.1 Conclusions and Recommendations

1. There are no real indications in superior creep rupture strength of Waspaloy over Haynes 25 at 1800° F for 10,000 hours. Haynes 25 can be expected to have a creep rupture strength of 1900 psi under these conditions, and Waspaloy can be expected to have a creep rupture strength of 2100 psi or less under these same conditions.
2. The test data of Waspaloy was accumulated at temperatures of 1600° F and less for periods of 1000 hours. Direct extrapolation to 1800° F and 10,000 hours from this limited data could be in considerable error. It is recommended that creep rupture data at 1800° F or 1900° F be obtained to support the selection of the materials for the Brayton cycle cavity receiver.
3. For 10,000 hours at 1800° F the creep rupture strength of Hastelloy alloy X is about 1000 psi.

8.7.2 References

1. Haynes Stellite Company, Haynes Alloy No. 25, June 1962, pp. 3, 6, 14.
2. Universal Cyclops Steel Corporation, High Temperature Metals, "Unitemp L-605," pp. 32 and 33, "Unitemp Waspaloy," pp. 36 and 37, 10M58.
3. The Carpenter Steel Company, Carpenter High Temperature Alloys, "Waspaloy," pp. 69 and 70, 5M1-62.
4. Special Metals, Inc., Alloy Performance Data, Waspaloy.
5. Simmons and Metzger, Compilation of Chemical Composition and Rupture Strengths of Super-Strength Alloys, ASTM, STP No. 170-B, ASTM, p. 5, 1961.
6. Haynes Stellite Company, Hastelloy Alloy X, 1961.

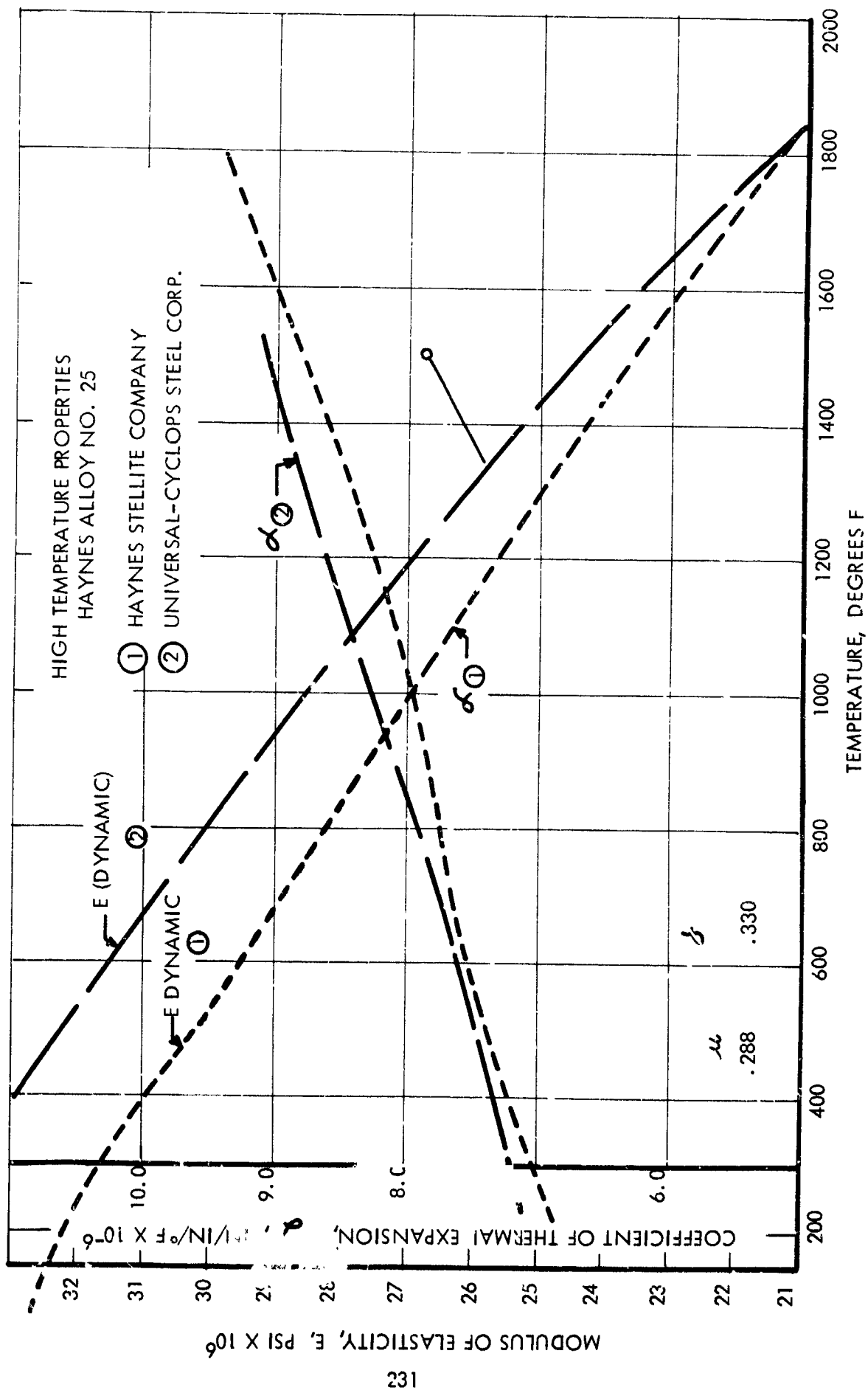


FIGURE 109

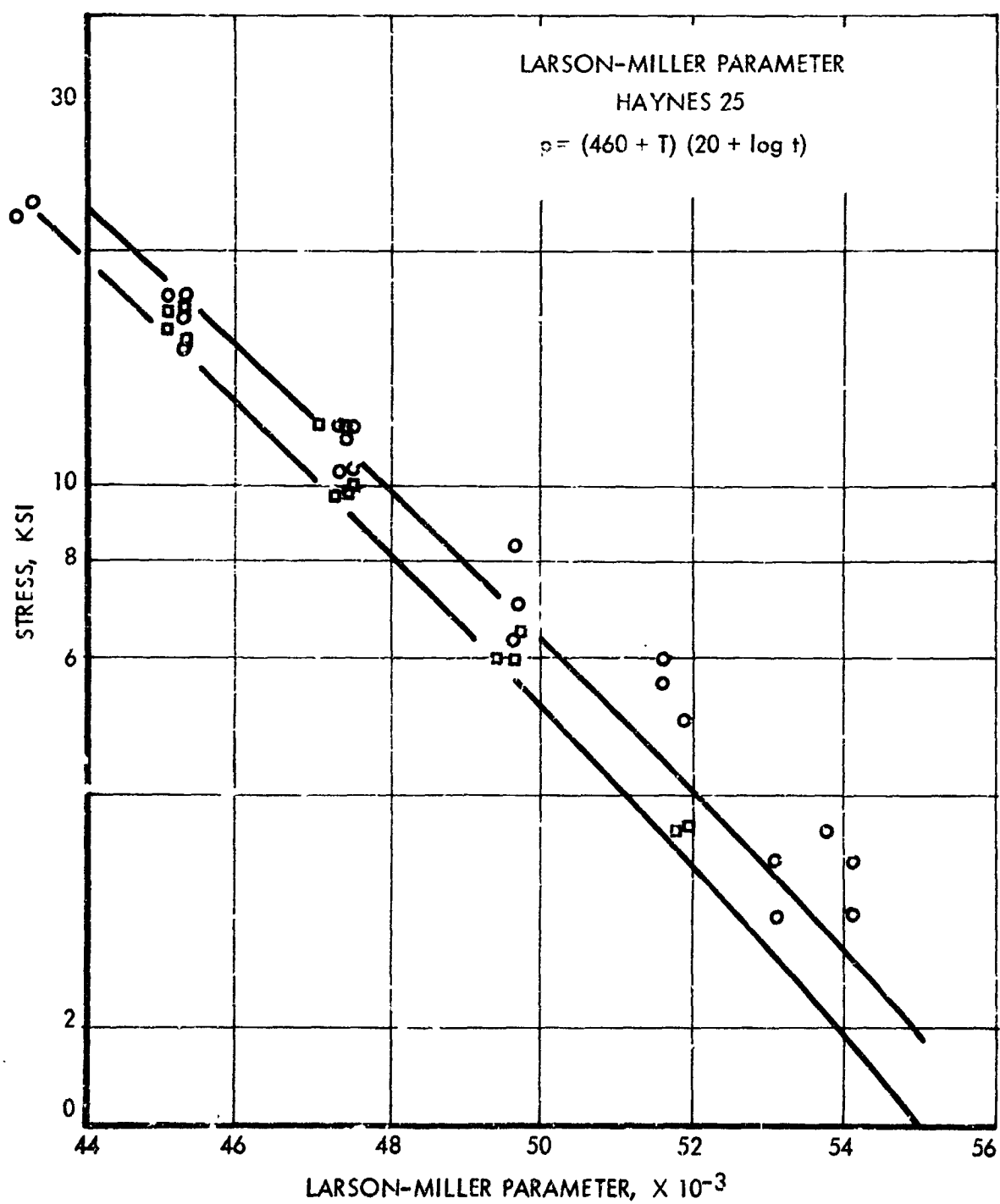


FIGURE 110

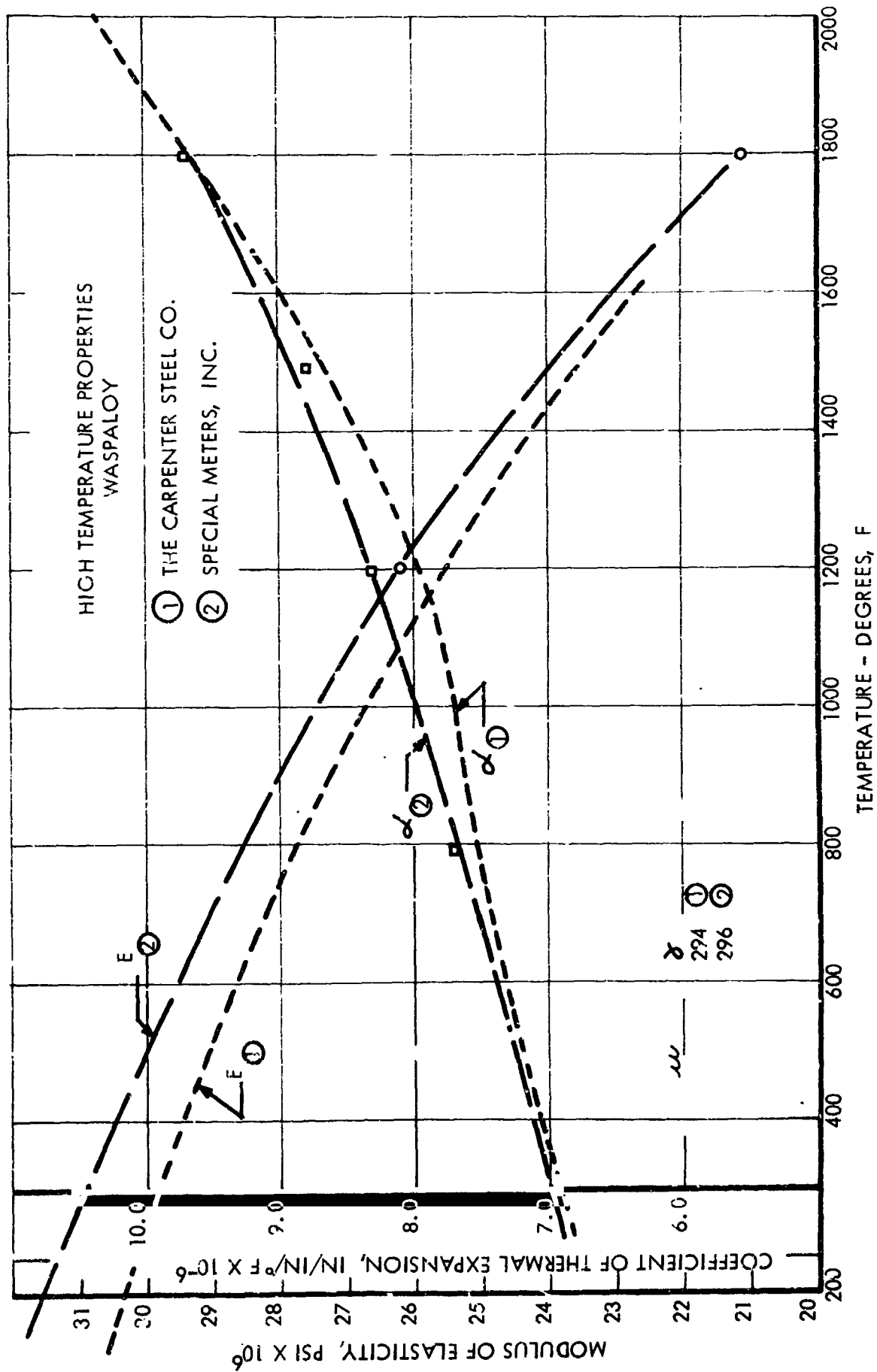


FIGURE 111

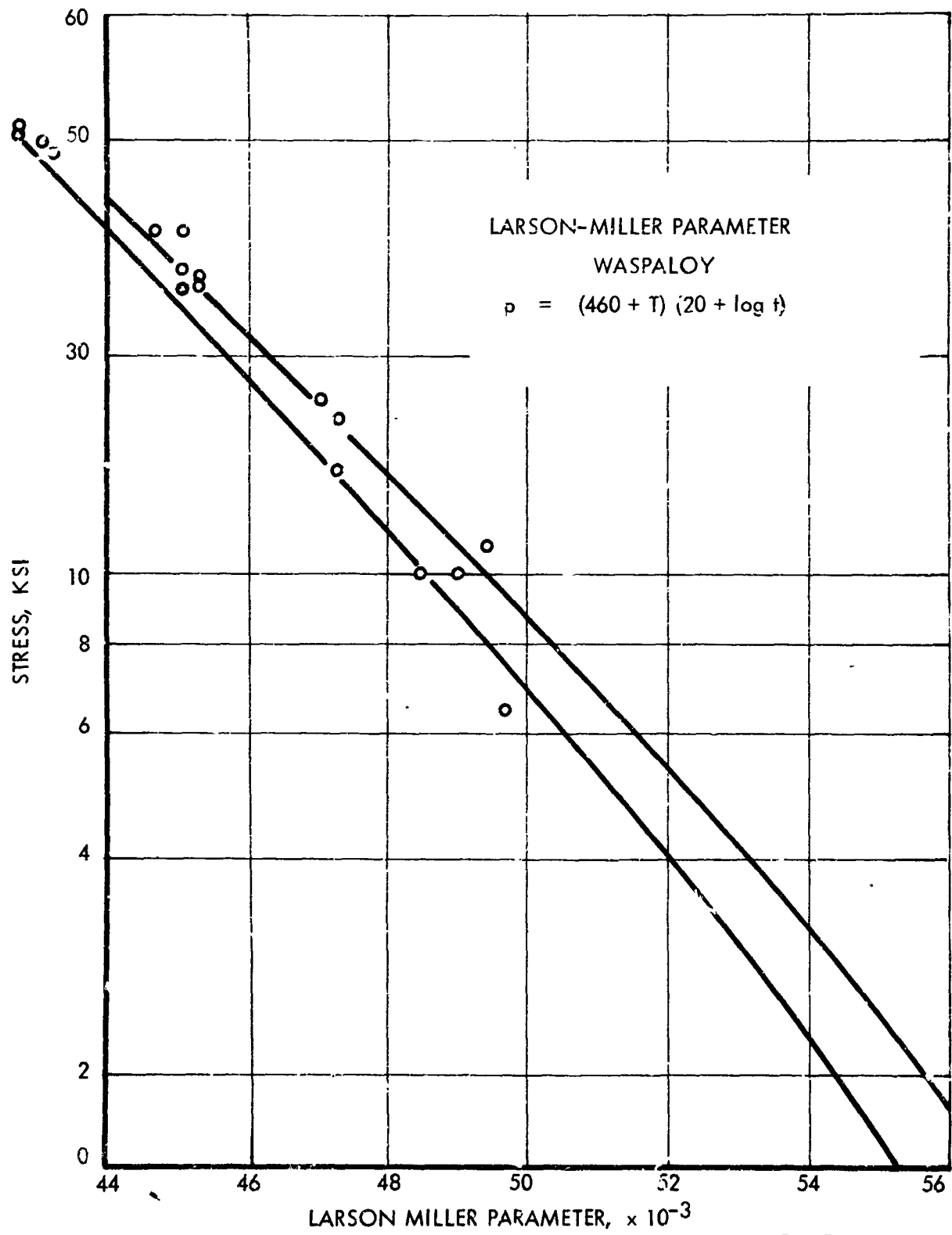


FIGURE 112

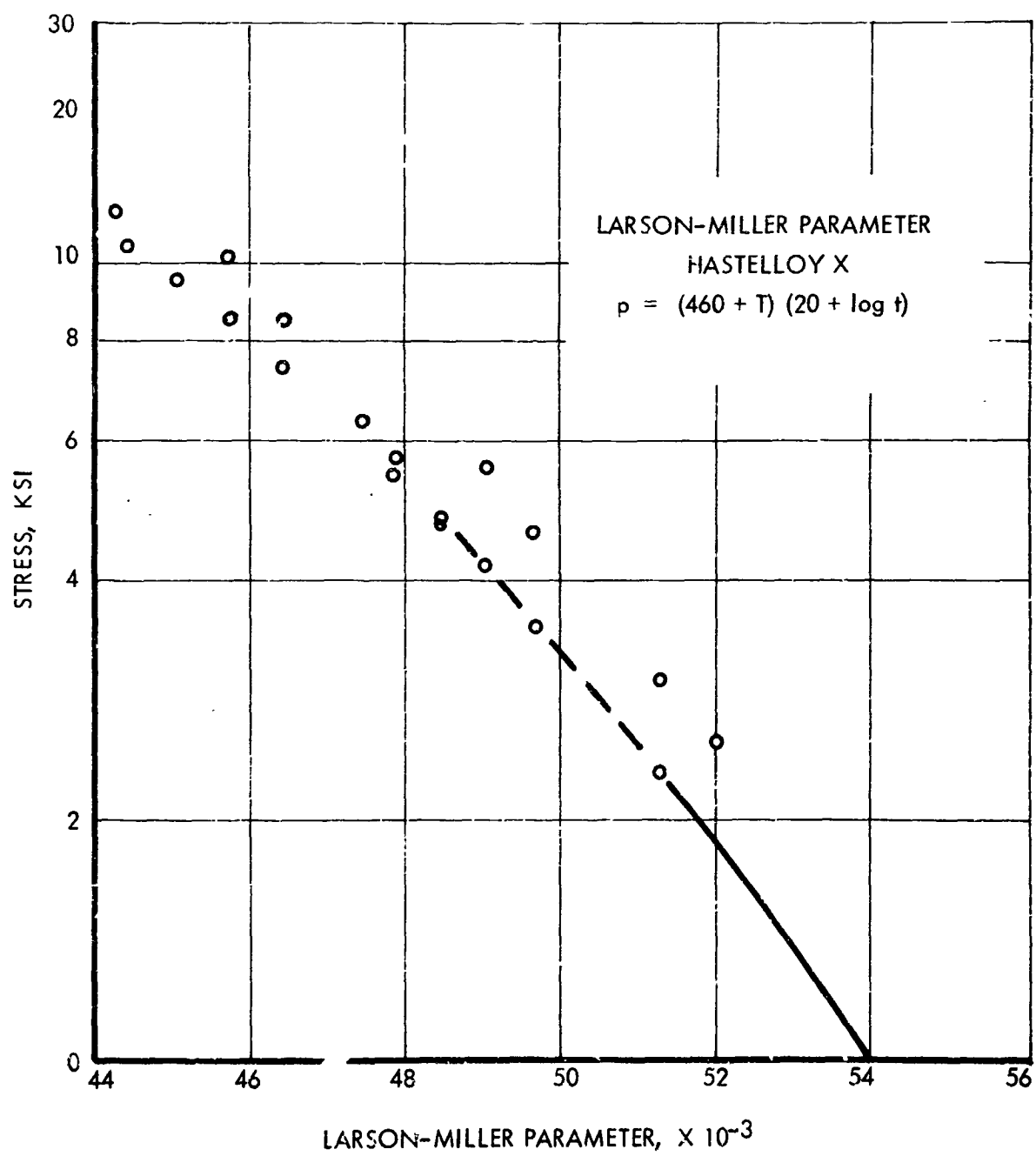


FIGURE 113

8.8 Structural Analysis

8.8.1 Introduction and Summary

This is an exploratory stress and load study of the Brayton Cycle Cavity Receiver.

This study established the range of stresses for various given loading and geometrical conditions. The basic shell thicknesses were set at 0.050 in. (minimum). Localized sections to 0.080 in. are recommended at the critical shell-header junctions to decrease discontinuity stresses. The required minimum thickness dimension for the upper header could be given in terms of an equivalent 0.25 in. thick cylindrical cup.

It is proposed that the gas manifold (reinforced or otherwise) would serve as a suspension ring for the cavity receiver. The suspension mounting ring has not been designed to date as this ring is NASA's responsibility. This also would determine the required minimum thickness for the lower header. Basically, this manifold-header combination serving as the suspension ring would help to suppress the transfer of some take-off and thermal loads from the structural suspension elements into the primary shell structure.

The subsequent low cycle fatigue ($\approx 10,000$ thermal cycles) and long life considerations (10,000 hours at 1560° F to 1750° F) indicate that these severe loading requirements could be satisfied by proper material selection and structural optimization.

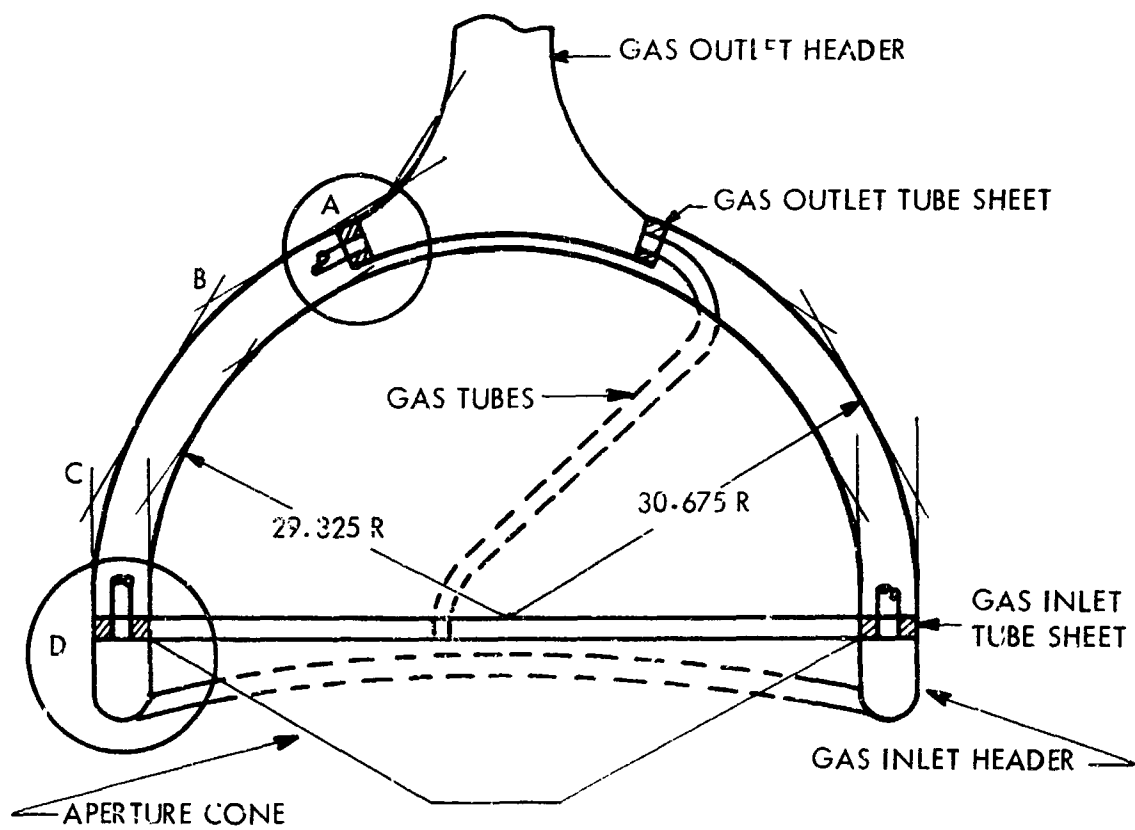
For this structural design two pertinent quantities were considered; namely, the Larson-Miller parameter and corresponding stress rupture strengths, and the permissible alternating stress intensity. Insufficient information on material properties for the required operational conditions precluded a confident evaluation of the candidate materials: Haynes 25, Waspaloy and Hastelloy. Based on the subsequent extrapolations, Waspaloy appears to be the leading candidate material for this structural application. (Sections 0.7 and 7.0.) Additional information including the corrosion test results and possibly some structural testing will be required for the final selection of material.

The established pertinent minimum dimensions and recommendation of the integrated shell-suspension ring design could serve as the inputs for finalizing the design of the cavity receiver and the entire structural suspension system. To insure the structural integrity, optimization and reliability, it is strongly suggested that the integrated shell-suspension system analysis be undertaken by means of digital computer calculations.

8.8.2 Pressure and Thermal Stresses

The primary intent of this stress analysis was to identify problem areas and establish the required structural details to resist the assessed pressure and thermal loads.

The next step would be to integrate the pre-sized shell structure with the load carrying members and suspension ring for final integrated Brayton cavity receiver structural design.



BRAYTON CYCLE CAVITY RECEIVER

FIGURE 114

The Brayton cycle cavity receiver will be subjected to the following mechanical and thermal loads:

The basic mechanical loads are:

- a) Take-off loads. The design of the shell should be based on the deformations transferable from the supporting structure into the shell structure.
- b) Atmospheric pressure: (14.7 psi) loading with the interior of the shells being at nearly vacuum conditions. Conditions (a & b) can be taken to occur at the room temperature level.
- c) The basic thermal loading: In this specific case, the thermal loading is characterized by the low internal and external pressures, high temperature levels and axi-symmetric thermal gradients varying with time. This type of loading could be described quite appropriately as a long duration - low cycle fatigue type loading. Specifically, the inner shell will be subjected to the loads of this type.

In the stress analyses, the inside and outside shells were considered in terms of cylinders and truncated cones as shown in the accompanying Figure 114. Then, by using the elastic deformation coefficients and compatibility relationships, the pressure and thermal discontinuity stresses were established. For this purpose the basic considered structural zones were: (See Figure 114)

Zone A) (upper header-outer shell junction zone)

With this zone being practically an isothermal zone (1560° F), only the pressure loads were considered. The upper header pressure was set at the 14 psi level.

Two designs for this junction were considered the "light bottom" (Fig. 115) and the reinforced (Figure 116) designs.

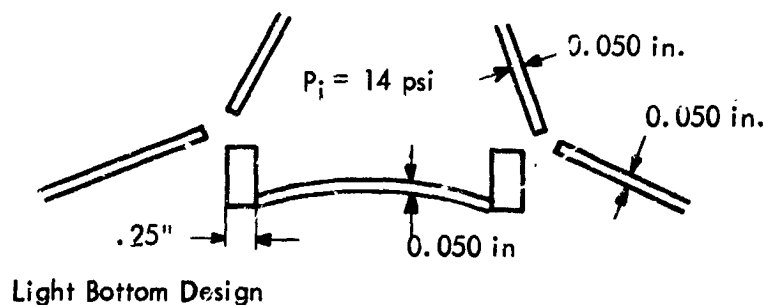


FIGURE 115

The "light bottom" design indicated excessive stresses, and, consequently a reinforced header design was introduced to determine the approximate equivalent minimum header thickness dimensions. The desirable minimum thickness dimension could be described by a .25 in. thick cylindrical cup. For the design shown in Figure 116 the maximum localized stress level was determined to be 7500 psi.

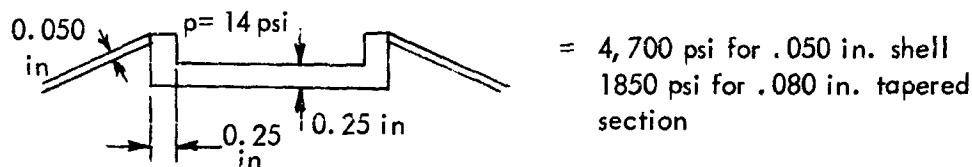


FIGURE 116

REINFORCED HEADER

These stress levels for the isothermal conditions of 1560° F, 14 psi, 10,000 hours and Waspaloy are satisfactory. With $\sigma_{rupture} = 10,000$ psi, (lower bound), the apparent margin of safety (M. S.) for zone A is

$$MS = \frac{10,000}{7,500} - 1 = +0.33 \text{ (Min.)}$$

It is further recommended that in the actual design the shell wall should be increased to .080 in. with the tapered section extending for about 10 in. to further increase the mechanical reliability of this joint. The comparatively rigid connections at Zone (A) can be considered to be insensitive to the possible rotations of the relatively soft tubes.

Zone B) Practically an isothermal junction - thermal stresses were not computed. The pressure stresses will be basically membrane stresses i. e., $PR/2t$.

For the space conditions, the membrane stresses are expected to be at about 60 psi level. For the ground test conditions, the membrane stresses were calculated to be at about 4500 psi level.

Zone C) The maximum thermal stresses using the elastic deformation coefficients and rigid thermal rotations were calculated to be

$$\sigma_{\theta} = 1010 \text{ psi}$$

(Section 8.8.6)

$$\sigma_{\theta} = 1620/\text{psi}$$

The pressure stresses for this zone will be practically membrane stresses and can be given as $(PR/2t)$. These stresses could be set at the levels given for Zone B.

Zone D) This zone will be primarily subjected to thermal loads in space with pressure loads being very low (10 mm Hg). This zone (inner shell detail) contains the largest thermal gradients and was analyzed by employing the short and long beam elastic deformation coefficients and rigid thermal rotations. For establishing the range of thermal stresses this zone was considered by using several thermal load and shell wall thickness combinations. (Figures 117 and 118 and Appendix, Section 8.8.6.)

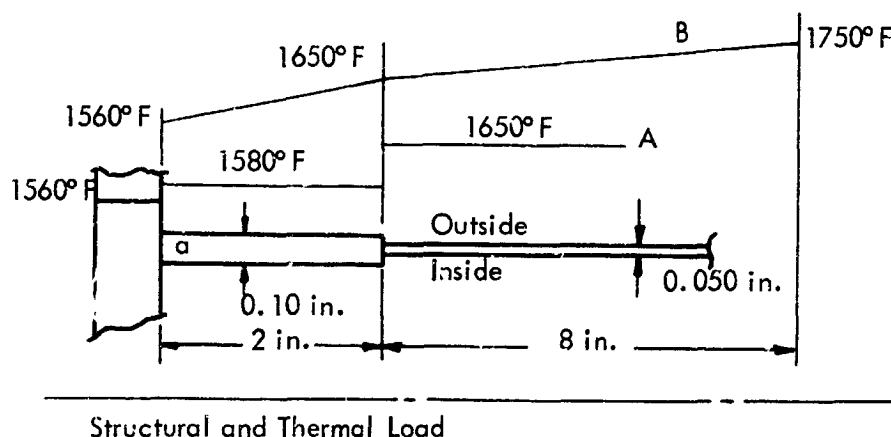


FIGURE 117

For the structural combination and very severe thermal load (A) application shown in Figure 117, the maximum thermal stresses are:

$$\sigma_{\theta} = \pm 7,780 \text{ psi } \begin{matrix} \text{(-outside)} \\ \text{(+inside)} \end{matrix}$$

$$\sigma_{\theta} = -15,280 \text{ psi outside} \quad (\text{pt. b, Figure 117})$$

$$\sigma_{\theta} = -10,750 \text{ psi inside}$$

$$\sigma_{\theta} = \pm 15,020 \text{ psi } \begin{matrix} \text{(-outside)} \\ \text{(+inside)} \end{matrix}$$

$$\sigma_{\theta} = -1200 \text{ psi (inside)} \quad (\text{pt. a, Figure 117})$$

$$\sigma_{\theta} = -9850 \text{ psi (outside)}$$

The corresponding maximum stress intensities are:

$$S_{\max} = \sigma_{\theta} - \sigma_{\theta} = /18,620/\text{psi (pt. b)}$$

$$\text{and } S_{\max} = /16,220/\text{psi (pt. a)}$$

With S_{\max} principally consisting of thermal stresses, the maximum alternating stress intensity S_{alt} and the maximum mean stress intensity, S_{mean} , will be taken as

$$S_{alt} = S_{mean} = 1/2 \times S = 1/2 \times 18,620 = 9,310 \text{ psi (pt. b)}$$

and

$$S_{alt} = 8,110 \text{ psi (pt. a)}$$

For the more realistic thermal loading B, Figure 117, the maximum stresses are:

$$\sigma_{\phi} = \pm 28,550 \text{ psi } \left(\begin{smallmatrix} +\text{outside} \\ -\text{inside} \end{smallmatrix} \right) \quad (\text{pt. a Figure 117})$$

$$\sigma_{\theta} = \pm 8,220 \text{ psi } \left(\begin{smallmatrix} +\text{outside} \\ -\text{inside} \end{smallmatrix} \right)$$

$$\sigma_{\phi} = \pm 3,050 \text{ psi } \left(\begin{smallmatrix} +\text{outside} \\ -\text{inside} \end{smallmatrix} \right)$$

$$\sigma_{\theta} = -6,990 \text{ psi (inside)} \quad (\text{pt. b, Figure 117})$$

$$\sigma_{\theta} = -7,240 \text{ psi (outside)}$$

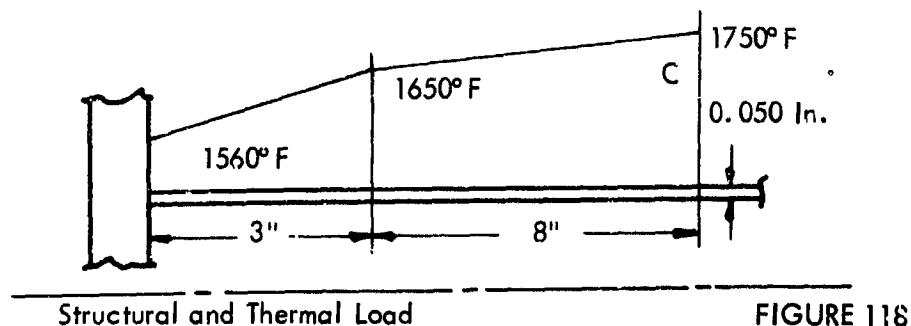
The corresponding maximum stress intensity may be given as

$$S_{\max} = /28,550 - 8,220/ = /20,330/\text{psi} \quad (\text{pt. a})$$

and

$$S_{alt} = S_{mean} = 1/2 \times 20,330 = 10,170 \text{ psi}$$

A third structural and thermal load possibility considered is shown in Figure 118. For this calculation, the cone aperture zone was taken as 3.0 in. long.



For this thermal loading the maximum stresses are:

$$\sigma_{\theta} = \pm 10,700 \text{ psi } \begin{matrix} (+\text{outside}) \\ (-\text{inside}) \end{matrix} \quad (\text{pt. a, Figure 118})$$

$$\sigma_{\theta} = \pm 3,080 \text{ psi } \begin{matrix} (+\text{outside}) \\ (-\text{inside}) \end{matrix}$$

$$\sigma_{\theta} = \pm 1530 \text{ psi } \begin{matrix} (+\text{outside}) \\ (-\text{inside}) \end{matrix} \quad (\text{pt. b, Figure 118})$$

$$\sigma_{\theta} = 1290 \text{ psi (inside)}$$

$$60 \text{ psi (outside)}$$

The corresponding stress intensities for this case may be given as

$$S_{\max} = 7,620 \text{ psi} \quad (\text{pt. a, Figure 118})$$

$$S_{\text{alt}} = S_{\text{mean}} = 1/2 \times 7,620 = 3810 \text{ psi}$$

$$S_{\max} = 800 \text{ psi} \quad (\text{pt. b, Figure 118})$$

$$S_{\text{alt}} = S_{\text{mean}} = 400 \text{ psi}$$

The stresses at the critical junction, i.e., shell to lower header are entirely dependent upon the description of thermal loading. With the defined thermal loading the structural design of this junction will be optimized.

8.8.3 Fatigue Considerations

The previous paragraphs established the shell-lower header junction to be the critically stressed zone of this Brayton cycle cavity receiver.

This zone will be subjected to the low-cycle type thermal fatigue cycling. Speculative fatigue diagrams (Figures 119 and 120)* of the modified Goodman diagram type will be employed for evaluating the long duration - low cycle fatigue material requirements.

These fatigue diagrams based on the limited and extrapolated data on material properties tend to indicate that Waspaloy is a more suitable material for this structural application.

*Lower limits of T_{rp} are used in Figures 119 and 120, also see Section 8.7.

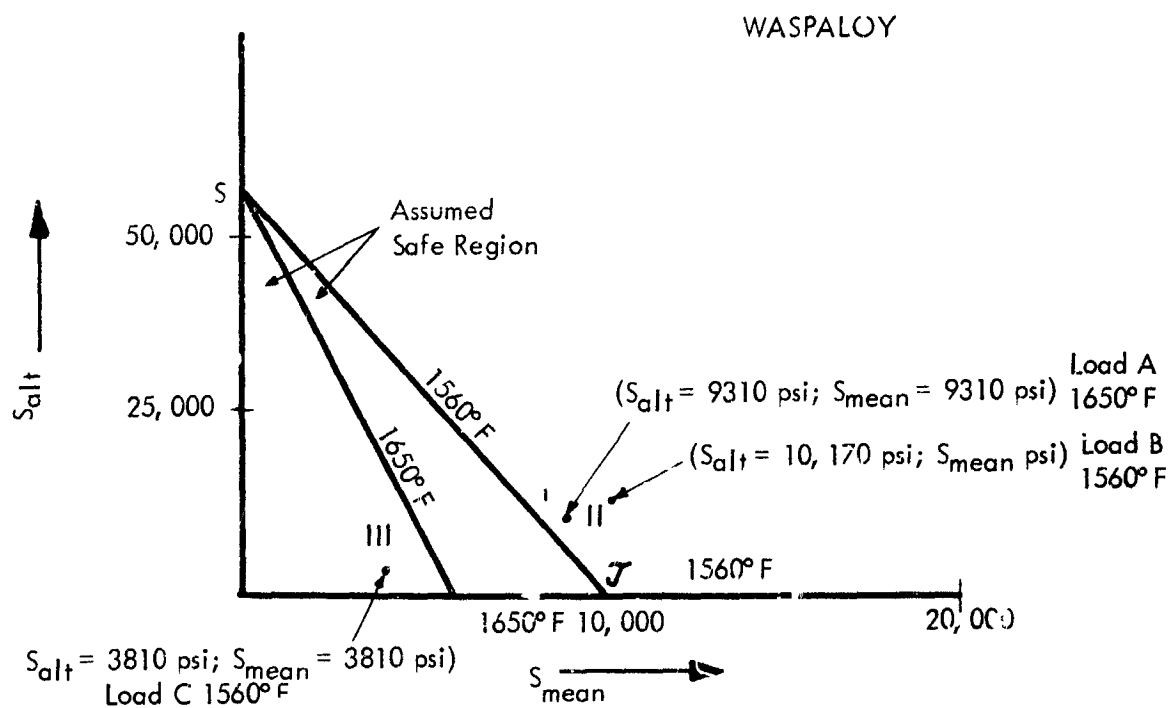


FIGURE 119

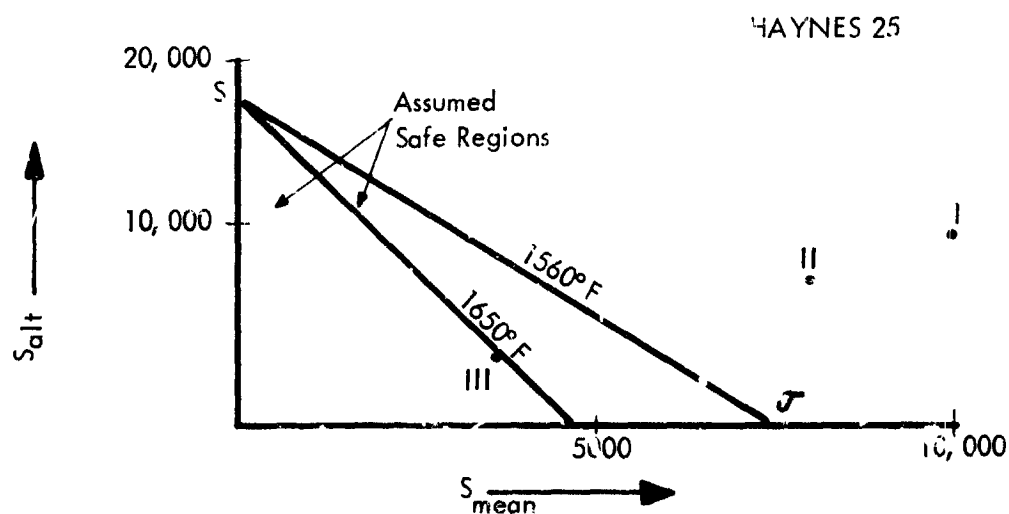


FIGURE 120

Some of the stress intensity points in Figures 119 and 120 already satisfy the long duration requirements without taking into account stress relaxation effects. Waspaloy and Haynes 25, considering stress relaxation effects, apparently will satisfy most if not all of the suggested Salt, Smean combinations.

As it was pointed out previously, more detailed thermal information is required for an optimum design of this particular junction.

Other zones are basically subjected to pressure loads of about 14 psi at isothermal conditions. The apparent highest stress level for the zones subjected to these loading conditions is represented by the 7500 psi levels at 1560°F (Zone A). Again, without going into an optimization study of the structure, Waspaloy having an apparent higher extrapolated stress rupture strength appears to be the leading candidate material for this structural application.

8.8.4 Stress Relaxation

This discussion will be based on the inside shell calculations. Specifically, this discussion will be limited to the inner shell .050 in. wall thickness - lower header junction at 1560°F (isothermal). Further, in this illustrative calculation the above mentioned junction was considered to be an isothermal zone subjected to an external pressure of 14.7 psi (ground test, full vacuum between the shells).

The following parallel remarks are applicable here:

- a) The above loading conditions and the resulting stresses approximately correspond to the shell-lower-header junctions in space pressurized to 14.7 psi.
- b) With no pressurization in space, the maximum mean thermal stress intensities correspond very nearly to the equivalent stress of 8600 psi given below.

At the inner shell-header junction, the calculated pressure stresses were:

$$\sigma_{\theta} = 4310 \text{ psi (membrane) and } 5560 \text{ psi (discontinuity bending stress)}$$

$$\sigma_{\theta} \text{ Total} = 9870 \text{ psi}$$

$$\sigma_{\theta} \text{ Total} = 5910 \text{ psi}$$

The corresponding equivalent stress based on the distortion energy theory is equal to 8600 psi.

This equivalent uniaxial stress of 8600 psi exceeds the stress rupture strength of 7300 psi for Haynes 25 at 1560°F and 10,000 hours.

For the above loading condition, stress relaxation due to creep was considered. Here it was taken that the stress will remain constant for the interval of time during which a predetermined amount of creep will occur. At the end of this interval of time the stress was assumed to relax in proportion to the creep strain which occurred during that interval. This process was repeated until time in excess of 10,000 hours had been accumulated. The time, strain and stress relationships for Haynes 25 were taken from Reference 10. Similar data on time, strain-stress relationships were not available for Waspaloy.

Applying this method of stress relaxation in discrete steps of 500 psi, 25% of the 5560 psi discontinuity bending stress was relaxed in about 110 hours, 50% in 740 hours, 75% after 2700 hours and complete relaxation of bending stresses after about 19,000 hours. At 1560°F the discontinuity bending stress of 5560 psi was stress relaxed after a loss of about 9% of creep rupture life based on creep strain.

The approximate strain after 10,000 hours $\epsilon_{10,000}$ may be given as

$$\epsilon_{10,000} = \frac{\sigma}{E} + \sum \dot{\epsilon} \Delta t$$

$$\epsilon_{10,000} = \frac{4400}{21.3 \times 10^6} + 261 \times 10^{-6} = 467 \times 10^{-6} \text{ in/in}$$

A pseudo radial deflection after 10,000 hours at the junction could be given as

$$\Delta_r = R \times \epsilon_{10,000}$$

$$\Delta_r = 30 \times 467 \times 10^{-6} = .014 \text{ in.}$$

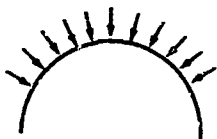
This creep deflection (ripple type) will occur locally near the lower head inner shell junction for the equivalent 14.7 psia pressure level and 0.050 in. shell wall thickness after 10,000 hours.

8.8.5 Instability Loads

Instability of Shells Under Pressure

For this purpose considering the inside and outside shells as spheres, the classical critical elastic buckling pressures (P_{cr}) were calculated to be:

A. Ground Test



Outside shell

100° F, P = 14.7 psi

a = 30.65 in.



Inside shell

100° F p = 14.7 psi

a = 29.35 in.

Outside Shell

$P_{cr} = 104$ psi Haynes 25

Buckling pressures

$P_{cr} = 98$ psi Waspaloy

The corresponding critical membrane stresses for the outer shell are:

$$\sigma_{cr} = P_{cr} \times \frac{a}{2t} = 31,570 \text{ psi (Haynes 25)}$$

and

$$\sigma_{cr} = P_{cr} \times \left(\frac{a}{2t}\right) = 29,750 \text{ psi (Waspaloy)}$$

The membrane stress due to 14.7 psi pressure for the outside shell is

$$\sigma = \frac{pa}{2t} = \frac{14.7 \times 30.65}{2 \times .050} = 4550 \text{ psi}$$

Inside Shell

The membrane stress due to 14.7 psi pressure for the inside stress is

$$\sigma = \frac{pa}{2t} = \frac{14.7 \times 29.35}{2 \times .050} = 4310 \text{ psi}$$

Instability of Shells Under Pressure

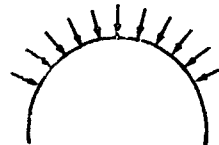
3. Space Conditions



Outside Shell

1560° F, .1934 psi

$a = 30.65$ in.



Inside Shell

1750° F, .1934 psi

$a = 29.35$ in.

Outside Shell

The membrane stress due to .1934 psi pressure for the outside shell is

$$\sigma = \frac{pa}{2t} = \frac{.1934 \times 30.65}{2 \times .050} = 60 \text{ psi}$$

Inside Shell

The critical elastic buckling pressures for space conditions are:

$$P_{Cr} = 76.5 \text{ psi (Haynes 25)}$$

$$P_{Ci} = 75.5 \text{ psi (Waspaloy)}$$

The corresponding critical membrane stress are:

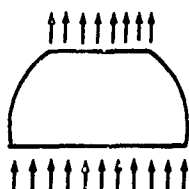
$$\sigma_{cr} = 22,200 \text{ psi (Haynes 25)}$$

$$\sigma_{cr} = 22,000 \text{ psi (Waspaloy)}$$

The membrane stress due to .1934 psi pressure is

$$\sigma = \frac{pa}{2t} = \frac{.1934 \times 29.35}{2 \times .050} = 57 \text{ psi}$$

Buckling of a Truncated Hemisphere Under Axial Tension



The buckling tensile load was determined to be 48.25 lbs per inch at the equator of shell.

The preliminary pipe deflection calculations indicated very low pipe forces ($\ll 48.25$ lb/in) transcribed into the shell structure. Consequently, with the comparatively rigid lower and upper headers these piping loads should not present any structural problems.

Instability of gas tubing

In case the hemispherical shells should be pressurized, the collapsing external pressure on the tubes (.020 in. wall thickness) was calculated. The collapsing tube pressure was found to be 309 psi at 1750° F.

8.8.6 Suspension Ring and Structural Members

For the optimum structural design of the Brayton Cycle Cavity Receiver, the mechanical and thermal loads transferable into the shell from the surrounding structure should be minimized.

These goals could be achieved by the special supporting structure geometry and integrated gas manifold - suspension ring design. It is proposed that the gas manifold (reinforced or otherwise) Figure 121, would serve as a suspension ring for the cavity receiver.

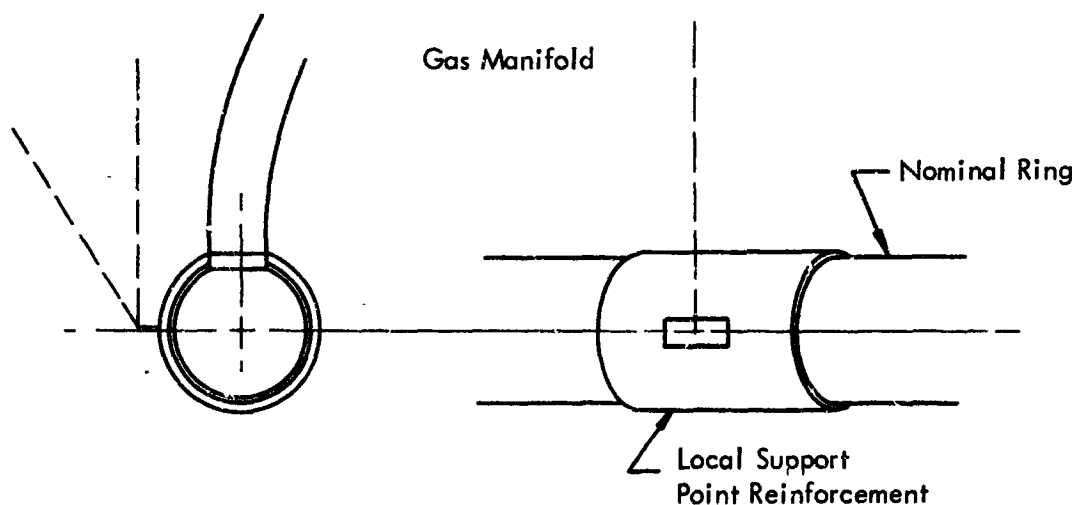


FIGURE 121

For the preliminary sizing purposes of the combined manifold - suspension ring, the equivalent "g" loads acting on the ring were taken as 15 g's. The combined manifold-suspension ring elements were considered from the stress point of view with the suspension ring design stress taken at 40,000 psi for the take-off conditions. Without digital computer studies, the preliminary calculations based on the loads acting in the axial direction, established the apparent minimum geometrical dimensions of the equivalent integrated gas manifold-suspension ring design.

For these loading conditions, a ring toroidal section of 5 in. OD, 1/8 in. thick (nominal) on three point suspension will satisfy the above indicated design stress level. Also a square box toroidal section 4 in. x 4 in. x 1/8 in. thick (nominal) on six point suspension would satisfy the above conditions.

With the appropriate local reinforcements at the joining points to the structure, the above rings are also expected to satisfy the simultaneous structural horizontal loads.

It should be pointed out that the cavity receiver shell structure design for the take-off loads should be based on the suspension ring deformations. For this task and also to insure a structural reliability, the integrated shell-suspension ring design should be undertaken by means of digital computations.

The above mentioned combined manifold-suspension ring designs would limit the long duration 14 psi manifold pressure discontinuity stresses at 1500° F to safe levels (≤ 7000 psi for the square section with rounded corners, and considerably lower stress levels for the circular section). The magnitudes of the suspension structure-ring-shell thermal load will depend upon the suspension structure geometry, materials and the type of joints of the structural elements. This again should be considered as the integral part of the entire Brayton cycle cavity receiver design. For example, this cavity receiver ($R_{\text{mean}} \approx 30$ in.) will expand at the base as $\Delta_t = R \times \alpha \times \Delta T$

$$\Delta_t = 30 \times 8.95 \times 10^{-6} \times (1560 - 70) = 400 \times 10^{-3} = .4 \text{ in. (radially)}$$

This .4 in. displacement will have to be accommodated by the thermal expansions of the suspension system and possibly by some mechanical joints.

8.8.7 Discussion of Candidate Material Properties

For this structural application two quantities of material properties are of special interest, namely, the Larson-Miller parameter (LMP) and corresponding stress rupture strength, and the permissible alternating stress intensity (S).

The high temperature properties of Haynes 25 and Waspaloy which are the primary candidate materials for the Brayton Cycle Cavity Receiver have abstracted from literature and prepared in graphical form. These graphs were presented in Section 8.7.

Haynes 25 Appendix, Section 8.7

Modulus of elasticity vs. temperature, Figure 109

Coefficient of thermal expansion vs. temperature, Figure 109

Creep rupture stress vs. Larson Miller Parameter, Figure 109

Waspaloy Appendix, Section 8.7

Modulus of elasticity vs. temperature, Figure 111

Coefficient of thermal expansion vs. temperature, Figure 111

Creep rupture stress vs. Larson Miller parameter, Figure 113

Hastelloy X Appendix, Section 8.7

Creep rupture stress vs. Larson Miller parameter, Figure 114

The Larson-Miller parameter (LMP) is given in the following form

$$LMP = (460 + ^\circ F) [20 + \log_{10} (t)]$$

where

T - temperature, $^\circ F$

t - time, hrs.

Here, for the design purposes two temperature levels are of greatest interest, namely, 1750 $^\circ F$ and 1560 $^\circ F$ for 10,000 hours.

The Larson-Miller parameters (LMP) for these temperatures and 10,000 hours are:

$$(LMP) = (460 + 1750) (20 + \log_{10} 10,000) = 53.1 \times 10^3$$

1750 $^\circ F$

and

$$(LMP) = (460 + 1560) (20 + \log_{10} 10,000) = 48.5 \times 10^3$$

1560 $^\circ F$

For these high (LMP) parameters not much informative data on the candidate material properties are available. The available information on Haynes 25 for high (LMP) parameters seemingly exceeds similar information obtainable for Waspaloy.

The available information on Haynes 25 seems to predict the rupture strength levels with a higher confidence level for the required (LMP) parameter levels.

The experimental point in Figure 113, for Waspaloy at (LMP) 49.5×10^3 seems to disrupt the lower limit of the extrapolated rupture strength curve. This point is either a "mis-measured experimental point" or a suggestion that serious physical changes take place in Waspaloy as temperature greater than 1600°F. The apparent lower bounds of the stress-rupture values for the design purposes are:

Haynes 25

(LMP) = 53.1×10^3 (1750°F)

$\sigma_{rp} = 2500$ psi

(LMP) = 48.5×10^3 (1560°F)

$\sigma_{rp} = 7500$ psi

Waspaloy

$\sigma_{rp} = 2500$ psi (low confidence level - need more information)

$\sigma_{rp} = 10,000$ psi

The stress rupture values will be used for assessing the mean stress intensities in fatigue evaluation.

The apparent upper bounds of the stress rupture values for the design purposes could be speculatively set* at

Haynes 25

(LMP) = 53.1×10^3 (1750°F)

$\sigma_{rp} = 3100$ psi

(LMP) = 48.5×10^3 (1560°F)

$\sigma_{rp} = 9000$ psi

Waspaloy

$\sigma_{rp} = 4,000$ psi

$\sigma_{rp} = 12,000$ psi

ADDITIONAL COMMENTS

1. There are no real presently available indications in superior creep rupture strength of Waspaloy over Haynes 25 at 1750°F for 10,000 hours.
2. The test data of Waspaloy was accumulated at temperatures of 1600°F and less for periods of 1000 hours. Direct extrapolation to higher temperatures and 10,000 hours from this limited data could result in a considerable error. It is recommended that creep rupture data at temperatures exceeding 1600°F be obtained to support the selection of Waspaloy as the material for the Brayton cycle cavity receiver.

*Based on the mean square curvilinear regression study of Haynes 25 & Waspaloy data

3. For 10,000 hours at 1780° F the lower bound of the creep strength of Hastelloy Alloy X is undefined due to lack of the available information.

For the low cycle fatigue evaluation, the allowable alternating stress intensity(s) may be calculated in terms of the material ductility, elastic modulus and endurance limit, as shown in Equation (a) below

$$S = \frac{E}{4(N)^{1/2}} \times \left[\ln \frac{100}{100-RA} \right] + S_e \quad (a)^*$$

where

S_e = endurance limit, psi

E = elastic modulus, psi

RA = percent reduction of area in tensile test

S_e = endurance limit psi

Haynes 25

Taking the minimum R.A. of 10% in the range from 1500-1750° F, $\sigma_{ult} = 30,000$ psi, (Ref. 18) the calculated S for $N = 10,000$ cycles is

$$S = \frac{E \text{ 1750° F}}{4 N} \times \left[\ln \left(\frac{100}{100-RA} \right) \right] + S_e$$

$$S = \frac{21.8 \times 10^6}{4 \times 10} \times \left[\ln \left(\frac{100}{90} \right) \right] + S_e = 5670 + S_e$$

Taking for approximation $\sigma_e = .4 \sigma_{ult} = .4 \times 30,000 = 12,000$ psi

$$S = 5670 + .4 \times 30,000 = 17,670 \text{ psi (based on sheet properties)}$$

Waspaloy

Taking the average quantities in the range from 1500 - 1750° F (Ref. 13, 14 and 22), $E = 23.5 \times 10^6$ psi, $RA = 45\%$, $\sigma_{ult} = 50,000$ and $N = 10,000$ cycles, we obtain

*Taken from Reference 11

$$S = \frac{23.5 \times 10^6}{4 \times 10^4} \times \left[\ln \left(\frac{100}{55} \right) \right] + .4 \times 50,000$$

$$S = 35,000 + .4 \times 50,000 = 55,000 \text{ psi (based on bar properties)}$$

Again, the lacking pertinent information for calculating the allowable S values does not permit a direct and strong comparison, of Haynes 25 and Waspaloy. However, Waspaloy appears to be the stronger candidate material for this particular fluctuating thermal load application.

8.8.8 SOLAR BRAYTON CYCLE SPACE POWER SYSTEM ENVIRONMENTAL SPECIFICATION

SPECIFICATION NO. P0055-1 With Revision A - June 19, 1964

1.0 SCOPE

- 1.1 This specification covers the anticipated environmental conditions listed below to which the Solar Brayton Cycle Space Power System and components shall be designed to withstand without malfunction or performance degradation.

This specification does not cover development and/or acceptance tests.

1.2 Environments

Environmental conditions specified are applicable to each of the components and the complete solar space power system through manufacture, storage, transportation, lift-off, boost, orbit, and orbital transfer.

2.0 ENVIRONMENTAL CONDITIONS

2.1 Storage and Transportation

The components and their associated equipment shall be capable of withstanding without performance impairment the following loads applied along each of three mutually perpendicular axes of its container.

- 2.1.1 Shock - 4 G shock within one of the following times and wave shape:

- 2.1.1.1 Triangular pulse of 10 milliseconds.

- 2.1.1.2 Half-sine pulse of 8 milliseconds.

- 2.1.1.3 Rectangular pulse of 5 milliseconds.

2.1.2 Vibration:

- 2.1.2.1 2 - 10 cps 0.40 inches double amplitude

- 2.1.2.2 10 - 500 cps 2.0 G peak

2.2 Launch, Lift-off, Boost

The non-operating system and components shall be capable of withstanding without performance impairment the following simultaneous launch loads applied at the system mounting points and in the directions and magnitudes specified:

2.2.1 Shock

35 G shock along each of three mutually perpendicular axes within one of the wave shape and pulse times in 2.1.1 above.

2.2.2 Vibration

Sinusoidal input applied at the system mounting points along each of three mutually perpendicular axes.

16 - 100 cps @ 6 G peak

100 - 180 cps @ 0.0118" double amplitude

180 - 2000 cps @ 15 G peak

2.2.3 Acceleration

The non-operating system and/or each of its components shall be capable of withstanding each of the following combinations of longitudinal and lateral accelerations for five (5) minutes duration each.

2.2.3.1 Max Q - 2 g's longitudinal and 0.25 g's lateral.

2.2.3.2 Max boost acceleration - 4.6 g's longitudinal and no lateral acceleration. The longitudinal accelerations are positive along the vehicle lift-off axis. No negative longitudinal accelerations will be experienced during the launching phase.

2.2.3.3 4.5 G all directions in plane normal to lift-off axis.

2.2.4 Acoustic Noise

The non-operating system and its components shall be capable of withstanding the induced vibrations while subjected to an acoustic noise field with an integrated level of 148 d.b., Re 0.0002 micro bar.

2.3 Orbital Operation

The equipment shall be designed to be capable of start-up and continuous operation at rated power in earth orbits of from 300 to 20,000 nautical miles without malfunction for 10,000 hours time.

2.3.1 Shock

Prior to system startup and deployment, the components shall sustain up to 7 G shock (course correction) along the lift-off or flight axis with one of the wave forms and time durations indicated in paragraph 2.1.1.

2.3.2 Vibration

The system and components will sustain vibrations in orbit while in operation of 0.25 G peak over a frequency range of 5 to 2000 cps for a time period of five minutes for each occurrence.

2.3.3 Acceleration

2.3.3.1 Undeployed

The undeployed system and components will sustain accelerations of $3\frac{1}{2}$ G in one direction along the lift-off axis, and plus or minus 1 G in all directions in the plane normal to the lift-off axis. These accelerations will be sustained individually for a period of five minutes maximum for each occurrence.

2.3.3.2 Deployed

The deployed operating system will also be required to be capable of sustaining a continuous, unidirectional acceleration arising from a 4 RPM spin rate of the spacecraft. The G loading on the system components will be a function of their radial location with respect to the spin axis. For the purposes of this application, the centerline axis of the collector and system is located at a radius of 33 feet from the spin axis and experiences an 0.18 G acceleration.

8.9 Aperture Control Design Analysis

8.9.1 Summary

This appendix contains the detailed design of the Brayton cycle cavity receiver temperature control and aperture control systems. Both controls are actuated by a vapor pressure bulb-bellows system. Increased temperature of the bulb causes a higher vapor pressure and thereby bellows pressure which causes the bellows to expand and actuate the mechanisms. NaK78 is the working fluid.

8.9.2 Discussion

The design of the temperature and aperture control for the Brayton cycle cavity receiver was based on the following criteria:

1. The design must be simple to give it maximum reliability for a 10,000 hour life.
2. There will be no maintenance over its orbital life.
3. Because of the high vacuum environment, sliding or rubbing metal to metal contacts must be minimized, or, if possible, eliminated to avoid self welding.
4. For maximum life, bellows strokes will be kept to a minimum.
5. The systems must operate in both 0-g and 1-g environment.
6. System will not be operating during launch.

8.9.3 Activating Fluid Selection

The activating fluid selection was based on the following criteria:

1. Vapor pressure change over the control temperature range must be large enough to give a reasonable bellows size since the activating force (F) is the product of the pressure times the mean effective area (MEA) of the bellows.
2. The absolute vapor pressure level cannot be too high due to the high temperature (1700° F) of the sensing bulb and bellows pressure limits.
3. The fluid must be compatible with bellows material (316 SS - AM 350).
4. If possible the fluid should be a liquid at room temperature for filling.
5. Handling characteristics of the fluid must be known.

A review of bellows characteristics showed that the pressure level should be kept under 100 psia to insure reasonable cycle life. Adding a safety factor to this figure, a 50 psia limit was chosen. The detail design proves this to be a reasonable value.

Using a 50 psia limit left a choice between NaK (78) and sodium, NaK (78) was picked because of its higher ΔP and also because it is a liquid at room temperature.

8.9.4 Temperature Control

The temperature control system will consist of four rectangular openings to allow reradiation to space. The total open area is set at 346 in.². Each opening is covered by two doors which can be opened by one of two sets of bellows. When the temperature of the sensing bulbs reaches the required temperature (1680° F), the door will start to open. At 1720° F the NaK (78) vapor pressure will be high enough to pressurize the bellows so they will expand enough to swing the doors 15° to their full open position.

Since lubrication and self welding is a problem, no sliding or rubbing contact was allowed in this design. The doors rotate on flex pivots where only bending occurs. The bellows displacement is transferred to the doors through thin flexing metal arms. Since rotation and displacements were kept small, bending stress is within allowable limits.

The manufacturing tolerances of the spring system are compensated for by adjusting the compression on the calibration spring. A 20% adjustment was designed into the system. A torsion spring is used to keep a preload on the closed doors and to close the doors during cool down process.

The bellows will be made of 316 SS which is not only a good bellows material but also is not attacked by the NaK (78). In order to keep the spring relaxation rate below 2%, the springs will be made from Inconel X wire (No. 1 temper). Stress levels in the spring are held around 50,000 psi at a temperature of 800° F.

8.9.5 Recommendations

1. The controls should be tested in a vacuum at temperature to determine
 - a) Temperature effect on spring rates
 - b) Cycle life (can be accelerated)
 - c) Actual performance of the physical hardware and system reliability.
2. Ultra-high vacuum tests of the rubbing contacts should be run to make sure self-welding does not occur.
3. A thermal map should be made analytically and then confirmed by tests to establish actual component temperatures.

4. Further design modifications should be held until firm system design and performance specifications are in hand.
5. Careful attention should be observed on the assumptions for each design. Changes in the system which nullify the assumptions could also nullify the design.
6. During launch the temperature control doors and the aperture doors should be tied down either with explosive bolts or low temperature melting wire.
7. A detailed stress analysis should be made once the structure and system have been defined. Careful attention should be given to loads and vibrations present during launch.

8.9.6 Detail Design Temperature Control

8.9.6.1 Design Assumptions

1. 346 in² (area of 21" dia opening) is required to radiate enough energy to keep cavity receiver surface from overheating.
2. Temperature control band on receiver surface $1700 \pm 20^\circ \text{F}$.
3. Temperature control to be proportional.
4. Actuator environment (bellows and springs) to be insulated to keep operating temperature at $800 \pm 50^\circ \text{F}$.
5. Hinge and flexure elements to be insulated to hold their temperature at $450 \pm 50^\circ \text{F}$.
6. Required cycle

1 cycle/90 min - 16 cycles/day

Total time 10,000 hours

Total full cycles $60/90 \times 10,000 = 6667$ cycles
7. The required control area will be divided into four equal rectangular areas that will be opened and closed by temperature sensitive liquid-vapor bulbs.
8. The control must work in both 1 "g" and 0 "g" environments.
9. The mechanism must survive a rocket launch -- 40 g shock
Non-operating - can be tied down.

10. Space environment requirement does cause metal to metal self welding - high vacuum.

11. Material properties Ref. Aerospace Structural Metal Handbook Vol. I March, 1963.

Material	Property	70° F	400° F	800° F	1000° F	1200° F
316 SS	$E_y \times 10^{-6}$ psi	28	27	25	23	22
	$F_{ty} \times 10^{-3}$ psi	38	22	20	19.5	19.0
Inconel X	$E_y \times 10^{-6}$	31	30	27.5	26.5	26
	6×10^{-6}	11	10.2	9.5	9	8
	$F_{ty} \times 10^3$	115		100	98	95

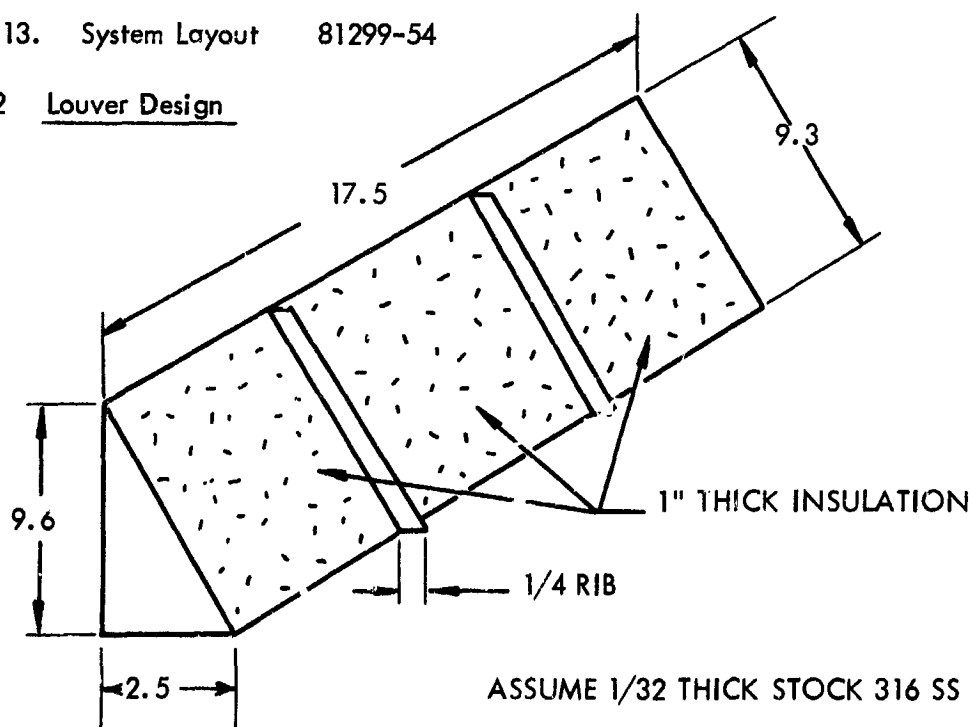
12. Activating Fluid - NaK 78

V_p @ 1680° F - 41 psia

V_p @ 1720° F - 47.5 psia

13. System Layout 81299-54

8.9.6.2 Louver Design



Weight of Steel

$$wt_s = .284 \text{ lb/in}^3 (9.6 \times 2.5 + .7.5 \times 9.9) .032$$

$$.284 (24.0 + 173) .032 = 1.80 \text{ lb}$$

Weight of Insulation

$$wt_I = (.01 \text{ lb/ft}^3) (197) \times 1 = 1.97 \text{ lb}$$

$$\text{Door Weight} = 1.80 + 1.97 = 3.77 \text{ lb}$$

Design Load (40 "g" Shock)

$$D.L. = 3.77 \text{ lb} \times 40 = \underline{\underline{15.08 \text{ lb}}}$$

8.9.6.3 Hinge Design

Use Bendix flexural pivot for hinge.

Use pivot 6016-600

Material - AISI 420

$$\text{Rate spring rate } 6.96 \frac{\text{lb-in}}{\text{rad}}$$

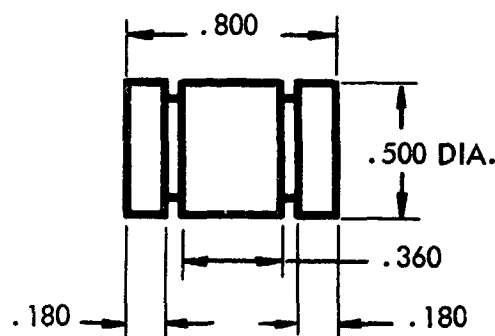
Total rotation $\pm 15^\circ$

Load capacity - compression $P_c = 80 \text{ lb}$

tension $P_t = 400 \text{ lb}$

Using 2 pivots per door $\therefore P_c = 160 \text{ lb}$

$P_t = 800 \text{ lb}$



Mounting the pivot so that the flexing element is in tension (P_t) radial load

Developed load 150.8 lb - capacity/ten . 800
capacity/comp = 180

At 450° F the hinge spring rate (SR_H)

$$SR_{He450} = \frac{E_{450}}{E_{70}} \times SR_{H70} = \frac{28.5}{30} \times 6.96 \frac{\text{lb-in}}{\text{rad}} = 6.62 \frac{\text{lb-in}}{\text{rad}}$$

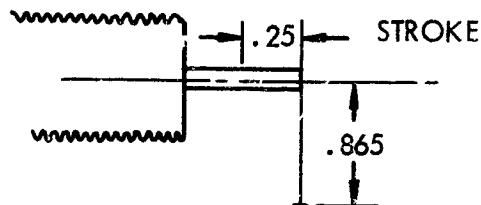
For 15° Deflection

$$\text{Torque} = \tau_{450} = \frac{15}{57.3} \times 6.62 = \underline{\underline{1.73 \text{ in.-lb}}}$$

$$\tau_{70} = \frac{15}{57.3} \times 6.96 = \underline{\underline{1.82 \text{ in.-lb}}}$$

Hinge Force = F_H

Hinge force referenced
to bellows center line



$$@ 450^\circ \text{F } F_H = \frac{1.73 \text{ in./lb}}{.86 \text{ in.}} \underline{\underline{2.0 \text{ lb}}}$$

$$@ 70^\circ \text{F } F_H = \frac{1.82}{.86} = \underline{\underline{2.11 \text{ lb}}}$$

Hinge Spring Reflected to Bellows \mathcal{C}

$$SR_{H450} = \frac{2.0 \text{ lb}}{.25 \text{ in}} = 8.0 \text{ lb/in.} \quad SR_{H70} = \frac{2.11}{.25} = 8.44 \text{ lb}$$

8.9.6.4 Bellows

Use 4 bellows - 2 on each end of doors

Each bellows assembly must work against

Design	One Bellows Failure
1. 1 Bellows	2 Bellows
2. 1 Hinge	2 Hinges
3. 1/2 Return Spring	1 Return Spring

Use Flexonics Corp. bellows C-10007

I.D. = 1.5 in.
 O.D. = 2.06 in.
 Wall = .006 in.
 Pitch = .167 in/conv.
 Max α = .038 in/conv.
 MEP = 2.30 in²

S.R. = 350 lb/in/conv.
 α /psi = .0066 in/psi/conv.
 Max. press. = 125 psi @ 20° F
 Max. no. conv. = 95
 Material 316 S.S.

Maximum Pressure @ 800° F

$$P_{min800} = \frac{F_{ay 800}}{F_{ty 70}} \times P_{70} = \frac{20,000}{38,000} \times 125 = 66 \text{ psi}$$

Detailed Bellows Design

Required Stroke = 0.25 in. = S

No. Convolutions = 15

Free Height = 15 x .167 = 2.5 in = L

$$\frac{S}{L} = \frac{.25}{2.5} = .1$$

$$\frac{L}{D} = \frac{2.5}{2.06} = 1.21 \text{ OK Bellows Should Not Buckle or Squirm}$$

$$\% \text{ Max. Press.} = \frac{47.5}{66} = 72\%$$

$$SR @ 70^\circ F = \frac{350 \text{ lb/in/conv}}{15 \text{ conv}} = 23.3 \text{ lb/in}$$

$$SR @ 800^\circ F = \frac{E_{800}}{E_{70}} \times SR @ 70 = \frac{25}{28} \times 23.3 = \underline{\underline{19.9 \text{ lb/in}}}$$

Max. Stroke Allowable = 15 x .038 in/con = 0.57 in

$$\% \text{ Max. Stroke Used} = \frac{.25}{.57} = 44\%$$

Cycle life based on Robertshaw Fulton Catalog Page 11 Chart

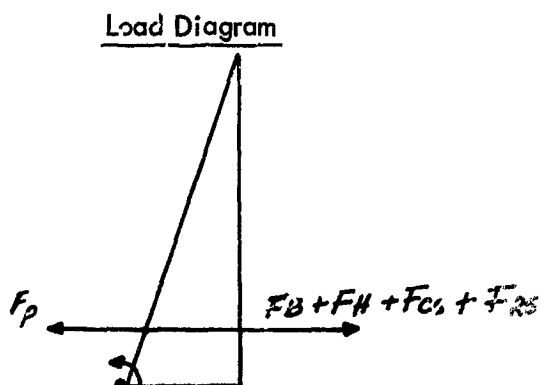
Cycle life expected 20,000 Full Stroke (.25 in.)

Required Full Stroke 6,667

Half Stroke Cycles (.125)

Cycle Life Expected 100,000

Required 70,000



F_p = Pressure Force (1/End)
 F_B = Bellows Force (1/End)
 F_H = Hinge Force (1/End)
 F_{cs} = Calibration spring force (1/End)
 F_{RS} = Return spring force (1/4 End)

$$\text{Pressure Force} = P \times \text{MEA} = F_p$$

$$F_{p \max} = 42.5 \times 2.30 = 109.25 \text{ lb} \quad (1720^\circ \text{F})$$

$$F_{p \min} = 41 \times 2.30 = 94.3 \quad (1680^\circ \text{F})$$

$$\Delta F_p = 109.25 - 94.3 = 14.95 \text{ lb}$$

$$\text{System Spring Rate} = SR_{\text{sys}} = \frac{14.95 \text{ lb}}{.25 \text{ in}} = 59.8 \text{ lb/in}$$

Door must not open before 1680°F . . .

$$\text{Preload must} = F_{p \min} = 94.3 \text{ lb}$$

Load to be taken by calibration and return springs may

$$\begin{aligned}
 F_{cs \max} + F_{RS \max} &= F_{p \max} - (F_{B \max} + F_{H \max}) \quad F_B = 19.9 \text{ lb/in} \times .25 \text{ in} = 4.90 \text{ lb} \\
 &= 109.25 - (4.96 + 2)
 \end{aligned}$$

$$F_{cs \max} + F_{RS \max} = 102.29 \text{ lb}$$

$$\text{Min } (F_{cs} + F_{RS})_{\min} = F_{p \min} - (F_B + F_H)_{\min} = 94.3 - 0 = 94.3 \text{ lb}$$

$$\Delta F = 7.95 \text{ lb}$$

$$SR_{cs} + SR_{rs} = \frac{102.29 - 94.3}{.25} = \frac{7.95 \text{ lb}}{.25 \text{ in.}} = \underline{31.9 \text{ lb/in}}$$

8.9.6.5 Return Spring

Use one return spring on each door

Return spring preload -- 10 lb

Return spring rate 8 lb/in

Each bellows will carry half the return spring load material Inconel X

Return Spring Design

Ref. to Bellows ϕ \therefore 8 lb/in @ .865 lever arm

$$\Delta F = 8 \text{ lb/in} \times .75 \text{ in} = 2 \text{ lb}$$

$$\frac{\text{Torque}}{\text{rev}} = \frac{2 \text{ lb} \times .865 \text{ in}}{15^\circ} \times 360^\circ = 41.5 \frac{\text{in lb}}{\text{rev}}$$

$$F_{H \text{ max}} = 10 \text{ lb} + 2 \text{ lb} = 12 \text{ lb}$$

Use $S_{\text{max}} = 65,000 \text{ psi}$ - safe for Inconel X @ 800°F

$$\text{Total Moment} = F \times d = 12 \text{ lb} \times .865 \text{ in} = 10.4 \text{ in-lb}$$

$$S = \frac{32 M}{\pi d^3} \quad d = \sqrt[3]{\frac{32 M}{\pi S}} = \sqrt[3]{\frac{32 \times 10.4}{\pi \times 65,000}}$$

$$d = \sqrt[3]{1.63 \times 10^{-3}} = 1.176 \times 10^{-1}$$

$$d = \underline{0.1176 \text{ in wire dia.}}$$

$$M_a = \frac{E d''}{10.8 \text{ DN}}$$

$$m_a = 41.5 \text{ in-lb/rev}$$

$$E = 27.5 \times 10^6 \text{ psi @ 800°F}$$

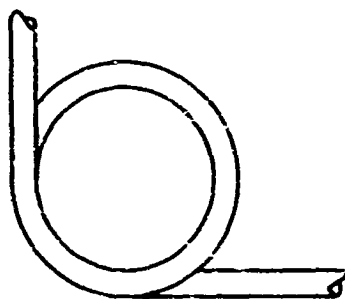
$$d = 0.1176 \text{ in}$$

$$DN = \frac{E d^4}{10.8 Ma} = \frac{27.5 \times 10^6 \times (1.1176 \times 10^{-1})^4}{10.8 \times 41.5}$$

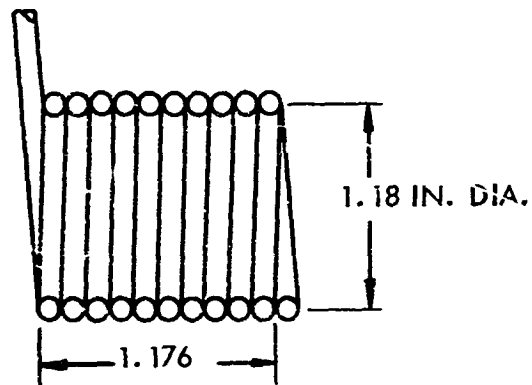
$$DN = \frac{27.5 \times 10^6 \times 1.92 \times 10^{-4}}{10.8 \times 41.5} = 11.8$$

For $N = 10$ $D = 1.18$ in mean coil dia.

Coil length = $1.1176 \times 10 = 1.176$ in



Return Spring



8.9.6.6 Calibration Spring

$$SR_{cs} + SR_{RS} = 31.9 \text{ lb/in}$$

Since the load of the return spring is shared by two bellows.

$$SR_{cs} = 31.9 - 8/2 \text{ lb/in} = \underline{27.9 \text{ lb/in}}$$

$$\text{Max } F_{cs} = F_{p \text{ max}} - F_{D \text{ max}} - F_{RS \text{ max}} - F_{H \text{ max}} = 109.25 - 4.96 - 6 - 2 = \underline{96.29 \text{ lb}}$$

$$\text{Min } F_{cs} = F_{p \text{ min}} - F_{B \text{ min}} - F_{RS \text{ min}} - F_{H \text{ min}} = 94.3 - 0 - 5.0 = \underline{8.93 \text{ lb}}$$

$$SR_{cs} = \frac{96.29 - 89.3}{.25} = \frac{6.99 \text{ lb}}{.25 \text{ in.}} = \underline{27.9 \text{ lb/in}}$$

Calibration Spring Design

Required $SR_{@800} = 27.9 \text{ lb/in}$ Temp. = 800°F

Preload = 89.3 lb

Max load = 96.29 lb

$$SR_{@70} = G_{20}/G_{800} \times SR_{@800} = 11/9.5 \times 27.9 = 32.3 \text{ lb/in}$$

Use Inconel X wire

Allowable Stress @ 800°F 55,000 psi

Use 0.250 dia wire

Coil top 3.125 O.D.

From A.M. Wahl - Mechanical Springs

Load @ 100,000 psi stress - - 191 lb corrected

$$SR/coil = 237 \text{ lb/in/coil @ } 70^\circ\text{F}$$

$$\text{No. coils} = \frac{237 \text{ lb/in/coil}}{32.3 \text{ lb/in}} = 7.35 \text{ use 10 coils}$$

$$\text{Solid height} = .250 \times 10 = 2.5 \text{ in.}$$

$$\text{Deflection for max load} = \frac{96.29 \text{ lb}}{27.9 \text{ lb/in}} = 3.45 \text{ in}$$

$$\text{Min height allowed} = \frac{2.5}{.9} = 2.78 \text{ in}$$

$$\text{For 20\% adjustment max deflection} = \frac{3.45}{.8} = 4.11 \text{ in}$$

$$\text{Free length} = 4.11 + 2.78 = 6.89$$

$$\text{Preload deflections} = \frac{89.3}{27.9} = 3.20 \text{ in}$$

$$\text{Preloaded length} = 6.89 - 3.20 = 3.69 \text{ in}$$

$$\text{Max load length} = 6.89 - 3.45 = 3.44 \text{ in}$$

$$\text{Stress at max load} = \frac{96.29}{191} \times 100,000 = 50,200 \text{ psi}$$

Allowable stress 55,000 psi

∴

From Wahl - pp 47

For Inconel X - No. 1 Temperature at 800° F

Relaxation = 2.2% 95% of this occurs in first three days.
This could be adjusted out during calibration Tests

Buckling Check

$$\text{Critical Buckling Ratio} = \frac{\delta_{cr}}{L_0}$$

where δ_{cr} = Critical Buckling Deflection

L_0 = Free Length

$$\text{Ratio } \frac{L_0}{D} = \frac{\text{Free Length}}{\text{Mean Coil Dia.}} = \frac{6.89}{2.875} = 2.75$$

From Wahl pp. 69 for $L_0/D = 2.75$ $\delta_{cr}/L_0 \propto$

Both ends fixed

∴ Spring will not buckle

8.9.6.7 Sensing Bulb Design - Temperature Control

Enough liquid must be vaporized to displace adequate liquid to fill the increased bellows volume.

One sensing bulb supplies two bellows.

Bellows displacement = MEA x stroke

$$= 2.30 \text{ in}^2 \times .25 \text{ in}$$

$$= .575 \text{ in}^3/\text{bellows}$$

For two bellows vol. req. = $2 \times .575 = 1.150 \text{ in}^3$

The pound of liquid required to do this is calculated as follows:

At 1700° F density of NaK 78 = 40.5 lb/ft³

By wt NaK 78 is 78% K

For 1 lb NaK 78 22% Na

$$N_k = \frac{m}{M} = \frac{.78}{39.1} = 19.95 \times 10^{-3} \text{ moles}$$

$$N_{Na} = \frac{.22}{23} = 9.57 \times 10^{-3} \text{ moles}$$

$$h_{NaK} = h_k + h_{Na} = (19.95 + 9.59) \times 10^{-3} = 29.52 \times 10^{-3} \text{ moles}$$

Mole fractions are

$$x_k = \frac{h_k}{n} = \frac{19.95}{29.52} = .676$$

$$x_{Na} = \frac{h_{Na}}{h} = \frac{9.57}{29.52} = .324$$

$$x_{NaK} = 1 = x_k + x_{Na} = .676 + .324 = 1.000$$

The average molecular wt

$$\begin{aligned} M &= x_k M_k + x_{Na} m_{Na} \\ &= .676 \times 39.1 + (.324) (23) \end{aligned}$$

$$m = 26.41 + 7.45 = 33.86$$

Mixture gas constant

$$R = \frac{\bar{R}}{M} = \frac{1545}{33.86} = 45.7 \frac{\text{ft-lb}}{\text{lb}^\circ\text{R}}$$

$$\text{Min. vol required} = 1.150 \text{ in}^3$$

To take care of tolerances use 1.5 in^3 for ΔV

$$\Delta V = \frac{MRT}{P}$$

$$M = \frac{VP}{RT} = \frac{1.5 \text{ in}^3 \times 47.5 \text{ lb/in}^2 \times 144 \text{ in}^2/\text{ft}^2}{\frac{1728 \text{ in}^3}{\text{ft}^3} \times 45.7 \frac{\text{ft-lb}}{\text{lb}^\circ\text{R}} \times 2120^\circ\text{R}}$$

$$M = 6.13 \times 10^{-5} \text{ lb}$$

$$\text{Mass of Liquid in Bulb} = \frac{1.5 \text{ in}^3}{1728 \frac{\text{in}^3}{\text{ft}^3}} \times 40.5 \frac{\text{lb}}{\text{ft}^3} = .0352 \text{ lb 110 NaK}$$

More than enough liquid is available

Change in NaK volume in bellows tube and bulb with change in temperature of 1000° F.

$$\text{Volume of bellows cold} = 2.30 \times 2.5 \text{ in} = 5.75 \text{ in}^3$$

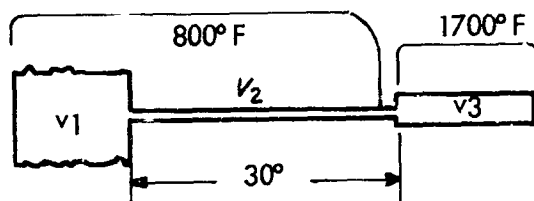
$$\text{Volume of Feed Line (3/16 tube - .035 wall)} = .01075 \text{ in}^2 \times 30 \text{ in} = .32 \text{ in}^3$$

$$\text{To system volume cold} = 5.75 + .321 + 1.5 = \underline{7.571 \text{ in}^3}$$

$$\rho_{70^\circ \text{F}} = 54 \text{ lb/ft}^3$$

$$\rho_{800^\circ \text{F}} = 48.05 \text{ lb/ft}^3$$

$$\rho_{1700^\circ \text{F}} = 40.5 \text{ lb/ft}^3$$



$$V_{1-30} = V_{170} \times \frac{70}{800} = 6.07 \times \frac{54}{48.05} = 6.82$$

$$\Delta V_{1+2} = 6.82 - 6.07 = 0.75 \text{ in}^3$$

$$\Delta V_{1+2} + V_{3L} + V_{3L} = 1.5$$

$$V_{3L} + V_{3L} = 1.5 - .75 = .75 \text{ in}^3$$

$$V_{3L} + .33 V_{36} = .75 \text{ in}^3$$

$$1.33 V_{36} = .75 \text{ in}^3$$

$$V_{3L} = \frac{.75}{1.33} = .564 \text{ in}^3$$

$$\Delta V_{3L} = V_{1700} - V_{70}$$

$$V_{1700} = V_{70} \times \frac{\rho_{70}}{\rho_{1700}} = V_{70} \times \frac{54}{40.5}$$

$$V_{1700} = V_{30} \times 1.33$$

$$\Delta V_{3L} = 1.33 V_{30} - V_{70}$$

$$\Delta V_{3L} = .33 V_{30}$$

∴ @ 70° F system should be filled with the following amount of liquid

$$6.07 + .564 = 6.634 \text{ in}^3 \text{ or } \frac{6.634 \text{ in}^3}{1728 \frac{\text{in}^3}{\text{ft}^3}} \times 54 \text{ lb/ft}^3$$

wt of fill .24 lb NaK 78

8.9.6.8 Design Summary - Temperature Control

Bellows

Type	Flexonics Corp.	C-10007
ID		1.5 in.
OD		2.06 in.
Wall		.006 in.
Pitch		.167 in/conv.
Max ρ		.038 in/conv.
Mea		2.30 in.
SR		19.9 lb/in @ 800° F 23.3 lb/in @ 70° F
f/psi		.0066 in/psi/conv @ 70° F

Max. Press.	125 psi @ 70° F
Material	316 SS
Stroke	.25 in. extension
No conv.	15
Free Height	2.5 in.
No. Required	4

Hinge

Type	Bendix Flexural Pivot	6016-600
Material		AISI 420
Rotation		15°
Torque		1.73 in. lb @ 1150° F
No. Required		2 per door 16 Total

Return Spring

Type	Torsional	No. Required 1/Door
O.D.	1.18 in.	Total 8
Wire Dia.	.0117 in.	
No. Coils	10	
Coil Length Solid -	1.176 in.	
Torque	41.5 in-lb/rev. @ 800° F	
Preload	2 lb	

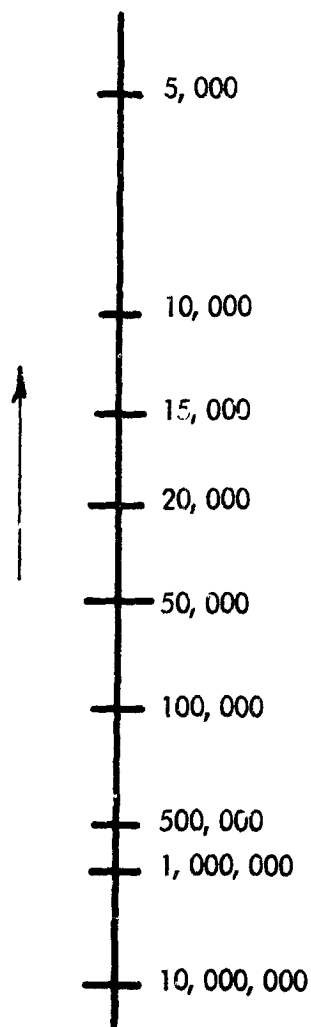
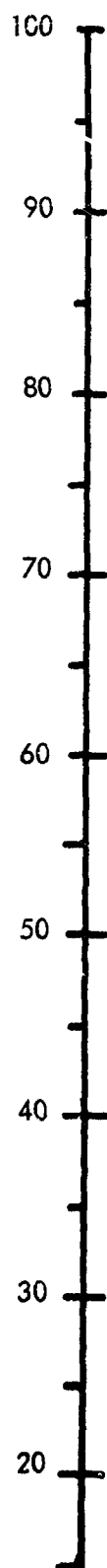
Calibration Spring

Spring Rate @ 800° F	27.9 lb/in
Spring Rate @ 70° F	32.3 lb/in
Material	Inconel X Ware No. 1 Temper.
Wire Dia.	0.250 in.
Coil Dia. O.D.	3.125 in.
Solid Height	2.5 in.
Min. Working Height	2.78 in.
Free Height	6.89 in.
No. Coils	10
Max. Load 800° F	96.29 lb
Preload 800° F	89.30 lb
Deflection for Preload	3.20 lb
Life	10,000 hrs @ 800° F
Max. Deflection	3.45 in.

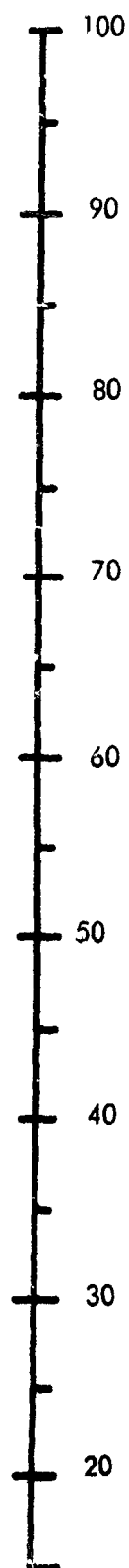
HIGH TEMPERATURE FLUID PROPERTIES

Fluid	V. P. @ 1700°F	$\Delta VP - \frac{1720}{1680}$	$\frac{\Delta VP}{\Delta T}$
	PSIA	PSID	PSIA/°F
NaK 28	47.5	6.0	.150
Sodium	22.5	4.0	.216
Potassium	63.0	10.0	.188
Rubidium	88.0	11.0	.143
Cesium	94.0	10.0	.119
Lithium	1.9	1.74	.005
Bismuth	.034	.009	.0002
Water	Above Critical Pressure		
Mercury	3044	696	6.91

BELLOWS CYCLE LIFE



FROM - ROBERTSHAW-FULTON
CATALOG "R"



VAPOR PRESSURE OF NaK (78)

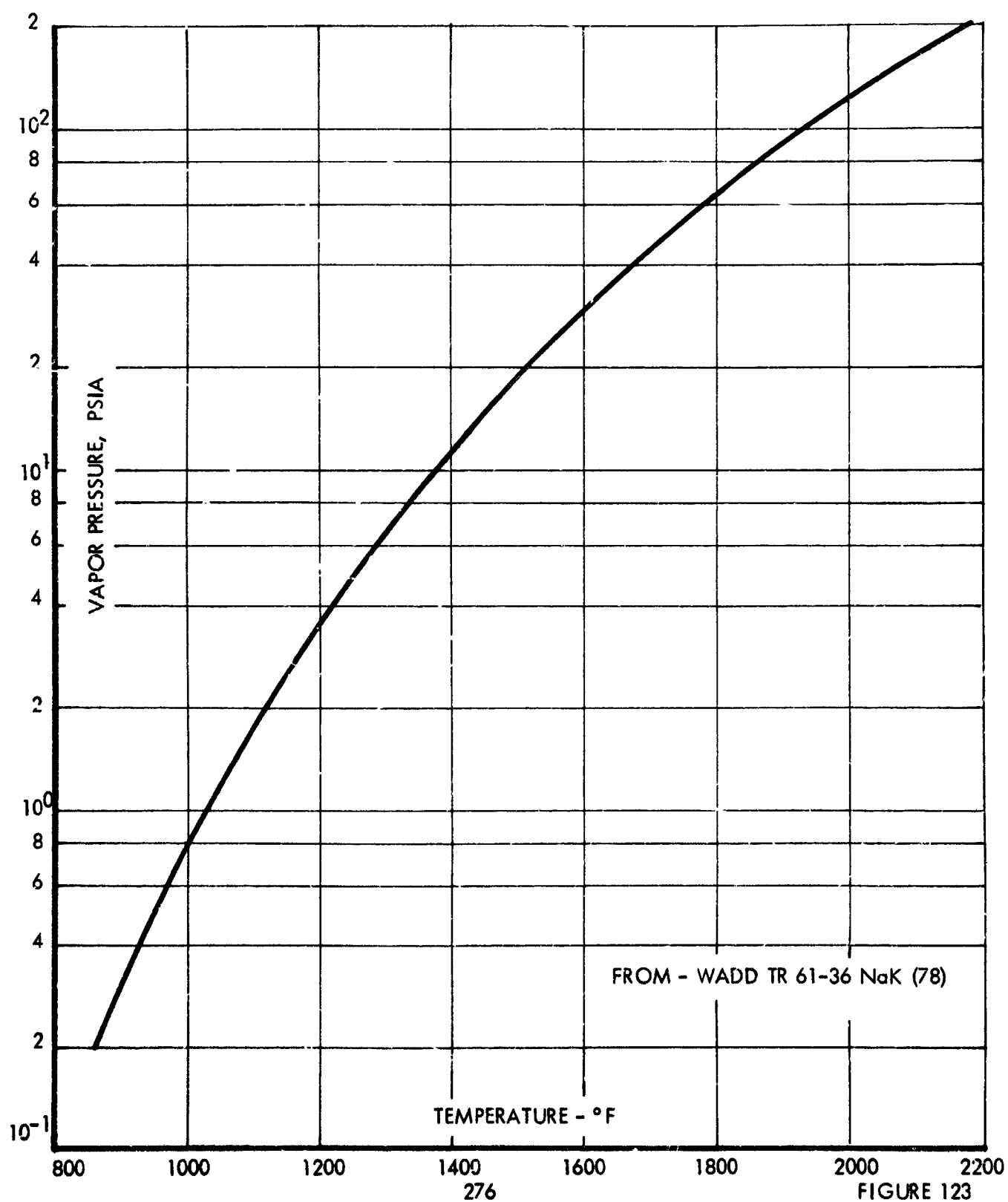


FIGURE 123

DENSITY OF LIQUID NaK (78)

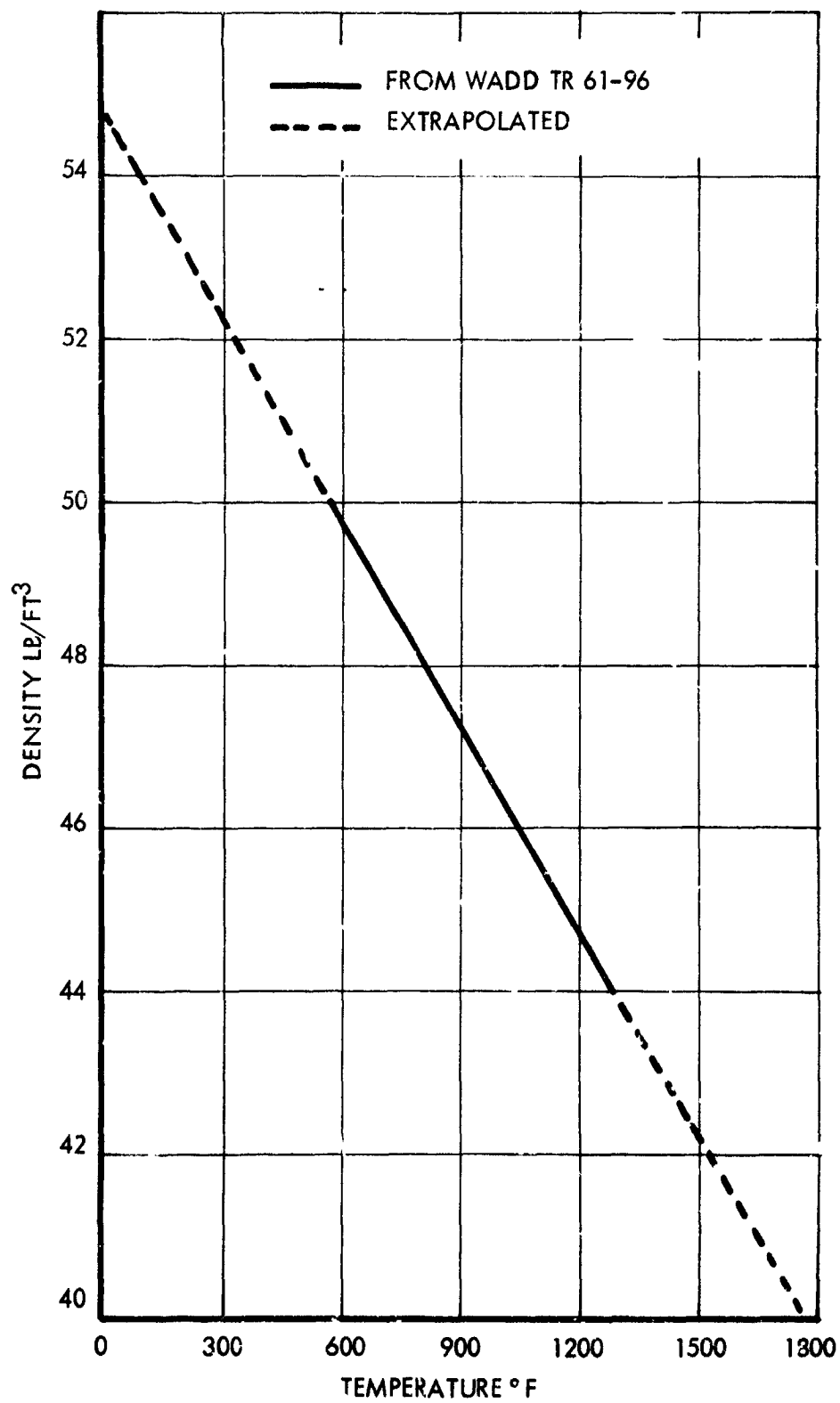


FIGURE 124

8.10 Cavity Temperature Distribution Analysis

Let us consider the calculation of the performance of a spherical-conical heat receiver. The approach to be utilized can best be described as an "open cavity" Fredholm integral equation approach¹. Because of the availability of a generalized reflector model², no specific directional distributions for the incident radiation will be utilized in this approach; instead, the actual energy flux incident on the wall of the heat receiver will be used.

Consider the sketch shown in Figure 125. Define:

x = a generalized co-ordinate specifying a point on the hemispherical-conical heat receiver;

$i(x)$ = incident energy/flux/unit area on the wall of the heat receiver, as predicted by the generalized reflector model²;

$T(x)$ = temperature distribution on the inside wall of the heat receiver;

σ Stefan-Boltzmann constant;

ϵ emissivity of the heat receiver wall;

α_s solar absorptivity of the heat receiver wall;

α_T = thermal absorptivity of the heat receiver wall;

$K(x, x')$ = kernel of the integral equation -- a geometrical factor that describes the heat receiver (it is an infinitesimal area view factor);

$\mathcal{V}_s(x)$ = total solar energy flux/unit area reflected and emitted from the point x of the heat receiver;

$\mathcal{V}_T(x)$ = total thermal energy flux-unit area reflected and emitted from the point x of the heat receiver;

$Q_s(x)$ = solar component of the heat flux/unit area flowing through the heat receiver walls (into the thermal energy storage material);

¹G. L. Schrenk, "Solar Collection Limitations for Dynamic Converters -- Simulation of Solar-Thermal Energy Power Systems," Proceedings of the AGARD Conference, Cannes, France, March 16-20, 1964.

²G. L. Schrenk, Final Report -- Analysis of Solar Reflectors -- Mathematical Theory and Methodology for Simulation of Real Reflectors, Air Force Contract AF04-695-335, Allison Division G. M. C., EDR 3693, December 16, 1963.

$Q_T(x)$ = thermal component of the heat flux/unit area flowing through the heat receiver walls (into the thermal energy storage material);

$Q(x)$ = total heat flux/unit area flowing through the heat receiver walls (into the thermal energy storage material).

In this analysis, the material walls of the heat receiver are assumed to emit and reflect radiation diffusely; specular reflection has been neglected.

From the above definitions, it readily follows that we can write for the solar and thermal components:

$$v_s(x) = (1 - \alpha_s) f(x) + \iint_{\text{Walls of the Heat Receiver}} K(x, x') v_s(x') dx'$$

Walls of the Heat Receiver

$$v_T(x) = \epsilon \sigma T^4(x) + (1 - \alpha_T) \iint_{\text{Walls of the Heat Receiver}} K(x, x') v_T(x') dx'$$

Walls of the Heat Receiver

Here the integrals extend over only the material walls of the heat receiver; conduction along the walls of the heat receiver has been neglected.

For the heat flux/unit area flowing through the walls of the heat receiver (into the thermal energy storage material), we can write

$$Q_s(x) = f(x) + \iint_{\text{Walls of the Heat Receiver}} K(x, x') v_s(x') dx' - v_s(x)$$

Walls of the Heat Receiver

$$Q_T(x) = \iint_{\text{Walls of the Heat Receiver}} K(x, x') v_T(x') dx' - v_T(x)$$

Walls of the Heat Receiver

$$Q(x) = Q_s(x) + Q_T(x)$$

Let us now consider the calculation of the kernel $K(x, x')$. Consider two infinitesimal areas dS and dS' . Let r denote the distance between these two areas, as shown in Figure 126. θ and θ' are the angles between the normals to dS and dS' and the line connecting these two areas. Let the total energy flux radiated from the area dS' be $\mathcal{V}(x') dS'$. If we assume that this flux is being radiated according to the cosine law (i.e., the area dS' is a Lambertian radiator), it can be shown that the total energy flux per unit area intercepted by the area dS is

$$\frac{\mathcal{V}(x') dS'}{\pi} \frac{\cos \theta \cos \theta'}{r^2}$$

Thus

$$\iint_{\text{Walls of the Heat Receiver}} K(x, x') \mathcal{V}(x') dS'$$

really denotes

$$\iint_{\text{Walls of the Heat Receiver}} \frac{\mathcal{V}(x')}{\pi} \frac{\cos \theta \cos \theta'}{r^2} dS'$$

So far all that we have said is completely general and applies to any geometry. Let us now evaluate this expression for a hemispherical-conical heat receiver. The expression to be evaluated contains several terms, as we must take into account on which surface both dS and dS' are located. In other words, we have

$$\iint_{\text{Walls of the Heat Receiver}} = \iint_{\text{Hemisphere}} + \iint_{\text{Cone}}$$

Let us first consider the case where both dS and dS' are located on the hemisphere. This is the simplest case and illustrates the procedures employed. The first essential step to choose a convenient co-ordinate system; for both dS and dS' on the hemisphere, the co-ordinate system chosen is shown in Figure 127. From this figure it readily follows that

$$r = a (\cos \theta + \cos \theta')$$

and since the triangle is isosceles, $\theta = \theta'$.

Thus

$$\frac{\cos \theta \cos \theta'}{r^2} = \frac{1}{4a^2}$$

$$dS' = a^2 \sin \theta' d\theta' d\theta'$$

and

$$\begin{aligned} & \iint_{\text{Hemisphere}} \frac{V(x')}{\pi} \frac{\cos \theta \cos \theta'}{r^2} dS' \\ &= \iint_{\text{Hemisphere}} \frac{V_{\text{hemisphere}}(\theta', \theta')}{\pi} \frac{1}{4a^2} \sin \theta' d\theta' d\theta' \end{aligned}$$

Similar expressions can be evaluated for the other cases. Although the algebra is considerably more complex, the principles are the same as above. Using the additional quantities defined in Figure 128, the results are:

For dS on the hemisphere (with spherical co-ordinates a, θ, θ'):

$$\begin{aligned} & \iint_{\text{Wall of the Heater Receiver}} \frac{V(x')}{\pi} \frac{\cos \theta \cos \theta'}{r^2} dS' \\ &= \iint_{\text{Hemisphere}} \frac{V_{\text{hemisphere}}(\theta', \theta')}{4 a^2 \pi} \sin \theta' d\theta' d\theta' \\ &+ \iint_{\text{Cone}} \frac{V_{\text{cone}}(\rho', \theta')}{\pi} \frac{\cos \theta_{cs} \cos \theta'_{cs}}{r_{cs}^2} \frac{\rho' d\rho' d\theta'}{\sin \tau} \end{aligned}$$

where

$$\cos \theta'_{cs} = \left\{ B r_{cs}^2 - B (B^2 + f^2) \left(\frac{\rho'^2}{f^2} - \frac{2\rho'}{f} \right) - B^3 - B a^2 + 2a \left(\frac{\rho' (B^2 + f^2)}{f} - B^2 \right) \cos \theta \right\} / 2 r_{cs} \rho' \sqrt{B^2 + f^2}$$

$$\cos \theta_{cs} = \frac{r_{cs}^2 + a^2 - \rho'^2 - B^2 \left(\frac{\rho'}{f} - 1 \right)^2}{2 a r_{cs}}$$

$$r_{cs}^2 = \rho'^2 + Z'^2 + a^2 - 2a Z' \cos \theta - 2a \rho' \sin \theta \cos (\theta - \theta')$$

$$Z' = B \left(\frac{\rho'}{f} - 1 \right)$$

For dS on the cone (with cylindrical co-ordinates ρ, θ):

$$\iint \frac{v(x')}{\pi} \frac{\cos \theta \cos \theta'}{r^2} d\theta'$$

Wall of the
Heat Receiver

$$= \iint_{\text{hemisphere}} \frac{v_{\text{hemisphere}}(\theta', \theta')}{\pi} \frac{\cos \theta_{sc} \cos \theta'_{sc}}{r_{sc}^2} a^2 \sin \theta' d\theta' d\theta'$$

$$+ \iint_{\text{cone}} \frac{v_{\text{cone}}(\theta', \theta')}{\pi} \frac{\rho \rho' B^2 [1 - \cos (\theta - \theta')]}{r_{cc}^2 (B^2 + f^2)} \frac{\rho' d\rho' d\theta'}{\sin T}$$

where

$$\cos \theta_{sc} = \left\{ B r_{sc}^2 - B (B^2 + f^2) \left(\frac{\rho^2}{f^2} - \frac{2\rho}{f} \right) - B^3 - B a^2 \right. \\ \left. + 2a \frac{\rho (B^2 + f^2)}{f} - B^2 \cos \theta' \right\} / 2 r_{sc} \sqrt{B^2 + f^2}$$

$$\cos \theta'_{sc} = \frac{r_{sc}^2 + a^2 - \rho^2 - B^2 \frac{\rho}{f} - 1}{2 a r_{sc}}$$

$$r_{sc}^2 = \rho^2 + Z^2 + a^2 - 2a Z \cos \theta' - 2a \rho \sin \theta' \cos (\theta - \theta')$$

$$Z = B \left(\frac{\rho}{f} - 1 \right)$$

$$r_{cc}^2 = \frac{B^2}{f^2} + 1 (\rho - \rho')^2 + 2 \rho \rho' (1 - \cos (\theta - \theta'))$$

If \mathcal{V} hemisphere (θ', θ') and $\mathcal{V}_{\text{cone}}(\rho', \theta')$ are axially symmetric, the $d\theta'$ integral in the above equations can be carried out analytically. This results in:

For dS on the hemisphere:

$$\iint_{\text{Wall of the Heat Receiver}} \frac{\mathcal{V}(x')}{\pi} \frac{\cos \theta \cos \theta'}{r^2} ds' \\ = \int \mathcal{V}_{\text{hemisphere}}(\theta') \frac{\sin \theta'}{2a^2} d\theta' \\ + \int \frac{\mathcal{V}_{\text{cone}}(\rho')}{\pi \sin T} \rho' d\rho' \left\{ 2\pi A_1 + \frac{2\pi A_2}{\sqrt{e^2 - g^2}} + \frac{2\pi e A_3}{(e^2 - g^2)^{3/2}} \right\}$$

where

$$A_1 = \frac{B}{4 a \rho' \sqrt{B^2 + f^2}}$$

$$A_2 = \left\{ B \left[a^2 - \rho'^2 - B^2 \left(\frac{\rho'}{f} - 1 \right)^2 \right] - B (B^2 + f^2) \left(\frac{\rho'^2}{f^2} - \frac{2\rho'}{f} \right) \right. \\ \left. - B^3 - B a^2 + 2a \left(\frac{\rho' (B^2 + f^2)}{f} - B^2 \right) \cos \theta \right\} / 4 a \rho' \sqrt{B^2 + f^2}$$

$$A_3 = \left\{ a^2 - \rho'^2 - B^2 \left(\frac{\rho'}{f} - 1 \right)^2 \right\} \left\{ - B (B^2 + f^2) \left(\frac{\rho'^2}{f^2} - \frac{2\rho'}{f} \right) \right. \\ \left. - B^3 - B a^2 + 2a \left(\frac{\rho' (B^2 + f^2)}{f} - B^2 \right) \cos \theta \right\} / 4 a \rho' \sqrt{B^2 + f^2}$$

$$e = \rho'^2 + Z'^2 + a^2 - 2a Z' \cos \theta$$

$$g = -2 \rho' \sin \theta$$

$$Z' = B \left(\frac{\rho'}{f} - 1 \right)$$

If $e = |g|$, the second integral on the right hand side of the above equation for \iint_{wall} becomes

$$\int \frac{v_{\text{cone}}(\rho')}{\pi \sin \theta} \rho' d\rho' \left\{ 2 \pi A_1 \right\}$$

For dS on the cone:

$$\iint_{\text{Wall of the Heat Receiver}} \frac{V(x')}{\pi} \frac{\cos \theta \cos \theta'}{r^2} dx' =$$

$$\int \frac{V_{\text{hemisphere}}(\theta')}{\pi} a^2 \sin \theta d\theta' \left\{ 2\pi A_4 + \frac{2\pi A_5}{\sqrt{e_2^2 - g_2^2}} + \frac{2\pi A_6 e_2}{(e_2^2 - g_2^2)^{3/2}} \right\}$$

$$+ \int \frac{V_{\text{cone}}(\rho')}{\pi \sin \tau} \rho' d\rho' \left\{ 2\pi A_7 + \frac{2\pi A_8}{\sqrt{e_1^2 - g_1^2}} + \frac{2\pi e_1 A_9}{(e_1^2 - g_1^2)^{3/2}} \right\}$$

where

$$A_4 = \frac{B}{4a\rho\sqrt{B^2 + f^2}}$$

$$A_5 = \left\{ B \left[a^2 - \rho^2 - B^2 \left(\frac{\rho}{f} - 1 \right)^2 \right] - B(B^2 + f^2) \left(\frac{\rho^2}{f^2} - \frac{2\rho}{f} \right) \right. \\ \left. - B^3 - B a^2 + 2a \left(\frac{\rho(B^2 + f^2)}{f} - B^2 \right) \cos \theta' \right\} / 4a\rho\sqrt{B^2 + f^2}$$

$$A_6 = \left\{ a^2 - \rho^2 - B^2 \left(\frac{\rho}{f} - 1 \right)^2 \right\} \left\{ -B(B^2 + f^2) \left(\frac{\rho^2}{f^2} - \frac{2\rho}{f} \right) \right. \\ \left. - B^3 - B a^2 + 2a \left(\frac{\rho(B^2 + f^2)}{f} - B^2 \right) \cos \theta' \right\} 4a\rho\sqrt{B^2 + f^2}$$

$$e_2 = \rho^2 + Z^2 + a^2 - 2aZ \cos \theta'$$

$$Z = B \left(\frac{\rho}{f} - 1 \right)$$

$$g_2 = -2a \rho \sin \theta'$$

$$A_7 = \frac{B^2}{B^2 + f^2} \frac{1}{4\rho\rho'}$$

$$A_8 = \frac{-2B^2}{f^2} \frac{(\rho - \rho')^2}{4\rho\rho'}$$

$$A_9 = \frac{B^2(B^2 + f^2)}{f^4} \frac{(\rho - \rho')^4}{4\rho\rho'}$$

$$e_1 = \left(\frac{B^2}{f^2} + 1 \right) (\rho - \rho')^2 + 2\rho\rho'$$

$$g_1 = -2\rho\rho'$$

If $e_2 = |g_2|$, the first integral on the right hand side of the above equation for \iint_{wall} becomes

$$\int \frac{v_{\text{hemisphere}}(\theta')}{\pi} a^2 \sin \theta' d\theta' \left\{ 2\pi A_4 \right\}$$

Thus, our basic equations for the axially symmetric case become:

SOLAR COMPONENT

$$v_{\text{hemisphere}}(\theta) = (1 - \alpha_s) \left[f(x) + \int v_{\text{hemisphere}}(\theta') \frac{\sin \theta'}{2a^2} d\theta' + \int \frac{v_{\text{scone}}(\rho')}{\pi \sin T} \rho' d\rho' \left\{ 2\pi A_1 + \frac{2\pi A_2}{\sqrt{e^2 - g^2}} + \frac{2\pi e A_3}{(e^2 - g^2)^{3/2}} \right\} \right]$$

$$v_{\text{cone}}(\rho) = (1 - \alpha_s) \left[f(x) + \int \frac{v_{\text{hemisphere}}^{(\theta')}}{\pi} a^2 \sin \theta' d\theta' \left\{ 2\pi A_4 + \frac{2\pi A_5}{\sqrt{e_2^2 - g_2^2}} + \frac{2\pi A_6 e_2}{(e_2^2 - g_2^2)^{3/2}} \right\} + \int \frac{v_{\text{cone}}(\rho')}{\pi \sin T} \rho' d\rho' \left\{ 2\pi A_7 + \frac{2\pi A_8}{\sqrt{e_1^2 - g_1^2}} + \frac{2\pi e_1 A_9}{(e_1^2 - g_1^2)^{3/2}} \right\} \right]$$

THERMAL COMPONENT

$$v_{\text{hemisphere}}^{(\theta)} = \epsilon \sigma T_{\text{hemisphere}}^4 + (1 - \alpha_T) \left[\right]$$

$$v_{\text{hemisphere}}^{(\theta')} \frac{\sin \theta'}{2 a^2} d\theta' + \int \frac{v_{\text{Tcone}}(\rho')}{\pi \sin T} \rho' d\rho' \left\{ 2\pi A_1 + \frac{2\pi A_2}{\sqrt{e^2 - g^2}} + \frac{2\pi e A_3}{(e^2 - g^2)^{3/2}} \right\}$$

$$v_{\text{Tcone}}(\rho) = \epsilon \sigma T_{\text{cone}}^4(\rho) + (1 - \alpha_T) \left[\right]$$

$$\int \frac{v_{\text{hemisphere}}^{(\theta')}}{\pi} a^2 \sin \theta d\theta' \left\{ 2\pi A_4 + \frac{2\pi A_5}{\sqrt{e_2^2 - g_2^2}} + \frac{2\pi C_2 A_6}{(e_2^2 - g_2^2)^{3/2}} \right\} + \int \frac{v_{\text{Tcone}}(\rho')}{\pi \sin T} \rho' d\rho' \left\{ 2\pi A_7 + \frac{2\pi A_8}{\sqrt{e_1^2 - g_1^2}} + \frac{2\pi e_1 A_9}{(e_1^2 - g_1^2)^{3/2}} \right\} \right]$$

Let us now consider how to solve these Fredholm integral equations. For the solar component, the equations can be solved by using the well-known Liouville-Neumann series. In this iteration procedure the n -th approximation is given in terms of the $(n-1)$ -th approximation by

$$v_{sn}(x) = (1 - \alpha_s) \left[f(x) + \iint_{\substack{\text{Walls of the} \\ \text{Heat Receiver}}} K(x, x') v_{s, n-1}(x') dx' \right]$$

where the 0-th order term is given by

$$v_{s0}(x) = (1 - \alpha_s) f(x)$$

This procedure is continued until

$$\left| \frac{v_{sn}(x) - v_{s, n-1}(x)}{v_{sn}(x)} \right| < \epsilon$$

for all x . Experience has shown that $\epsilon \leq 0.01$ can be achieved within 5 to 8 iterations for the heat receiver geometry under study here.

Once the solar solution $v_s(x)$ is known, the solar component of the heat flux/unit area flowing into the thermal energy storage material surrounding the heat receiver can be calculated from the equation

$$Q_s(x) = f(x) + \iint_{\substack{\text{Walls of the} \\ \text{Heat Receiver}}} K(x, x') v_s(x') dx' - v_s(x)$$

Once the solar solution $\mathcal{U}_s(x)$ is known, the solar component of the heat flux/unit area flowing into the thermal energy storage material surrounding the heat receiver can be calculated from the equation

$$Q_s(x) = f(x) + \iint_{\text{Walls of the Heat Receiver}} K(x, x') \mathcal{U}_s(x') dx' - \mathcal{U}_s(x)$$

The solution procedure for thermal component is not so simple, as it is necessary to know $T(x)$. This function, however, depends on $Q(x) = Q_s(x) + Q_T(x)$ and on the boundary conditions imposed by the thermal energy storage material.

One possible approach is to assume a $T(x)$, solve for $\mathcal{U}_T(x)$ and thus for $Q(x)$. Using this value of $Q(x)$, the thermal energy storage problem is then solved. This solution yields a new $T(x)$ which is then used to correct the old value of $T(x)$ and this process is repeated. This iteration continues until the desired accuracy is obtained. This procedure, however, rather long and cumbersome; since it involves two successive iterations, it can require a considerable amount of computer time.

A better approach to this problem -- involving only one iteration -- has been discovered. This approach utilized a numerical iterative procedure to solve a set of coupled nonlinear integral equations.

Our basic equation for the thermal component is

$$\mathcal{U}_T(x) = \epsilon \sigma T^4(x) + (1 - \epsilon_T) \iint_{\text{Walls of the Heat Receiver}} K(x, x') \mathcal{U}_T(x') dx'$$

Let us assume that there exists a definite melt line at each point in the thermal energy storage material surrounding the heat receiver. Since this melt line is always at the melt temperature T_m , the total heat flux/unit area into the thermal energy storage material can be written as

$$Q(x) = B_c(x) (T(x) - T_m)$$

where $B_c(x)$ is the heat transfer coefficient. $B_c(x)$ is a function of the material, of the geometry of the thermal energy storage configuration, and of time (via the percentage of the material melted). In this analysis it is assumed that $B_c(x)$ has been determined experimentally.

Now, we also know that

$$Q(x) = Q_s(x) + Q_T(x) = Q_s(x) + \iint_{\text{Walls of the Heat Receiver}} K(x, x') V_T(x') dx' - V_T(x)$$

Thus, by equating these two expressions for $Q(x)$ and by substituting in the basic equation for $V_T(x)$, we obtain

$$\epsilon \sigma T^4(x) + B_c(x) T(x) = Q_s(x) + B_c(x) T_m + \alpha_T \iint K(x, x') V_T(x') dx'$$

Hence, we must now develop a solution procedure for the equations

$$V_T(x) = \epsilon \sigma T^4(x) + (1 - \alpha_T) \iint K(x, x') V_T(x') dx'$$

$$\epsilon \sigma T^4(x) + B_c(x) T(x) = Q_s(x) + B_c(x) T_m + \alpha_T \iint K(x, x') V_T(x') dx'$$

These equations have been solved successfully by the following iteration procedure:

Let the 0-th order approximation for $T(x)$ be obtained from the following quartic equation:

$$\epsilon \sigma T_0^4(x) + B_c(x) T_0(x) = Q_s(x) + B_c(x) T_m$$

For $V_{T_0}(x)$, we shall use

$$V_{T_0}(x) = \epsilon \sigma T_0^4(x)$$

The n-th order approximation for $T(x)$ is obtained by solving the quartic

$$\epsilon \sigma T_n^4(x) + B_c(x) T_n(x) = Q_s(x) + B_c(x) T_m + \alpha_T \iint K(x, x') V_{T_{n-1}}(x') dx'$$

The n-th order approximation for $V_{T_n}(x)$ is obtained from

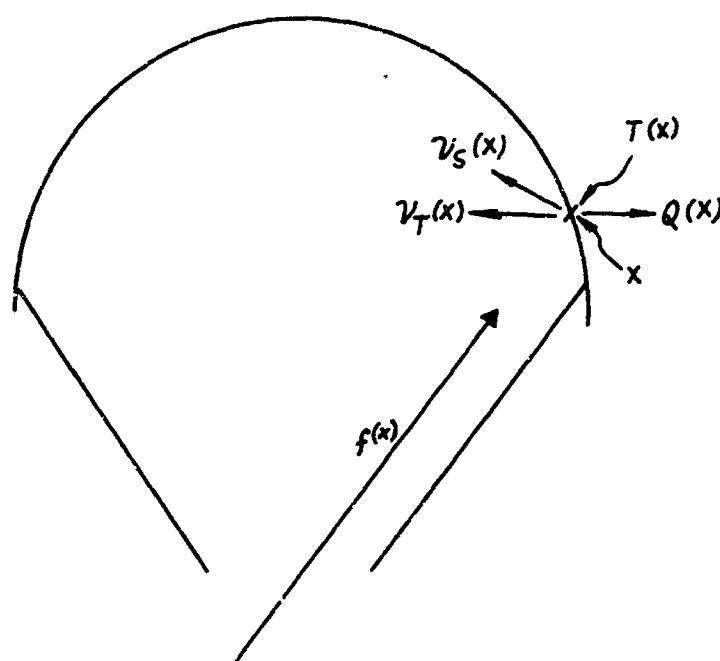
$$V_{T_n}(x) = \epsilon \sigma T_n^4(x) + (1 - \alpha_T) \iint K(x, x') V_{T_{n-1}}(x') dx'$$

This procedure is continued until

$$\left| \frac{v_{T_n}(x) - v_{T_{n-1}}(x)}{v_{T_n}(x)} \right| \leq \epsilon$$

for all x . Experience has shown that $\epsilon \leq 0.01$ can be achieved within 5 to 8 iterations for the heat receiver geometry under study here.

This solution is a function of time through the dependence of $B_c(x)$ on time. This time dependence, however, is treated in the quasi-steady state approximation. Thus, at each instant of time when the heat receiver is solved, the coefficient $B_c(x)$ are treated as if they were functions of x only. The computation of new values of $B_c(x)$ at each succeeding time interval involves the solution of the heat exchanger.

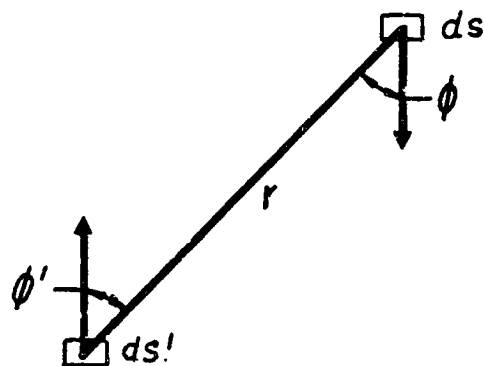


DEFINITION OF TERMS USED IN THE HEAT RECEIVER ANALYSIS

FIGURE 125

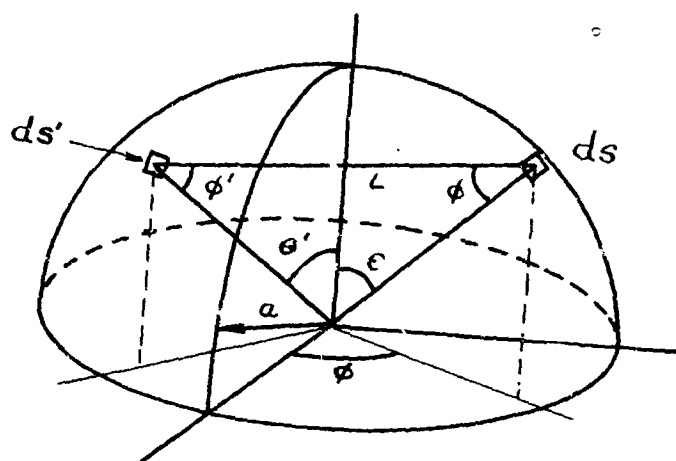
TABLE XII
TUBE STATION LOCATIONS IN TERMS OF
 θ , GRID - 30 TUBE, 2% DESIGN

Tube Section	Station	θ Degrees	θ Radians	Volume Available for LiF	Volume Required for Solid LiF
1	1	90	1.570		
	2	86.08	1.502	.0442	.01013
2	1	86.08	1.502		
	2	83.05	1.450	.0341	.01015
3	1	83.05	1.450		
	2	81.617	1.424	.0164	.00958
4	1	81.617	1.424		
	2	78.684	1.373	.00754	.00880
5	1	78.684	1.373		
	2	75.833	1.324	.00754	.00785
6	1	75.833	1.324		
	2	72.900	1.272	.00754	.00700
7	1	72.900	1.272		
	2	70.033	1.227	.00754	.00625
8	1	70.033	1.227		
	2	67.100	1.171	.00754	.00558
9	1	67.100	1.171		
	2	64.183	1.120	.00754	.00498
10	1	64.183	1.120		
	2	61.317	1.069	.00754	.00444
11	1	61.317	1.069		
	2	58.450	1.021	.00617	.00397
12	1	58.450	1.021		
	2	55.583	.968	.00525	.00354
13	1	55.583	.968		
	2	52.717	.917	.00525	.00316
14	1	52.717	.917		
	2	49.733	.865	.00525	.00283
15	1	49.733	.865		
	2	46.617	.812	.00525	.00253
16	1	46.617	.812		
	2	43.317	.755	.00525	.00226
17	1	43.317	.755		
	2	39.300	.685	.00525	.00192
18	1	39.300	.685		
	2	36.05	.612	.00525	.00192
19	1	36.05	.612		
	2	31.50	.5500	.00525	.00153
20	1	31.50	.5500		
	2	26.65	.4650	.00525	.00153
21	1	26.65	.4560		
	2	18.05	.3150	.01007	.00126
22	1	18.05	.3150		
	2	11.70	.2040	.00734	.00116



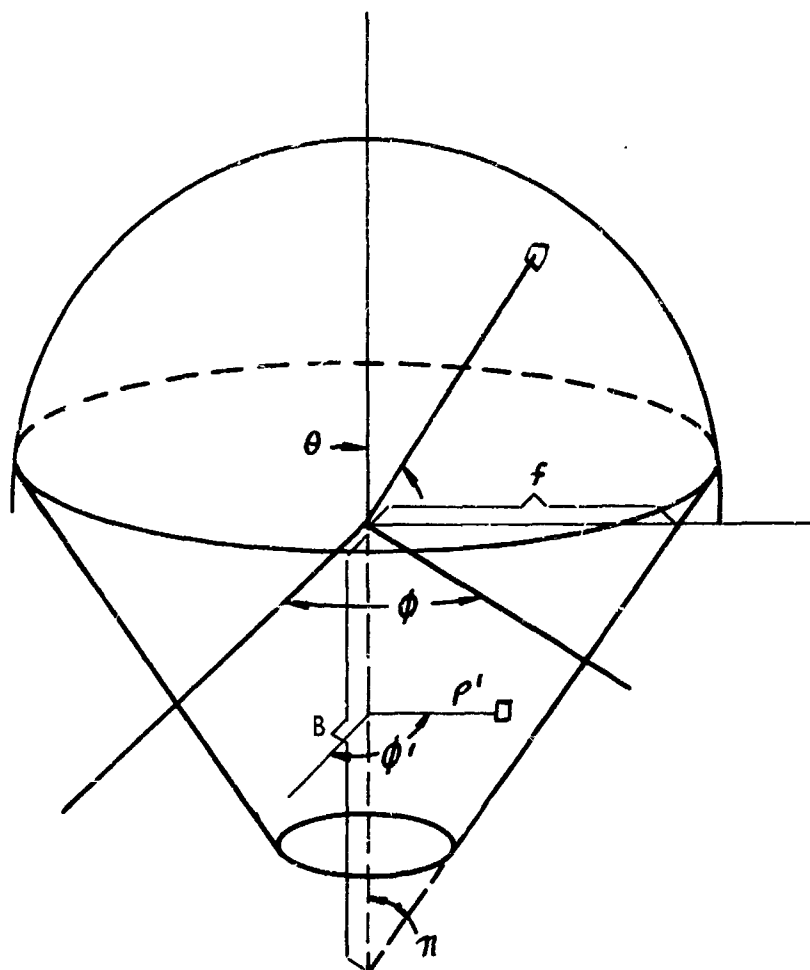
INFINITESIMAL AREA GEOMETRY USED FOR CALCULATION OF $K(x, x')$

FIGURE 126



CO-ORDINATE SYSTEM AND GEOMETRY USED FOR
CALCULATIONS OF $K(x, x')$ FOR CASE WHERE ds AND
 ds' ARE BOTH ON A HEMISPHERE

FIGURE 127



DEFINITION OF QUANTITIES USED IN CALCULATION OF $K(x, x')$

FIGURE 128

9.11 Reliability Estimates

As an integral part of the design study, reliability studies were conducted to identify areas with low reliability and to guide the design approach to achieve higher levels. These estimates are reported in two parts. The first part is based on a complete study of the four percent design. The second part is based on a study of the revised cavity maximum temperature control. The results of the first part clearly illustrated the need for this revision. The basic cavity and storage material container employ no moving parts and indicate reasonable reliability rates.

BRAYTON CYCLE CAVITY RECEIVER

Reliability Failure Mode Analysis

Purpose - The purpose of a failure mode analysis is to evaluate the design, materials, and fabrication of an equipment and to determine, in advance, the possible ways the equipment could fail or malfunction. This systematic, qualitative approach provides the means of taking preventive measures to assure a more reliable design at greatest cost savings.

Upon completion of the failure mode analysis, the failure modes will be classified by the failure severity (failure severity = an arbitrary classification describing the extent of the failure effect upon the end item) and the failure probability (failure probability = the expected failure rate in number of failures per mission, failures percent per thousand hours, and other similar measurements.) In examining the failure mode, we determine the effect of the failure on the component being evaluated and on each of the higher assemblies, as well as on the end item.

The classification of failures of the Brayton Cycle Receiver was limited to the effect of the failure upon the over-all system and is further limited to these three categories:

1. Critical - A failure that could result in the loss of life and/or the whole system.
2. Major - A failure that could lead to failure of the mission or to the abortion of the mission.
3. Minor - All failures that are not covered in categories 1 or 2.

The initial failure mode analysis used on the Brayton Cycle Receiver was prepared from the two preliminary drawings to illustrate the analysis procedure and to provide early inputs to engineering.

In describing the enclosed failure analysis forms, the upper part of the form provides identification of the item, its operating environment and functions. The lower part of the form is divided into five columns.

The first column -- Failure Mode -- is used to record the possible ways in which the particular part could fail.

The second column -- Class -- is for entering the classification of the failure: code MI = Minor; MA = Major; CR = Critical.

The third column -- Detection Method -- is used to record the nature of that occurrence which gives an indication of the malfunction or the failure.

The fourth column -- Compensation or Control -- is used by Reliability personnel to record their corrective recommendations.

The fifth column -- Effect on Next Higher Assembly -- states the effect upon and the extent to which a next higher assembly could be affected.

As a result of this initial failure mode and effects analysis the following problem areas are designated for further surveillance.

(a) The design of the shade and heat regulating door assemblies

This statement pertains to the mechanical structure of the bellows, the linkage, the hinges, and to the other components such as the sensors.

(b) The materials and material thickness

This pertains to structural strength and to fabrication.

(c) Fabrication

This pertains to forming and welding.

A more complete failure mode analysis will be performed when final (R&D) drawings become available.

RELIABILITY PREDICTIONS BRAYTON CYCLE CAVITY RECEIVER

CAVITY RECEIVER	FAILURE RATE PER MILLION HOURS	APERTURE RING ASSEMBLY	NO. IN INDIVIDUAL ASSY. FR $\times 10^6$	OVERALL FR $\times 10^6$
1. Inlet Header	1.1	1. Aperture Ring	1	1.0
2. Inner & Outer Shells	1.1	2. Bellows Housing-Temp. Segments	.4	.16
3. Tubes	2.02	3. Bellows - Temp. Segments	4	8.8
4. Flow Fairing	0.1	4. Bellows Housing-Shade Segments	4	0.16
5. Ring Outlet	1.1	5. Bellows - Shade Segments	4	8.8
6. Insulation	0.5	6. Linkage	24	2.8
Total	5.92 $\times 10^{-6}$ Hours	7. Jeweled Bearings	40	20.0
		8. Hinges - Temp. Segments	8	4.0
		9. Hinges - Shade Segments	8	4.0
		10. Segments - Temp.	4	4.0
		11. Segments - Shade	4	4.0
		12. Heat Sensors	4	13.2
		Total		70.92 $\times 10^{-6}$ Hours

For one year mission,

$$R_{C.R.} = e^{-t} = e^{-8760 \times 5.92 \times 10^{-6}}$$

$$R_{C.R.} = .948$$

where

$$R_{C.R.} = \text{Reliability of Cavity Receiver for One Year Mission}$$

$$R_{A.R.} = e^{-t} = e^{-8760 \times 70.92 \times 10^{-6}}$$

$$R_{A.R.} = .54$$

where

$$R_{A.R.} = \text{Reliability of Aperture Ring Assembly}$$

$$\text{TOTAL RELIABILITY} = R_{C.R.} \times R_{A.R.} = .948 \times .54 = .512 \text{ or } 51.2\%$$

FAILURE MODE ANALYSIS

ST: OF

ITEM DESCRIPTION

Inlet Header

NEXT HIGHER ASS'Y.

Cavity Receiver

ITEM/PART NO.

SPECIFICATION

SUPPLIER

PREP'D BY

FUNCTION

Direct Gas Flow from Compressor through Heater Tubes

DATE

OPERATING CONDITIONS

CRITICAL ENVIRONMENTS

Vibration; long operating time, vacuum operation

FAILURE MODE	CLASS	DETECTION METHOD	COMPENSATION OR CONTROL	EFFECT ON NEXT HIGHER ASSEMBLY
Weld failure	MA	Loss of system pressure.	Improve welding technique. Improve in-process inspection and final proof pressure test.	Loss of system
Structural failure	MA	Loss of system pressure.	Use higher strength metal. Improve inspection of surface for defects. Improve final proof pressure test redesign.	Loss of system.

FAILURE MODE ANALYSIS

SH. _____ OF _____

ITEM DESCRIPTION Inner Shell NEXT HIGHER ASS'Y. Cavity Receiver

ITEM/PART NO. _____ SPECIFICATION _____ SUPPLIER _____ PREP'D BY _____

FUNCTION Structural Shell to form Sealed Cavity Around Tubes and to Provide Heat Absorbing Surface DATE _____

OPERATING CONDITIONS One year life; temperature

CRITICAL ENVIRONMENTS Vibration; long operating time; vacuum, lithium fluoride, sunlight

FAILURE MODE	CLASS	DETECTION METHOD	COMPENSATION OR CONTROL	EFFECT ON NEXT HIGHER ASSEMBLY
Structural failure	MA	Loss of lithium fluoride and degradation of system efficiency.	Use higher strength metal. Improve inspection of surface. Improve final proof pressure test.	Loss of system.
Weld failure	MA	Loss of lithium fluoride and degradation of system efficiency.	Improve welding techniques. Improve in-process inspection and final proof pressure test.	Loss of system.
Degradation of coating	MI	Degradation of system efficiency.	Improve coating and method of coating. Improve inspection of surface before and after processing.	Degradation of system

FA' LURE MODE ANALYSIS

SH. _____ OF _____

ITEM DESCRIPTION _____ Outer Shell _____

NEXT HIGHER ASS'Y. _____ Cavity Receiver _____

ITEM/PART NO. _____

SPECIFICATION _____ SUPPLIER _____ PREP'D BY _____

FUNCTION _____ Provide Structural Shell and Form Sealed Cavity to Hold Lithium Fluoride _____

DATE _____

OPERATING CONDITIONS _____

CRITICAL ENVIRONMENTS _____

Vibration, long operating time, vacuum, lithium fluoride

FAILURE MODE	CLASS	DETECTION METHOD	COMPENSATION OR CONTROL	EFFECT ON NEXT HIGHER ASSEMBLY
Structural failure	MA	Loss of lithium fluoride and degradation of system efficiency.	Use higher strength metal. Improve inspection of surface. Improve final proof pressure test.	Loss of system.
Weld failure	MA	Loss of lithium fluoride and degradation of system efficiency.	Improve welding techniques. Improve in-process inspection and final proof pressure test.	Loss of system.

FAILURE MODE ANALYSIS				
ITEM DESCRIPTION _____		SH. _____ OF _____		
Flow Firing		NEXT HIGHER ASS'Y. _____		Cavity Receiver
ITEM/PART NO. _____		SPECIFICATION _____		PREP'D BY _____
FUNCTION _____		Directing Argon Flow from Heater to Turbine		DATE _____
OPERATING CONDITIONS _____				
CRITICAL ENVIRONMENTS <u>Vibration; long operating life</u>				
FAILURE MODE	CLASS	DETECTION METHOD	COMPENSATION OR CONTROL	EFFECT ON NEXT HIGHER ASSEMBLY
Weld failure	MI	Degradation of system performance.	Improve welding and quality control during manufacturing.	Degrade system performance.

FAILURE MODE ANALYSIS					SH. ____ OF ____
ITEM DESCRIPTION		Tubes		NEXT HIGHER ASS'Y. Cavity Receiver	
ITEM/PART NO.		SPECIFICATION		PREP'D BY	
FUNCTION		Transport Argon from Inlet Header to Turbine		DATE	
OPERATING CONDITIONS					
CRITICAL ENVIRONMENTS High temperature; lithium fluoride, vibration, long operating life					
FAILURE MODE	CLASS	DETECTION METHOD	COMPENSATION OR CONTROL	EFFECT ON NEXT HIGHER ASSEMBLY	
Weld failure at inlet header or ring outlet.	MA	Loss of argon. Presence of liquid fluoride in argon sections.	Redesign. Improve quality control and in-process testing. Improve final proof pressure test.	Loss of system.	
Tube structural failure	MA	Loss of argon. Presence of liquid fluoride in argon sections.	Redesign. Improve tube fixturing. Use higher strength metal. Improve final proof pressure test.	Loss of system.	

FAILURE MODE ANALYSIS

SH. _____ OF _____

ITEM DESCRIPTION Ring Outlet _____ NEXT HIGHER ASS'Y. Cavity Receiver _____

ITEM/PART NO. _____ SPECIFICATION _____ SUPPLIER _____ PREP'D BY _____

FUNCTION Direct Argon Flow from Heater Tubes to Turbine _____ DATE _____

OPERATING CONDITIONS _____

CRITICAL ENVIRONMENTS Vibration; long operating life; vacuum operation; lithium fluoride _____

FAILURE MODE	CLASS	DETECTION METHOD	COMPENSATION OR CONTROL	EFFECT ON NEXT HIGHER ASSEMBLY
Weld failure	MA	Loss of argon gas. Degradation of the system.	Improve test and inspection methods. Redesign weld configuration, improve weld procedure and control. Retrain welding personnel, change machine welding.	System failure
Structural failure	MA	Loss of argon gas. Degradation of the system.	Redesign for greater stress load. Redesign weld configuration. Improve weld procedure and control. Stress relieve.	System failure

<div style="display: flex; justify-content: space-between;"> <div>FAILURE MODE ANALYSIS</div> <div>SH. _____ OF _____</div> </div>				
<div style="display: flex; justify-content: space-between;"> <div>ITEM DESCRIPTION <u>Insulation</u></div> <div>NEXT HIGHER ASS'Y. _____</div> </div>				
<div style="display: flex; justify-content: space-between;"> <div>ITEM/PART NO. _____</div> <div>SPECIFICATION _____</div> <div>SUPPLIER _____</div> <div>PREP'D BY _____</div> </div>				
<div style="display: flex; justify-content: space-between;"> <div>FUNCTION <u>Reduce Heat Escape from Heater</u></div> <div>DATE _____</div> </div>				
OPERATING CONDITIONS _____				
CRITICAL ENVIRONMENTS _____				
FAILURE MODE	CLASS	DETECTION METHOD	COMPENSATION OR CONTROL	EFFECT ON NEXT HIGHER ASSEMBLY
Becomes dislodged	MA	System malfunction	Improve method of attaching. Improve assembly technique. Redesign for better materials.	System malfunction. System failure.
Tears or flakes off	MA	System malfunction	Improve bonding technique. Improve adhesive. Improve assembly technique. Improve inspection methods and quality control procedures.	System malfunction.

FAILURE MODE ANALYSIS

SH. _____ OF _____

ITEM DESCRIPTION Heat Sensors and Tubes NEXT HIGHER ASS'Y. Actuator Assembly

ITEM/PART NO. _____ SPECIFICATION _____ SUPPLIER _____ PREP'D BY _____

FUNCTION Sense Sun to Signal Opening Temperature Segments DATE _____

OPERATING CONDITIONS Operates on each orbit; one year life

CRITICAL ENVIRONMENTS Long operating life; vacuum; sunlight.

FAILURE MODE	CLASS	DETECTION METHOD	COMPENSATION OR CONTROL	EFFECT ON NEXT HIGHER ASSEMBLY
Leaking	MI	Slow response on heat segment. Degradation of system performance.	Use more temperature resistant metals. Improve welding and seals. Improve quality control and proof pressure test during manufacturing.	Degradation of system
Distortion	MI	Slow response on heat segment. Degradation of system performance.	Redesign with higher strength metal. Re-evaluate loads. Improve quality control during manufacturing and test.	Degradation of system
Rupture of structural failure	MI	Slow response on heat segment. Degradation of system performance.	Redesign with higher strength metal. Re-evaluate loads. Improve quality control during manufacturing and proof pressure test.	Degradation of system
Degradation of surface	MI	Slow response on heat segment. Degradation of system performance.	Redesign with improved surface treatment; use protective coating.	Degradation of system

FAILURE MODE ANALYSIS

SH. _____ OF _____

ITEM DESCRIPTION Linkage and Bearings NEXT HIGHER ASS'Y. Actuator Assembly

ITEM/PART NO. _____ SPECIFICATION _____ SUPPLIER _____ PREP'D BY _____

FUNCTION Provide Connection Between Bellows and Heat and Temperature Segments. DATE _____

OPERATING CONDITIONS Operates on each orbit to open and close segments; one year life.

CRITICAL ENVIRONMENTS Long unattended life; vacuum; vibration in temperature.

FAILURE MODE	CLASS	DETECTION METHOD	COMPENSATION OR CONTROL	EFFECT ON NEXT HIGHER ASSEMBLY
Distortion	MI	Degradation of system performance.	Redesign with higher strength metals Re-evaluate loads required for operation. Redesign with alternate linkage.	Degradation of system.
Structural failure	MI	Degradation of system performance.	Redesign with higher strength metals Re-Evaluate loads required for operation. Improve quality control and additional inspection methods.	Degradation of system.
Binding	MI	Degradation of system performance. High actuation force limits segment travel.	Redesign for higher loads. Bearing configuration, lubrication or sealing or new bearing materials. Improve quality control and in-process testing and inspection.	Degradation of system.
Excessive clearance	MI	Degradation of system performance. Lack of sufficient segment travel.	Study tolerances, materials and processes. Redesign for higher loads. Improve quality control and in-process test methods.	Degradation of system
Seizing	MI	Degradation of system performance. High actuation force limits segment travel.	Redesign for higher loads. Improve surface finishes. Improve or change bearing configuration. Improve quality control procedures and in-process testing and inspection.	Degradation of system.

FAILURE MODE ANALYSIS

SH. _____ OF _____

ITEM DESCRIPTION _____ Bellows and Linkage _____ NEXT HIGHER ASS'Y. _____ Aperture Ring Assembly _____

ITEM/PART NO. _____ SPECIFICATION _____ SUPPLIER _____ PREP'D BY _____

FUNCTION _____ Provide actuation of linkage for heat and temperature segments. _____ DATE _____

OPERATING CONDITIONS _____ Operates on each orbit. _____

CRITICAL ENVIRONMENTS _____ Vibration; long operating life. _____

FAILURE MODE	CLASS	DETECTION METHOD	COMPENSATION OR CONTROL	EFFECT ON NEXT HIGHER ASSEMBLY
Rupture	MI	Loss of segment operation and reduction of heater performance.	Redesign bellows; redesign for redundant bellows. Redesign for another means of actuation.	Erratic system performance system failure.
Collapsing	MI	Loss of segment operation of heater performance. Malfunction of the system.	Same as above.	Same as above.
Bulging	MI	Degradation of heater performance. Malfunction of the system.	Same as above.	Same as above.
Leaking	MI	Degradation of heater performance.	Same as above.	Same as above.
Linkage binding	MI	Degradation of heater performance. Malfunction of the system.	Redesign bearings. Redesign linkage.	Same as above.

FAILURE MODE ANALYSIS					SH. ____ OF ____
ITEM DESCRIPTION		Bellows Housing		NEXT HIGHER ASS'Y. Bellows Assembly	
ITEM/PART NO.		SPECIFICATION		SUPPLIER PREP'D BY	
FUNCTION		Retain Actuator Bellows		DATE	
OPERATING CONDITIONS One year life.					
CRITICAL ENVIRONMENTS Long unattended life; actuation forces.					
FAILURE MODE	CLASS	DETECTION METHOD	COMPENSATION OR CONTROL	EFFECT ON NEXT HIGHER ASSEMBLY	
Weld failure --- at base	MI	Loss of segment operation and reduction of heater performance.	Improve welding and quality control.	Degradation of system.	
Structural failure	MI	Loss of segment operation and reduction of heater performance.	Redesign with higher strength metal. Improve quality control and proof pressure test.	Degradation of system.	

FAILURE MODE ANALYSIS

SH. _____ OF _____

ITEM DESCRIPTION _____ Linkage and Bearings _____ NEXT HIGHER ASS'Y. _____

ITEM/PAFT NO. _____ SPECIFICATION _____ SUPPLIER _____ PREP'D BY _____

FUNCTION _____ DATE _____

OPERATING CONDITIONS _____

CRITICAL ENVIRONMENTS _____

FAILURE MODE	CLASS	DETECTION METHOD	COMPENSATION OR CONTROL	EFFECT ON NEXT HIGHER ASSEMBLY
Dislodgement of bearings	MI	Degradation of system performance. Erratic segment movement.	Improve captive feature. Improve assembly technique Improve quality control and inspection methods. Redesign for other bearing configuration.	Degradation of system.
Bearing fatigue	MI	Degradation of system performance. High actuation force limits segment travel.	Improve assembly technique. Improve quality control and inspection methods. Redesign for greater loads, encapsulate bearing.	Degradation of system.

FAILURE MODE ANALYSIS

SH. _____ OF _____

ITEM DESCRIPTION Heat & Temperature Control Segments NEXT HIGHER ASS'Y. Aperture Ring Assembly

ITEM/PART NO. _____ SPECIFICATION _____ SUPPLIER _____ PREP'D BY _____

FUNCTION Provide Means to Control Heat Input to Argon DATE _____

OPERATING CONDITIONS Actuate on each orbit; one year life.

CRITICAL ENVIRONMENTS Long unattended life; vacuum; variation in temperature.

FAILURE MODE	CLASS	DETECTION METHOD	COMPENSATION OR CONTROL	EFFECT ON NEXT HIGHER ASSEMBLY
Distortion	MI	Binding. Degradation of heater control and system performance.	Redesign using more temperature. Insensitive metals. Provide greater rigidity.	Degradation of system.
Structural failure	MI	Degradation of heater control and system performance.	Redesign using higher strength metals. Redistribute loads.	Degradation of system.

FAILURE MODE ANALYSIS

SH. _____ CF _____

ITEM DESCRIPTION _____ Hinges _____ NEXT HIGHER ASS'Y. _____ Aperture Ring Assembly _____

ITEM/PART NO. _____ SPECIFICATION _____ SUPPLIER _____ PREP'D BY _____

FUNCTION _____ Provide Pivot Points for Heat and Temperature Segments _____ DATE _____

OPERATING CONDITIONS _____ Actuate on Each Orbit; One Year Life _____

CRITICAL ENVIRONMENTS _____ Vacuum; long unattended mission; vibration _____

FAILURE MODE	CLASS	DETECTION METHOD	COMPENSATION OR CONTROL	EFFECT ON NEXT HIGHER ASSEMBLY
Binding	MI	System malfunction. System failure.	Improve quality control and inspection methods and tests. Redesign for higher loads. Improve surface finishes.	System malfunction
Seizing	MI	System malfunction. System failure.	Improve processes. Improve quality control and inspection tests. Redesign hinges.	System malfunction
Excessive clearance	MI	System malfunction. Inter. failure. System failure.	Tighten tolerances to improve fit. Improve processes. Improve quality control and inspection methods. Redesign for other materials.	System malfunction
Structural failure	MI	System malfunction System failure.	Redesign for higher loads. Improve tests.	System malfunction. System failure.
Distortion	MI	System malfunction.	Redesign for higher loads.	System malfunction.
Pivot fatigue	MI	System malfunction. System failure.	Redesign for higher loads. Change pivot point.	System malfunction. System failure.